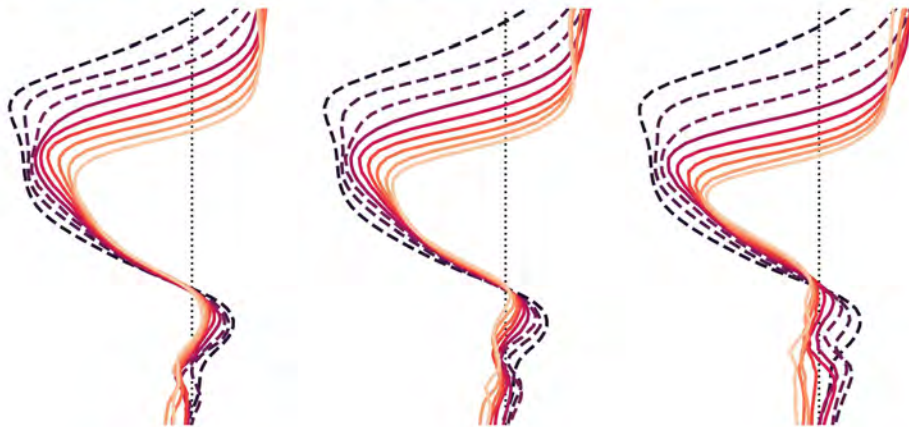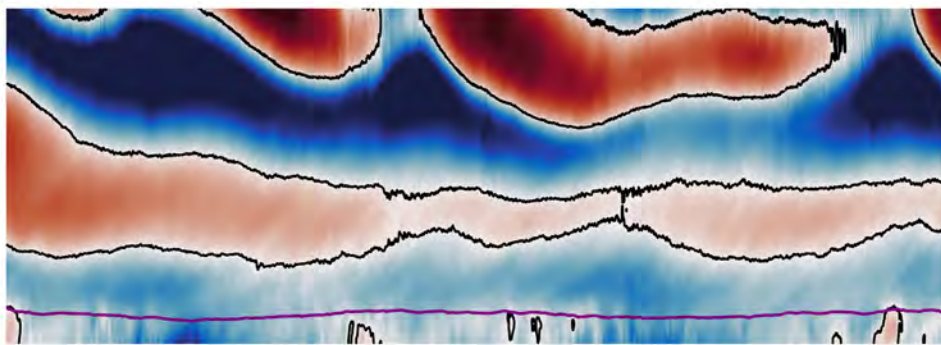# The Quasi-Biennial Oscillation in a Warming Climate

Henning Franke

Hamburg 2024

Hinweis

Die Berichte zur Erdsystemforschung werden vom Max-Planck-Institut für Meteorologie in Hamburg in unregelmäßiger Abfolge heraus-gegeben.

Sie enthalten wissenschaftliche und technische Beiträge, inklusive Dissertationen.

Die Beiträge geben nicht notwendigerweise die Auffassung des Instituts wieder.

Die "Berichte zur Erdsystemforschung" führen die vorherigen Reihen "Reports" und "Examens-arbeiten" weiter.

Anschrift / Address

Max-Planck-Institut für Meteorologie
Bundesstrasse 53
20146 Hamburg
Deutschland

Tel./Phone: +49   (0)40 4 11 73 - 0
Fax: +49   (0)40 4 11 73 - 298

name.surname@mpimet.mpg.de
www.mpimet.mpg.de

Notice

The Reports on Earth System Science are published by the Max Planck Institute for Meteorology in Hamburg. They appear in irregular intervals.

They contain scientific and technical contribu-tions, including PhD theses.

The Reports do not necessarily reflect the opinion of the Institute.

The "Reports on Earth System Science" continue the former "Reports" and "Examensarbeiten" of the Max Planck Institute.

Layout

Bettina Diallo and Norbert P. Noreiks Communication

Copyright

Photos below: ©MPI-M
Photos on the back from left to right:
Christian Klepp, Jochem Marotzke,
Christian Klepp, Clotilde Dubois,
Christian Klepp, Katsumasa Tanaka

Henning Franke

aus Sulingen, Deutschland

Max-Planck-Institut für Meteorologie
The International Max Planck Research School on Earth System Modelling
(IMPRS-ESM)
Bundesstrasse 53
20146 Hamburg

Tag der Disputation: 5. April 2024

Folgende Gutachter empfehlen die Annahme der Dissertation:
Prof. Dr. Bjorn Stevens
Dr. Marco A. Giorgetta

Vorsitzender des Promotionsausschusses:
Prof. Dr. Hermann Held

Dekan der MIN-Fakultät:
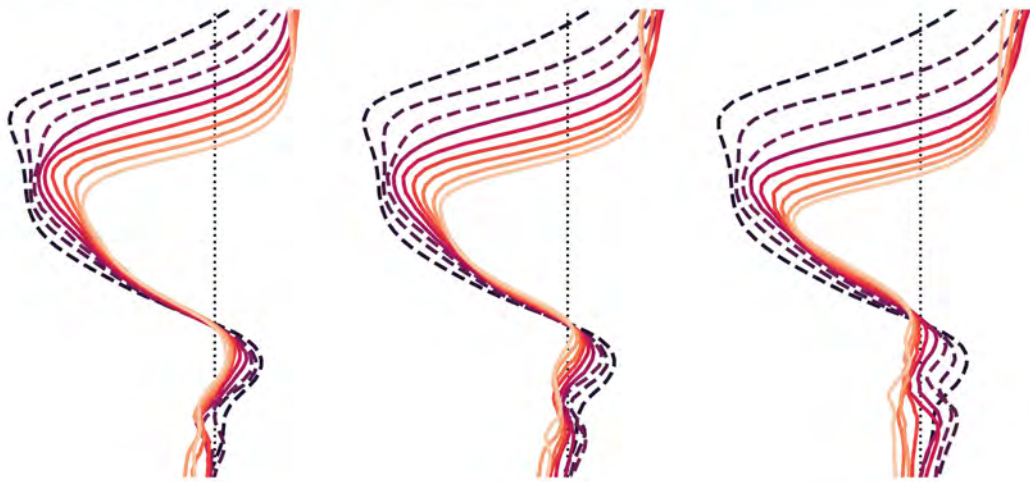Prof. Dr.-Ing. Norbert Ritter
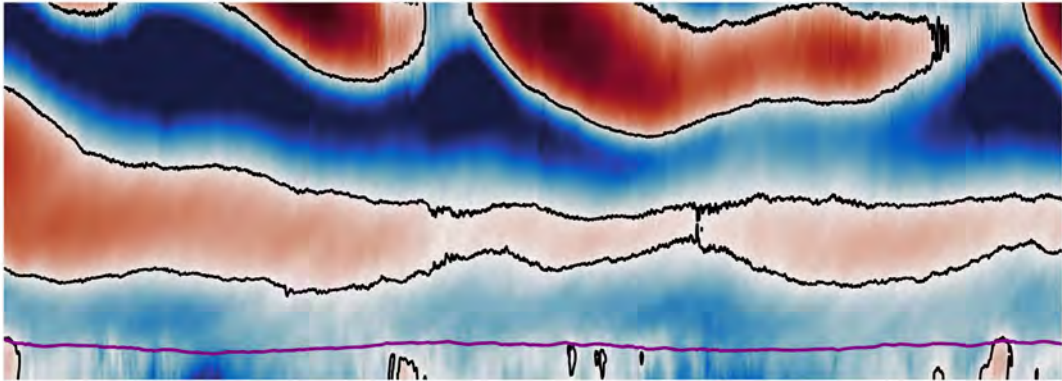
Titelgrafik: von Henning Franke
Top: Time-altitude cross section of QBO-like zonal winds as simulated by the global storm-resolving model ICON over a period of two years. Bottom: Downward propagation of QBO-like zonal wind jets with time as simulated by ICON for three different climate states.

The Quasi-Biennial Oscillation in a Warming Climate

Henning Franke

Hamburg 2024

ABSTRACT

The quasi-biennial oscillation (QBO) of the tropical stratosphere is characterized by the alternating descent of easterly and westerly wind jets and has a period of about 28 months. The QBO is driven by a broad spectrum of upward propagating waves which are generated by tropical deep convection, including small-scale gravity waves. Deep convection and small-scale gravity waves typically have to be parameterized in conventional general circulation models and the inherent uncertainties in these parameterizations lead to large uncertainties with regard to possible changes of the QBO due to global warming. These uncertainties could be reduced by global storm-resolving models (GSRMs), which no longer parameterize deep convection and gravity waves, but instead simulate both processes explicitly by employing a high horizontal resolution. However, so far no direct simulation of the QBO in a GSRM has been attempted. In this dissertation, I thus explore how the dynamics of the QBO are represented in a state-of-the-art GSRM and how the gravity wave forcing of the QBO and the QBO itself respond to a warming climate in such a model.

In the first part of this dissertation, I show that a state-of-the-art GSRM with a horizontal resolution of about 5 km is, in principle, capable of adequately representing the fundamental dynamics driving the QBO. In the lowermost stratosphere, however, the downward propagation of the QBO jets stalls and their magnitude is weaker than observed. As a consequence, the model does not simulate a closed QBO cycle. The stalling of the QBO is caused by an underestimation of its planetary-scale wave forcing, which I attribute to a pronounced lack of convectively coupled equatorial waves in the tropical troposphere. Thus, I conclude that the realistic representation of large-scale spatio-temporal variability of tropical deep convection is currently the main roadblock towards a direct simulation of the QBO in the present GSRM.

In the second part of this dissertation, I use the same state-of-the-art GSRM to investigate how the gravity wave forcing of the QBO responds to an idealized warming. I show that the gravity wave sources become stronger in a warmer climate, and thus generate gravity waves with a larger amplitude. As a consequence, the gravity wave momentum flux entering the lower stratosphere becomes larger and the downward propagation of the QBO jets becomes faster. Furthermore, I show that the gravity wave spectrum shifts towards larger zonal phase speeds in a warmer climate, which I attribute to a warming-induced deepening of tropical deep convection. As a result, the QBO jets in the upper QBO domain become stronger. Thereby, my work provides a simple conceptual argument that can explain the observed increase in QBO amplitude in the upper QBO domain over the last 65 years, during which a warming of about 1 K has already been observed.

In summary, this dissertation demonstrates the chances of direct QBO simulations by GSRMs and in particular their potential for better understanding and constraining the response of the QBO to global warming. However, to fully exploit this potential in the present GSRM, its current QBO biases need to be resolved.

ZUSAMMENFASSUNG

Die quasi-bienniale Oszillation (engl. *quasi-biennial oscillation*, QBO) der tropischen Stratosphäre ist durch sich abwechselnd abwärts bewegende östliche und westliche Windbänder gekennzeichnet und hat eine Periode von etwa 28 Monaten. Die QBO wird durch ein breites Spektrum sich vertikal ausbreitender Wellen angetrieben, einschließlich kleinskaliger Schwerewellen, die alle durch tiefe Konvektion in den Tropen angeregt werden. Tiefe Konvektion und kleinskalige Schwerewellen müssen in konventionellen globalen Zirkulationsmodellen jedoch typischerweise parametrisiert werden, und die inhärenten Unsicherheiten dieser Parametrisierungen führen zu großen Unsicherheiten in Hinblick auf mögliche Änderungen der QBO aufgrund der globalen Erwärmung. Diese Unsicherheiten könnten durch globale konvektionsauflösende Modelle (engl. *Global Storm Resolving Models*, GSRMs) reduziert werden, die tiefe Konvektion und Schwerewellen nicht mehr parametrisieren, sondern beide Prozesse explizit simulieren, indem sie eine sehr hohe horizontale Auflösung verwenden. In dieser Dissertation untersuche ich, wie ein modernes GSRM die Dynamik der QBO darstellt und wie der Schwerewellenantrieb der QBO und die QBO selbst in einem solchen Modell auf eine Klimaerwärmung reagiert.

Im ersten Teil dieser Dissertation zeige ich, dass ein GSRM auf dem aktuellen Stand der Technik mit einer horizontalen Auflösung von etwa 5 km prinzipiell in der Lage ist, die grundlegende Dynamik der QBO adäquat darzustellen. In der untersten Stratosphäre kommt die Abwärtsbewegung der QBO-Winde jedoch zum Stillstand, und die Stärke der Winde ist geringer als beobachtet. Aus diesem Grund simuliert das Modell keinen vollständigen Zyklus der QBO. Der Stillstand der QBO ist auf eine Unterschätzung ihres Antriebs durch planetare Wellen zurückzuführen, die ich wiederum auf eine deutliche Unterschätzung von konvektiv gekoppelten äquatorialen Wellen in der tropischen Troposphäre zurückführe. Daraus schließe ich, dass die realistische Darstellung der großskaligen räumlich-zeitlichen Variabilität der tropischen tiefen Konvektion derzeit das größte Hindernis für eine direkte Simulation der QBO in dem vorliegenden GSRM ist.

Im zweiten Teil dieser Dissertation benutze ich dasselbe hochmoderne GSRM, um herauszufinden, wie der Schwerewellenantrieb der QBO auf eine idealisierte Erwärmung reagiert. Ich zeige, dass die Quellen der Schwerewellen in einem wärmeren Klima stärker werden und daher Schwerewellen mit größeren Amplituden erzeugen. Infolgedessen wird auch der mit den Schwerewellen verbundene Impulsfluss in die untere Stratosphäre stärker und die Abwärtsbewegung der QBO-Jets beschleunigt sich. Außerdem zeige ich, dass sich das Spektrum der Schwerewellen in einem wärmeren Klima hin zu höheren zonalen Phasengeschwindigkeiten verschiebt, was ich auf eine durch die Erwärmung bedingte größere vertikale Ausdehnung der tiefen Konvektion zurückführe. Infolgedessen werden die QBO-Winde im oberen Teil der QBO stärker. Damit liefert meine Arbeit ein einfaches konzeptionelles Argument, das die beobachtete Zunahme der QBO-Amplitude im oberen Bereich der QBO in den letzten 65 Jahren erklären könnte, in denen bereits eine Erwärmung von etwa 1 K beobachtet wurde.

Zusammenfassend zeigt diese Dissertation die Chancen direkter Simulationen der QBO durch GSRMs und insbesondere ihr Potential, die Reaktion der QBO auf die globale Erwärmung besser zu verstehen und einzugrenzen. Um dieses Potenzial im vorliegeden GSRM voll auszuschöpfen, müssen jedoch dessen derzeitige Fehler in der Darstellung der QBO beseitigt werden.

PUBLICATIONS

The following two publications are part of this dissertation and are included in the appendix:

Appendix A

H. Franke and M. Giorgetta (2024). "Towards a direct simulation of a full cycle of the quasi-biennial oscillation in a global storm-resolving model." In: *preparation for submission to the Journal of Advances in Modeling Earth Systems*

Appendix B

H. Franke, P. Preusse, and M. Giorgetta (2023a). "Changes of tropical gravity waves and the quasi-biennial oscillation in storm-resolving simulations of idealized global warming." In: *Quarterly Journal of the Royal Meteorological Society* 149.756, pp. 2838–2860. DOI: 10.1002/qj.4534

As a PhD student, I have contributed to four other publications, one of which is a first-author publication based on the results of my master's thesis:

M. A. Giorgetta, W. Sawyer, X. Lapillonne, P. Adamidis, D. Alexeev, V. Clément, R. Dietlicher, J. F. Engels, M. Esch, **H. Franke**, C. Frauen, W. M. Hannah, B. R. Hillman, L. Kornblueh, P. Marti, M. R. Norman, R. Pincus, S. Rast, D. Reinert, R. Schnur, U. Schulzweida, and B. Stevens (2022). "The ICON-A model for direct QBO simulations on GPUs (version icon-cscs:baf28a514)." In: *Geoscientific Model Development* 15.18, pp. 6985–7016. DOI: 10.5194/gmd-15-6985-2022

H. Franke, U. Niemeier, and D. Visioni (2021). "Differences in the quasi-biennial oscillation response to stratospheric aerosol modification depending on injection strategy and species." In: *Atmospheric Chemistry and Physics* 21.11, pp. 8615–8635. DOI: 10.5194/acp-21-8615-2021

D. K. Weisenstein, D. Visioni, **H. Franke**, U. Niemeier, S. Vattioni, G. Chiodo, T. Peter, and D. W. Keith (2022). "An interactive stratospheric aerosol model intercomparison of solar geoengineering by stratospheric injection of SO_2 or accumulation-mode sulfuric acid aerosols." In: *Atmospheric Chemistry and Physics* 22.5, pp. 2955–2973. DOI: 10.5194/acp-22-2955-2022

I. Quaglia, C. Timmreck, U. Niemeier, D. Visioni, G. Pitari, C. Brodowsky, C. Brühl, S. S. Dhomse, **H. Franke**, A. Laakso, G. W. Mann, E. Rozanov, and T. Sukhodolov (2023). "Interactive stratospheric aerosol models' response to different amounts and altitudes of SO_2 injection during the 1991 Pinatubo eruption." In: *Atmospheric Chemistry and Physics* 23.2, pp. 921–948. DOI: 10.5194/acp-23-921-2023

ACKNOWLEDGMENTS

When I started studying Meteorology almost ten years ago, I could never have imagined that one day I would be on the verge of submitting a dissertation. Of course, this would not have been possible without the support of many people, to whom I would like to express my gratitude at this point.

First of all, I would like to thank my PhD supervisors Marco Giorgetta and Ulrike Niemeier for their continuous support over the last three and a half years. Thank you, Marco, for giving me the guidance and advice I needed, while allowing me to develop my work and ideas freely and independently. I feel very fortunate to have had a supervisor whose door was always open, who always took the time necessary to answer my questions thoroughly, and who shared his vast knowledge of ICON and the QBO, from which I benefited greatly. Thank you, Ulrike, for always motivating and supporting me, especially when some of my simulations and analyses didn't work out again. Discussing my results with you helped me a lot to reflect on my own work and to condense my ideas. I would also like to thank my Panel Chair Bjorn Stevens for monitoring the progress of my PhD project, for intervening when I was in danger of losing sight of the bigger picture, and for providing a lot of inspiration.

In addition, many people who were not officially involved in my supervision helped me a lot during my PhD. Here, special thanks go out to all members of the *Wave Driven Circulations* research group during the last three and a half years: Monika Esch, Renate Brokopf, Andrea Schneidereit, Sebastián Ortega, and Janina Tschirschwitz. Without your support in various forms, be it technical help, provision of analysis software and quickplots, or fruitful discussions, I doubt I would have made it to the finish line of my PhD. Furthermore, I have benefited from the support of many other colleagues at the MPI-M, three of whom I would like to thank in particular: Luis Kornblueh, for his immense technical support in getting ICON and other software to work on the various HPC systems I used throughout my PhD, Clarissa Kroll for many valuable discussions about our science, and Angel Peinado for being a great office mate. In addition to my colleagues at the MPI-M, I would like to thank Peter Preusse, Manfred Ern, and Dina Khordakova at the Forschungszentrum Jülich for discussing my results with me during the various QUBICC project meetings and for patiently teaching me the S3D analysis software.

Any piece of writing needs objective feedback for improvement. Therefore, I would like to thank Ulrike, Clarissa, Sebastián, Janina, Lara, and Daniel for their constructive and very valuable feedback on earlier versions of this dissertation.

I consider myself very lucky to have been part of such a great graduate school as the IMPRS-ESM, and it was a pleasure to meet and work with so many other smart and inspiring PhD students from many different cultures. I also benefited a lot from the straightforward administrative support of the IMPRS office, which made all the more or less bureaucratic aspects of my PhD run very smoothly. Therefore, I would like to express my gratitude to the IMPRS office team: Connie, Michaela, and especially Antje.

Last but not least, I am incredibly grateful for all of my friends and family. To my friends back home in Siedenburg and Sulingen, and to all my friends in Hamburg, my second home: Thank you for always reminding me that there is so much more to life than science, for providing the necessary and recharging distractions, and for always giving me something to look forward to. And finally, but most importantly, to my parents and my sister: Thank you for always backing me up, for always encouraging me to follow my interests, and for unconditionally supporting me in everything I do — without you I would not have made it this far.

CONTENTS

BDC Brewer-Dobson circulation

CCEW Convectively coupled equatorial wave

CMIP Coupled Model Intercomparison Project

CMIP5 Coupled Model Intercomparison Project phase 5

CMIP6 Coupled Model Intercomparison Project phase 6

CPU Central Processing Unit

ERA5 ECMWF Reanalysis v5

EP Eliassen-Palm

FFT Fast Fourier transform

GCM General circulation model

GPU Graphics processing unit

GSRM Global storm-resolving model

GW Gravity wave

GWMF Gravity wave momentum flux

HPC High-performance computing

ICON Icosahedral Nonhydrostatic

IMERG Integrated Multi-satellite Retrievals for the Global Precipitation Measurement

ITCZ Intertropical Convergence Zone

MJO Madden-Julian oscillation

MRG Mixed Rossby-gravity

QBO Quasi-biennial oscillation

QBOi Quasi-Biennial Oscillation initiative

SAO Semiannual oscillation

SDPD Simulated days per day

SEW Stratospheric equatorial wave

SIC Sea ice concentration

SMC Secondary meridional circulation

SST Sea surface temperature

TEM Transformed Eulerian mean

TTL Tropical tropopause layer

Part I

UNIFYING ESSAY

INTRODUCTION

Perhaps a simple explanation will soon be found, and what now seems an intriguing mystery will be relegated to the category of a meteorological freak.

— *Reed (1967) on the recently discovered QBO*

To find the origins of this dissertation, we have to travel back in space and time to today's Indonesia in late August of 1883. Here, in the Sunda Strait between Java and Sumatra, one of the most devastating volcanic eruptions of the last centuries took place: The eruption of Mt. Krakatau on August 27, 1883. While undoubtedly a huge human tragedy, this eruption also marks the beginning of a remarkable voyage of discovery in the tropical stratosphere.

The eruption ejected massive amounts of ash into the lower stratosphere, which enabled the very first direct observations of stratospheric winds in the tropics. It was soon realized that these winds were easterly, which led to them becoming known as "Krakatau easterlies" (Russell, 1888). In 1908, however, balloon measurements in equatorial East Africa revealed westerly winds near the tropopause, which became known as the "Berson westerlies" after their discoverer A. Berson. It was not until the 1960s that the seemingly contradictory "Krakatau easterlies" and "Berson westerlies" could finally be explained as one and the same phenomenon. Based on much more regular balloon observations in the context of nuclear weapon testing, Ebdon (1960) and Reed et al. (1961) independently showed that the winds in the tropical stratosphere are characterized by an alternating downward propagation of zonally symmetric easterly and westerly wind jets, as shown in Figure 1.1. These jets originate in the upper stratosphere and vanish near the tropopause, and at every altitude in between, the resulting oscillation in the zonal wind was found to have a period of slightly more than two years (Veryard and Ebdon, 1961). This fact led Angell and Korshover (1964) to term the newly discovered phenomenon the *quasi-biennial oscillation (QBO)* — a term that later became generally accepted.

However, when we turn from the history of the QBO to its future, things become much less clear. Although it is generally expected that the QBO could change substantially as anthropogenic global warming progresses, Richter et al. (2020b) demonstrated that the details of these changes and their magnitude are highly uncertain. They showed that the root cause of this uncertainty lies in the deficiencies of conventional climate models in representing the gravity wave forcing of the QBO. Motivated by the current uncertainty in QBO projections, in this dissertation I aim to shed light on the question of how the QBO might respond to global warming by using a fundamentally new approach to modeling it.

Before outlining the current gap in understanding the QBO's response to global warming and my approach to filling it in more detail, I will first provide some background on the QBO.

1.1.1 *The QBO and its relevance to the global climate system*

The QBO is the dominant mode of internal variability in the lower tropical strato-
sphere, i.e. between 17 km and 35 km (Wallace, 1973; Baldwin et al., 2001). Its
morphology is nowadays well established, based on the ever-growing amount of
balloon-borne observations of the tropical stratosphere since the 1950s (Naujokat,
1986; Schenzinger et al., 2017). The QBO has an average period of 28 months, with a
substantial cycle-to-cycle variability ranging from 20–34 months. The average ampli-
tude of the QBO depends strongly on altitude and peaks at around 15 hPa, where
the easterly and westerly jets reach a velocity of about $-30\,\mathrm{m\,s^{-1}}$ and $+15\,\mathrm{m\,s^{-1}}$,
respectively. The QBO is further characterized by a pronounced asymmetry in
the lowermost stratosphere, where the westerly phase lasts much longer than the
easterly phase (see Fig. 1.1). With growing distance from the equator, the amplitude
of the QBO decreases rapidly, so that its latitudinal extent ranges from about 10°S
to about 10°N, depending on the exact definition (Dunkerton and Delisi, 1985;
Schenzinger et al., 2017). After having been quasi-regular for at least 60 years, the
QBO was disrupted twice in a row in the boreal winters of 2015/16 and 2019/20
(see Fig. 1.1).

As discovered by Reed (1964) and Angell and Korshover (1964), the QBO does
not only exhibit a pronounced signal in zonal wind, but also in temperature. The
temperature signature of the QBO has an amplitude of about 4 K and emerges as
a consequence of the rising and sinking motions associated with the secondary
meridional circulation (SMC) of the QBO (Baldwin et al., 2001). The SMC itself
emerges in order to restore thermal wind balance within the shear zones of the
QBO (Plumb and Bell, 1982) and modifies the mean meridional circulation in the
tropical stratosphere.

As a result of the QBO-induced temperature anomalies and the varying transport
patterns associated with the SMC, the QBO further exhibits a clear signature in
many stratospheric trace gases (Zawodny and McCormick, 1991; Dunkerton, 2001;
Shuckburgh et al., 2001; Schoeberl et al., 2008), in particular ozone (Reed, 1964;
Gray and Pyle, 1989; Logan et al., 2003). This signature can be usually found in
both the tropical and extratropical stratosphere. The QBO-induced temperature
anomalies also modify the temperature of the tropical tropopause layer (TTL),
which determines how much water vapour enters the tropical stratosphere (Brewer,
1949; Mote et al., 1996). Therefore, the QBO also influences stratospheric water
vapour (Randel et al., 1998; Geller et al., 2002; Fueglistaler and Haynes, 2005). In
addition, the QBO affects the transport of ash and sulfate aerosols after strong
tropical volcanic eruptions (Trepte and Hitchman, 1992; Hitchman et al., 1994; Choi
et al., 1998).

The QBO further has a well-known impact on the circulation in the troposphere
in the form of various teleconnections. In the tropics, a clear QBO signature in deep
convection (Collimore et al., 2003; Liess and Geller, 2012; Gray et al., 2018) and
related phenomena such as monsoons (Giorgetta et al., 1999) or the Madden-Julian
oscillation (MJO; Yoo and Son, 2016; Son et al., 2017; Martin et al., 2021) has been
found. The tropical QBO teleconnections are mostly attributed to the QBO-induced
modification of the temperatures and winds in the TTL (Gray et al., 2018; Hitchman
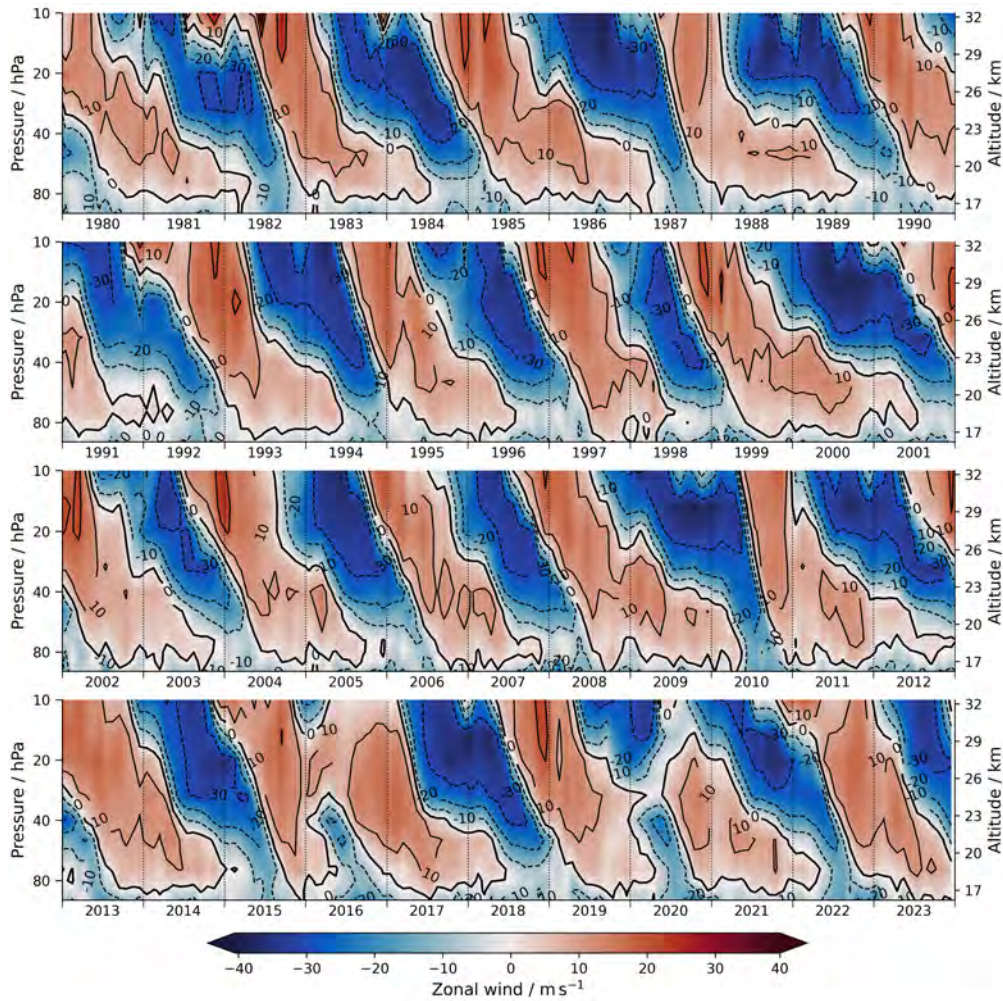
Figure 1.1: Time-altitude cross section of the zonal wind measured by radiosondes launched in Singapore (1.3° N, 103.9° E). Red colors indicate westerly winds and blue colors indicate easterly winds. Contour lines mark isotachs in intervals of $10\,\text{ms}^{-1}$ with the $0\,\text{ms}^{-1}$-isotach highlighted by a thicker contour. Altitude values on the right ordinate are only given for reference and have been calculated from pressure values by the hydrostatic equation with a constant scale height of $7\,\text{km}$ and a surface pressure of $1013.25\,\text{hPa}$. Data courtesy: NASA/GSFC (2024).

et al., 2021; Anstey et al., 2022a). In contrast, the extratropical teleconnections of the QBO are mostly a result of its direct influence on the wintertime stratospheric polar vortices, especially in the Northern Hemisphere (Holton and Tan, 1980; Anstey and Shepherd, 2014), but also in the Southern Hemisphere (Baldwin and Dunkerton, 1998). The modification of the polar vortex by the QBO is often also referred to as the Holton-Tan mechanism (Holton and Tan, 1980). As the Northern Hemispheric polar vortex itself has a profound impact on the boreal tropospheric winds and surface pressure (Baldwin et al., 2021; Kidston et al., 2015), the QBO ultimately also has a signature in boreal surface winter weather (Anstey and Shepherd, 2014; Gray et al., 2018). Given the high long-range QBO predictability of multiple months ahead (Scaife et al., 2014; Stockdale et al., 2020), the QBO teleconnections offer a great potential for subseasonal to seasonal predictions in the troposphere (e.g., Boer and Hamilton, 2008; Lim et al., 2019).

1.1.2   *The basic dynamics of the QBO*

Based on the concurrent breakthroughs in atmospheric wave theory (Matsuno, 1966; Booker and Bretherton, 1967), Lindzen and Holton (1968) and Holton and Lindzen (1972) presented the fundamental mechanism explaining the downward propagation of the QBO soon after the QBO's discovery. According to their theory, the downward propagation of the QBO is driven by an alternating filtering and dissipation of upward propagating waves originating from the tropical troposphere. This mechanism — slightly updated — is still the accepted standard paradigm for explaining the QBO today. In the following, I will explain the QBO mechanism in more detail.

According to linear theory, the upward propagation of a wave with zonal phase speed c_x depends fundamentally on the zonal background wind $\overline{u}$ (see, e.g., Fritts and Alexander, 2003): eastward propagating waves can only propagate upward for $c_x > \overline{u}$, while westward propagating waves can only propagate upward for $c_x < \overline{u}$. Depending on the profile of the zonal background wind, i.e., the QBO zonal wind profile, waves generally continue to propagate upward until their zonal phase speed approaches the background wind. The altitude where $c_x = \overline{u}$ marks the so-called critical level of the wave. Here, the wave can no longer propagate further upward and is therefore dissipated very efficiently by various mechanisms such as wave breaking, radiative damping, and mechanical damping. As part of the dissipation process, the momentum carried by the wave is transferred to the mean flow, locally accelerating it toward the phase speed of the wave. This process, which I will refer to as the *QBO wave forcing* from now on, ultimately causes the downward propagation of the QBO jets until they dissipate near the TTL.

The QBO mechanism is illustrated by Figure 1.2 for two upward propagating waves with equal zonal phase speeds c_x of opposite sign, in this case $c_x = \pm 25\,\mathrm{m\,s^{-1}}$. In the case of the QBO zonal wind profile shown in the left part of Figure 1.2, the westward propagating wave can propagate upward throughout the westerly QBO jet until it reaches its critical level in the easterly shear zone around 32 km, where it dissipates and exerts a local westward acceleration driving the downward propagation of the easterly jet aloft. In contrast, the eastward propagating wave cannot propagate through the QBO westerly jet in the lowermost stratosphere, as the zonal phase speed of the wave gets close to the zonal background wind. Thus, the wave is already efficiently damped in the westerly shear zone around 20 km and drives the downward propagation of the westerly QBO jet aloft. In the case of the QBO zonal wind profile shown in the right part of Figure 1.2, the same process occurs the other way around.

The wave spectrum that drives the QBO is predominantly excited by tropical deep convection in the troposphere. It is broad, ranging from equatorially trapped planetary-scale waves, such as equatorial Kelvin waves or mixed Rossby-gravity (MRG) waves, down to small-scale gravity waves with horizontal wavelengths as short as $\mathcal{O}(10\,\mathrm{km})$ (Dunkerton, 1997). Currently, it is assumed that gravity waves provide about half of the eastward momentum necessary to drive the downward propagation of the westerly QBO jet, and the majority of the westward momentum necessary to drive the downward propagation of the easterly QBO jet (Anstey et al., 2022a). The remaining eastward momentum is mainly provided by equatorial Kelvin waves, while the remaining westward momentum is mainly provided by
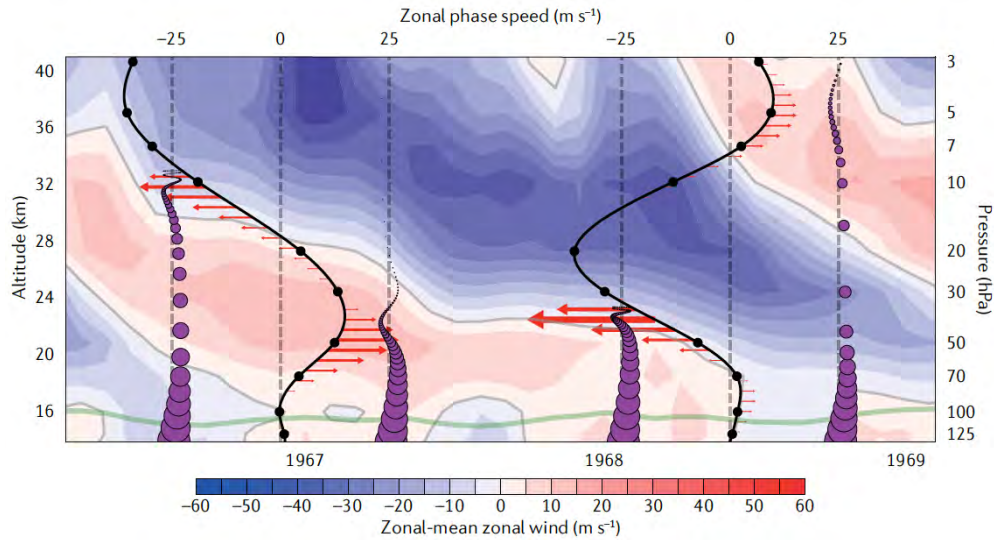
Figure 1.2: Schematic illustration of the QBO mechanism based on one full QBO cycle. The color shading shows a time-altitude cross section of the monthly and zonal mean zonal wind from the JRA-55 reanalysis (Kobayashi et al., 2015). The two thick black lines represent two idealized profiles of the monthly and zonal mean zonal wind in December 1966 (left profile) and June 1968 (right profile) with the zonal wind speed given on the upper abscissa. The purple dots associated with each profile represent the zonal momentum carried by two waves with $\pm 25\,\mathrm{m\,s^{-1}}$, with the area of the dots being proportional to the zonal momentum reaching that level. The decrease in area highlights the convergence of the momentum flux close to the critical levels of the waves. The local zonal acceleration of the zonal wind due to the convergence of the wave momentum flux is indicated by the red arrows. The green line shows the altitude of the tropopause for reference. This illustration is taken from Anstey et al. (2022a) and originally partly based on Match and Fueglistaler (2021).

equatorial Rossby and MRG waves. However, the exact partitioning of different wave modes in driving the QBO is still uncertain and not conclusively clarified (see Anstey et al., 2022a, and references therein).

The wave-driven downward propagation of the QBO is substantially slowed down by the vertical advection of zonal momentum by the tropical upwelling associated with the rising branch of the Brewer-Dobson circulation (BDC; Saravanan, 1990; Dunkerton, 1991). The resulting balance between the vertical advection and the QBO wave forcing determines, to a good approximation, the rate of QBO downward propagation and, ultimately, the QBO period. This basic momentum balance forms the essence of simple mechanistic one- and two-dimensional models of the QBO, which have proven sufficient to understand many of its fundamental aspects (Lindzen and Holton, 1968; Holton and Lindzen, 1972; Plumb, 1977; Plumb and Bell, 1982; Saravanan, 1990). The contribution of meridional advection of zonal momentum and of dissipation of meridionally propagating waves to the QBO momentum balance is usually small (Baldwin et al., 2001). Nevertheless, the momentum provided by the dissipation of meridionally propagating waves can be at times important as demonstrated by the recent QBO disruptions, which have been caused by anomalous wave momentum fluxes associated with equatorward propagating extratropical Rossby waves (Osprey et al., 2016; Anstey et al., 2021).

1.1.3 *Modeling the QBO in conventional GCMs*

In light of the various impacts of the QBO on the global climate system, it is desirable for a general circulation model (GCM) to have a realistic representation of the QBO. However, modeling the QBO still poses a major challenge to what I will refer to as *conventional GCMs*, that are global atmospheric GCMs with a horizontal grid spacing of $\mathcal{O}(100\,\mathrm{km})$, which requires these models to employ a parameterization of deep convection and, in most cases, gravity waves. For example, even in the Coupled Model Intercomparison Project (CMIP) phase 6 (CMIP6) just 15 out of 30 participating models generated a realistic QBO (Richter et al., 2020a). In this section, I will present the difficulties of simulating the QBO in conventional GCMs in more detail, since they are closely related to the current limitations in the understanding of how the QBO may respond to a warming climate.

The reasonable representation of the QBO in conventional GCMs depends on many factors and their subtle interaction with each other (Baldwin et al., 2001; Anstey et al., 2022a). Hence, there is no simple recipe for successfully modeling the QBO in a conventional GCM, and it is usually achieved by thorough parameter tuning of the model. Nevertheless, some factors have been identified to be important. First, the parameterization of deep convection must ensure a reasonable spatio-temporal variability of tropical deep convection in order to generate a broad spectrum of explicitly resolved tropical waves (Ricciardulli and Garcia, 2000; Horinouchi et al., 2003). Second, the vertical resolution of the model must be sufficiently fine to resolve the vertical propagation and the wave-mean flow interactions of resolved waves with short vertical wavelengths. This usually requires a vertical grid spacing of less than 1 km in the stratosphere (Boville and Randel, 1992; Giorgetta et al., 2006; Geller et al., 2016a; Garfinkel et al., 2022). Third, the diffusion and damping employed by the model must not be too strong in order to achieve the propagation of the resolved waves close to their critical levels without them being excessively damped before (Takahashi, 1996, 1999). A sufficiently weak damping and diffusion also ensures that the QBO jets are not damped directly (Scaife et al., 2002). Fourth, conventional GCMs with a reasonable model setup typically require a well-tuned non-orographic gravity wave parameterization (Scaife et al., 2000; Giorgetta et al., 2002; Giorgetta et al., 2006; Bushell et al., 2020).

Ensuring the first three factors in combination with a rather high horizontal resolution can be already sufficient to generate a QBO-like oscillation in a conventional GCM without the need for any parameterized gravity wave effects (Takahashi, 1996, 1999; Hamilton et al., 1999, 2001; Kawatani et al., 2010a,b). However, such simulations typically require exceptionally weak diffusion or overly active convection schemes to the detriment of other aspects of the simulated climate, and the resulting QBO attains rather unrealistic periods and amplitudes. Therefore, the fourth factor, a well-tuned gravity wave parameterization, is indeed required for a successful simulation of the QBO.

Non-orographic gravity wave parameterizations account for small-scale gravity waves that are not resolved explicitly by the model but substantially contribute to driving the downward propagation of the QBO. Like all parameterizations, also gravity wave parametrizations are inherently uncertain, as they are an empirical representation of the underlying physics with corresponding simplifications. For gravity wave parameterizations, the major simplifications are that they only allow

for instantaneous and vertical wave propagation, and that they mostly prescribe a fixed gravity wave source spectrum instead of coupling it to deep convection (Plougonven et al., 2020). The prescribed gravity wave source spectrum is still poorly constrained by observations (Alexander et al., 2010) and is thus typically used as a default screw to tune the model QBO towards the observed one (e.g., Garfinkel et al., 2022). In some more advanced gravity wave parameterizations, the source spectrum is coupled directly or indirectly to the simulated convective latent heating field and is thus more physics-based (e.g., Beres et al., 2004; Richter et al., 2010; Bushell et al., 2015). However, the latent heating field is calculated by the parameterization of deep convection, which introduces new uncertainties to the gravity wave source spectrum.

The parameterization of deep convection further has a control on the resolved wave forcing of the QBO (Ricciardulli and Garcia, 2000; Horinouchi et al., 2003), as it impacts the representation of convectively coupled equatorial waves (CCEWs) in the tropical troposphere (Straub et al., 2010; Frierson et al., 2011). CCEWs are closely coupled to the stratospheric equatorial waves (SEWs) that ultimately drive the QBO (e.g., Kawatani et al., 2009; Maury et al., 2013). Therefore, also the resolved wave forcing of the QBO in a conventional GCM must be considered uncertain.

The uncertainties in the resolved and parameterized wave forcing of the QBO associated with the parameterizations of deep convection and gravity waves impose substantial uncertainty to the overall momentum budget of the QBO. As shown in the recent model intercomparison project *Quasi-Biennial Oscillation initiative* (*QBOi*, Butchart et al., 2018), the relative contribution of parameterized gravity waves to the total wave forcing of the QBO is highly model-dependent and varies between 40 % and 80 % among the participating models (Bushell et al., 2020). As a result, the details of the QBO wave forcing are overall still uncertain, and thus the spatio-temporal structure of the modeled QBO itself also varies considerably among models (see left panel of Fig. 1.3).

The deficiencies of the parameterizations and their uncertainties likely also contribute to the systematic QBO biases in conventional GCMs, although their detailed root causes are still unclear (Anstey et al., 2022a). The most prominent systematic bias of the QBO is an underestimation of the QBO amplitude in the lowermost stratosphere (Bushell et al., 2020; Richter et al., 2020a), usually accompanied by a lack of QBO downward propagation to the tropopause (Stockdale et al., 2020). This bias is one reason for the fact that conventional GCMs typically underestimate QBO teleconnections (Kim et al., 2020; Anstey et al., 2022b).

1.2 THE SCIENTIFIC PROBLEM: RESPONSE OF THE QBO TO GLOBAL WARMING

After having provided the necessary background on the QBO, I will continue with discussing the current understanding of how the two main characteristics of the QBO — its period and amplitude — might respond to a warming climate. In doing so, I will work out the main uncertainties that motivate this dissertation.

From simple one-dimensional QBO theory, the response of the QBO period to possible warming-induced changes in its main forcing processes is well understood: a stronger QBO wave forcing would lead to a faster downward propagation of the QBO, and vice versa, while a stronger tropical upwelling would lead to a slower

downward propagation of the QBO, and vice versa. Depending on which effect dominates, the QBO period would become either shorter or longer in a warming climate. Practically, however, the response of the QBO period to a warming climate varies widely among conventional GCMs, which has already arisen from the synopsis of early single-model studies (Giorgetta and Doege, 2005; Kawatani et al., 2011; Watanabe and Kawatani, 2012). Even within the more recent multi-model frameworks of CMIP phase 5 (CMIP5, Kawatani and Hamilton, 2013), CMIP6 (Butchart et al., 2020), and QBOi (Richter et al., 2020b), some models show a shortening of the QBO period, while others show a lengthening or even collapse of the QBO (see Fig. 1.3). Therefore, the overall response of the QBO period to warming is still unclear.

Richter et al. (2020b) showed that this large uncertainty in QBO projections by conventional GCMs can be ultimately attributed to the uncertain response of the parameterized gravity wave forcing of the QBO to a warming climate. They found that, depending on the employed gravity wave parameterization, in some models the parameterized gravity wave forcing becomes slightly weaker or does not change at all in a warming climate, while in other models it becomes substantially stronger. This uncertainty is a consequence of the inherent conceptual limitations of the gravity wave parameterizations, which in most cases cannot adequately respond to the warming-induced intensification of tropical deep convection, especially if they impose a fixed gravity wave source spectrum. The results of Richter et al. (2020b) confirm previous work of Schirber et al. (2015), who showed that even the same GCM can either simulate a warming-induced shortening or lengthening of the QBO period, depending on the employed gravity wave parameterization.

The overall uncertainty in the response of the QBO period to a warming climate is further enhanced by the quantitative uncertainty in warming-induced changes in both the resolved planetary-scale wave forcing of the QBO and the tropical upwelling. While the changes in these two processes are at least qualitatively constrained — both processes are expected to become stronger in a warmer climate — their quantitative extent is still highly model-dependent (Richter et al., 2020b). In case of the planetary-scale wave forcing, this is mainly due to general uncertainties in the representation of CCEWs in conventional GCMs associated with the parameterization of deep convection (see Sec. 1.1.3). This uncertainty is further compounded by potential changes in upper-tropospheric wave filtering (Richter et al., 2020b), and the impact of increased radiative damping of waves in the QBO shear zones due to the increase in CO_2 concentrations (Zhou et al., 2021).

In contrast to the QBO period, the response of the QBO amplitude to a warming climate is better constrained, at least in the lowermost stratosphere. Here, conventional GCMs project a robust warming-induced weakening of the QBO amplitude (Kawatani et al., 2011; Kawatani and Hamilton, 2013; Butchart et al., 2020; Richter et al., 2020b). This result was found to be consistent with the observational record (Kawatani and Hamilton, 2013), which also shows a decreasing trend in the QBO amplitude in the lowermost stratosphere since the late 1950s, since when the climate has already warmed by about 1 K (NOAA/NCEI, 2022). In the upper QBO domain, however, the observational record shows an increase in QBO amplitude. This disagrees with projections by conventional GCMs, which show a consistent decrease in QBO amplitude throughout the whole vertical domain of the QBO (Butchart et al., 2020; Anstey et al., 2022a). The root cause of this discrepancy is currently
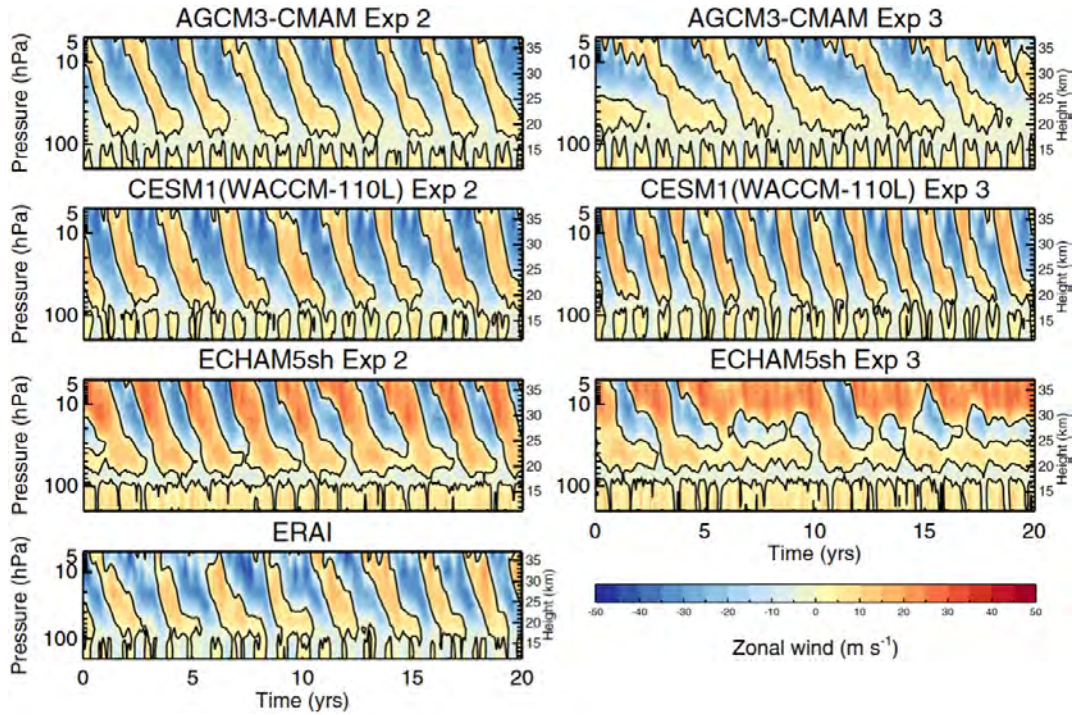
Figure 1.3: Illustration of current uncertainties in modeling the QBO based on results of the model intercomparison project QBOi (Butchart et al., 2018). The left panel shows the QBO as modeled by three of the participating models for a reference climate state representative for the end of the last century and as seen by the reanalysis ERA-Interim (ERAI, Dee et al., 2011) for the years 1979–1998. The right panel shows the QBO as modeled by the same three models for an idealized 2 K warmer climate state. This figure is adapted from Fig. 4 of Richter et al. (2020b).

unclear. In general, however, there are still doubts as to whether the observational trends in the QBO amplitude are statistically significant, since the observational period of the QBO is still comparatively short (Match and Fueglistaler, 2021).

The response of the QBO to global warming is further modified by ozone feedbacks (DallaSanta et al., 2021), and a warming may also lead to more frequent QBO disruptions similar to those observed in 2015/16 and 2019/20 (Anstey et al., 2021).

In light of the important role of the QBO in the climate system, it is clear that the current uncertainty in the response of the QBO, especially its period, to a warming climate needs to be reduced. Since this uncertainty is commonly attributed to the inability of gravity wave parameterizations to adequately respond to a warming climate (Schirber et al., 2015; Richter et al., 2020b), one must in particular understand how gravity waves generated by tropical deep convection respond to a warming climate. This motivates the overarching research question of this dissertation:

RQ1. How do the gravity waves that drive the QBO and the downward propagation of the QBO shear zones respond to a warming climate?

Obviously, I need a new modeling approach to answer this question, since the current one — modeling the QBO in conventional GCMs — works only to a limited extent, and it is questionable whether it will provide fundamental new insights in the foreseeable future.

1.3   MODELING APPROACH

In order to answer the overarching research question of this dissertation, I employ a fundamentally new class of GCMs to simulate the QBO: so-called *global storm-resolving models* (*GSRMs*; see Satoh et al., 2019, and references therein). Unlike conventional GCMs, GSRMs no longer parameterize deep convection, but instead simulate it explicitly by solving the non-hydrostatic equations on horizontal grids with a very fine grid spacing of $\mathcal{O}(1\,\mathrm{km})$–$\mathcal{O}(10\,\mathrm{km})$. As a result, simulations by GSRMs no longer suffer from the uncertainties associated with the parameterization of deep convection required in conventional GCMs. This has been shown to result in a multitude of benefits, including a reduction in long-standing biases of conventional GCMs and an overall more realistic simulated climate (e.g., Marsham et al., 2013; Prein et al., 2013; Satoh et al., 2017, 2019; Stevens et al., 2020). As a side effect, the very high horizontal resolution of GSRMs also allows them to explicitly simulate most of the gravity wave spectrum. For this reason, GSRMs generally no longer employ a gravity wave parameterization, and it has been shown that they are in principle capable of faithfully representing many aspects of the tropical stratospheric gravity wave spectrum (Müller et al., 2018; Stephan et al., 2019a,b; Polichtchouk et al., 2021).

The fact that GSRMs no longer suffer from the uncertainties associated with the parameterizations of deep convection and gravity waves makes them a promising tool for overcoming the uncertainties in QBO simulations by conventional GCMs. GSRMs are the first models that can, in principle, explicitly and self-consistently simulate the entire wave spectrum that drives the QBO, from its self-consistent generation by explicitly simulated deep convection all the way to explicitly simulated wave-mean flow interactions with the QBO jets. In doing so, GSRMs allow for a much more physics-based representation of the QBO than conventional GCMs, which has the potential to substantially advance our understanding of the QBO. From now on, I will thus refer to the simulation of the QBO in a GSRM as a *direct QBO simulation*.

Prior to this dissertation, no direct simulation of the QBO existed, mainly due to computational constraints. Due to their very high horizontal resolution, most GSRMs can only afford a relatively coarse vertical resolution of $\mathcal{O}(1\,\mathrm{km})$ or do not include the full stratosphere at all (Stevens et al., 2019, see their Tab. 2). Furthermore, simulations by GSRMs were usually only reasonably affordable for simulated periods of $\mathcal{O}(10\,\mathrm{days})$–$\mathcal{O}(100\,\mathrm{days})$, since their computational performance on high-performance computing (HPC) systems with a classic Central Processing Unit (CPU)[1] architecture was typically about 5 simulated days per day (SDPD; Stevens et al., 2019, see their Tab. 5). Since the simulation of the QBO typically requires a vertical resolution of less than 1 km in the stratosphere (see Sec. 1.1.3), and it would be further desirable to simulate at least one full QBO cycle ($\sim$28 months), a simulation of the QBO with a GSRM was simply not feasible so far.

For this reason, the code of the global storm-resolving Icosahedral Nonhydrostatic (ICON) model, developed jointly by the Max-Planck-Institute for Meteorology and the German weather service DWD, has recently been ported to run on HPC systems using hybrid graphics processing unit (GPU)[2] architectures (Giorgetta et al., 2022).

---

[1] CPUs are the standard class of computer processors.
[2] GPUs are a class of computer processors that are typically faster than CPUs.

The associated increase in model performance now allows the simulation of periods that would cover a full QBO cycle in a global storm-resolving model configuration with a high vertical resolution of well below 1 km throughout the stratosphere.

To answer RQ1, I thus use the GPU-enabled ICON model in a global storm-resolving configuration employing the R2B9 horizontal grid, which has a grid spacing of 4.93 km, with 191 vertical levels up to an altitude of 83 km, which results in a vertical grid spacing of about 350 m in the tropopause region and about 560 m in the stratopause region. From now on, I will refer to this configuration as the *R2B9L191 configuration*. The horizontal resolution of 4.93 km lies within the so-called *convective gray zone*, which encompasses horizontal resolutions where deep convection is partially but not entirely resolved, typically between $\mathcal{O}(1\,\text{km})$ and $\mathcal{O}(10\,\text{km})$. At this horizontal resolution, the full stratospheric gravity wave spectrum, which encompasses waves with horizontal wavelengths as short as 10 km (Preusse et al., 2008), is also not effectively resolved[3]. While some climate modelers are thus reluctant to switch off the corresponding parameterization within the gray zone, I argue that my explicit model configuration is justified and sufficient to gain the conceptual understanding necessary to answer RQ1. As shown by Hohenegger et al. (2020), the R2B9 grid of ICON simulates tropical deep convection overall realistically, and Vergara-Temprado et al. (2020) showed that the explicit simulation of deep convection leads to equal or better model skill than the parameterized representation of deep convection at horizontal resolutions throughout the gray zone. In addition, the total resolved tropical gravity wave momentum flux (GWMF) in the lower stratosphere has been found to be independent of horizontal resolution within the gray zone when deep convection is treated explicitly (Polichtchouk et al., 2021).

Since there has been no direct QBO simulation to date, the question naturally arises how the QBO and its dynamics are represented in a GSRM and whether it actually simulates a reasonable full QBO cycle at all. This leads to the second main research question of this dissertation:

RQ2. How well does a state-of-the-art GSRM simulate a full QBO cycle and its dynamics?

Please note that I will answer RQ2 before RQ1 in the further course of this dissertation, as this follows a more logical order with regard to my work. Before addressing these two research questions, however, I will take a step back and begin with a basic validation of my modeling approach.

---

3 The effective resolution of a GCM is the smallest scale that the GCM can reliably represent and is based on kinetic energy spectra (Skamarock, 2004). It is usually around 6–8 times the horizontal grid spacing.

BASIC VALIDATION OF MY MODELING APPROACH

Undoubtedly the most satisfactory way to model the quasi-biennial
oscillation will involve general circulation modeling
—— a "brute force" approach.

— Dunkerton (1985)

A direct simulation of the QBO would undoubtedly take the "brute force" approach envisioned by Dunkerton (1985) to its extreme, and it would open a whole new chapter in QBO modeling. However, attempting the simulation of a phenomenon with a fundamentally new class of models is usually a difficult and time-consuming task as there is not much practical experience or „common wisdom" to build on. Indeed, finding a long-term numerically stable setup of the R2B9L191 configuration of ICON that is in principle capable of simulating a wave-driven downward propagation of the QBO jets required many trials and iterations. Nevertheless, it was finally successful.

In the following, I will show that the R2B9L191 configuration of the GPU-enabled ICON (Giorgetta et al., 2022) is able to simulate a reasonable wave-driven downward propagation of the QBO jets. This is the basic proof of concept for my modeling approach, and parts of this work have been published in Giorgetta et al. (2022, see their Chp. 7). Subsequently, I will present the process of optimizing the parameter setting of the R2B9L191 configuration of ICON, which also helped to assess the robustness of my modeling approach.

2.1 PROOF OF CONCEPT: WAVE-DRIVEN DOWNWARD PROPAGATION OF QBO JETS

Figure 2.1a shows the spatio-temporal evolution of the QBO jets in the first successful direct QBO simulation using ICON over a period of 48 days. In this simulation, ICON simulates a notable downward propagation of the upper easterly QBO jet. This demonstrates that the R2B9L191 configuration of ICON is in principle capable of simulating the dynamics leading to a downward propagation of the QBO, at least during the considered short period. Nevertheless, the spatio-temporal structure of the simulated QBO jets still obtains some pronounced biases. This becomes obvious by a comparison to the QBO jets during the same period as represented in a corrected version of the ECMWF[1] Reanalysis v5 (ERA5; Hersbach et al., 2020), ERA5.1[2] (Fig. 2.1b). Most strikingly, the downward propagation of the upper easterly jet in the ICON simulation is too fast.

To analyze the forcing of the downward propagation of the QBO jets, I employ the transformed Eulerian mean (TEM) framework (Andrews and McIntyre, 1976). The

---

[1] The ECMWF is the European Centre for Medium-Range Weather Forecasts.

[2] ERA5.1 is a corrected version of the ECMWF Reanalysis v5 (ERA5) reanalysis during the years 2000–2006, when ERA5 shows pronounced stratospheric biases due to erroneous data assimilation (Simmons et al., 2020).
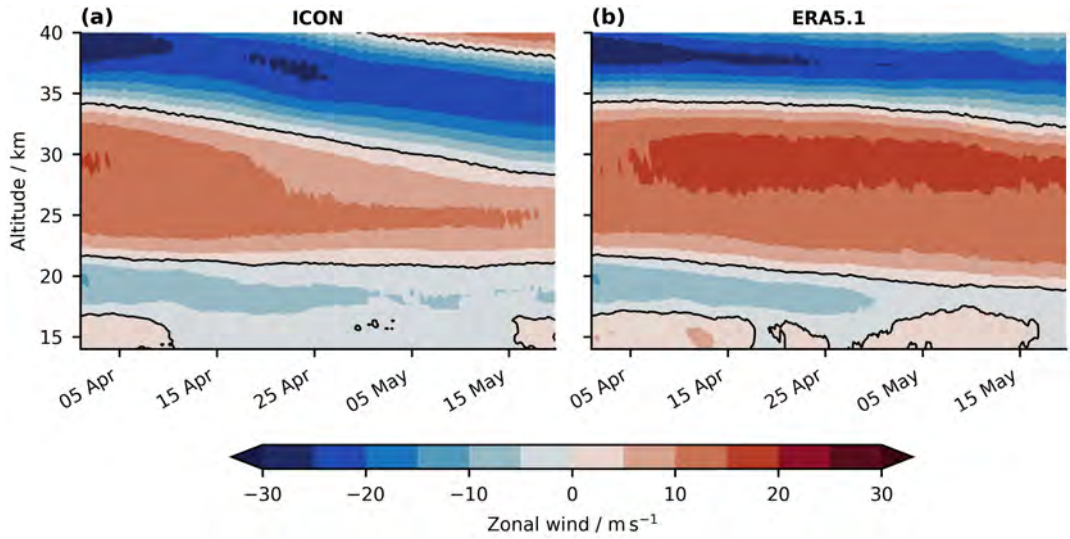
Figure 2.1: Time-altitude cross section of the 5° S–5° N mean zonal wind for **(a)** the initial short ICON simulation and **(b)** the ERA5.1 reanalysis starting on April 01, 2004. Red colors indicate westerly winds and blue colors indicate easterly winds. Thick black contour lines mark the $0\,\mathrm{ms}^{-1}$-isotach. This figure is adapted from Fig. 9 of Giorgetta et al. (2022).

TEM framework allows for a clear separation between tendencies of the zonal mean zonal wind due to wave-mean flow interactions and due to mean flow advection. It is therefore well suited for the analysis of the zonal momentum budget of the QBO. In the TEM framework, the tendencies of the zonal mean zonal wind due to wave-mean flow interactions are diagnosed as the divergence of the so-called Eliassen-Palm (EP) flux, which is a combined measure of wave momentum and wave heat fluxes. The EP flux divergence has a meridional and vertical component, representing the tendencies due to the wave-mean flow interactions of meridionally and vertically propagating waves, respectively. Consequently, the vertical EP flux divergence represents what I refer to as the QBO wave forcing throughout this dissertation (see Sec. 1.1.2). The advective tendency of the zonal mean zonal wind represents advection by the so-called residual circulation, which mainly comprises the BDC. It also has a meridional and vertical component, the latter representing the effect of the tropical upwelling associated with the BDC on the QBO. Typically, the sum of these four TEM tendencies does not equal the total tendency of the zonal mean zonal wind, so that the zonal momentum budget of the QBO is usually closed by a residual tendency.

Figure 2.2 shows the zonal momentum budget of the QBO jets in the ICON simulation and the ERA5.1 reanalysis in the TEM framework averaged over the first 30 days of the simulation. As shown by Figure 2.2a, the downward propagation of the upper easterly jet centered at about 38 km in the ICON simulation is indeed driven by resolved wave-mean flow interactions in the easterly shear zone between 30 km and 38 km. This wave-driven downward propagation of the upper easterly jet is slowed down by vertical advection by the tropical upwelling. Tendencies due to meridionally propagating waves and due to meridional advection are much smaller in this altitude range. This shows that the downward propagation of the QBO jets in
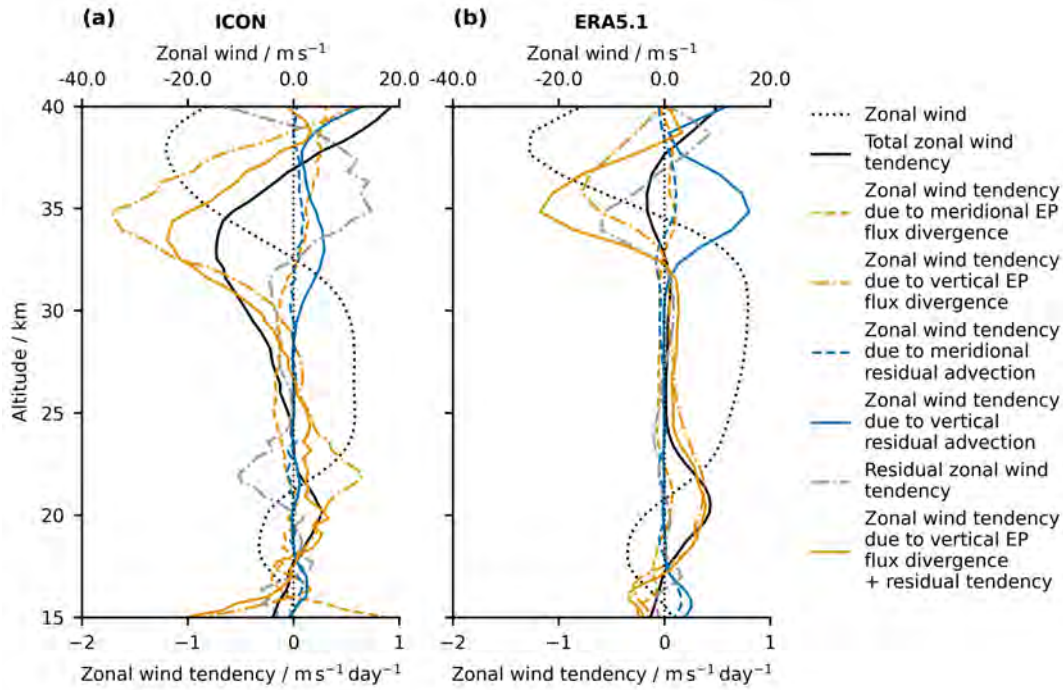
Figure 2.2: 5° S–5° N mean TEM zonal momentum budget averaged over the period April 01, 2004–April 30, 2004 for **(a)** the initial short ICON simulation and **(b)** the ERA5.1 reanalysis. The x-axis for the zonal wind $\overline{u}$ is given at the upper abscissa. This figure is adapted from Fig. 10 of Giorgetta et al. (2022).

the ICON simulation is indeed driven by the dissipation of vertically propagating waves, indicating that ICON captures the basic QBO dynamics.

However, the vertical EP flux divergence in the upper easterly shear zone between 30 km and 38 km is substantially stronger in the ICON simulation than in the ERA5.1 reanalysis (Fig. 2.2b). As a result, the TEM momentum budget in ICON is closed by a large residual, which opposes the vertical EP flux divergence. The nature of the residual in the ICON simulation and its root cause are overall unclear, but a more detailed discussion of this topic that I provide in Franke and Giorgetta (2024, see Appendix A) suggests that the compensating behavior between the vertical EP flux divergence and the residual may be a purely diagnostic issue. Therefore, I consider the sum of the vertical EP flux divergence and the residual as the *effective vertical wave forcing* from now on.

In the ERA5.1 reanalysis, the TEM residual has the same sign as the vertical EP flux divergence and is thus interpreted as the parameterized gravity wave forcing of the QBO. But even in this case it makes sense to consider the sum of both terms as an effective vertical wave forcing, as it represents the total vertical wave forcing of the QBO in ERA5.1. In terms of the effective vertical wave forcing, the difference between the ICON simulation and the ERA5.1 reanalysis in the easterly shear zone between 30 km and 38 km is much smaller. ICON still has a stronger effective wave forcing than ERA5.1, but this is consistent with the faster downward propagation of the upper easterly jet in the ICON simulation.

At this point, I thus conclude that the proposed R2B9L191 configuration of ICON is capable of simulating a wave-driven downward propagation of the QBO jets over a period of at least 1.5 months.

2.2   SENSITIVITY OF THE SIMULATED QBO ON PARAMETER SETTING

I continue the basic validation of my modeling approach by examining the sensitivity of the simulated QBO to changes in ICON's parameter setting as well as to changes in the boundary conditions. On the one hand, this helps to assess the robustness and uncertainty of my modeling approach. On the other hand, it may also help to find a parameter setting that results in the simulation of a more reasonable QBO than the current one, which is why one may also consider this step as *tuning*. In climate modeling, the term „tuning" refers to the process of empirically adjusting loosely constrained model parameters to improve the fit between the model and observations (e.g., Hourdin et al., 2017). Although some climate modelers have an aversion to the term „tuning" and the tuning process itself, I argue that careful and objective tuning is an inevitable and important step throughout the model development process. As pointed out by Hourdin et al. (2017), the tuning process can also help to gain a more fundamental understanding of the model, for example by facilitating the identification of more fundamental model shortcomings.

Testing the sensitivity of the simulated QBO jets to changes in ICON's parameter settings requires sufficiently long simulations. Therefore, I decided to run simulations for a period of one year. However, the maximum achievable simulation throughput of a numerically stable setup of the R2B9L191 configuration of ICON on the available HPC system was ∼44 SDPD, which does not allow for multiple sensitivity experiments within a reasonable amount of time. As a compromise between model fidelity and throughput, I thus make use of the R2B8 grid for the sensitivity experiments, which has a horizontal grid spacing of ∼9.86 km. Using the same 191-level vertical grid as in the R2B9L191 configuration, the resulting R2B8L191 configuration of ICON has a throughput of ∼106 SDPD on the available HPC system. As a drawback, the general deficiencies in the representation of deep convection and gravity waves in the gray zone are likely more pronounced in the R2B8L191 configuration than in the R2B9L191 one.

Figure 2.3a,b shows that the representation of the QBO jets in the R2B9L191 and R2B8L191 configurations differs in two main aspects. First, the R2B9L191 configuration results in a more reasonable representation of the upper stratosphere above 30 km (cmp. ERA5.1, Fig. 2.3j). Second, the QBO westerly jet is stronger in the R2B8L191 configuration. Nevertheless, the spatio-temporal structure of the simulated QBO jets agrees reasonably well between both configurations. This justifies the choice of the R2B8L191 configuration for the subsequent sensitivity experiments. An overview of the setup of all sensitivity experiments performed is given in Table 2.1, and the spatio-temporal structure of the QBO jets in these experiments is shown in Figure 2.3. All simulations were initialized on April 01, 2004, 0000 UTC.

As a first step, I change the boundary conditions of the simulation by applying El Niño-like (simulation `qbo03_nino_r2b8`) and La Niña-like (simulation `qbo04_nina_r2b8`) sea surface temperatures (SSTs), which are known to be associated with different
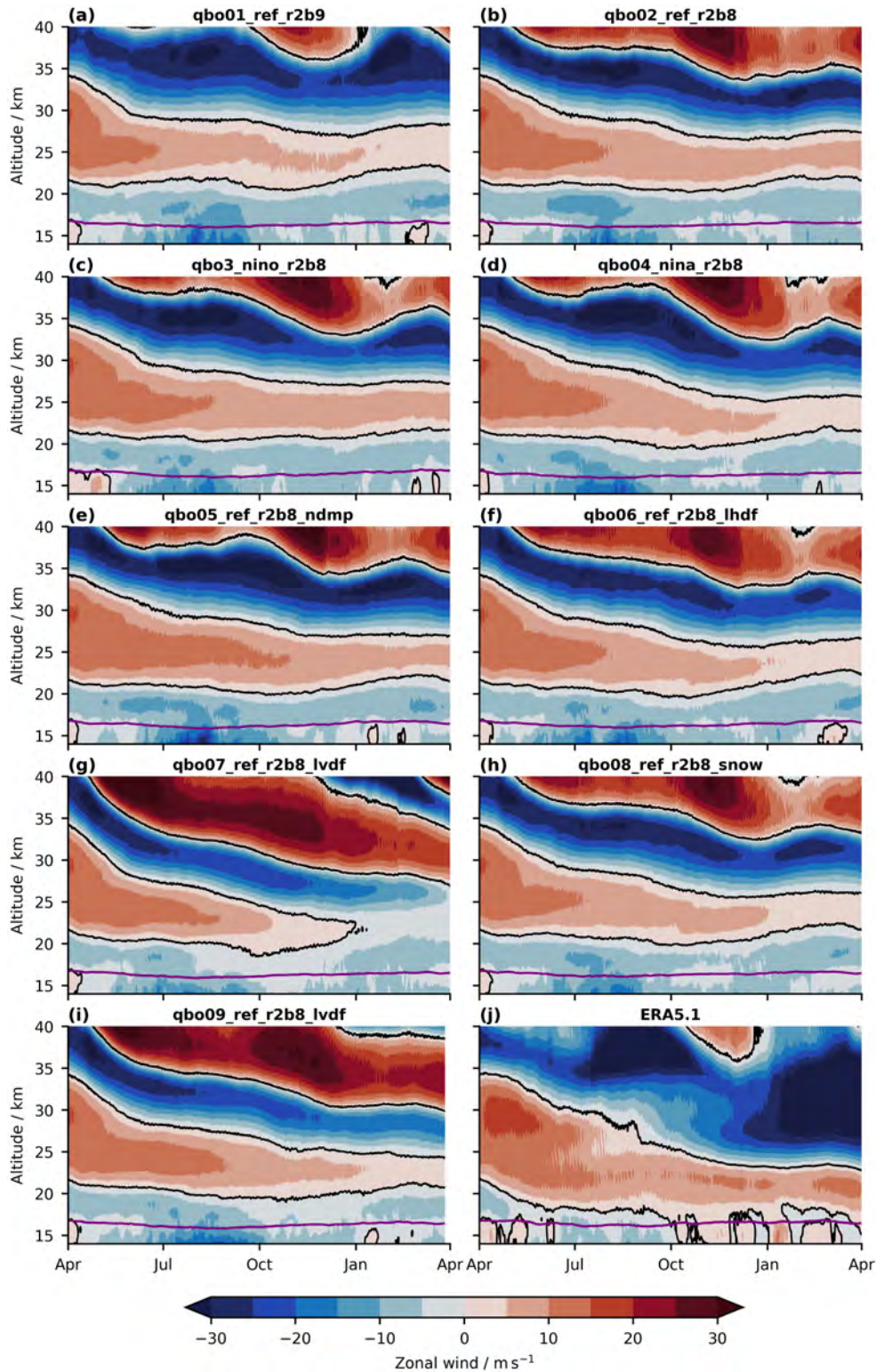
Figure 2.3: Time-altitude cross section of the 5° S–5° N mean zonal wind during the period April 01, 2004–April 01, 2005 for **(a-i)** the ICON sensitivity experiments (see Table 2.1) and **(j)** the ERA5.1 reanalysis. Red colors indicate westerly winds and blue colors indicate easterly winds. Thick black contour lines mark the 0 ms^{-1}-isotach. The purple contours mark the 370 K-isentrope, which is a proxy of the tropopause altitude.

patterns of equatorial convection and thus are expected to lead to differences in the wave forcing of the QBO (Geller et al., 1997). Consequently, I expect the QBO jets in the simulations qbo03_nino_r2b8 and qbo04_nina_r2b8 to differ. This is indeed the case, as the westerly jet in qbo04_nina_r2b8 propagates further down than in qbo03_nino_r2b8 and is weaker at the end of the simulation (Fig. 2.3c,d). This sensitivity to the SST boundary conditions indicates that the QBO in ICON is not overly robust and may show some reasonable internal variability in transient simulations.

A major shortcoming of the QBO in all simulations from qbo01_ref_r2b9 to qbo04_nina_r2b8 (Fig. 2.3a-d) is that the lower westerly jet does not propagate down to the tropopause as it does in the ERA5.1 reanalysis (Fig. 2.3j). Therefore, I investigated whether modifications in the parameter space of ICON may facilitate the QBO's downward propagation to the tropopause. In the global storm-resolving configuration, the parameter space of ICON consists mainly of the remaining parameterizations of cloud microphysics and vertical diffusion as well as of explicit diffusion and damping by the dynamical core.

As known from conventional GCMs, too strong diffusion and damping can excessively attenuate the waves that drive the QBO and the QBO jets themselves (see Sec. 1.1.3). Therefore, I perform sensitivity experiments with the divergence damping switched off (qbo05_r2b8_ndmp), and with a reduced strength of the horizontal (qbo06_r2b8_lhdf) and vertical (qbo07_r2b8_lvdf and qbo09_r2b8_lvdf) diffusion. The reduction of the strength in vertical diffusion is employed by reducing the maximum mixing length l_{max}, which caps the mixing length l calculated by ICON's vertical diffusion scheme and representative of the size of the largest eddies (Mauritsen et al., 2007; Pithan et al., 2015). Furthermore, it is known that the global storm-resolving configuration of ICON suffers from too spotty convection with potentially detrimental effects on the generation of tropical waves. In simulation qbo08_r2b8_snow, I thus reduce the terminal fall velocity of snow, which is expected to facilitate the organization of convection by giving snow crystals more time to spread horizontally.

As shown by Figure 2.3f-i, reducing the strength of the horizontal and vertical diffusion as well as reducing the terminal fall speed of snow has the anticipated effect as it tends to speed up the downward propagation of the main QBO easterly shear zone initially located between 30 km and 38 km compared to qbo02_ref_r2b8. These modifications further reduce the magnitude of the lower westerly jet towards the end of the simulation. In contrast, the QBO jets are rather insensitive to turning off the divergence damping (Fig. 2.3e), which may in part be due to the concurrent strengthening of the horizontal diffusion to ensure numerical stability (see Table 2.1). None of the investigated modifications of the parameter setting results in a downward propagation of the westerly jet to the tropopause. However, it should be noted here that I employed a heuristic rather than a systematic approach to my sensitivity study, which was necessary due to computational constraints. Thus, it is likely that I have not explored all possible sensitivities of the QBO, and a more drastic modification of some of the parameters tested would likely have resulted in a stronger modification of the simulated QBO.

Considering simulations qbo02_ref_r2b8 ($l_{max} = 150$ m), qbo09_ref_r2b8_lvdf ($l_{max} = 50$ m), and qbo07_ref_r2b8_lvdf ($l_{max} = 23$ m), the QBO jets in ICON indicate a systematic dependency on the strength of the vertical diffusion (Fig. 2.3b,g,i).

Weakening the vertical diffusion by reducing l_{max} leads to a faster and more pronounced downward propagation of the QBO jets. The parameterization of vertical diffusion could thus be a suitable tuning parameter for a directly simulated QBO in a GSRM. However, the root cause of this apparent systematic dependence of the simulated QBO jets on the strength of the vertical diffusion is unclear and requires further investigation. Possible root causes could be that the strength of the vertical diffusion impacts the spatio-temporal variability of deep convection, i.e. wave generation, or the damping of tropical waves before they reach the QBO shear zones, i.e. wave propagation.

To conclude, the QBO jets in ICON show clear sensitivities to modifications in the parameter space of ICON, which qualitatively agree with conceptual expectations. Furthermore, in all sensitivity experiments the QBO jets are sustained throughout the entire simulation and show a downward propagation. This indicates that my modeling approach is overall robust. Although the findings of the sensitivity experiments are not transferable one-to-one to the R2B9L191 configuration as the details of the parameter setting are always resolution-dependent, they could serve as a first guideline to optimize the parameter setting of the R2B9L191 configuration.

Table 2.1: Overview of the sensitivity experiments.

ICON namelist parameter	SST[1]	Grid[2]	Horizontal diffusion	Divergence damping	Vertical diffusion	microphysics	Effect of parameter change compared to qbo02_ref_r2b8
			hdiff_efdt_ratio, lhdiff_rcf hdiff_smag_fac	lmix_max	v0snow		
qbo01_ref_r2b9	climatological	R2B9	24.0, 0.025	.TRUE.	150.	25.	—
qbo02_ref_r2b8	climatological	R2B8	24.0, 0.025	.TRUE.	150.	25.	—
qbo03_nino_r2b8	El Niño-like	R2B8	24.0, 0.025	.TRUE.	150.	25.	—
qbo04_nina_r2b8	La Niña-like	R2B8	24.0, 0.025	.TRUE.	150.	25.	—
qbo05_ref_r2b8_ndmp	climatological	R2B8	6.0, 0.007	.FALSE.	150.	25.	no divergence damping, increased horizontal diffusion
qbo06_ref_r2b8_lhdf	climatological	R2B8	36.0, 0.015	.TRUE.	150.	25.	reduced horizontal diffusion
qbo07_ref_r2b8_lvdf	climatological	R2B8	24.0, 0.025	.TRUE.	23.	25.	strongly reduced vertical diffusion
qbo08_ref_r2b8_snow	climatological	R2B8	24.0, 0.025	.TRUE.	150.	12.5	reduced terminal fall velocity of snow
qbo09_ref_r2b8_lvdf	climatological	R2B8	24.0, 0.025	.TRUE.	50.	25.	slightly reduced vertical diffusion
qbo_full_cycle[3]	climatological	R2B9	36.0, 0.015	.TRUE.	50.	25.	reduced horizontal and vertical diffusion

1 SST is short for "sea surface temperature".

2 The R2B9 and R2B8 grid have a horizontal resolution of approximately 4.93 km and 9.86 km, respectively.

3 The experiment qbo_full_cycle aims at the direct simulation of a full QBO cycle and is analyzed in detail in Chapter 3.

TOWARDS A DIRECT SIMULATION OF A FULL QBO CYCLE IN A GLOBAL STORM-RESOLVING MODEL

Although several GCMs have produced simulations of the QBO, there is no simple set of criteria that guarantees a successful simulation.

— *Baldwin et al. (2001)*

Up until now, I gave the basic proof of concept of my modeling approach and validated its robustness by a series of sensitivity experiments. At this point, however, it is still unclear whether the simulated QBO jets will form a closed QBO cycle and thus become a true oscillation. This cannot be taken for granted, as already pointed out in the above quote from Baldwin et al. (2001) in the context of conventional GCMs, which motivated the second main research question of this dissertation as introduced in Section 1.3:

RQ2. How well does a state-of-the-art GSRM simulate a full QBO cycle and its dynamics?

To answer this question, I employed the R2B9L191 configuration of the GPU-enabled ICON (Giorgetta et al., 2022), since I found the R2B9L191 configuration to have a more reasonable representation of the upper stratosphere than the R2B8L191 configuration (see Sec. 2.2). Based on the findings of the sensitivity experiments, I employed a modified parameter setting with the goal to achieve a somewhat realistic QBO period (see Table 2.1, simulation `qbo_full_cycle`). Like the sensitivity experiments, this simulation was initialized on April 01, 2004, 0000 UTC. During the simulation, it became clear that the downward propagation of the QBO stalls in the second year of the simulation. This is why the simulation was stopped after two years, although it has not simulated a full QBO cycle by then.

I addressed RQ2 in detail in a manuscript which is in preparation for submission to the *Journal of Advances in Modeling Earth Systems* (Franke and Giorgetta, 2024, Appendix A). In the following two sections, I will summarize and discuss its key results.

3.1 BASIC PROPERTIES AND FORCING OF A DIRECTLY SIMULATED QBO

The spatio-temporal structure of the QBO jets in the ICON simulation is shown in Figure 3.1a. The simulation maintains a QBO-like zonal wind structure in the tropical stratosphere throughout the whole simulation period of two years. However, the downward propagation of the QBO jets tends to stall in the second year of the simulation. Consequently, the QBO jets do not form a closed QBO cycle within the simulation period.

To assess in more detail which aspects of the QBO are already well captured by the ICON simulation and which are not, I compared the simulated QBO with a
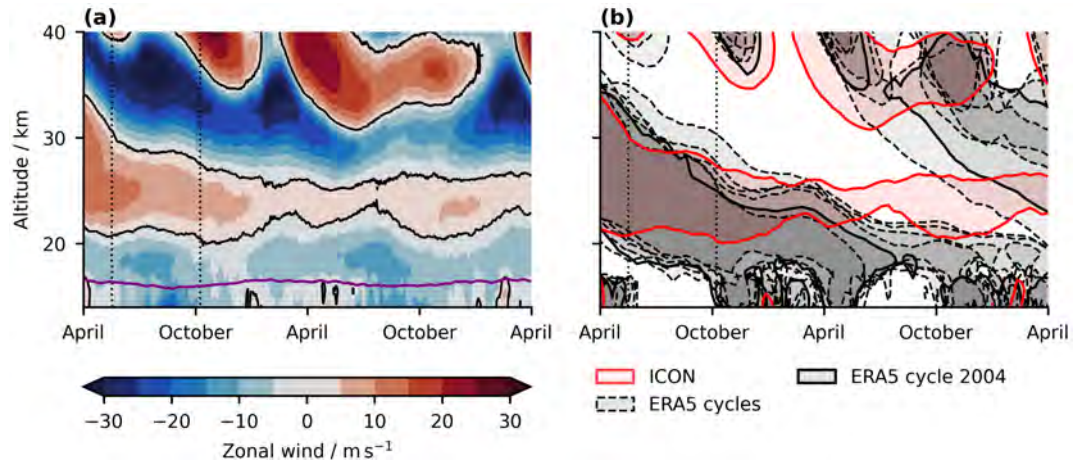
Figure 3.1: **(a)** Time-altitude cross section of the 5° S–5° N mean zonal wind in the ICON simulation starting on April 01, 2004. Red colors indicate westerly winds and blue colors indicate easterly winds. Thick black contour lines mark the $0\,\mathrm{m\,s^{-1}}$-isotach. The purple contour marks the 370 K-isentrope, which is a proxy of the tropopause altitude. **(b)** Time-altitude cross section of the 5° S–5° N daily mean zonal wind of the ICON simulation and the six QBO cycles of ERA5, which start on April 01 of the sampled years. The contour lines mark the $0\,\mathrm{m\,s^{-1}}$-isotach and shading highlights westerlies. The ERA5 QBO cycle starting on April 01, 2004 is highlighted by a thick black contour. The vertical dotted black lines in **(a)** and **(b)** mark the start and end of the period May 17, 2004–October 08, 2004, which is used to compare the momentum budgets of the 5° S–5° N mean zonal wind in ICON and ERA5.

set of six QBO cycles from the ERA5 reanalysis (Fig. 3.1b). These six cycles were sampled from the period 1980–2015[1], based on a criterion that ensures that they are in a QBO phase comparable to the QBO phase at the start of the ICON simulation[2]. To further evaluate the QBO forcing in the ICON simulation, I compared its zonal QBO momentum budget with that of the ERA5.1 reanalysis during the period May 17, 2004–October 08, 2004, which starts only ∼1.5 months after the beginning of the simulation. During this period, the vertical structure of the QBO jets in the ICON simulation and in the ERA5.1 reanalysis are still reasonably close to each other (see Fig. 3.1b), which is necessary for a reasonable comparison.

During the first year of the simulation, the easterly shear zone of the QBO, initially located between 30 km and 38 km, shows an overall reasonable downward propagation at a rate that is within the cycle-to-cycle variability of the six selected QBO cycles in the ERA5 reanalysis (Fig. 3.1b). This indicates that ICON is in principle capable of directly simulating the QBO dynamics, and indeed the QBO momentum budget in the easterly shear zone of the QBO is in good agreement between the ICON simulation and the ERA5.1 reanalysis (Fig. 3.2a,b). In particular, there is good quantitative agreement in the total wave forcing of the QBO, i.e. the sum of the effective vertical wave forcing and the meridional wave forcing, which differs by less than 4 % between ICON and ERA5.1 at the end of the comparison period. This is a promising result, as it indicates that a GSRM with a horizontal

---

1 During the period 2000–2006, I use ERA5.1 instead of ERA5, see Simmons et al. (2020).
2 The applied criterion is a change in the monthly mean 5° S–5° N mean zonal wind at some model level between 21 km and 22.5 km from easterly in March to westerly in April, as observed in 2004.

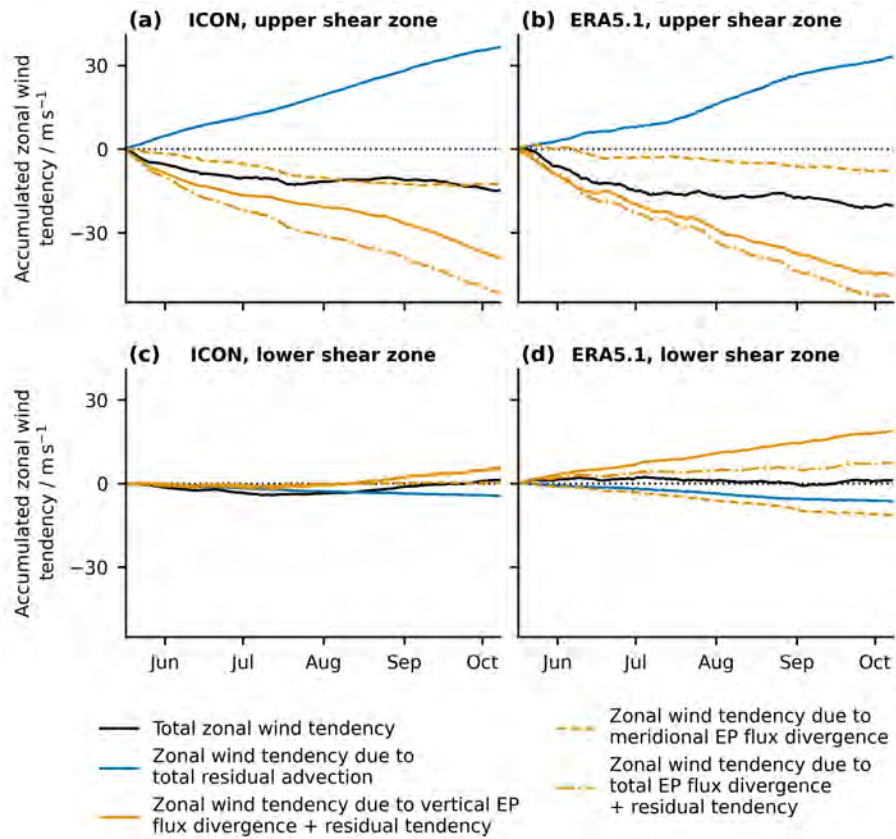Figure 3.2: Accumulated 5° S–5° N mean TEM tendencies of the zonal wind during the period May 17, 2004–October 07, 2004 for **(a,c)** the ICON simulation and **(b,d)** the ERA5.1 reanalysis. Panels **(a,b)** show tendencies averaged between an altitude of 29 km and 34 km, representative of the upper QBO shear zone during the considered period, and panels **(c,d)** show tendencies averaged between an altitude of 18 km and 23 km, representative of the lower QBO shear zone during the considered period. This figure is adapted from Fig. 6 of Franke and Giorgetta (2024, Appendix A).

resolution of $\mathcal{O}(5\,\text{km})$ is in principle capable of providing the wave momentum necessary to drive a reasonable downward propagation of the QBO. This conclusion is supported by the results of Polichtchouk et al. (2021), which suggest that the total tropical GWMF in a GSRM is already independent of the horizontal resolution below a grid spacing of 10 km.

However, it should be noted that it cannot be completely ruled out that the good agreement in the QBO momentum budget between the ICON simulation and the ERA5.1 reanalysis in the upper QBO shear zone is partly due to the initial conditions. Although there is sufficient time for spin-up of the ICON simulation before the comparison period, the long inherent memory of the stratosphere may support the reasonable representation of the QBO momentum budget during the comparison period.

An interesting feature of the ICON simulation is that a substantial fraction of the total wave forcing in the upper easterly shear zone of the QBO is provided by meridionally propagating waves (Fig. 3.2a). This is in contrast to the ERA5.1 reanalysis, where the meridional wave forcing is rather negligible (Fig. 3.2b), consis-

tent with the fact that the gravity wave parameterization employed in ERA5.1 does not allow for meridional gravity wave propagation (Orr et al., 2010). This finding supports the hypothesis that oblique gravity wave propagation may be relevant to the QBO, as recently suggested by Kim et al. (2023).

The main deficiency of the QBO in the ICON simulation is a pronounced lack of downward propagation in the lowermost stratosphere, which starts right at the beginning of the simulation (Fig. 3.1). As the simulation progresses, the downward propagation of the QBO jets stalls also at higher altitudes, and in the second year of the simulation, the jets stop propagating downward at all (Fig. 3.1a). This finding agrees with the sensitivity experiments, which suffered from a similar lack of QBO downward propagation in the lowermost stratosphere (Fig. 2.3). As shown by Figure 3.2c,d, the lack of downward propagation of the QBO jets in the lowermost stratosphere is due to a substantial lack of effective vertical wave forcing. In the lower westerly shear zone of the QBO (18 km–23 km), the eastward effective vertical wave forcing is about 75 % weaker in the ICON simulation than in the ERA5.1 reanalysis at the end of the comparison period. A spectral analysis of the vertical EP flux divergence revealed that this lack of eastward vertical wave forcing is preferentially due to slow eastward propagating planetary-scale waves with zonal wavenumbers k below 19, which mostly comprise equatorial Kelvin waves. At the same time, the total advective tendency, i.e. the sum of vertical and meridional advection, is small and in good agreement between the ICON simulation and the ERA5.1 reanalysis (Fig. 3.2c,d). This shows that a too strong tropical upwelling does not cause the lack of downward propagation of the QBO jets in the ICON simulation, which I confirmed in a more detailed analysis of the tropical upwelling.

3.2   ON THE REPRESENTATION OF PLANETARY-SCALE TROPICAL WAVES

A lack of downward propagation of the QBO to the tropopause is a common bias in GCMs (see Sec. 1.1.3), although it is particularly pronounced in the ICON simulation. In conventional GCMs, this bias is commonly attributed to an inadequate vertical resolution, which fails to resolve planetary-scale waves with short vertical wavelengths that are thought to drive the QBO in the lowermost stratosphere (e.g. Boville and Randel, 1992; Giorgetta et al., 2006; Anstey et al., 2016). However, the very high vertical resolution employed in the ICON simulation of 350 m–560 m in the stratosphere is usually considered sufficient to simulate a reasonable QBO (see Sec. 1.1.3). Therefore, it is unlikely that the underestimation of the vertical wave forcing in the lowermost stratosphere in the ICON simulation is due to an inadequate vertical resolution as in conventional GCMs. I confirmed this by analyzing the spatio-temporal structure of planetary-scale Kelvin waves in the ICON simulation, which revealed their overall reasonable propagation and dissipation, consistent with the theory of critical level filtering (Fig. 3.3). Therefore, a misrepresentation of wave propagation and dissipation in the ICON simulation is unlikely to be the root cause of the lack of QBO wave forcing in the lowermost stratosphere. However, it should be noted that recent observations suggest that waves with vertical wavelengths less than 1 km — which remain unresolved in ICON — may contribute notably to driving the QBO in the lowermost stratosphere (Bramberger et al., 2022). Therefore,
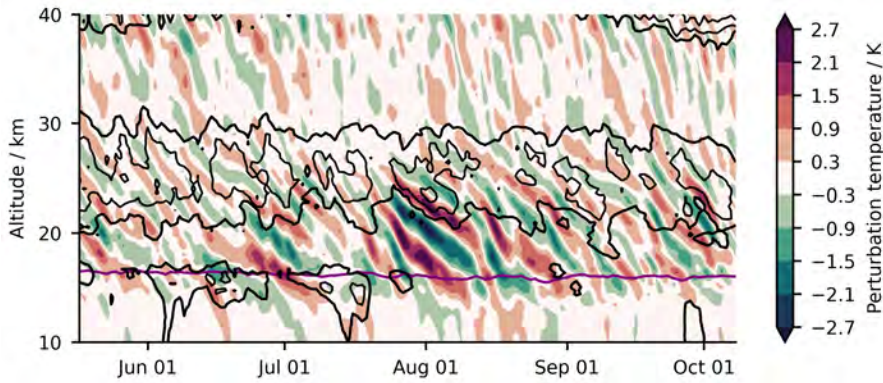
Figure 3.3: Time-altitude cross section of temperature perturbations induced by Kelvin waves with zonal phase speeds between $10\,\mathrm{m\,s^{-1}}$ and $20\,\mathrm{m\,s^{-1}}$ and a zonal wavenumber between 1 and 10 during the period May 17, 2004–October 07, 2004 at $0.1756°\,\mathrm{N}$, $180°\,\mathrm{E}$. Black contour lines show daily mean westerly winds in intervals of $10\,\mathrm{m\,s^{-1}}$, starting at $0\,\mathrm{m\,s^{-1}}$ (thick black contour). Contour lines of easterly winds are omitted for clarity. The purple contour line marks the $370\,\mathrm{K}$-isentrope, which is a proxy of the tropopause altitude. This figure is adapted from Fig. 11 of Franke and Giorgetta (2024, Appendix A).

a higher vertical resolution may still be advantageous for the representation of the QBO in ICON.

In the ICON simulation, the reason for the lack of QBO downward propagation in the lowermost stratosphere is a pronounced lack of vertical EP flux entering the stratosphere. As revealed by an analysis of the vertical EP flux at an altitude of about 17 km, just above the tropopause, the vertical EP flux entering the stratosphere is about 20 %–40 % weaker in the ICON simulation than in the ERA5.1 reanalysis over a wide range of scales ($|k| < 70$). Given the much stronger absolute EP flux at planetary scales ($|k| \leq 18$), this explains why the lack of QBO downward propagation in the lowermost stratosphere could be preferentially attributed to a lack of planetary-scale wave forcing.

I attribute the lack of planetary-scale vertical EP flux entering the stratosphere in the ICON simulation to the substantial underestimation of CCEWs in the tropical troposphere. As shown by Figure 3.4, there are much weaker signals of equatorial Kelvin waves, long n=0 equatorial Rossby waves, and MRG waves in the ICON simulation than in the ERA5.1 reanalysis and the observational Integrated Multi-satellite Retrievals for the Global Precipitation Measurement (IMERG) dataset (Huffman et al., 2022). Signals of inertia-gravity waves and the MJO are virtually missing in the ICON simulation. Although models can generate SEWs, which ultimately drive the QBO, also without substantial CCEWs (Lott et al., 2014; Holt et al., 2020), SEWs and CCEWs are usually closely coupled (Kawatani et al., 2009; Maury et al., 2013). Therefore, it is likely that the lack of QBO wave forcing in the lowermost stratosphere is ultimately caused by the lack of CCEWs in the ICON simulation. The reason for the lack of CCEWs itself is unclear.

The pronounced lack of CCEWs in the ICON simulation is certainly surprising, given that GSRMs have been found to result in an overall improved representation of CCEWs compared to conventional GCMs (e.g. Judt and Rios-Berrios, 2021). However, the CCEW signal in the ICON simulation is also not weaker than in some
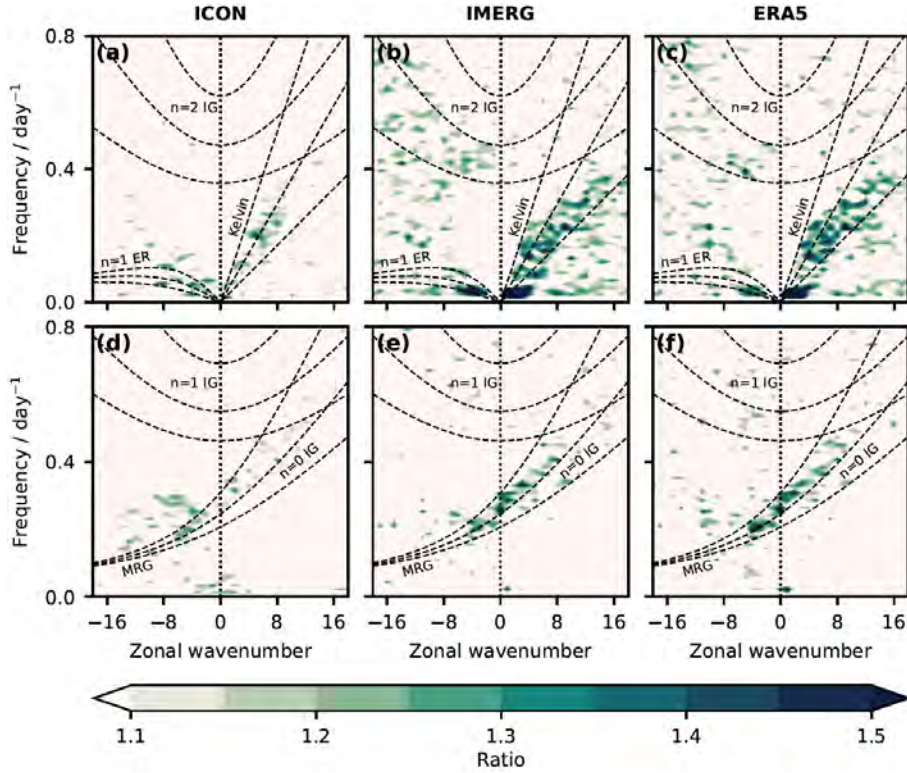
Figure 3.4: 15° S–15° N mean zonal wavenumber-frequency spectra of normalized **(a-c)** symmetric and **(d-f)** antisymmetric precipitation variance for **(a,d)** the ICON simulation, **(b,e)** the observational dataset IMERG, and **(c,f)** the ERA5 reanalysis averaged over 29 92-day windows with a 34-day overlap spanning the entire simulation period. The normalization with respect to the background spectra has been performed according to Wheeler and Kiladis (1999). Black dashed lines indicate ground-based theoretical dispersion curves of CCEWs with an equivalent depth of 10 m, 30 m, and 90 m. Please note the following abbreviations: ER, Equatorial Rossby wave; IG, Inertia-gravity wave; and MRG, Mixed Rossby-gravity wave. This figure is adapted from Fig. 14 of Franke and Giorgetta (2024, Appendix A).

conventional GCMs, which nevertheless simulated a reasonable QBO (cmp. Holt et al., 2020; Bushell et al., 2020). In contrast to GSRMs, conventional GCMs can compensate for biases in the resolved wave forcing of the QBO due to a lack of CCEWs by tuning their gravity wave parameterization. Conversely, this implies that the representation of the QBO in GSRMs is likely to be more sensitive to biases in the tropical troposphere. Therefore, my results suggest that an adequate representation of the tropical troposphere and its spatio-temporal variability across scales with a high degree of fidelity is a necessary — but not sufficient — prerequisite for a successful simulation of the QBO in a GSRM.

CHANGES OF TROPICAL GRAVITY WAVES AND THE QUASI-BIENNIAL OSCILLATION IN STORM-RESOLVING SIMULATIONS OF IDEALIZED GLOBAL WARMING

Improved representation of the processes governing the QBO is expected to lead to (...) more reliable future projections of QBO behaviour under climate change.

— *Anstey et al. (2022a)*

So far, I have focused on exploring the capability of the state-of-the-art GSRM ICON to directly simulate the QBO. Although such a simulation is already a major scientific achievement in itself, the direct simulation of the QBO is ultimately rather a tool for answering more fundamental research questions about the QBO that could not be answered by conventional GCMs. One of these fundamental questions is the overarching research question of this dissertation as introduced in Section 1.2:

RQ1. How do the gravity waves that drive the QBO and the downward propagation of the QBO shear zones respond to a warming climate?

As discussed in Section 1.2, the answer to this question is currently unclear due to the large uncertainties associated with the gravity wave parameterizations employed in conventional GCMs. In line with the above quote from Anstey et al. (2022a), I therefore aim at an improved representation of gravity waves to address RQ1 by using the global-storm resolving R2B9L191 configuration of ICON.

Given the short period of gravity waves, typically not exceeding $\mathcal{O}(1\,\text{day})$, relatively short simulations are sufficient to address RQ1. Therefore, I performed a series of 45-day-long simulations of three different climate states, including a reference climate and a 2 K and 4 K warmer climate[1], for two initially opposite QBO states: one with the main QBO jet being easterly and another one with the main QBO jet being westerly. The first 15 days of each simulation are considered as spin-up. Although the current setup of the R2B9L191 configuration of ICON does not simulate a full QBO cycle, it does simulate overall reasonable QBO dynamics during about the first year of a simulation (see Chp. 3). Therefore, it is justified to use this model setup for the short simulations of this study.

I addressed **RQ1** in detail in a study which was published in the *Quarterly Journal of the Royal Meteorological Society* (Franke et al., 2023a, Appendix B). In the following two sections, I will summarize and discuss its key results mainly based on the simulations initialized with the main QBO jet being easterly. For the simulations initialized with the main QBO jet being westerly, the results are qualitatively identical.

---

1 The warming was imposed as a globally uniform increase of the SST by 2 K or 4 K combined with a doubling or quadrupling of the CO_2 concentration, respectively.

4.1 CHANGES IN TROPICAL GRAVITY WAVES

Tropical gravity waves are typically generated by two different mechanisms associated with deep convection: 1) thermal gravity wave generation by latent heat release, and 2) mechanical gravity wave generation by the oscillation of convective updrafts around their level of neutral buoyancy at the cloud top (Fritts and Alexander, 2003). I show that both the convective latent heat release and the buoyancy oscillations of the convective updrafts of tropical convection become stronger in the warmer climate states (Fig. 4.1), which is the imprint of a general strengthening of tropical deep convection. This strengthening of deep convection leads to the generation of stronger gravity waves, i.e. gravity waves with a larger amplitude, by both mechanisms in a warmer climate state. A spectral analysis further reveals that the strengthening of deep convection is approximately uniform across all zonal scales. As a result, the wave momentum flux spectrum in the lowermost stratosphere (i.e. at ~20 km) is also approximately uniformly enhanced in the warmer climate states.

To analyze the GWMF and its spectral characteristics in the lowermost stratosphere — and thus before the gravity waves interact with the QBO jets — in more detail, I use the small-volume few-wave decomposition technique (S3D, Lehmann et al., 2012). The S3D method is well-suited to analyze gravity waves at individual timesteps. It determines the local wave vector and wave amplitude within limited three-dimensional cuboids spanning the tropical stratosphere by performing three-dimensional sinusoidal wave fits on perturbation temperature[2]. The S3D analysis reveals that in the warmer climate states, the eastward and westward GWMF associated with gravity waves with horizontal wavelengths below ~1155 km strengthens substantially in the lowermost stratosphere. However, this strengthening is not symmetric between westward and eastward propagating waves and not strictly

---

2 The perturbation temperature at a given grid point is the temperature deviation from a background containing temperature variations associated with zonal wavenumbers lower than 19.
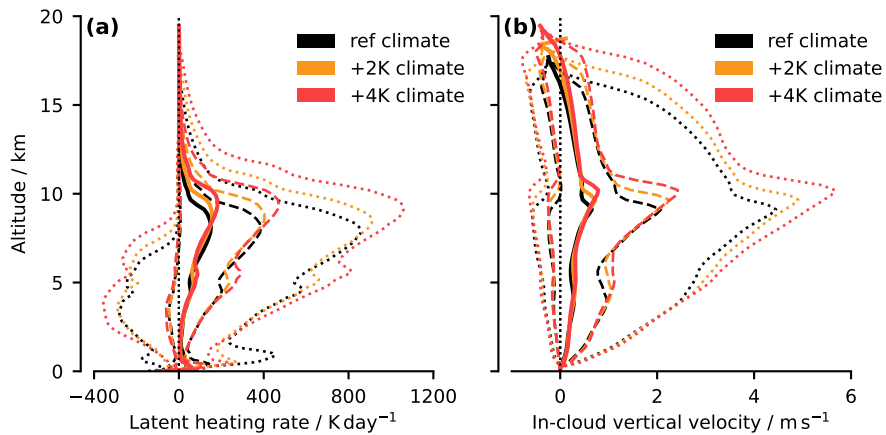

Figure 4.1: Profiles of the mean (solid), 10th and the 90th percentile (dashed), and 1st and the 99th percentile (dotted) of **(a)** in-cloud latent heating, and **(b)** in-cloud vertical velocity within 15° S–15° N and averaged over the last 30 simulation days. The vertical dotted black lines mark the zero lines. This figure is adapted from Fig. 4 of Franke et al. (2023a, Appendix B).
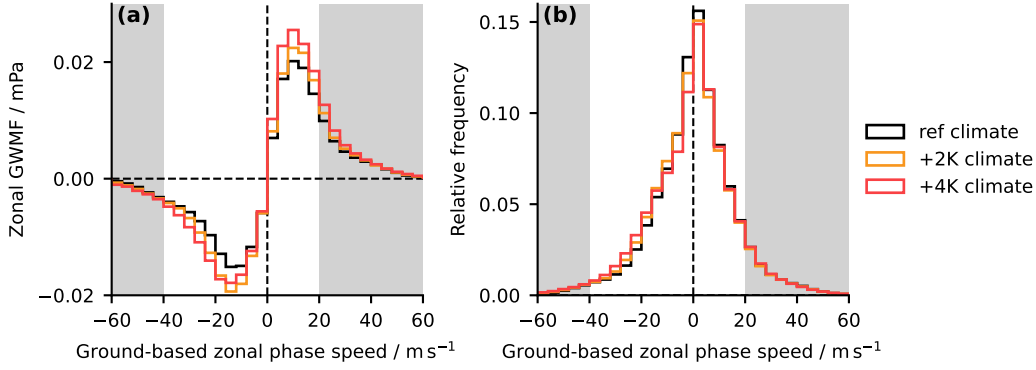
Figure 4.2: **(a)** Zonal GWMF, and **(b)** relative frequency of gravity waves as a function of ground-based zonal phase speed within 15° S–15° N at an altitude of 20 km and averaged over the last 30 simulation days. Light gray shading highlights zonal phase speeds that are unlikely to contribute to driving the QBO. This figure is adapted from Fig. 7 of Franke et al. (2023a, Appendix B).

linear with the amount of warming, suggesting subtle warming-induced changes in upper-tropospheric wave filtering.

I continue with analyzing whether the warming-induced increase in GWMF in the lowermost stratosphere is relevant for the QBO. According to QBO theory (see Sec. 1.1.2), only waves with zonal phase speeds approximately within the range of QBO background winds can contribute to accelerating the QBO jets. My analysis shows that the majority of the warming-induced increase in GWMF is associated with gravity waves that are relevant for the QBO based on their zonal phase speed (Fig. 4.2a). Only for eastward propagating gravity waves, a notable part of the increase in GWMF is associated with gravity waves that are too fast for the QBO.

The S3D analysis further shows that the relative frequency distribution of gravity waves shifts towards larger absolute zonal phase speeds $|c_x|$ in the warmer climate states (Fig. 4.2b). The average of $|c_x|$ increases by about $0.38 \, \mathrm{m\,s^{-1}}$ and $0.91 \, \mathrm{m\,s^{-1}}$ in the 2 K and 4 K warmer climate states, respectively. I attribute this shift towards larger absolute zonal phase speeds to a deepening of the tropical deep convection due to the imposed idealized warming. In the 2 K and 4 K warmer climate states, the depth of the mean convective latent heating becomes 0.75 km and 1.5 km larger, respectively (Fig. 4.1a). Following Salby and Garcia (1987), the depth of the convective latent heating sets the vertical wavelength of a purely thermally generated gravity wave, with a preferred vertical wavelength of twice the heating depth. The vertical wavelength λ_z of a gravity wave, however, is inherently coupled to its horizontal phase speed c_h via the dispersion relationship (see Eq. 33 of Fritts and Alexander, 2003):

$$|c_h - \overline{u}_h| = \frac{N \cdot |\lambda_z|}{2\pi}, \tag{4.1}$$

where N is the buoyancy frequency, and $\overline{u}_h$ is the local horizontal background wind. Consequently, in theory a warming-induced deepening of tropical deep convection is inevitably associated with faster gravity waves, and this relationship is reproduced by my simulations.

4.2   CHANGES IN THE QBO

Consistent with the substantial warming-induced changes in the lower-stratospheric gravity wave field, the QBO jets also respond to the imposed idealized warming. As a first key result, the downward propagation of the main shear zone above 30 km is faster in the warmer climate states, which corresponds to the found strengthening of the GWMF in the lowermost stratosphere (Fig. 4.3a). The magnitude of the increase in the rate of downward propagation of the QBO depends on the amount of warming, with a faster downward propagation for a greater warming. It is unclear whether this relationship is linear due to the short simulations and and the fact that I only simulated three climate states. Based on the faster downward propagation of the QBO jets alone, I would expect the period of the QBO to eventually shorten in a warming climate, but it should be noted that the present simulations are clearly too short to draw such definitive conclusions.

In the warmer climate states, the magnitude of the QBO jets becomes larger in the upper QBO domain, i.e. between 25 km and 31 km (Fig. 4.4). The extent of this strengthening of the QBO jets tends to depend on the amount of warming, with a stronger response for a greater warming. Since both the simulations initialized with the main QBO jet being easterly and those with the main QBO jet being westerly show this strengthening, my result suggests that the amplitude of the QBO will eventually become larger in a warming climate. As the QBO amplitude depends on the phase speed spectrum of the QBO wave forcing (Saravanan, 1990; Geller et al., 2016b), with faster waves resulting in a larger QBO amplitude, I attribute the strengthening of the QBO jets in the upper QBO domain to the warming-induced shift in the gravity wave spectrum towards faster waves. This means that the strengthening of the QBO jets in the upper QBO domain can ultimately be
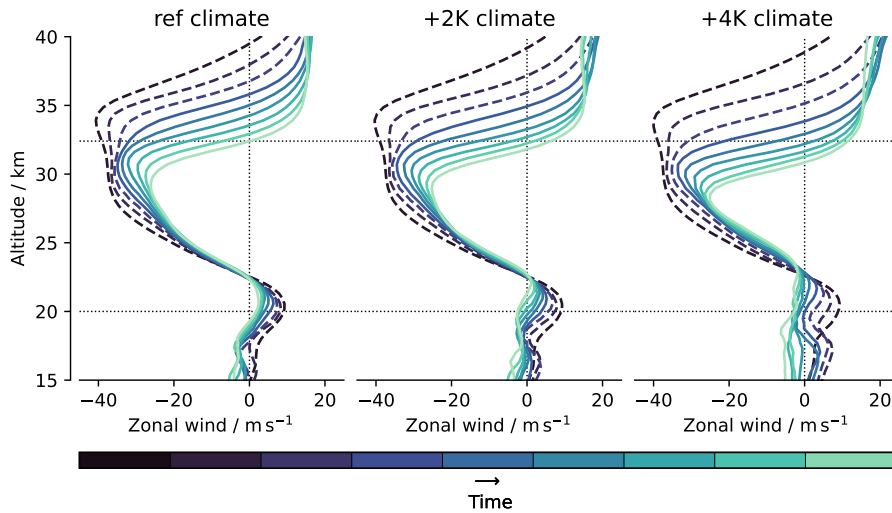

Figure 4.3: 5-day mean 5° S–5° N zonal mean zonal wind profiles. The colors indicate subsequent 5-day periods, thereby highlighting the downward propagation of the QBO throughout each experiment. The first three five-day periods, which are within the spin-up period, are dashed. Horizontal dotted lines are plotted for highlighting differences between the experiments. This figure is adapted from Fig. 8 of Franke et al. (2023a, Appendix B).
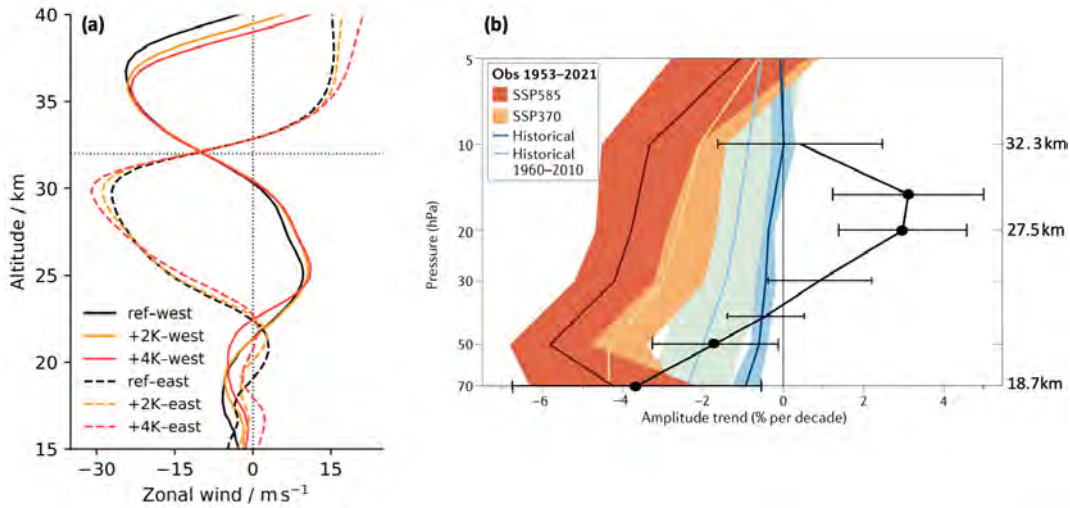
Figure 4.4: **(a)** 11-day mean profiles of the 5° S–5° N mean zonal wind that cross the $-10\,\mathrm{m\,s^{-1}}$-wind line closest at a reference altitude of 32 km, which is marked by the horizontal dotted black line. Panel **(a)** is adapted from Fig. 9 of Franke et al. (2023a, Appendix B). Panel **(b)** is adapted from Fig. 5 of Anstey et al. (2022a) and shows „[t]he multi-model mean trend (percentage per decade) in QBO amplitude in CMIP6 historical (blue), SSP370 (yellow) and SSP585 (red) simulations and FUB [radiosonde] observations from January 1953 to September 2021 (black) as a function of altitude. Shading denotes the uncertainty in the multi-model mean (± 2 standard error) and error bars of black lines are ranges of 95 % significance (filled circles satisfy 95 % significance)" (Anstey et al., 2022a). FUB is short for Free University of Berlin, and SSP370 and SSP585 are scenarios of strong and very strong global warming, respectively (cmp. O'Neill et al., 2016). The altitude values on the right ordinate are given for reference and correspond to the pressure values on the left ordinate based on the hydrostatic equation with a constant scale height of 7 km and a surface pressure of 1013.25 hPa. Please note that panels **(a)** and **(b)** are not referenced with respect to altitude.

attributed to the warming-induced deepening of tropical deep convection. However, also here it should be noted that the simulations are too short for this conclusion to be definitive.

Nevertheless, the warming-induced strengthening of the QBO jets is an interesting finding, considering that the observational record since the late 1950s also shows an increase in the QBO amplitude between 30 hPa and 10 hPa (about 25–32 km), which, however, cannot be reproduced or explained by conventional GCMs (Fig. 4.3b). It has been unclear whether this discrepancy between observations and conventional GCMs is due to shortcomings of the GCMs or whether the observed trend was rather an imprint of very slow internal variability of the QBO amplitude (Anstey et al., 2022a). My results now provide evidence for the first explanation, since it is likely that conventional GCMs cannot simulate the complex coupling between deep convection and gravity waves that is involved in shifting the gravity wave spectrum toward larger absolute phase speeds. Most gravity wave parameterizations prescribe a fixed gravity wave source spectrum and are thus per se not capable of capturing the impact of a warming-induced deepening of tropical deep convection on the gravity wave spectrum. In gravity wave parameterizations with an interactive source spectrum, wave generation still depends on a parameterized convective

latent heating, and it is unclear whether a warming-induced deepening of the convective latent heating would be adequately captured by parameterizations of deep convection. In light of these conceptual shortcomings, it is expectable that conventional GCMs do not reproduce a potential warming-induced increase of the QBO amplitude due to a deepening of deep convection.

In the lower QBO domain (i.e. below 25 km), the QBO jets tend to become marginally weaker in the warmer climate states (Fig. 4.3a). This is consistent with previous studies showing that a warming climate would result in a weakening of the QBO jets in the lower QBO domain due to a warming-induced strengthening of the tropical upwelling (Kawatani et al., 2011; Kawatani and Hamilton, 2013; Richter et al., 2020b). Furthermore, my simulations show that the QBO stops at a higher altitude in the warmer climate states, possibly due to a warming-induced upward shift of the tropopause. However, any warming-induced changes in the lowermost stratosphere should be interpreted with caution, as the QBO in the lowermost stratosphere is generally poorly represented in ICON as shown in Chapter 3.

CONCLUSIONS

[GSRMs] better represent physical understanding than do traditional climate (...) models because they solve the correct equations over a larger range of scales.

— *Satoh et al. (2019)*

The overarching goal of this dissertation was to shed light on the current uncertainty in the response of the QBO to anthropogenic global warming using a novel modeling approach: direct QBO simulations in a GSRM. As summarized by the above quote from Satoh et al. (2019), GSRMs have the simple but fundamental advantage of representing two key processes for the QBO — deep convection and gravity waves — in an explicit way, thus aiding the physical understanding of potential warming-induced changes. In Chapter 2 and Chapter 3, I investigated how the state-of-the-art GSRM ICON represents the QBO and its dynamics, showing that it is in principle capable of simulating a reasonable wave-driven downward propagation of the QBO jets. This work lays the groundwork for using the global storm-resolving ICON configuration as a reasonable research tool for studying the QBO and its response to warming. In Chapter 4, I addressed the overarching research question of this dissertation by investigating how the gravity waves that force the QBO and the QBO jets themselves change in short simulations of idealized warmer climate states.

Here, I will conclude by answering the research questions I posed in Chapter 1, and by putting my results into the scientific context.

5.1 ANSWERS TO THE RESEARCH QUESTIONS

Please note that I will answer RQ2 before RQ1, following the logical order with regard to my work.

RQ2. How well does a state-of-the-art GSRM simulate a full QBO cycle and its dynamics?
To answer this question, I conducted a two-year-long simulation with the state-of-the-art GSRM ICON in its R2B9L191 configuration, which has a horizontal resolution of 4.93 km and a vertical resolution between 350 m and 560 m throughout the stratosphere. This model configuration is not currently capable of directly simulating a full QBO cycle, despite an optimized parameter setting determined in a heuristic sensitivity study. Instead, the simulated QBO suffers from a pronounced lack of downward propagation in the lower QBO domain (below 25 km), which extends into the upper QBO domain in the second year of the simulation. The lack of downward propagation of the QBO in the lower QBO domain is the result of a pronounced lack of planetary-scale wave forcing, which I attribute to the underestimation of CCEWs in the troposphere. Nevertheless, the simulation does represent some aspects of the QBO in a reasonable way, in particular the spatio-temporal structure of the zonal wind in the upper QBO domain (above 25 km) during the

first year of the simulation. During this period, the downward propagation of the QBO shear zone in the upper QBO domain occurs at a reasonable rate. This can be explained by a good representation of the zonal momentum budget of the QBO jets between 25 km and 35 km, at least during the first six months of the simulation. Here, both the QBO wave forcing and the vertical advection by the tropical upwelling are in good agreement with the ERA5.1 reanalysis, indicating that the simulated QBO is right for the right reasons. This result implicitly shows that the horizontal and vertical resolution of the present model configuration is in principle sufficient to simulate a wave spectrum that can drive the QBO. Considering that this simulation was the very first attempt to directly simulate a full QBO cycle, and therefore deficiencies of the simulated QBO were to be expected, these results are overall promising.

RQ1. How do the gravity waves that drive the QBO and the downward propagation of the QBO shear zones respond to a warming climate?

To answer this question, I conducted a series of 45-day-long idealized warming simulations with the state-of-the-art GSRM ICON in its R2B9L191 configuration. The results of these simulations provide robust evidence that the lower-stratospheric GWMF relevant for the QBO is likely to increase in a warming climate due to a strengthening of tropical deep convection. As a consequence, the downward propagation of the QBO jets in the warmer climate states becomes faster. In light of these results, a shortening of the QBO period under global warming becomes more likely, but of course cannot be reliably concluded from the very short simulations. In addition, the global storm-resolving ICON simulations indicate that tropical deep convection will become deeper in a warming climate, ultimately causing a shift in the gravity wave spectrum towards larger absolute phase speeds. Given the established link between the phase speed spectrum of the waves driving the QBO and the QBO amplitude (Saravanan, 1990; Geller et al., 2016b), I argue that this shift in the gravity wave spectrum explains why, in my simulations, the magnitude of the QBO jets in the upper QBO domain becomes larger in the warmer climate states. In doing so, I present a stringent conceptual mechanism based on well-known first principles that can explain the observed strengthening of the QBO jets in the upper QBO domain since the late 1950s, which is potentially warming-driven and could not yet been explained based on simulations by conventional GCMs.

5.2   IMPLICATIONS AND PERSPECTIVES

So far, the response of the QBO period to global warming has been uncertain because the response of the parameterized gravity wave forcing of the QBO to global warming has been uncertain (Schirber et al., 2015; Richter et al., 2020b). I argue that my work has shifted this uncertainty. My results provide robust evidence that a warming climate will lead to the generation of stronger gravity waves, causing an increase in the GWMF entering the stratosphere. Based on this finding, I expect that the total QBO wave forcing — accumulated from small-scale gravity waves up to planetary-scale equatorial waves — will strengthen in a warming climate, acting to shorten the QBO period. At the same time, however, also the tropical upwelling is robustly projected to increase in a warming climate (e.g., Butchart et al., 2006;

Hardiman et al., 2014), acting to lengthen the QBO period (Kawatani et al., 2011; Watanabe and Kawatani, 2012; Richter et al., 2020b). Therefore, the uncertainty in projections for the QBO period now lies in the net effect of these two quantitatively uncertain changes, and depending on which one is stronger, the QBO period will become either shorter or longer.

Although my short simulations suggest that the strengthening of the QBO wave forcing may dominate as the QBO becomes faster, they cannot provide a reliable estimate of how the QBO period may change. This is due the fact that the simulations are too short to reliably represent any warming-induced change in the tropical upwelling and planetary-scale wave forcing of the QBO, both processes with a long characteristic timescale. This problem could be addressed by longer simulations of at least one full QBO cycle — but preferably even more — for different climate states, which is an important target for future work. However, given the current difficulties ICON has in simulating a reasonable full QBO cycle at all (see Chp. 3), such simulations are currently not reasonable.

Consequently, the question arises as to how the current biases in the representation of the QBO in ICON could be resolved. Here, it becomes helpful that I could narrow down the origin of the QBO biases to a pronounced lack of planetary-scale wave forcing, which I have attributed to the underestimation of CCEWs in the troposphere. This finding sets a clear pathway for future work, which must obviously aim at finding and remedying the root cause of this underestimation of CCEWs in ICON. The reasonable representation of CCEWs in other GSRMs employing horizontal grids with a comparable resolution (e.g., Judt and Rios-Berrios, 2021; Rios-Berrios et al., 2023; Takasuka et al., 2024) suggests that the underestimation of CCEWs in the present ICON configuration is rather a model-specific problem. Therefore, I propose to investigate the parameter setting of the current ICON configuration in more detail, as it may still be suboptimal for simulating the processes necessary for the formation of CCEWs. As shown by Takasuka et al. (2024) for the GSRM NICAM[1], the representation of CCEWs can be improved substantially by a systematic and targeted tuning of the remaining parameterizations of mixing and cloud microphysics. It is likely that a more systematic and targeted tuning approach would lead to improvements in the representation of CCEWs also in ICON, given that the sensitivity study in this dissertation followed a rather heuristic approach. The dependence of the simulated QBO on the magnitude of vertical diffusion found in the sensitivity study supports this claim.

However, if extensive tuning proves to resolve the current biases in CCEWs and the QBO in ICON, some people might be tempted to question the general value of global storm-resolving QBO simulations. In particular, one may ask whether we only shift the uncertainty in QBO simulations from one parameterization to the next one? This is a legitimate question, of course, but it also diminishes the immense scientific progress that this shift in uncertainty already allows for. As shown in this dissertation using ICON, even a GSRM with notable biases in its representation of the QBO already allows for a new conceptual understanding of the response of the QBO to global warming that would not have been possible by using conventional GCMs. Obviously, at least at this conceptual level of understanding of warming-

---

1 NICAM is short for "Non-hydrostatic Icosahedral Atmospheric Model" (Tomita and Satoh, 2004; Satoh et al., 2008).

induced changes of the QBO, the benefits of an explicit versus a parameterized representation of tropical deep convection and gravity waves clearly outweigh the remaining uncertainties in the representation of these two processes in the global storm-resolving configuration of ICON.

Despite the step change that GSRMs represent in simulating the QBO, one question that remains is the role of their horizontal resolution. There is clear evidence that individual deep convective cells (e.g., Prein et al., 2015) and details of the tropical gravity wave spectrum (Lane and Knievel, 2005; Polichtchouk et al., 2021) are still not adequately represented at the horizontal resolution of the R2B9L191 configuration, i.e. 4.93 km. At this point, however, it is unclear whether these details matter for the simulated QBO. Although my results indicate that the R2B9L191 configuration is in principle sufficient to simulate reasonable QBO dynamics in the upper QBO domain, the comparison between the R2B9L191 and R2B8L191 configurations (horizontal grid spacings of 4.93 km and 9.86 km, respectively) already showed that the simulated QBO still depends on the horizontal resolution (see Sec. 2.2). Thus, direct QBO simulations at even higher horizontal resolutions are a clear target for future research to test the resolution-dependency of the simulated QBO. This may be further extended to testing different vertical resolutions.

The understanding gained in global storm-resolving simulations eventually also allows for a more critical and informed assessment of the results of conventional GCMs. This is crucial because conventional GCMs with parameterizations of deep convection and gravity waves will certainly remain the backbone of climate projections for some time to come, given the immense computational requirements of GSRMs. The results of this dissertation clearly show that QBO projections from conventional GCMs which employ gravity wave parameterizations that impose a fixed source spectrum must be called into question and may be rejected with increasing confidence. More fundamentally, in light of my results the assumption of a fixed gravity wave source spectrum per se is no longer tenable under global warming, at least in the tropics where gravity waves are predominantly generated by deep convection. This highlights the need for physically advanced interactive gravity wave parameterizations for QBO projections in conventional GCMs and strongly supports recent calls for revisiting current gravity wave parameterizations in general (Plougonven et al., 2020; Achatz et al., 2024).

5.3 FINAL REMARKS

In this dissertation, I have shown that a state-of-the-art GSRM with an explicit representation of deep convection and gravity waves is in principle capable of simulating the dynamics of the QBO. I used this model to investigate how the QBO and its gravity wave forcing could respond to global warming. My work indicates that the gravity wave forcing of the QBO will become stronger in a warming climate and that the spectral distribution of the gravity wave forcing is likely to shift toward larger absolute phase speeds. As a result, my work shifts the uncertainty in projections of the QBO period and allows for a new explanation of recent, likely warming-driven observational trends in the QBO amplitude. Thereby, it ultimately continues the remarkable voyage of discovery in the tropical stratosphere that began with the eruption of Mt. Krakatau more than 140 years ago.

Part II

APPENDIX

TOWARDS A DIRECT SIMULATION OF A FULL CYCLE OF THE QUASI-BIENNIAL OSCILLATION IN A GLOBAL STORM-RESOLVING MODEL

The work in this appendix is in preparation for publication as:

H. Franke and M. Giorgetta (2024). "Towards a direct simulation of a full cycle of the quasi-biennial oscillation in a global storm-resolving model." In: *preparation for submission to the Journal of Advances in Modeling Earth Systems*

AUTHOR CONTRIBUTIONS

Marco Giorgetta and me conceptualized the study, and developed the methodology. I conducted the investigation, performed the formal analysis, visualized the results, and wrote the manuscript. Marco Giorgetta helped with the interpretation of the results, revised the initial manuscript, and supervised the study.

TOWARDS A DIRECT SIMULATION OF A FULL CYCLE OF THE QUASI-BIENNIAL OSCILLATION IN A GLOBAL STORM-RESOLVING MODEL

Henning Franke[1,2]**, Marco Giorgetta**[1]

[1]*Max Planck Institute for Meteorology, Hamburg, Germany*
[2]*International Max Planck Research School on Earth System Modelling, Max Planck Institute for Meteorology, Hamburg, Germany*

ABSTRACT

This study presents the first attempt to directly simulate a full cycle of the quasi-biennial oscillation (QBO) in a global storm-resolving model (GSRM) that explicitly simulates deep convection and gravity waves instead of parameterizing them. Using the Icosahedral Nonhydrostatic (ICON) model with a horizontal and vertical resolution of about 5 km and 400 m, respectively, we show that a state-of-the-art global storm-resolving model is in principle capable of simulating the basic dynamics leading to a QBO-like oscillation of the zonal wind in the tropical stratosphere. ICON shows overall good fidelity in simulating the downward propagation of the QBO jets in the upper QBO domain (25 km–35 km), and for the right reasons. In the lowermost stratosphere, however, ICON does not simulate the downward propagation of the QBO jets to the tropopause. This is the result of a pronounced lack of QBO wave forcing, mainly on planetary scales. As a consequence, the QBO jets degrade with increasing simulation time and substantially lose strength. We show that the lack of planetary-scale wave forcing in the lowermost stratosphere is caused by an underestimation of the planetary-scale wave momentum flux entering the stratosphere, which is too weak by 20 %–40 %. We attribute this lack of planetary-scale wave momentum flux to a substantial lack of convectively coupled equatorial waves in the tropical troposphere. While conventional general circulation models can compensate for a lack of resolved wave forcing to some degree by tuning their parameterized gravity wave forcing, global storm-resolving models no longer have this option, making their QBO more susceptible to model biases. Therefore, we conclude that in the present global storm-resolving model, simulating a realistic spatio-temporal variability of tropical convection is currently the main roadblock towards simulating a reasonable QBO.

A.1   INTRODUCTION

The quasi-biennial oscillation (QBO) is a more or less regular downward propagating oscillation of the zonal wind in the tropical stratosphere, driven by the breaking and dissipation of upwardly propagating tropical waves (Baldwin et al., 2001). The wave spectrum that drives the QBO ranges from large-scale planetary

waves to small-scale gravity waves (GWs), and the vast majority of these waves are generated by tropical deep convection (e.g., Holton, 1972; Fritts and Alexander, 2003). However, deep convection and a substantial part of the GW spectrum are not resolved by conventional general circulation models (GCMs), which typically employ horizontal grid spacings of $\mathcal{O}(100\,\text{km})$. Therefore, deep convection and GWs are usually parameterized in these models, which leads to considerable uncertainties in the simulated QBO (Bushell et al., 2020). In this study, we present the first attempt to overcome this uncertainty by a direct simulation of a full QBO cycle in a GCM that no longer parameterizes deep convection and GWs but instead explicitly simulates both processes — and thus the entire QBO forcing.

Successfully modeling the QBO in a realistic manner has ever since posed a major challenge to conventional three-dimensional GCMs, and the fidelity of simulated QBOs in such models has increased only slightly over the last two decades (Schenzinger et al., 2017; Richter et al., 2020a). This motivated the recent model intercomparison project Quasi-Biennial Oscillation initiative (QBOi), which aimed to asses the status quo of the ability of the latest GCMs to simulate a QBO and to identify possible avenues for improvement (Butchart et al., 2018). As one of the main results of QBOi, it was shown that the partitioning of the QBO wave forcing between resolved and parameterized waves is highly model-dependent, with the contribution of the parameterized GWs varying between 40 % and 80 % (Bushell et al., 2020). On the one hand, this large intermodel spread can be directly attributed to the inherent uncertainty of the GW parameterizations themselves, which results from the necessary simplifying assumptions in their formulation. These simplifications include that most GW parameterizations allow only for instantaneous and vertical GW propagation, often do not account for GW intermittency and secondary generation, and prescribe a fixed GW source spectrum (Plougonven et al., 2020; Achatz et al., 2024). The prescribed GW source spectrum is still poorly constrained by observations and thus varies widely between different models (Alexander et al., 2010). On the other hand, the uncertainty in the relative contribution of resolved and parameterized waves to driving the QBO is a consequence of the fact that GW parameterizations are often used to optimize the simulated QBO to achieve a somewhat realistic QBO period and amplitude (e.g., Garfinkel et al., 2022).

In part, the tuning becomes necessary to compensate for biases in the resolved wave forcing of the QBO. These biases often arise from the parameterization of deep convection, which affects the representation of convectively coupled equatorial waves (CCEWs; e.g., Lin et al., 2008; Straub et al., 2010; Frierson et al., 2011). Since CCEWs are closely coupled to SEWs, the details of the parameterization of deep convection can affect the resolved wave momentum fluxes in the lower stratosphere, which contribute to driving the QBO (Ricciardulli and Garcia, 2000; Horinouchi et al., 2003). Furthermore, the parameterization of deep convection directly or indirectly provides the input fields that are used to estimate the wave sources of interactive GW parameterizations (e.g., Beres et al., 2004; Richter et al., 2010; Bushell et al., 2015), thereby influencing the parameterized GW forcing of the QBO.

Obviously, the uncertainties associated with the parameterizations of deep convection and GWs lead to substantial uncertainty in the overall QBO momentum budget. This severely limits our current understanding of the details of the QBO forcing. Moreover, the tendency to overtune GW parameterizations toward a realistic representation of the present-day QBO prevents insight into out-of-sample

conditions, as demonstrated for the question of how the QBO may change due to global warming (Schirber et al., 2015; Richter et al., 2020b). Despite recent progress in the development of more sophisticated GW parameterizations (e.g., Bölöni et al., 2021; Kim et al., 2021), it is questionable whether the current approach to modeling the QBO will allow for fundamental new insights in the foreseeable future.

As a starting point to overcome this parameterization deadlock, Giorgetta et al. (2022) presented the first direct simulation of QBO jets over a short period of 48 days in a very high resolution GCM (∼5 km horizontal, ∼400 m vertical) that no longer employs a parameterization of deep convection and GWs. This type of GCMs is commonly referred to as global storm-resolving models (GSRMs) (e.g., Satoh et al., 2019; Stevens et al., 2019). GSRMs offer substantial potential for reducing the long-standing uncertainty in modeling the QBO. However, current GSRMs mostly employ horizontal grid spacings between $\mathcal{O}(1\,\text{km})$ and $\mathcal{O}(10\,\text{km})$. These grid spacings are often referred to as the "convective gray zone" because they partially but not fully resolve deep convection, and thus neither traditional parameterizations of deep convection nor its explicit treatment work satisfactorily (e.g., Prein et al., 2015; Tomassini et al., 2023). As shown by Polichtchouk et al. (2021), these problems in representing deep convection also affect the details of the simulated tropical GW spectrum, i.e. the partitioning of the resolved GWMF with respect to horizontal wavelength. They suggest that even at a horizontal grid spacing of less than 5 km, a scale-aware parameterization of deep convection may be necessary to accurately simulate the resolved GWMF.

However, it is currently unclear whether this fidelity in representing the details of the GW spectrum is really necessary for the simulation of a realistic QBO, or whether major aspects of the QBO are already well captured in a GSRM operating in the gray zone. This question cannot be answered by the short simulation of Giorgetta et al. (2022), although they have shown that a state-of-the-art GSRM is in principle capable of simulating a reasonable wave-driven downward propagation of the QBO jets over a period of 48 days. While such short simulations work as a first proof of concept and also allow for specific process studies (e.g., Franke et al., 2023a), they do not allow for a systematic evaluation of the QBO and its forcing, which requires the simulation of at least one full QBO cycle.

This situation motivates the present study, which aims at the first direct simulation of a full QBO cycle in a GSRM which neither applies a parameterization of deep convection nor GWs. The simulation was performed by the global storm-resolving Icosahedral Nonhydrostatic (ICON) model with a horizontal grid spacing of about 5 km and a vertical grid spacing between 350 m and 560 m in the stratosphere. As this is the first simulation of its kind over such a long period, we certainly do not expect the model to simulate a QBO that is already close to reality. Rather, we want to find out whether a GSRM in the chosen configuration is able to capture the basic characteristics and dynamics of the QBO and which aspects need further improvement. In doing so, we aim to provide a benchmark simulation to guide future model development. More specifically, we will address the following research questions:

1. *Is a state-of-the-art GSRM capable of directly simulating a full cycle of the QBO in a reasonable way? Which aspects of the QBO are well captured and which are not?*

2. *Why does the model simulate the QBO the way it does?*
   If the QBO is reasonably simulated, how is it forced in the simulation? Is it
   reasonable for the right reasons, or is it the product of compensating errors?
   If the QBO is not reasonably simulated, what are the sources of QBO biases?
   Are QBO biases caused by biases in other aspects of the simulation?

A.2 METHODS

A.2.1 *Global storm-resolving ICON simulation*

We conducted a two-year-long global storm-resolving simulation with the non-hydrostatic GSRM ICON in an atmosphere-only setup (Giorgetta et al., 2018). Following the scientific rationale of our study, this simulation employs neither a parameterization of deep convection nor a parameterization of both orographic and non-orographic GWs. Instead, the horizontal and vertical resolution allows for an explicit representation of these processes. Horizontally, the simulation uses the R2B9 grid, which has an equivalent grid spacing of $\sim$4.9 km (see Giorgetta et al., 2018, Tab. 1), and vertically it uses a grid with 191 levels up to an altitude of 83 km, resulting in a vertical grid spacing of $\sim$350 m in the tropopause region and $\sim$560 m in the stratopause region (see Giorgetta et al., 2022, Fig. 1). To ensure the numerical stability of the model, we performed the simulation with a timestep of 30 s, which was further divided into 8 dynamics substeps. In contrast, (Giorgetta et al., 2022) used a timestep of 40 s and 5 dynamics substeps, which proved to be not stable enough for longer simulations. Details on the dynamical substepping can be found in Zängl et al. (2015). Since this storm-resolving model setup is computationally very demanding, we performed the simulation with the GPU-enabled version of ICON (Giorgetta et al., 2022).

The storm-resolving configuration of ICON retains parameterizations for only three remaining processes: radiation, cloud microphysics, and turbulent vertical diffusion. For radiation, the GPU-enabled ICON employs the RTE+RRTMGP scheme (Pincus et al., 2019). Cloud microphysics is parameterized using a one-moment „graupel" microphysics scheme (Baldauf et al., 2011; Doms et al., 2021). The vertical diffusion of heat, momentum, and tracers is parameterized using a total turbulent energy scheme (Mauritsen et al., 2007; Pithan et al., 2015). This scheme represents the size of the largest turbulent eddies by calculating a turbulent length scale l, which by default is capped at $l_{max} = 150$ m outside the boundary layer (Pithan et al., 2015). In our simulation, we reduced l_{max} to 50 m because $l_{max} = 150$ m was found to lead to unreasonably strong vertical diffusion. For details on the parameterizations, please refer to Giorgetta et al. (2018) and Giorgetta et al. (2022).

In ICON, explicit horizontal diffusion is employed as a second-order Smagorinsky diffusion acting on potential temperature and horizontal velocity combined with a fourth-order background diffusion acting on horizontal velocity only with an e-folding time of 1080 s. In addition, ICON employs a fourth-order divergence damping acting on three-dimensional divergence in order to ensure numerical stability. To avoid the unphysical reflection of waves at the top of the model, ICON employs a Rayleigh damping acting on the vertical velocity above 50 km (Klemp

et al., 2008). Details on the formulation of the diffusion and damping acting in ICON can be found in Zängl et al. (2015).

The simulation itself was set up as a two-year-long time slice experiment initialized from the operational analysis of the Integrated Forecasting System of the European Centre for Medium-Range Weather Forecasts on April 1, 2004 at 00:00:00 UTC. The boundary conditions closely follow the experimental protocol of the QBOi Experiment 2 (Butchart et al., 2018). Accordingly, the SST and sea ice concentration (SIC) have been prescribed as a repeating annual cycle of the 1988–2007 monthly means from the corresponding Coupled Model Intercomparison Project phase 6 (CMIP6) input datasets (Durack and Taylor, 2019). The concentrations of carbon dioxide (CO_2) and other radiatively active trace gases except ozone (O_3) were also set to their 1988–2007 mean values from the CMIP6 input dataset (Meinshausen et al., 2017), resulting in a CO_2 concentration of 365.59 ppm. The O_3 concentration is modeled interactively using the linearized ozone scheme of Cariolle and Teyssèdre (2007). Tropospheric aerosols are prescribed with their 2002 monthly means from the Max Planck Institute aerosol climatology (MAC; Kinne et al., 2013), and the solar forcing is also prescribed with its 2002 monthly means. The year 2002 was chosen based on the QBOi experimental protocol (Butchart et al., 2018).

The simulation is analyzed based on three-hourly instantaneous output of atmospheric state variables and three-hourly averaged output of tendencies and fluxes. The output has been interpolated from the native triangular R2B9 grid to a regular n256 Gaussian grid, which has a grid spacing of ∼39 km at the equator, using a distance-weighted remapping of the 13 nearest neighbors. The three-dimensional output fields were then further interpolated vertically from the native terrain-following hybrid sigma height coordinate to geometric height levels corresponding to the sigma height levels over ocean. Since the transition from terrain-following coordinate surfaces to flat coordinate surfaces occurs at an altitude of 22.5 km, the target height levels of the vertical interpolation are identical to the model levels above this altitude.

A.2.2   *Reference datasets*

To evaluate the simulated QBO, its zonal momentum budget, and the equatorial wave field, we compare the simulation to observationally constrained reference datasets.

A.2.2.1   *ERA5 reanalysis*

As a reference for the QBO and its zonal momentum budget, we use the ECMWF Reanalysis v5 (ERA5; Hersbach et al., 2020). We use only one reanalysis dataset as a reference because the representation of the QBO is very similar in different recent state-of-the-art reanalyses (SPARC, 2022, Chp. 9). The representation of the QBO in ERA5 itself has been investigated in detail by Pahlavan et al. (2021a,b).

ERA5 has a spectral truncation of T639, corresponding to an n320 Gaussian grid, which has a grid spacing of ∼31 km, and 137 hybrid sigma pressure levels up to 1 hPa. The three wind components, temperature, and the surface geopotential are provided on the original T639 spectral grid, while tracer and two-dimensional

surface fields are provided on a reduced n320 Gaussian grid (Hersbach et al., 2018b,a). Thus, in a first step, we interpolated the raw ERA5 data to the same regular n256 Gaussian grid as the ICON output using a distance-weighted remapping of the four nearest neighbours. We then interpolate the ERA5 data to the 191 geometric height levels of the postprocessed ICON output.

Please note that we used ERA5.1 instead of ERA5 for the period 2000–2006. This is due to the fact that ERA5 has a pronounced stratospheric cold bias during these years due to incorrect data assimilation, which has been fixed in ERA5.1 (Simmons et al., 2020). When we refer to ERA5 throughout this manuscript, we implicitly mean ERA5.1 during the years 2000–2006.

A.2.2.2 *IMERG precipitation observations*

As an additional reference dataset for tropical precipitation, we use a satellite-based observational product, the Integrated Multi-satellite Retrievals for the Global Precipitation Measurement (IMERG) for the period April 1, 2004–March 31, 2006 (Huffman et al., 2022). IMERG provides the half-hourly mean precipitation rate with a spatial resolution of $0.1° \times 0.1°$. We resampled the data to three-hourly mean precipitation rates to match the temporal resolution of the ICON output. Afterwards, we interpolated the data to the same regular n256 Gaussian grid as the ICON output, using a distance-weighted average remapping of the four nearest neighbours.

A.2.3 *Diagnostics*

A.2.3.1 *Equatorial wave spectra*

We investigate the equatorial wave field by means of spectral analysis in longitude λ and time t. The two-dimensional power spectrum P_x of a quantity $x(\lambda, t)$ with respect to zonal wavenumber k and frequency ω is calculated as

$$P_x(k, \omega) = \frac{1}{N_\lambda^2 N_t^2} \mathcal{F}_x(k, \omega) \tilde{\mathcal{F}}_x(k, \omega), \tag{A.1}$$

where $\mathcal{F}_x$ is the complex Fourier transform of x, $\tilde{\mathcal{F}}_x$ is its complex conjugate, N_λ denotes the number of grid points in longitude, and N_t denotes the number of samples in time. The chosen normalization of $P_x(k, \omega)$ satisfies Parseval's theorem as

$$\frac{1}{N_\lambda N_t} \sum_{i=1}^{N_\lambda} \sum_{j=1}^{N_t} \left| x_{i,j}^2 \right| = \sum_{k=-N_\lambda/2}^{N_\lambda/2} \sum_{\omega=-N_t/2}^{N_t/2} P_x(k, \omega). \tag{A.2}$$

Analogously, we define the cospectrum of two quantities $x(\lambda, t)$ and $y(\lambda, t)$ as

$$P_{xy}(k, \omega) = \frac{1}{N_\lambda^2 N_t^2} \mathfrak{R} \left(\mathcal{F}_x(k, \omega) \tilde{\mathcal{F}}_y(k, \omega) \right), \tag{A.3}$$

where $\mathfrak{R}$ denotes the real part.

To diagnose CCEWs, we follow the methodology of Wheeler and Kiladis (1999) and split a quantity $x(\lambda, \phi, t)$, which depends on latitude ϕ into its symmetric and antisymmetric component with respect to the equator, $x_{\text{sym}}(\lambda, \phi, t)$ and $x_{\text{asym}}(\lambda, \phi, t)$, respectively:

$$
\begin{aligned}
x_{\text{sym}}(\lambda, \phi, t) &= \frac{x(\lambda, \phi, t) + x(\lambda, -\phi, t)}{2} \\
x_{\text{asym}}(\lambda, \phi, t) &= \frac{x(\lambda, \phi, t) - x(\lambda, -\phi, t)}{2}.
\end{aligned}
\tag{A.4}
$$

We then compute the zonal wavenumber-frequency spectra of $x_{\text{sym}}(\lambda, \phi, t)$ and $x_{\text{asym}}(\lambda, \phi, t)$ as described in Eq. A.1 and normalize them by a smoothed background spectrum.

A.2.3.2 *QBO momentum budget*

To understand what processes drive the QBO in the ICON simulation, we diagnose the QBO zonal momentum budget in the transformed Eulerian mean (TEM) framework (Andrews and McIntyre, 1976). The TEM framework allows for a clear separation between the different forcing processes of the QBO. We calculate the TEM zonal momentum budget based on the hydrostatic primitive equations in geometric height coordinates (Hardiman et al., 2010):

$$
\overline{u}_{,t} = \overline{v}^* \left(f - \frac{(\overline{u}\cos\phi)_{,\phi}}{A\cos\phi} \right) - \overline{w}^* \overline{u}_{,z} + \frac{\nabla \cdot \boldsymbol{F}}{\overline{\rho} a \cos\phi} + \overline{X}.
\tag{A.5}
$$

Here, u denotes the zonal wind, f denotes the Coriolis parameter, ρ denotes the air density, a denotes Earth's mean radius, which we set to $a = 6371\,\text{km}$, ϕ denotes the latitude, v^* and w^* denote the meridional and vertical residual velocity, respectively, and $\boldsymbol{F}$ denotes the Eliassen-Palm (EP) flux. Furthermore, an overbar represents the zonal mean, and the subscripts $(,t)$, $(,\phi)$, and $(,z)$ denote the partial derivatives with respect to time, latitude, and altitude, respectively.

In Eq. A.5, the first and second term on the right-hand-side represent the acceleration of $\overline{u}$ by the meridional and vertical residual advection of zonal mean axial angular momentum per unit mass, respectively. The third term on the right-hand-side of Eq. A.5 represents the wave forcing of $\overline{u}$ which is resolved by the analysis grid, and $\nabla \cdot \boldsymbol{F}$ is given by

$$
\nabla \cdot \boldsymbol{F} = \frac{\left(\cos\phi F^{(\phi)} \right)_{,\phi}}{a\cos\phi} + F^{(z)}_{,z},
\tag{A.6}
$$

where $F^{(\phi)}$ and $F^{(z)}$ denote the meridional and vertical component of $\boldsymbol{F}$, respectively. They are given by

$$
\begin{aligned}
F^{(\phi)} &\equiv -a\cos\phi\,\overline{(\rho v)' u'} + \psi \overline{u}_{,z} \\
F^{(z)} &\equiv -a\cos\phi\,\overline{(\rho w)' u'} - \psi \left(\frac{(\overline{u}\cos\phi)_{,\phi}}{A\cos\phi} - f \right).
\end{aligned}
\tag{A.7}
$$

Here, a prime represents the deviation from the zonal mean, and ψ denotes the „difference stream function" (cf. Hardiman et al., 2010) and is defined as

$$
\psi \equiv \frac{a\cos\phi}{\left| \nabla \overline{\theta} \right|^2} \left(\overline{(\rho v)' \theta'}\, \overline{\theta}_{,z} - \overline{(\rho w)' \theta'}\, \frac{\overline{\theta}_{,\phi}}{a} \right),
\tag{A.8}
$$

where θ denotes the potential temperature. The fourth term on the right-hand-side of Eq. A.5, $\overline{X}$, represents the residual which remains when subtracting the previous three terms from the actual zonal wind tendency simulated by ICON. This means that $\overline{X}$ contains all tendencies from processes not resolved by the TEM analysis, including the parameterized tendency from vertical diffusion and diffusive tendencies from the dynamical core itself.

Following Horinouchi et al. (2003), we also calculate spectra of F as a function of zonal wavenumber k and frequency ω:

$$F^{(\phi)}(k,\omega) \equiv -a\cos\phi\, P_{(\rho v)'u'}(k,\omega) + \psi(k,\omega)\,\overline{u}_{,z}$$
$$F^{(z)}(k,\omega) \equiv -a\cos\phi\, P_{(\rho w)'u'}(k,\omega) - \psi(k,\omega)\left(\frac{(\overline{u}\cos\phi)_{,\phi}}{A\cos\phi} - f\right) \tag{A.9}$$

with

$$\psi(k,\omega) \equiv \frac{a\cos\phi}{\left|\nabla\overline{\theta}\right|^2}\left(P_{(\rho v)'\theta'}(k,\omega)\,\overline{\theta}_{,z} - P_{(\rho w)'\theta'}(k,\omega)\,\frac{\overline{\theta}_{,\phi}}{a}\right). \tag{A.10}$$

Here, the cospectra $P_{(\rho v)'u'}$ and $P_{(\rho v)'u'}$ as well as $P_{(\rho v)'\theta'}$ and $P_{(\rho v)'\theta'}$ are calculated based on Eq. A.3. For both ICON and ERA5, we compute the TEM diagnostics based on the postprocessed data on the n256 Gaussian grid with 191 geometric height levels. This procedure follows the recommendations of Hardiman et al. (2010) for comparing TEM diagnostics between datasets on different native grids. It should be noted that the vertical remapping of the ERA5 data prior to the calculation of the TEM diagnostics can result in artefacts in the calculates wave forcing. However, we found this effect to be negligible.

A.3 GENERAL STRUCTURE OF THE QBO-LIKE OSCILLATION IN THE ICON SIMULATION

Figure A.1a shows the time evolution of the stratospheric 5° S–5° N mean zonal wind in the ICON simulation. Throughout the entire simulation, ICON sustains a QBO-like zonal wind structure of easterly and westerly wind jets alternating with altitude. The easterly shear zone (i.e., a change of winds from westerly to easterly with altitude), which is initially located between ∼30 km and ∼38 km, shows a clear downward propagation during the first year of the simulation. This indicates that ICON is in principle able to simulate the dynamics that drive the QBO. However, the downward propagation of the easterly shear zone stops in the second year of the simulation, and the westerly shear zone, which is initially located between 18 km and 25 km, does not propagate downward at all. As a result, the westerly jet stalls and does not complete within the simulated period of two years, which means that ICON does not simulate a closed cycle of the QBO. Nevertheless, from now on we will refer to the zonal wind structure in the equatorial stratosphere in the ICON simulation as the *ICON-QBO*.

In the following, we compare the ICON-QBO with selected individual QBO cycles in the ERA5 reanalysis during the years 1980–2015. This period has boundary conditions reasonably close to those of the ICON simulation, and it is free of QBO disruptions such as those observed in 2015/16 and 2019/20 (see Osprey et al., 2016;
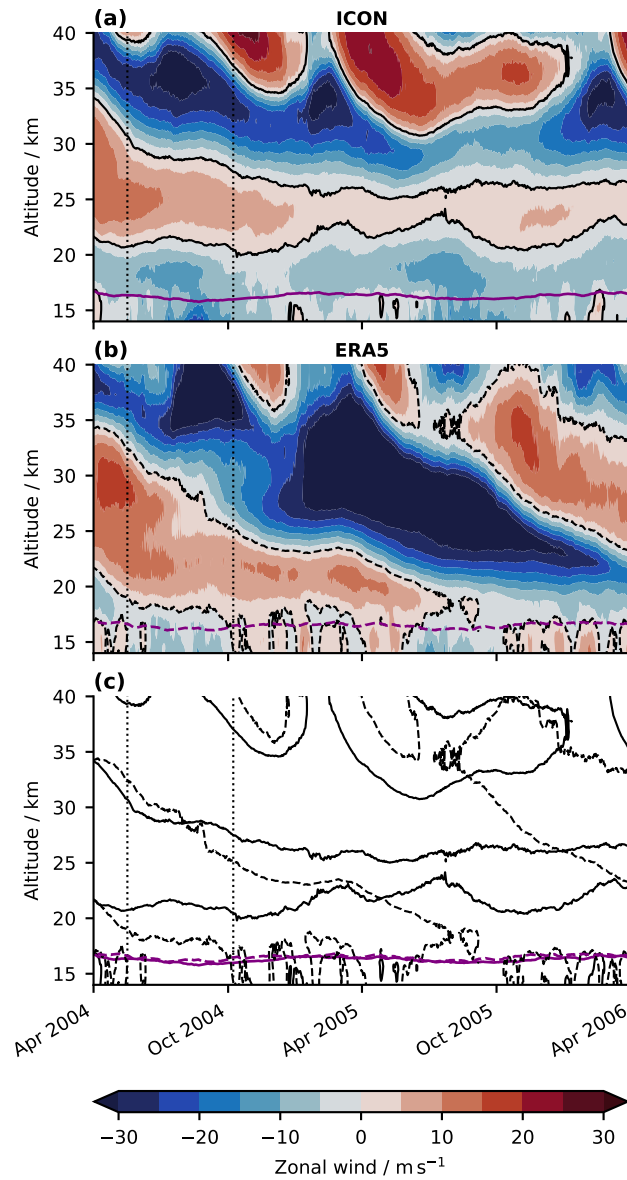
Figure A.1: Time-altitude cross section of the 5° S–5° N mean zonal wind for **(a)** the ICON simulation and **(b)** the ERA5 reanalysis during April 1, 2004–March 31, 2006. The **(a)** solid and **(b)** dashed black contour lines mark the $0 \, \mathrm{m \, s^{-1}}$-isotach. The **(a)** solid and **(b)** dashed purple contour lines mark the $370 \, \mathrm{K}$-isentrope, which serves as a proxy for the tropopause altitude. Panel **(c)** shows the $0 \, \mathrm{m \, s^{-1}}$-isotachs and $370 \, \mathrm{K}$-isentropes of panels **(a)** and **(b)** to allow a direct comparison between ICON and ERA5. The vertical dotted black lines in all panels mark the beginning and end of the period used to compare the zonal momentum budgets of the 5° S–5° N mean zonal wind in ICON and ERA5 (see Section A.4.2.2).

Anstey et al., 2021). To select reasonable individual QBO cycles for comparison, we first determine those years in which the QBO in March and April was in a phase comparable to that of March and April 2004 because we initialized the ICON simulation on April 01, 2004. The applied criterion for this subsampling is a change of the monthly mean 5° S–5° N mean zonal wind at one of the four levels between 21 km and 22.5 km (i.e., 22.432 km, 22.051 km, 21.672 km, 21.296 km) from easterly

in March to westerly in April. This criterion is fulfilled by six years (1985, 1990, 1997, 2004, 2008, and 2013), which we will hereafter refer to as the *ERA5-QBO-ensemble*.

In Figure A.2, we compare the time evolution of the 5° S–5° N mean zonal wind between the ICON simulation and the ERA5-QBO-ensemble. The basic structure of the ICON-QBO is approximately within the cycle-to-cycle variability of the ERA5-QBO-ensemble in the first year of the simulation (Fig. A.2a). During this period, ICON simulates an overall reasonable downward propagation of the $0\,\mathrm{m\,s^{-1}}$-isotach, which is initially located at ~34 km, at a rate comparable to that of individual cycles in the ERA5-QBO-ensemble. This also applies to the zonal wind jets associated with the semiannual oscillation (SAO) between 35 km and 40 km. In the lowermost stratosphere, the comparison between the ICON-QBO and the ERA5-QBO-ensemble reveals the unrealistic lack of downward propagation of the westerly jet of the ICON-QBO right from the beginning of the simulation, which was already identified in Figure A.1a. During the second year of the simulation, the spatio-temporal structure of the ICON-QBO is no longer consistent with the ERA5-QBO-ensemble throughout the entire stratosphere.

Figure A.2b further shows that the jets of the ICON-QBO are weaker than those of the ERA5-QBO-ensemble in both the lower and upper QBO domain throughout the entire simulation. The vertical structure of ICON-QBO is not consistent with the ERA5-QBO-ensemble right from the beginning of the simulation. In addition, Figure A.2b clearly shows that the ICON-QBO is trapped at the end of the simulation due to its lack of downward propagation.

Although the six individual QBO cycles of the ERA5-QBO-ensemble do not provide a statistically significant reference sample, we conclude at this point that the ICON-QBO is not realistic. It suffers from a pronounced lack of downward propagation, which begins in the lowermost stratosphere right at the beginning of the simulation and appears to spread upward subsequently. During the last months of the simulation, basically the entire ICON-QBO below ~30 km no longer propagates downward.

To further highlight the shortcomings of the ICON-QBO in more detail, we compare it to one specific QBO cycle of the ERA5-QBO-ensemble, which is the cycle beginning on April 1, 2004 (Fig. A.1b). The comparison with a single QBO cycle is justified because all individual QBO cycles of the ERA5-QBO-ensemble agree reasonably well among each other, except for the cycle affected by the eruption of Mt. Pinatubo (Fig. A.2b). From now on, we will refer to the ERA5 QBO cycle beginning on April 1, 2004 as the *ERA5-QBO*. The comparison between the ICON-QBO and the ERA5-QBO basically confirms the previous results, and in particular highlights that the ICON-QBO has too weak jets below 30 km, especially during the second year of the simulation. During this period, the jets of the ICON-QBO also have a much smaller vertical extent than those of the ERA5-QBO. In addition, the vertical gradient of the zonal wind within the shear zones of the ICON-QBO is much weaker than in those of the ERA5-QBO, at least below 30 km.

Figure A.1 also shows that the altitude of the tropopause in the ICON simulation and the ERA5 reanalysis is approximately identical. Thus, we already rule out a too high tropopause in ICON as a root cause for the lack of downward propagation of the ICON-QBO in the lowermost stratosphere. Instead, the downward propagation of the ICON-QBO stops well above the tropopause, while the ERA5-QBO propagates down to the tropopause.
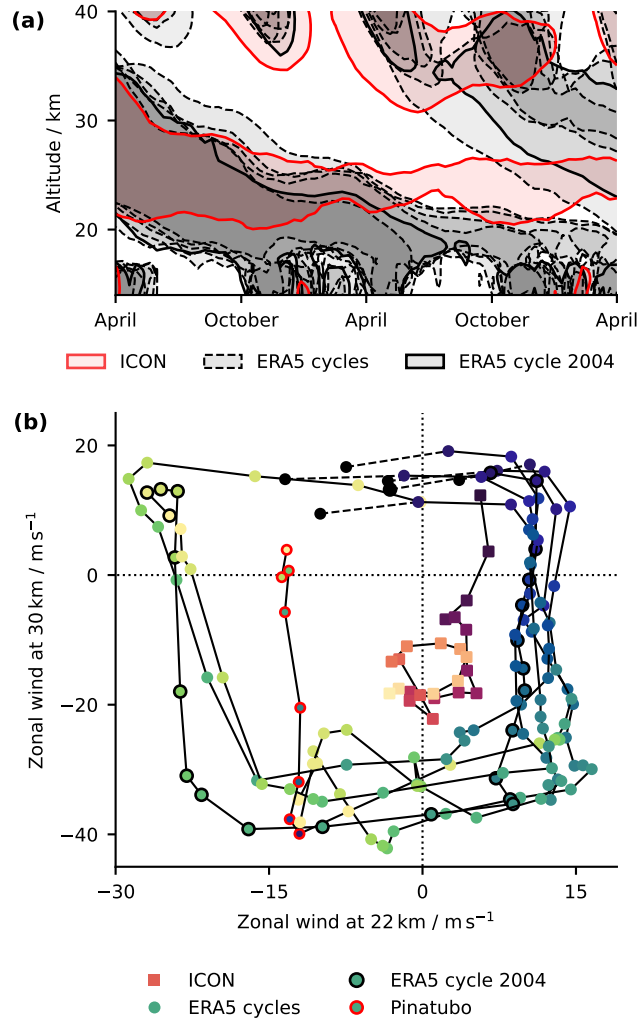
Figure A.2: **(a)** Time-altitude cross section of the 5° S–5° N daily mean zonal wind of the ICON simulation and the six individual QBO cycles of the ERA5-QBO-ensemble, starting on April 1 of the years 1985, 1990, 1997, 2004, 2008, and 2013. The shading highlights westerlies, and the contour lines mark the $0\,\mathrm{m\,s^{-1}}$-isotach, with the ERA5 QBO cycle starting on April 1, 2004 being highlighted by a solid black contour. **(b)** Temporal trajectory of pairs of 5° S–5° N monthly mean zonal wind at ~22 km and ~30 km for the ICON simulation and the six individual QBO cycles of the ERA5-QBO-ensemble, starting in April of the years 1985, 1990, 1997, 2004, 2008, and 2013. The trajectories start at the dark points, and for the ERA5-QBO-ensemble, the very first dark point, which is connected by a dashed line, marks the wind pair of March prior the "official" two-year-period starts. In the ERA5 QBO cycle starting on April 1, 1990, months after the eruption of Mt. Pinatubo in June 1991 are highlighted by red circles.

A.4   THE MOMENTUM BUDGET OF THE ICON-QBO

To understand why the ICON-QBO shows the pronounced lack of downward propagation as identified in Section A.3, we evaluate its zonal momentum budget in the Navier-Stokes framework (Sec. A.4.1) and in the TEM framework (Sec. A.4.2).

A.4.1 *The QBO momentum budget in the Navier-Stokes framework*

The simulation of the atmospheric flow in ICON is based on the primitive equations. In this framework, the zonal momentum balance in Cartesian coordinates x, y, and z is given by the Navier-Stokes equation:

$$\frac{\partial u}{\partial t} = -\left(u\frac{\partial u}{\partial x} + v\frac{\partial u}{\partial y} + w\frac{\partial u}{\partial z}\right) - \frac{1}{\rho}\frac{\partial p}{\partial x} + (fv - 2\Omega\cos\phi\, w) + X_u. \tag{A.11}$$

Here, u, v, and w are the zonal, meridional, and vertical wind components, respectively, t is time, ρ is density, p is pressure, f is the Coriolis parameter, Ω is the Earth's rotation rate, and ϕ is latitude. The term on the left-hand-side of Eq. A.11 represents the total zonal wind tendency, while the first, second, and third terms on its right-hand-side represent the zonal wind tendency due to advection, the pressure gradient force, and the Coriolis force, respectively. X_u is the sum of all diffusive forces,

$$X_u = X_{u,hdf} + X_{u,dmp} + X_{u,vdf}, \tag{A.12}$$

where $X_{u,hdf}$ is the zonal wind tendency due to explicit horizontal diffusion applied by ICON's numerical core, $X_{u,dmp}$ is the zonal wind tendency due to ICON's divergence damping, and $X_{u,vdf}$ is the zonal wind tendency due to parameterized vertical diffusion.

Figure A.3 shows the time-altitude cross sections of the different terms of Eq. A.11, averaged over $5°\,$S–$5°\,$N. Please note that we show the sum of the zonal wind tendency due to advection and the zonal wind tendency due to Coriolis force, since both are intrinsically coupled in the zonal mean. The dominant forces of the ICON-QBO are the sum of advection and the Coriolis force on the one hand, and the pressure gradient force on the other hand. Both terms tend to scale with the magnitude of the zonal wind jets to a first order approximation. The sum of advection and the Coriolis force acts to accelerate a jet of a given sign, while the pressure gradient force acts to decelerate a jet of a given sign. As a result, the two terms tend to cancel each other out to some extent, highlighting that the QBO is approximately in geostrophic balance. However, this cancellation is not exact especially in the shear zones of the ICON-QBO. This ultimately results in the downward propagation of the main easterly shear zone, which is initially located between $\sim$30 km and $\sim$38 km, during the first year of the simulation.

In addition, the tendency due to diffusive forces is negligibly small in the entire stratosphere, except for the tropopause region and the shear zones below the SAO jets. This shows that the diffusive forces do not directly damp the jets of the ICON-QBO, which is possible in the case of too strong diffusion (Baldwin et al., 2001, and references therein). Therefore, we conclude that too strong diffusive forces are not the root cause of the lack of downward propagation of the ICON-QBO in the sense that they directly damp the QBO.
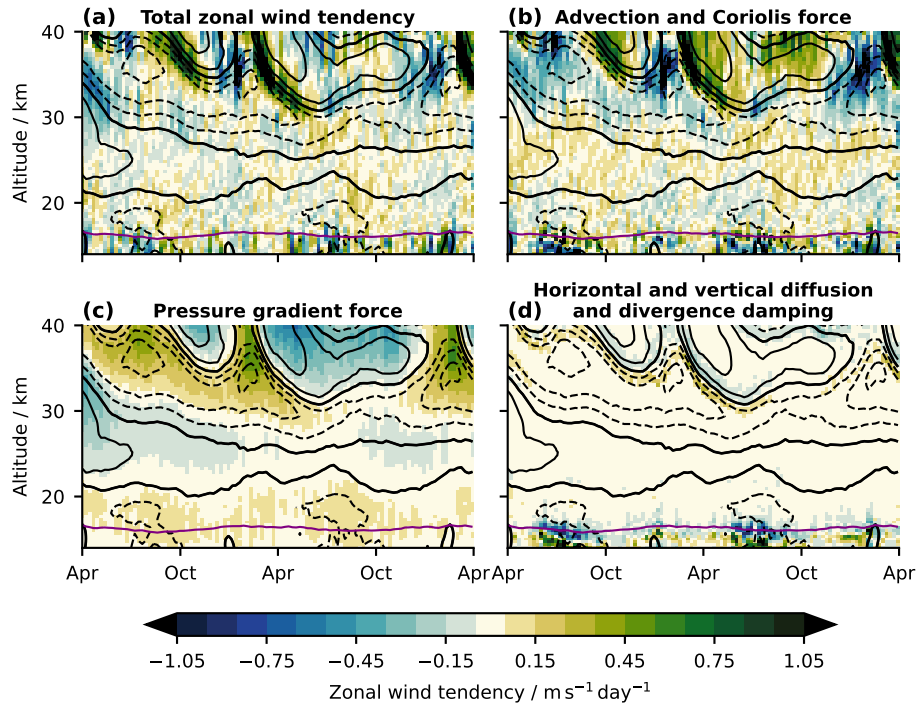
Figure A.3: Time-altitude cross section of the 5° S–5° N mean weekly-averaged zonal wind tendencies in the ICON simulation starting on April 01, 2004: **(a)** total zonal wind tendency, **(b)** zonal wind tendency due to advection and the Coriolis force, **(c)** zonal wind tendency due to pressure gradient force, and **(d)** zonal wind tendency due to explicit horizontal diffusion, parameterized vertical diffusion, and divergence damping. Black contour lines show isotachs of the 5° S–5° N mean zonal wind in intervals of $10\,\mathrm{m\,s^{-1}}$ with negative values being dashed, positive values being solid, and the $0\,\mathrm{m\,s^{-1}}$-isotach being bold solid. Purple contours mark the $370\,\mathrm{K}$-isentrope, which is a proxy for the tropopause altitude.

A.4.2   *The QBO momentum budget in the TEM framework*

A.4.2.1   *Spatio-temporal structure of the TEM forcing in the equatorial stratosphere in the ICON simulation*

Figure A.4 shows the time-altitude cross sections of the stratospheric 5° S–5° N mean zonal wind tendencies in the TEM framework, calculated as described in Section A.2.3.2. Please note that we do not analyze the tendencies due to meridional and vertical residual advection separately, but only consider their sum, the total residual advection.

In general, the spatio-temporal structure of the various TEM tendencies corresponds well to the standard QBO paradigm. The zonal wind tendency due to the vertical EP flux divergence is centered in the shear zones of the ICON-QBO and acts to drive their downward propagation (Fig. A.4b). In contrast, the zonal wind tendency due to the total residual advection acts against the downward propagation of the QBO shear zones, especially that of the easterly shear zone, which is initially located between 30 km and 38 km (Fig. A.4c). The magnitude of the advective tendency seems to scale with the magnitude of the vertical gradient of the zonal wind
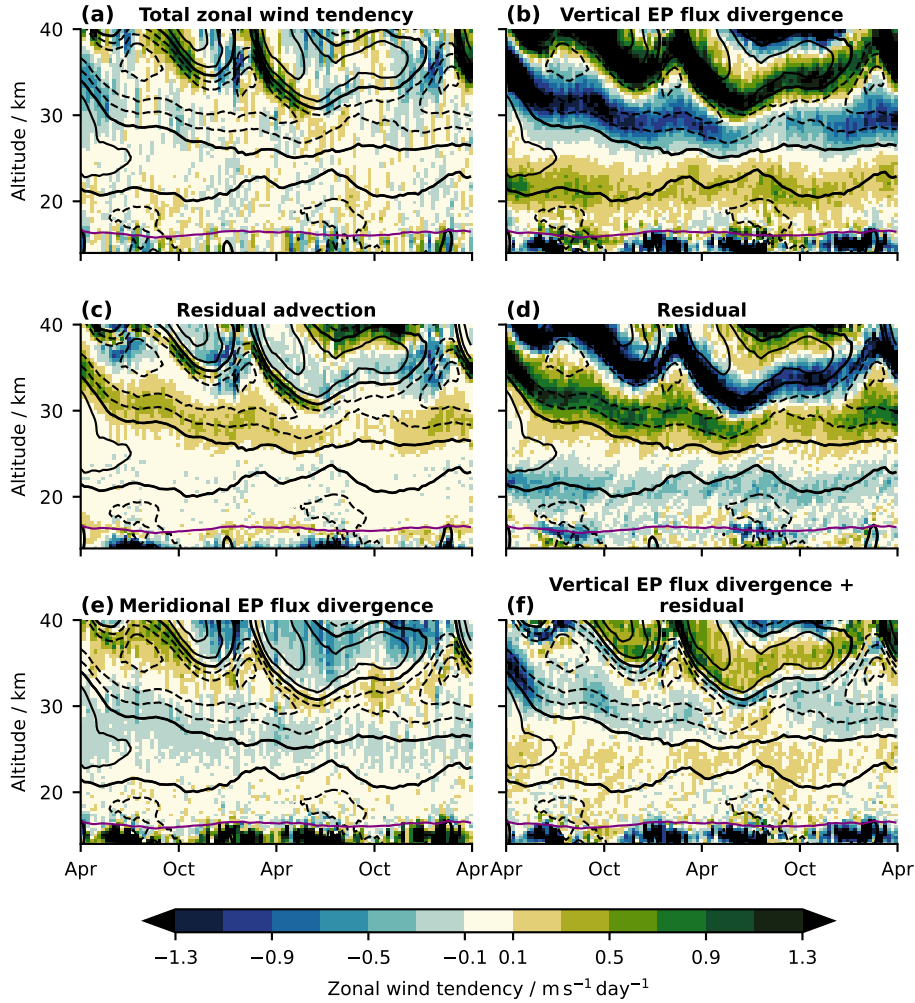
Figure A.4: Time-altitude cross section of the 5° S–5° N mean weekly-averaged TEM zonal wind tendencies in the ICON simulation starting on April 01, 2004: **(a)** total zonal wind tendency, **(b)** zonal wind tendency due to vertical EP flux divergence, **(c)** zonal wind tendency due to residual advection, **(d)** TEM residual, **(e)** zonal wind tendency due to meridional EP flux divergence, and **(f)** sum of the zonal wind tendency due to vertical EP flux divergence and the TEM residual. Black contour lines show isotachs of the 5° S–5° N mean zonal wind in intervals of $10\,\mathrm{m\,s^{-1}}$ with negative values being dashed, positive values being solid, and the $0\,\mathrm{m\,s^{-1}}$-isotach being bold solid. Purple contours mark the 370 K-isentrope, which is a proxy for the tropopause altitude.

in the shear zones. These findings highlight that the basic dynamics of the QBO are well captured by the global storm-resolving ICON simulation.

The zonal wind tendency due to the meridional EP flux divergence is strongest in the shear zones above ∼25 km (Fig. A.4e). Here, it facilitates the downward propagation of the zonal wind jets, and its absolute magnitude is comparable to that of the zonal wind tendency due to total residual advection. Consequently, the zonal wind tendency due to the meridional EP flux divergence is important for the dynamics of the SAO in ICON. Below 25 km, the zonal wind tendency due to meridional EP flux divergence is small overall.

However, the sum of all TEM tendencies does not match the total zonal wind tendency of the ICON simulation (Fig. A.4a) Consequently, the TEM zonal momentum budget of the ICON-QBO is closed by a large residual (Fig. A.4d). Figure A.4 shows that the residual strongly counteracts the zonal wind tendency due to vertical EP flux divergence, which apparently is much too strong. The strong cancellation between the vertical EP flux divergence and the residual is very similar to the findings of Yao and Jablonowski (2013, 2015). They argue that the strong residual of the TEM momentum budget is due to the direct effect of diffusion, damping, and radiative damping on the QBO jets. This attribution is questionable for the ICON simulation, since the diffusive tendencies in the equatorial stratosphere are negligible throughout the entire simulation (Fig. A.3d). This raises the question of an alternative root cause of the residual in the ICON simulation. In-depth analysis has shown that the overestimation of the EP flux, which ultimately causes the residual, is generated at individual model levels, and does not propagate vertically (not shown). This suggests a non-physical root cause. We hypothesize that the residual is a consequence of high-frequency small-scale noise, the possible root cause of which is, however, still unclear and will be discussed in more detail in Section A.6.3.

Given the strong cancellation between the zonal wind tendency due to vertical EP flux divergence — that is, the vertical wave forcing of the ICON-QBO — and the TEM residual, we compute their sum to obtain an *effective vertical wave forcing* (Fig. A.4f). The magnitude of the effective vertical wave forcing looks much more reasonable compared to the remaining TEM zonal wind tendencies than the actual vertical wave forcing. The effective vertical wave forcing also acts to drive the downward propagation of the shear zones of the ICON-QBO, indicating that the actual vertical wave forcing slightly overcompensates for the residual.

A.4.2.2   *Comparison with the TEM momentum budget of the ERA5-QBO*

According to the standard QBO paradigm, a lack of downward propagation of the QBO jets can have two possible root causes: a too strong tropical upwelling as part of a too strong Brewer-Dobson circulation (BDC), or a too weak vertical wave forcing, i.e. in our case too weak effective vertical wave forcing. In the following, we will investigate which of these two root causes is responsible for the lack of downward propagation of the ICON-QBO by comparing its TEM momentum budget with that of the ERA5-QBO.

For the reasonable comparison of QBO momentum budgets, it is essential that they are calculated for the same phase of the QBO. This is usually achieved by constructing so-called QBO composites, which are averages over several QBO cycles referenced at a fixed altitude based on a certain criterion (see, e.g., Krismer and Giorgetta, 2014; Bushell et al., 2020). However, due to the comparatively short simulation period of the ICON simulation, this methodology is not applicable for us. Instead, we compare the momentum budgets of the ICON-QBO and the ERA5-QBO for a fixed period, which is already well away from the initialization of the ICON simulation, but during which both QBOs are still reasonably close to each other. For this purpose, we choose the period May 17, 2004–October 07, 2004, which is highlighted by the vertical dashed lines in Figure A.1. By doing the

comparison for a fixed period, we also ensure that both, the ICON-QBO and the ERA5-QBO have the same seasonal boundary conditions.

Figure A.5 shows the TEM momentum budgets of the ICON-QBO and the ERA5-QBO averaged over the analysis period May 17, 2004–October 07, 2004 as a function of altitude. Figure A.6 shows the accumulated TEM tendencies in the upper (29 km–34 km) and lower (18 km–23 km) shear zones of the ICON-QBO and the ERA5-QBO. Both figures indicate that a too strong tropical upwelling is not the root cause for the lack of downward propagation of the ICON-QBO. Throughout the whole QBO domain (17 km–35 km), the zonal wind tendency due to residual advection, which is dominated by its vertical component, is of comparable magnitude for the ICON-QBO and the ERA5-QBO (Fig. A.5). Also in both shear zones, the accumulated tendency due to residual advection is in good agreement between the ICON simulation and the ERA5 reanalysis (Fig. A.6).

This finding is confirmed by Figure A.7, which shows the residual vertical velocity w^* averaged over the simulation period. The $30°$ S–$30°$ N mean w^*, a proxy for the strength of the rising branch of the BDC, is weaker in the ICON simulation than in
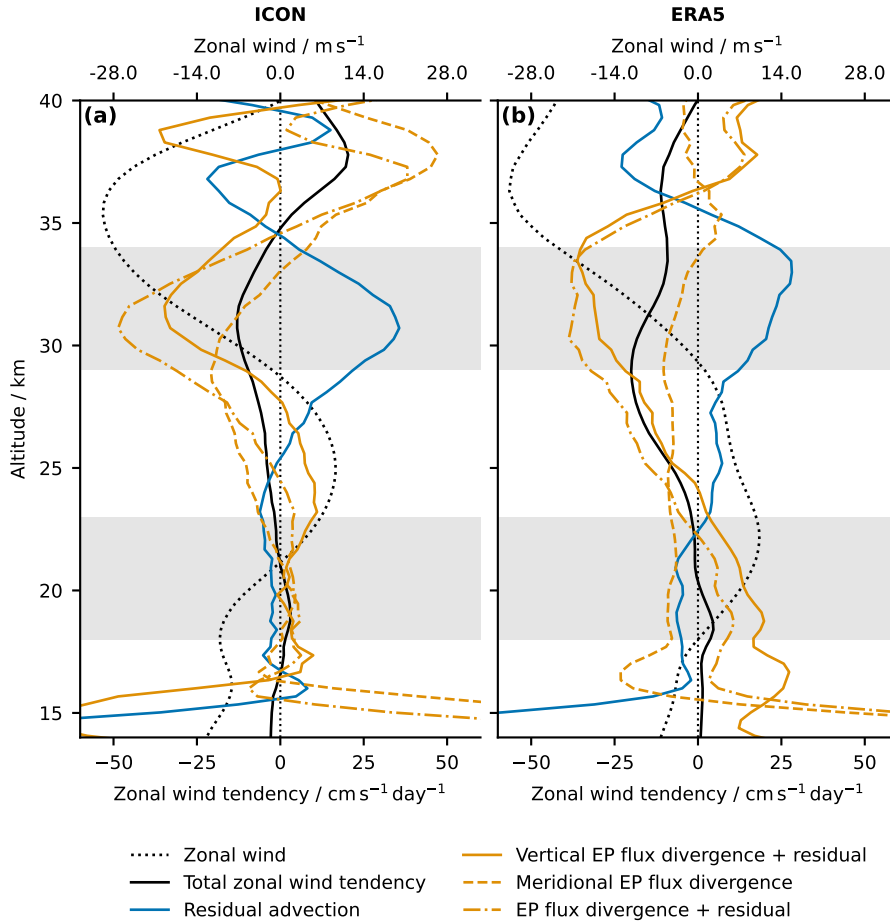
Figure A.5: $5°$ S–$5°$ N mean profiles of the TEM zonal wind tendencies averaged over the period May 17, 2004–October 07, 2004 in **(a)** the ICON simulation and in **(b)** the ERA5 reanalysis. The x-axis for the zonal wind $\overline{u}$ is given at the upper spine. Light gray bars mark the altitude ranges of the lower and upper shear zones in Figure A.6.
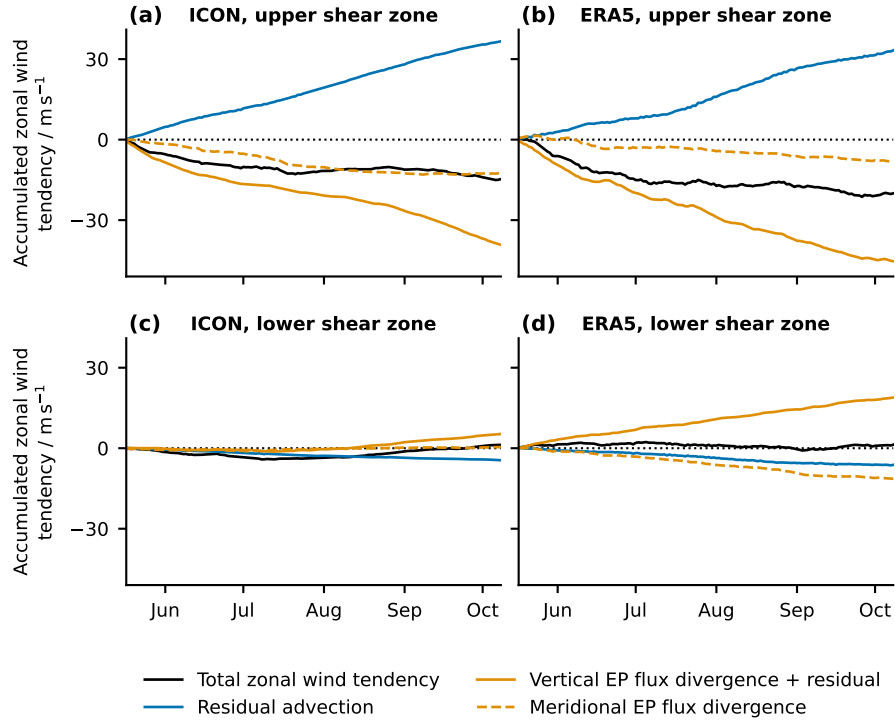
Figure A.6: Accumulated 5° S–5° N mean TEM zonal wind tendencies during May 17, 2004–October 07, 2004 for **(a,c)** the ICON simulation and **(b,d)** the ERA5 reanalysis. Panels **(a,b)** show tendencies averaged between an altitude of 29 km and 34 km, which is representative of the upper QBO shear zone during the accumulation period, and panels **(c,d)** show tendencies averaged between an altitude of 18 km and 23 km, which is representative of the lower QBO shear zone during the accumulation period. These altitude ranges are highlighted in Figure A.5.

the ERA5 reanalysis at all altitudes, except for two narrow regions around 25 km and 34 km. The 5° S–5° N mean w^*, which is ultimately relevant for the QBO, is also weaker in ICON than in ERA5 at all altitudes, except for the altitudes between 24 km and 28.5 km. The oscillating vertical structure of the w^* profiles in the ICON simulation, which causes them to locally exceed those of the ERA5 reanalysis, is the imprint of the persistent secondary meridional circulation (SMC) of the stalling ICON-QBO itself. We conclude that the tropical upwelling associated with the BDC is not too strong in the ICON simulation, but rather too weak compared to the ERA5 reanalysis. Therefore, it cannot be the root cause of the lack of downward propagation of the ICON-QBO.

Before we proceed with the comparison of the wave forcing between the ICON-QBO and the ERA5-QBO, it should be mentioned that it is reasonable to consider the sum of the zonal wind tendency due to the vertical EP flux divergence and the TEM residual as the effective vertical wave forcing also in the ERA5 reanalysis. In ERA5, the TEM residual is dominated by the zonal wind tendency of the GW parameterization, so the effective vertical wave forcing represents the total zonal forcing due to vertically propagating waves.

In the upper shear zone, the effective vertical wave forcing is in good agreement between the ICON simulation and the ERA5 reanalysis (Fig. A.6a,b). This corresponds well to the overall reasonable downward propagation of this shear zone in
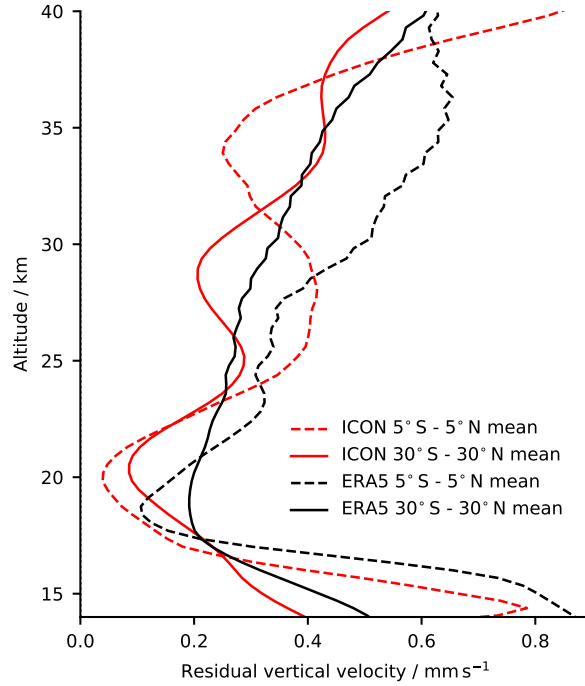
Figure A.7: Residual vertical velocity w^* of the ICON simulation and the ERA5 reanalysis averaged over the period April 01, 2004–March 31, 2006.

the first year of the ICON simulation (Fig. A.1). In contrast, the effective vertical wave forcing in the lower shear zone is much weaker in the ICON simulation than in the ERA5 reanalysis, and at the end of the analysis period the accumulated effective vertical wave forcing is more than three times weaker in ICON than in ERA5 (Fig. A.6c,d). This shows that the root cause of the lack of downward propagation of the ICON-QBO in the lowermost stratosphere is a too weak effective vertical wave forcing.

The zonal wind tendency due to meridional EP flux divergence differs qualitatively between the ICON simulation and the ERA5 reanalysis. In ERA5, it is approximately constant throughout the whole QBO domain between 18 km and 34 km (Fig. A.5b), while in ICON it clearly depends on altitude and shows a local maximum in the upper shear zone at ~30 km (Fig. A.5a). As a consequence, the accumulated zonal wind tendency due to meridional EP flux divergence in the upper shear zone is twice as large in ICON as in ERA5 at the end of the analysis period (Fig. A.6a,b). This shows that the meridional wave forcing is obviously important for the ICON-QBO and contributes significantly to the downward propagation of the upper shear zone.

Overall, we conclude that the TEM momentum balance of the ICON-QBO in the upper QBO domain during the analysis period is reasonable. Here, the residual advection, the effective vertical wave forcing, and the total zonal wind tendency show good quantitative agreement with ERA5 (Fig. A.6a,b). In contrast, the wave forcing of the ICON-QBO in the lowermost stratosphere is essentially zero and thus substantially weaker than in ERA5, leading to a biased QBO momentum balance. The root cause of the lack of downwelling of the ICON-QBO is a lack of effective vertical wave forcing in the lowermost stratosphere.

A.4.3 *Spectral decomposition of the QBO wave forcing*

So far, we have only considered the total wave forcing, which does not allow any conclusions to be drawn about the types and scales of the waves driving the ICON-QBO. To understand which part of the wave spectrum is responsible for the lack of vertical wave forcing in the ICON simulation, we compute zonal wavenumber-frequency spectra of the vertical EP flux and its divergence for 20 non-overlapping, non-tapered 36-day windows spanning the period April 11, 2004–March 31, 2006 (see Sec. A.2.3.2 for details). Subsequently, we sum the spectra over certain zonal wavenumber and ground-based zonal phase speed ranges corresponding to different wave types (see Table A.1). The time-altitude cross section of the vertical EP flux divergence in the tropical stratosphere associated with these wave types in the ICON simulation and in the ERA5 reanalysis is shown in Figure A.8 for eastward propagating waves and in Figure A.9 for westward propagating waves.

Figure A.8 shows that the lack of downward propagation of the ICON-QBO is mainly due to a lack of vertical wave forcing by slow eastward propagating planetary-scale waves, i.e. slow equatorial Kelvin waves (Fig. A.8a,b). The absolute magnitude of the zonal wind tendency due to vertical EP flux divergence associated with these waves in the lower westerly shear zone (i.e. 18 km–23 km) is much weaker in the ICON simulation than in the ERA5 reanalysis. In the ICON simulation, it is further distributed rather uniformly over a wide vertical range ($\sim$17 km–25 km, while in the ERA5 reanalysis it is strongly concentrated in the westerly shear zone in the lowermost stratosphere. The large vertical spread of the vertical waves forcing by slow eastward propagating planetary-scale waves in the ICON simulation can be partly attributed to the very weak westerly jet of the ICON-QBO itself, at least in the second year of the simulation. Because of the weak westerly jet, only very slow waves with a ground-based zonal phase speed close to $0\,\mathrm{m\,s}^{-1}$ dissipate in the shear zone below this jet, while faster waves can propagate through it.

For the vertical wave forcing by eastward propagating intermediate-scale waves, the situation is very similar (Fig. A.8e,f). Again, the absolute magnitude of the wave forcing in the lower westerly shear zone (i.e. 18 km–23 km) is weaker in the ICON simulation than in the ERA5 reanalysis, and it is distributed over a larger

Table A.1: Zonal wavenumber and ground-based zonal phase speed ranges corresponding to different wave types for which we compute the vertical EP flux and its divergence. Please note that the sampling interval of the data of 3 h does only allow for the detection of waves with a frequency of $< 4\,\mathrm{cpd}$. Thus, the largest detectable ground-based zonal phase speed of waves with $|k| \geq 101$ is $18.35\,\mathrm{m\,s}^{-1}$.

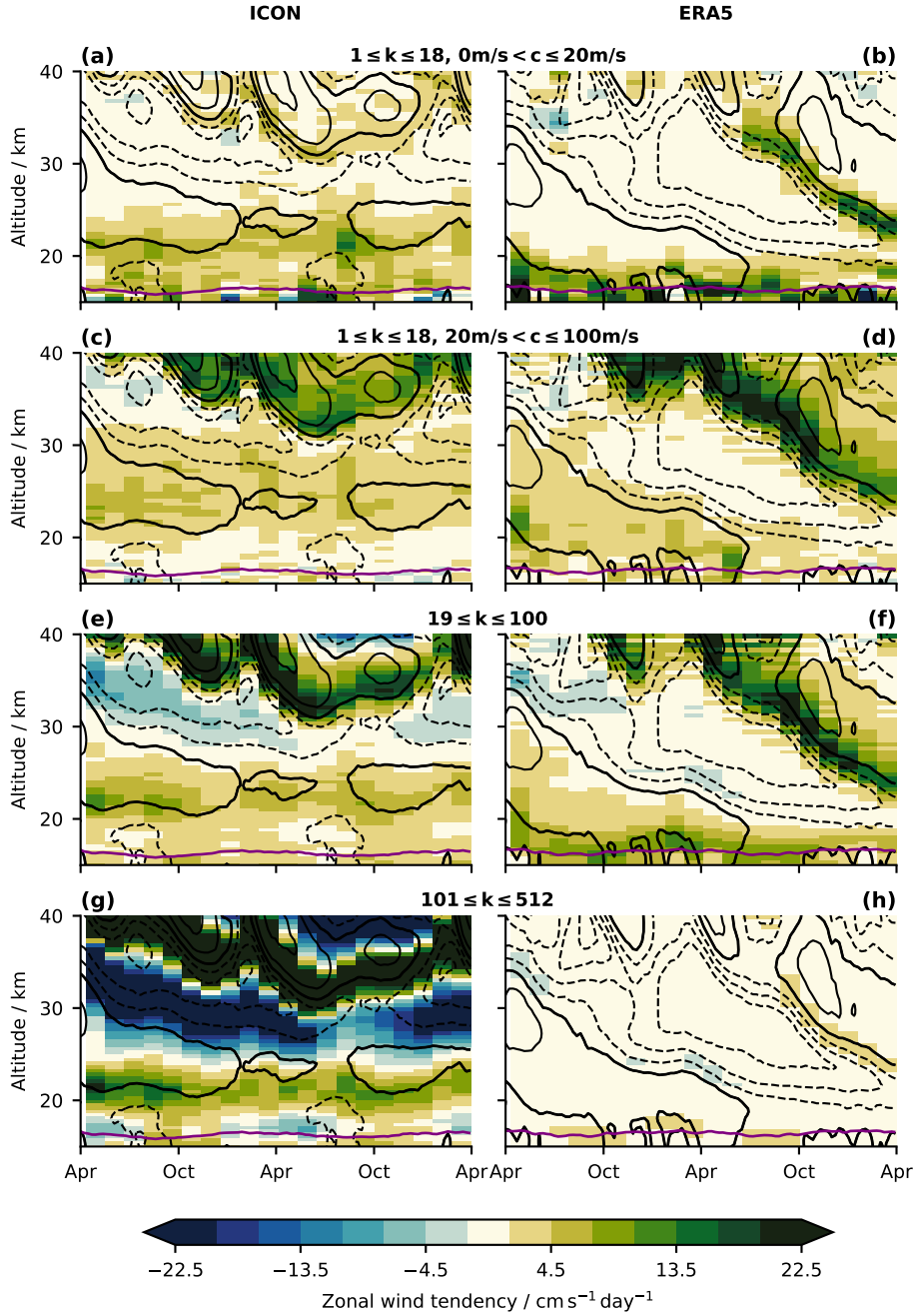| Wave type	Zonal wavenumber (eastward)	Zonal wavenumber (westward)	Ground-based zonal phase speed / $\mathrm{m\,s}^{-1}$
Slow planetary-scale	$1 \leq k \leq 18$	$-18 \leq k \leq -1$	$0 < |c| \leq 20$
Fast planetary-scale	$1 \leq k \leq 18$	$-18 \leq k \leq -1$	$20 < |c| < 100$
Intermediate-scale	$19 \leq k \leq 100$	$-100 \leq k \leq -19$	$0 < |c| < 100$
Small-scale	$101 \leq k \leq 512$	$-512 \leq k \leq -101$	$0 < |c| < 18.35$

Figure A.8: Time-altitude cross sections of the $10°$ S–$10°$ N mean zonal wind tendency due to vertical EP flux divergence associated with eastward propagating waves for (left panels) the ICON simulation and (right panels) the ERA5 reanalysis, separated into different wave types as defined in Table A.1: **(a,b)** slow planetary-scale waves, **(c,d)** fast planetary-scale waves, **(e,f)** intermediate-scale waves, **(g,h)** small-scale waves. The purple contour lines mark the 370 K-isentrope, which is a proxy for the tropopause altitude.

vertical range. Therefore, the lack of downward propagation of the ICON-QBO in the lowermost stratosphere is in part also attributable to this wave type.

The magnitude of the vertical wave forcing of the ICON-QBO by fast eastward propagating planetary-scale waves, i.e. fast equatorial Kelvin waves, is overall
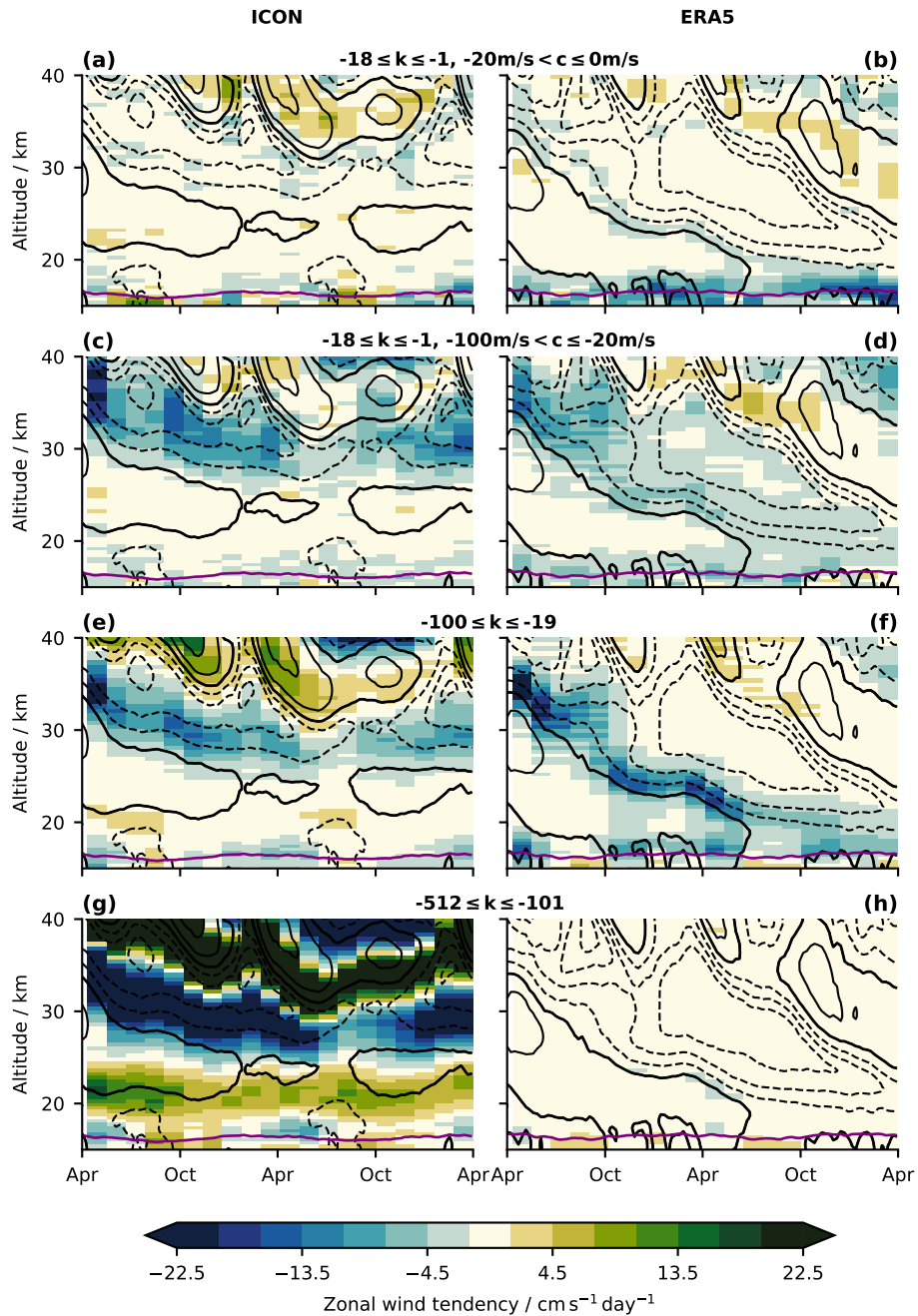
Figure A.9: As Figure A.8, but for westward propagating waves.

comparable to that of the ERA5-QBO (Fig. A.8c,d). However, in the ICON simulation a large fraction of this wave forcing also occurs in the easterly shear zone between ~25 km and ~31 km, and thus opposes the downward propagation of this shear zone. We think that this is likely one reason for the lack of downward propagation of the upper easterly jet of the ICON-QBO in the second year of the simulation.

For westward propagating waves (Fig. A.9), the differences between the ICON simulation and the ERA5 reanalysis are smaller than for eastward propagating waves. For both the ICON-QBO and the ERA5-QBO, slow westward propagating planetary-scale waves, including n=0 equatorial Rossby waves, do not contribute to the downward propagation of the easterly shear zone, which is initially located

between 30 km and 38 km (Fig. A.9a,b). In contrast, the downward propagation of this shear zone is mainly driven by fast westward propagating planetary-scale waves, including mixed Rossby-gravity waves (Fig. A.9c,d), and by intermediate-scale westward-propagating waves (Fig. A.9e,f) for both the ICON-QBO and the ERA5-QBO. The vertical wave forcing by these two wave types is in good agreement between the ICON simulation and the ERA5 reanalysis, given the different spatio-temporal structure of their QBOs.

The largest differences in the vertical wave forcing between the ICON simulation and the ERA5 reanalysis are found for both eastward and westward propagating small-scale waves, i.e. GWs (Fig. A.8g,h and Fig. A.9g,h). In the ERA5 reanalysis, the vertical wave forcing by these waves is virtually zero throughout the stratosphere. This is a consequence of the comparatively low native horizontal resolution of the ERA5 reanalysis of $\sim$31 km, which inhibits the effective resolution of these small-scale waves. In contrast, in the ICON simulation, the absolute magnitude of the wave forcing due to small-scale waves is much stronger than for all other wave types. Obviously, the small-scale waves are the root cause of the strong overestimation of the vertical EP flux divergence and the associated large TEM residual (see Fig. A.4b,d). In addition, the vertical wave forcing by small-scale waves in the individual shear zones of the ICON-QBO is independent of the zonal propagation direction of the waves (cmp. Fig. A.8g and Fig. A.9g). This behavior is not consistent with the theory of critical level filtering of vertically propagating waves, and thus is an indication of a non-physical root cause of the overestimation of the vertical EP flux and the associated TEM residual.

A.5 EVALUATION OF THE TROPICAL WAVE FIELD IN THE ICON SIMULATION

In the previous section, we showed that the lack of downward propagation of the ICON-QBO in the lowermost stratosphere is due to a lack of vertical wave forcing, preferably by slow eastward propagating planetary-scale waves, mainly comprising equatorial Kelvin waves. In principle, a lack of vertical wave forcing of the QBO can have three possible root causes: (1) a misrepresentation or lack of wave generation in the troposphere, (2) a misrepresentation or lack of vertical wave propagation from the troposphere into the stratosphere, and (3) a misrepresentation or lack of wave dissipation and damping in the shear zones of the QBO. Here, we investigate which of these possible root causes is responsible for the lack of vertical wave forcing in the ICON simulation.

A.5.1 *Dissipation and damping of SEWs in the lowermost stratosphere*

To analyze the damping and dissipation of SEWs in the ICON simulation, we follow the methodology of Krismer and Giorgetta (2014, see their Sec. 5 c), and consider four different processes: the damping and diffusion of wave-induced zonal wind perturbations by (1) divergence damping, (2) explicit horizontal diffusion, and (3) parameterized vertical diffusion, as well as (4) the damping of wave-induced temperature perturbations by longwave radiation. First, we compute the amplitude spectra of the tendency variables associated with these four processes and the corresponding state variable on which the tendency variable acts, as a

function of zonal wavenumber and frequency. The spectra are computed for four non-overlapping and non-tapered 36-day windows spanning the period May 17, 2004–October 07, 2004, which is the same period we used to compare the zonal momentum budgets of the ICON-QBO and the ERA5-QBO (see Sec. A.4.2.2). We then average the spectra over all windows and over the $10°$ S–$10°$ N region. Since we are interested in the damping and dissipation of SEWs in the lower shear zone of the ICON-QBO, we further average the spectra over the 18 km–23 km altitude range (cmp. Sec. A.4.2.2). The spectra averaged in this way are shown in the left column panels of Figure A.10. The right column panels of Figure A.10 show the spectra of the quotient of the tendency variable and its corresponding state variable, which can be interpreted as the *e*-folding time of the particular dissipation or damping process associated with the tendency (see Krismer and Giorgetta, 2014). The shorter the *e*-folding time, the more efficient a particular dissipation or damping process is. In the following, we will analyze the dissipation and damping of large-scale waves, as they have been shown to be the root cause of the underestimation of the vertical wave forcing of the ICON-QBO.

The divergence damping appears to strongly damp very slow waves with $\omega < 0.5$ cpd and $|k| > 10$, while only leaving large-scale planetary waves with $|k| < 10$ and $\omega < 0.5$ cpd nearly unaffected (Fig. A.10b). This is due to the fact that the divergence damping of the zonal wind depends strongly on frequency, but is more or less independent of zonal wavenumber (Fig. A.10a). It is strongest for very slow or steady perturbations and decreases rapidly with increasing frequency. In principle, this behavior is to be expected because the divergence damping is employed in ICON to remove quasi-stationary small-scale checkerboard patterns. The spectrum of the parameterized vertical diffusion of the zonal wind also shows a first-order dependence on frequency, but it has a larger magnitude than the divergence damping, except for the lowest frequencies (Fig. A.10c). As a result, parameterized vertical diffusion very efficiently damps all waves except large-scale planetary waves with $|k| < 10$ and $\omega < 0.5$ cpd (Fig. A.10d). It further is the dominant damping mechanism for waves with $|k| > 15$ across the four mechanisms considered. The explicit horizontal diffusion of the zonal wind is virtually independent of frequency and zonal wavenumber and has a much smaller magnitude than the parameterized vertical diffusion and divergence damping over the entire spectral range considered (Fig. A.10e). Therefore, explicit horizontal diffusion does not substantially damp waves with $|k| < 25$ and $\omega < 1$ cpd (Fig. A.10f). For waves with larger zonal wavenumbers and higher frequencies, wave damping by horizontal diffusion is still of secondary importance compared to wave damping by divergence damping and vertical diffusion. In contrast to the diffusive wave damping processes of the zonal wind, the radiative damping of waves depends mainly on intrinsic zonal phase speed and is most efficient for slow waves (Fig. A.10h), which agrees with theory (e.g., Fels, 1982). Therefore, radiative damping is the dominant damping mechanism of large-scale planetary waves with $|k| < 10$ and $\omega < 0.5$ cpd.

The basic result that planetary-scale waves with $|k| < 10$ and $\omega < 0.5$ cpd are mainly damped by radiation in the ICON simulation, while smaller-scale waves with $|k| > 10$ and higher-frequency waves with $\omega > 0.5$ cpd are mainly damped by diffusive processes, agrees well with the results of Krismer and Giorgetta (2014). The overall damping of large-scale waves in the lower shear zone of the ICON-QBO appears to be reasonable and not distorted. However, we found that the diffusive
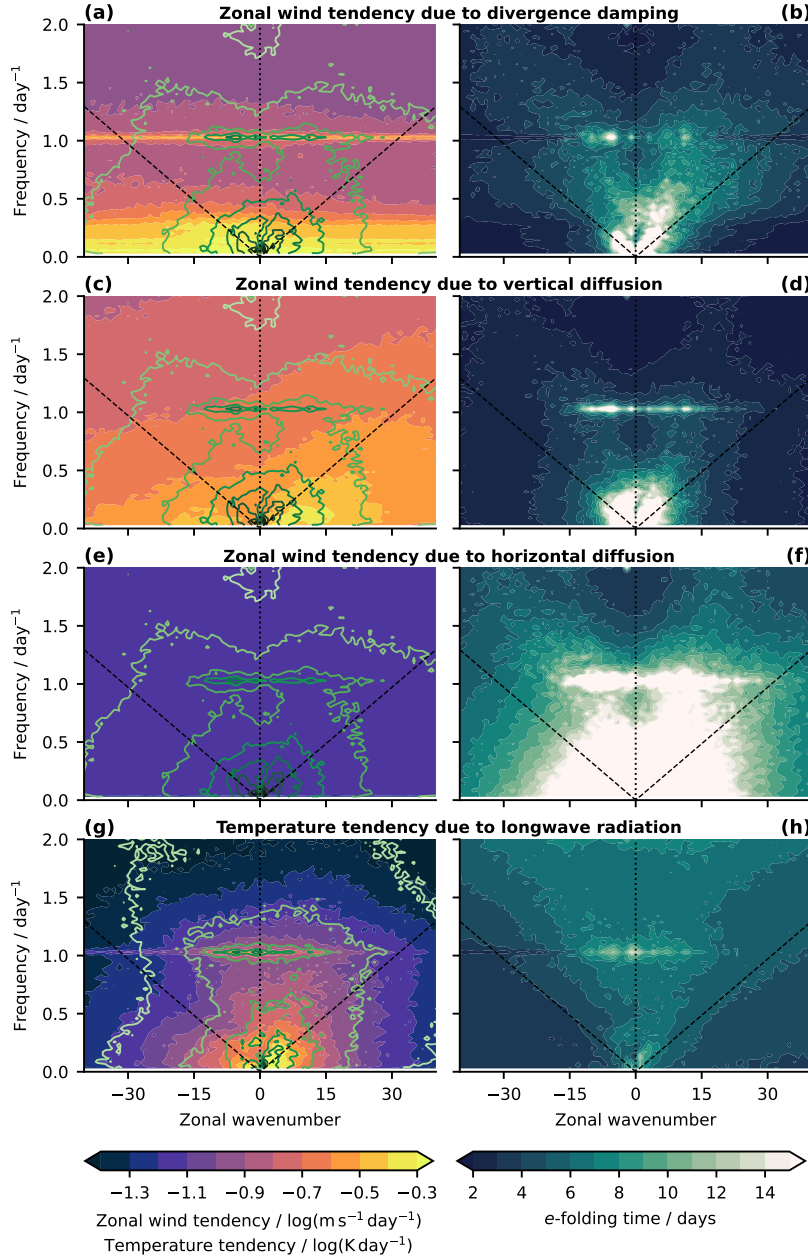
Figure A.10: $10°$ S–$10°$ N mean zonal wavenumber-frequency spectra of (left panels) the amplitude of a particular tendency variable (colors) and its corresponding state variable (contours), and of (right panels) the quotient of this particular tendency variable and its corresponding state variable, i.e. the *e*-folding time. The spectra were computed for and averaged over four non-overlapping non-tapered 36-day windows during the period May 17, 2004–October 07, 2004 They were further averaged between 18 km and 23 km, which is representative of the lower shear zone of the ICON-QBO. Contour lines are logarithmic with an interval of **(a,c,e)** $0.3 \log(\mathrm{m\,s}^{-1})$ and **(g)** $0.3 \log(\mathrm{K})$ with darker lines indicating a larger amplitude. Panels **(a,b)** show the divergence damping of the zonal wind, **(c,d)** the explicit horizontal diffusion of the zonal wind, **(e,f)** the parameterized vertical diffusion of the zonal wind, and **(g,h)** the temperature tendency due to longwave radiation. Black dashed lines in all spectra mark lines of a constant zonal phase speed of $|c| = 15\,\mathrm{m\,s}^{-1}$ for visual guidance.

damping of waves in the ICON simulation is dominated by divergence damping and parameterized vertical diffusion instead of horizontal diffusion. It is unclear to what extent this partitioning of the diffusive wave damping in the ICON simulation is reasonable, and whether it indicates that individual diffusion and damping schemes are too strong or too weak. At least the divergence damping, which is implemented to reduce small-scale checkerboard patterns, has a surprisingly large impact on wave damping.

To validate these conclusions, we analyze the vertical propagation of exemplary Kelvin waves in physical space, which implicitly depends on all possible damping mechanisms present in ICON. Therefore, any gross misrepresentation of wave damping and dissipation in ICON would become apparent in this representation. To isolate the Kelvin waves, we first computed the Fourier transform of the non-tapered but detrended symmetric perturbation temperature in longitude and time. The perturbation temperature is the deviation of the temperature from its zonal and temporal mean. Subsequently, we performed an inverse Fourier transform only on the spectral components with $1 \leq k \leq 10$, $0\,\mathrm{cpd} < \omega \leq 0.4\,\mathrm{cpd}$, and $0\,\mathrm{m\,s^{-1}} < c \leq 10\,\mathrm{m\,s^{-1}}$ (very slow Kelvin waves), $10\,\mathrm{m\,s^{-1}} < c \leq 20\,\mathrm{m\,s^{-1}}$ (slow Kelvin waves), and $20\,\mathrm{m\,s^{-1}} < c \leq 50\,\mathrm{m\,s^{-1}}$ (fast Kelvin waves).

Figure A.11 shows the vertical propagation of the equatorial Kelvin waves isolated in this way at a randomly selected equatorial location in the ICON simulation during May 17, 2004–October 07, 2004. The spatio-temporal structure of the three different classes of Kelvin waves is reasonable and agrees well with the standard theory of critical level filtering of vertically propagating waves. The filtering of Kelvin waves by the westerly jet of the ICON-QBO, which has a magnitude of $10\,\mathrm{m\,s^{-1}}$–$20\,\mathrm{m\,s^{-1}}$, clearly depends on their zonal phase speed. The very slow Kelvin waves are more or less completely damped in the lower part of the westerly jet and are absent above it. The slow Kelvin waves are also strongly damped in the westerly shear zone below the westerly jet, but there are still spurious small-amplitude signals of these waves above the westerly jet. The fast Kelvin waves, which do not reach their critical levels within the westerly jet, propagate through the jet without a substantial loss in amplitude. In general, except for the westerly shear zone between 18 km and 25 km, there is no substantial damping of the Kelvin waves. Therefore, we conclude that the vertical propagation of equatorial Kelvin waves in the stratosphere and their damping and diffusion are reasonably well represented in the ICON simulation. We rule out a gross misrepresentation of wave damping and propagation as the root cause of the lack of downward propagation of the ICON-QBO.

A.5.2   *Vertical EP flux spectra in the lowermost stratosphere*

In the following, we will analyze the vertical EP flux in the ICON simulation at an altitude of 17 km, just above the tropopause, because it allows us to analyze the upward propagating wave field before it interacts with the QBO jets. Thus, this analysis can reveal whether the lack of vertical wave forcing of the ICON-QBO is due to an underestimation of the wave momentum fluxes entering the stratosphere. As a first step, we compute the zonal wavenumber-frequency spectra of the vertical EP flux at 17 km for the same 20 non-overlapping, non-tapered 36-day windows
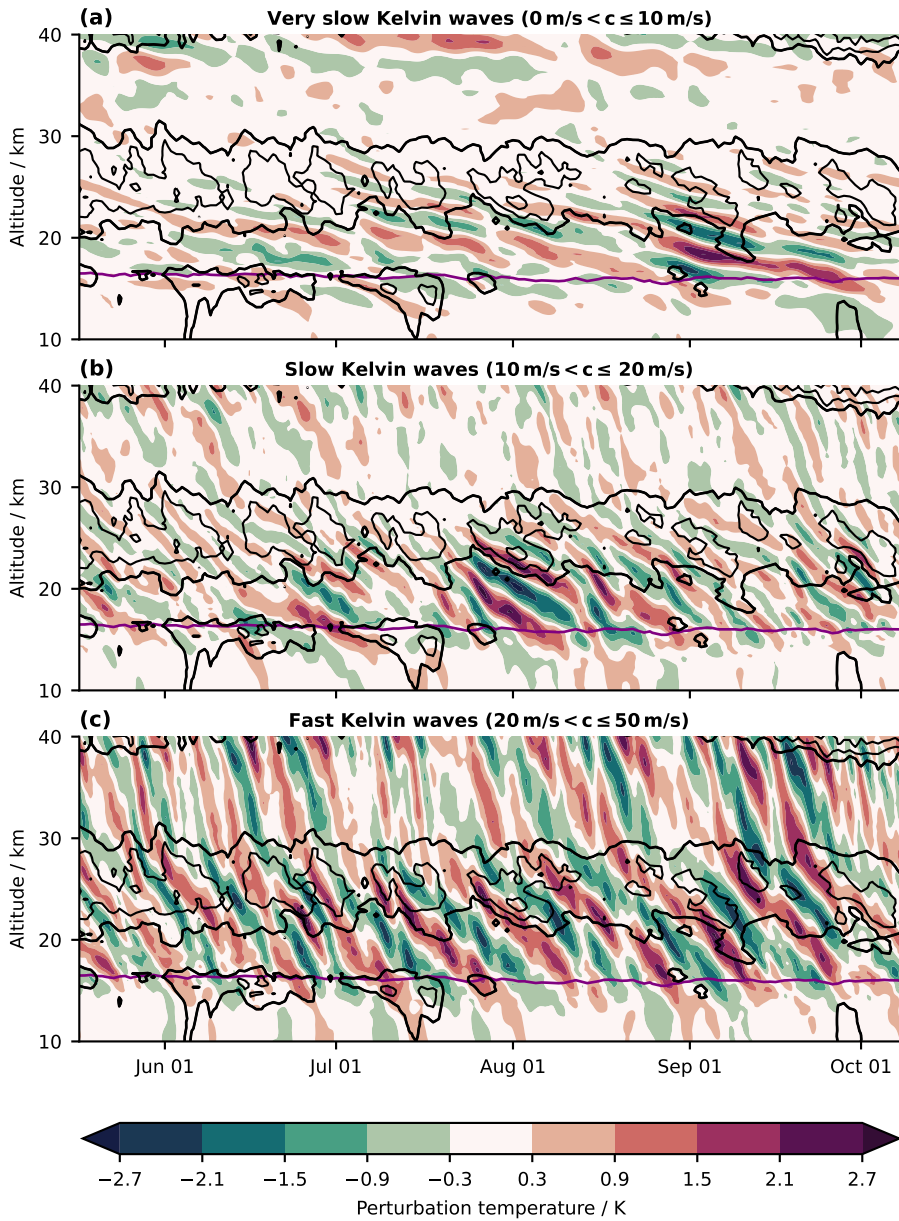
Figure A.11: Time-altitude cross section of the temperature perturbations induced by **(a)** very slow Kelvin waves with $0\,\mathrm{m\,s}^{-1} < c \leq 10\,\mathrm{m\,s}^{-1}$, **(b)** slow Kelvin waves with $10\,\mathrm{m\,s}^{-1} < c \leq 20\,\mathrm{m\,s}^{-1}$, and **(c)** fast Kelvin waves with $20\,\mathrm{m\,s}^{-1} < c \leq 50\,\mathrm{m\,s}^{-1}$ in the ICON simulation during the period May 17, 2004–October 07, 2004 at 0.1756° N, 180° E. Black contour lines show daily mean westerly winds in intervals of $10\,\mathrm{m\,s}^{-1}$, starting at $0\,\mathrm{m\,s}^{-1}$ (thick black contour). Contour lines for easterly winds are not plotted for clarity. The purple contour lines mark the 370 K-isentrope, which is a proxy for the tropopause altitude.

spanning the period April 11, 2004–March 31, 2006 as in Section A.4.3. We then average these spectra over all windows and over the 10° S–10° N region.

Figure A.12a,b shows the averaged spectra of the vertical EP flux of the ICON simulation and the ERA5 reanalysis. While the basic structure of both spectra agrees, there are also notable differences between the ICON simulation and the ERA5 reanalysis. For the ERA5 reanalysis, the spectrum is much smoother than

for the ICON simulation, and it shows some weak organization into a double-lobe structure along phase speeds close to $|c| = 30\,\mathrm{m\,s^{-1}}$ and $|c| = 50\,\mathrm{m\,s^{-1}}$. While the spectrum of the ICON simulation organizes along similar phase speed lines, it is substantially noisier than the spectrum of the ERA5 reanalysis. In addition, the spectrum of the ICON simulation is less powerful than that of the ERA5 reanalysis, especially at high frequencies of $\omega > 1\,\mathrm{cpd}$. At these high frequencies, the vertical EP flux decreases rapidly in the ICON simulation and much faster than in the ERA5 reanalysis.

We further accumulate the averaged zonal wavenumber-frequency spectra of the vertical EP flux over all frequencies. The resulting zonal wavenumber spectra of the vertical EP flux of the ICON simulation and the ERA5 reanalysis are shown in Figure A.12c. They reveal that for both westward and eastward propagating waves with $|k| < 70$, the vertical EP flux is substantially weaker in the ICON simulation than in the ERA5 reanalysis. For eastward propagating waves ($k > 0$), the vertical EP flux in the ICON simulation is about 20 % weaker than in the ERA5 reanalysis, approximately uniformly over all zonal wavenumbers up to $k = 70$. For westward propagating waves ($k < 0$), the difference between the ICON simulation and the ERA5 reanalysis is even stronger, and the vertical EP flux in ICON is more than 40 % weaker than in ERA5 for zonal wavenumbers between $k = -20$ and $k = -45$. Since the absolute magnitude of the vertical EP flux is generally much larger for planetary-scale waves ($|k| \lesssim 18$) than for smaller-scale waves (see Fig. A.12c), the uniform relative underestimation of the vertical EP flux in the ICON simulation over a wide range of zonal wavenumbers shows that — in absolute terms — the lack of incoming vertical EP flux is largest for planetary-scale waves. Therefore, the lack of — mainly planetary-scale — vertical wave forcing of the ICON-QBO (see Sec. A.4.3) can ultimately be attributed to a lack of — mainly planetary-scale — vertical EP flux entering the lower stratosphere.

The fact that the underestimation of the vertical EP flux in the ICON simulation is even more pronounced for westward than for eastward propagating waves can be attributed to differences in upper-tropospheric wave filtering between ICON and ERA5. The ICON simulation has a substantial easterly bias in the upper troposphere and the tropopause region of up to $-6\,\mathrm{m\,s^{-1}}$ compared to the ERA5 reanalysis (see Fig. A.13). These easterlies in the ICON simulation result in a strong filtering of slow westward propagating waves, which thus do not reach the lower stratosphere. The strong filtering of slow westward propagating waves in the ICON simulation can be seen in the zonal wavenumber-frequency spectrum of the vertical EP flux, which shows basically no westward, i.e. positive, vertical EP flux for westward propagating waves with $-15\,\mathrm{m\,s^{-1}} < c < 0\,\mathrm{m\,s^{-1}}$ (Fig. A.12a, also cmp. Fig. A.12b). This substantial lack of westward EP flux associated with slow westward propagating waves likely contributes to the lack of downward propagation of the easterly shear zone of the ICON-QBO in the second year of the simulation (Fig. A.1a). Here, the easterly jet becomes so weak that it can only effectively absorb westward propagating waves with $-15\,\mathrm{m\,s^{-1}} < c < 0\,\mathrm{m\,s^{-1}}$, which are mostly already filtered out in the upper troposphere. This leaves the easterly jet of the ICON-QBO with virtually no wave forcing.

Looking further at the distribution of the vertical EP flux as a function of the ground-based zonal phase speed (Fig. A.12d), it can be seen that the underestimation of the vertical EP flux in ICON basically occurs over all zonal phase speeds. However,

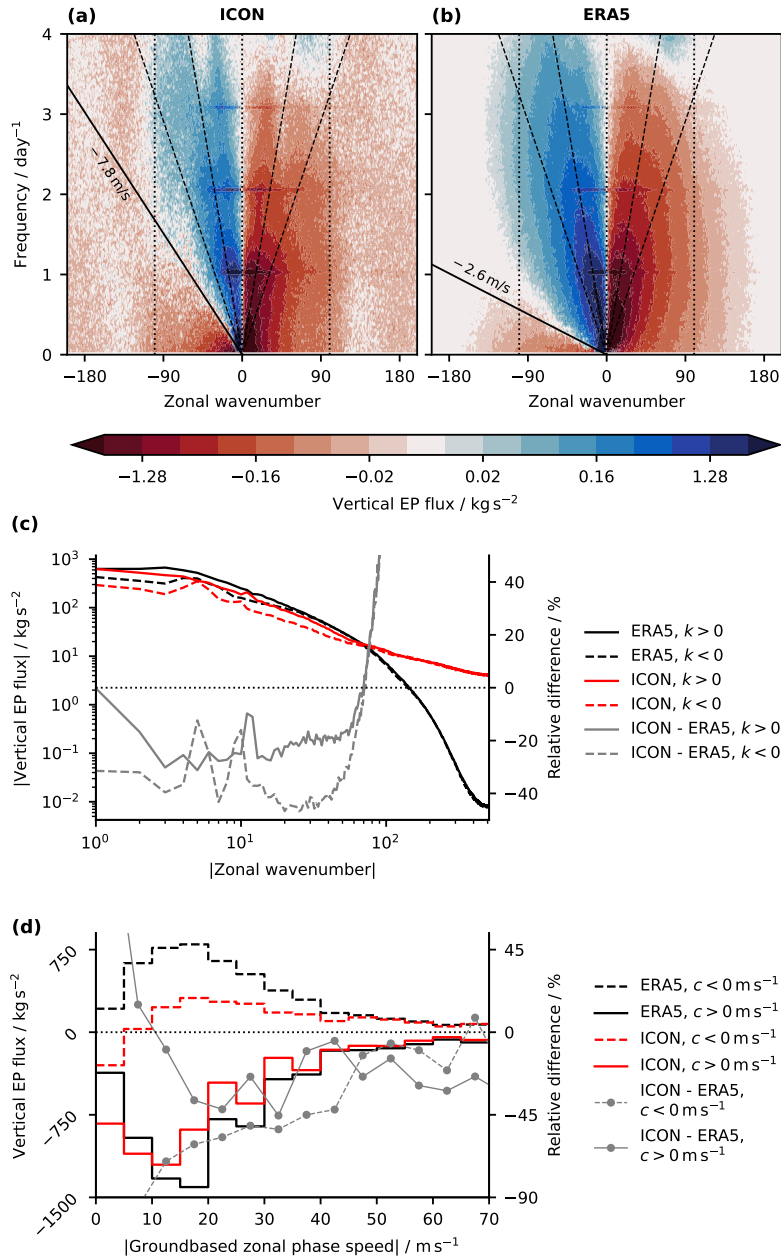Figure A.12: Spectral characterization of the $10°$ S–$10°$ N mean vertical EP flux at an altitude of 17 km, averaged over individual spectra calculated for 20 non-overlapping, non-tapered 36-day windows spanning the period April 11, 2004–March 31, 2006. Panels **(a,b)** show zonal wavenumber-frequency spectra for **(a)** the ICON simulation and **(b)** the ERA5 reanalysis. The solid black lines in panels **(a,b)** mark the zonal mean zonal wind at 17 km of the ICON simulation and theERA5 reanalysis, respectively, while the dashed black lines mark lines of constant ground-based zonal phase speed of $|c| = 15\,\mathrm{m\,s^{-1}}$ and $|c| = 30\,\mathrm{m\,s^{-1}}$. The vertical dotted lines mark the zonal wavenumbers $|k| = 100$ and $k = 0$. Panel **(c)** shows zonal wavenumber spectra of the vertical EP flux, and panel **(d)** shows the vertical EP flux binned to zonal phase speeds with a bin width of $5\,\mathrm{m\,s^{-1}}$ for waves with $|k| < 100$. In panels **(c)** and **(d)**, the y-axis for the relative difference between ICON and ERA5 (gray lines) is given at the right spine, and the horizontal dotted line marks a relative difference of 0 %.
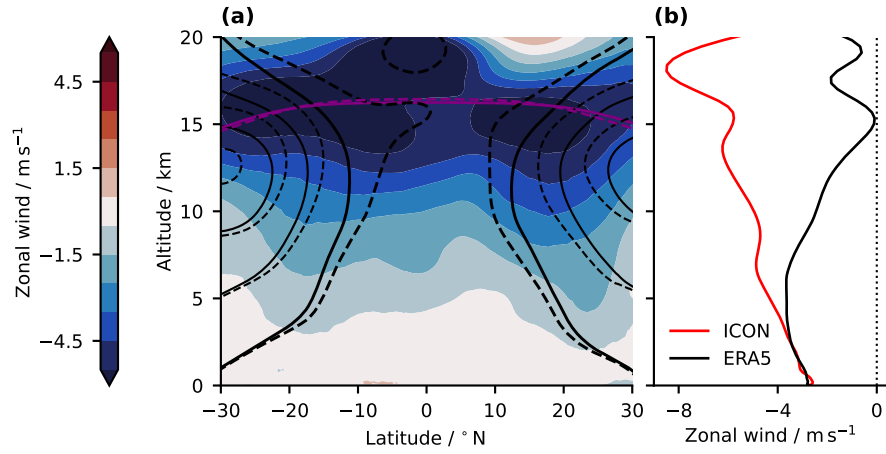
Figure A.13: **(a)** Latitude-altitude cross section of the zonal mean zonal wind difference between the ICON simulation and the ERA5 reanalysis, averaged over the period April 01, 2004–March 31, 2006. Solid and dashed black contours indicate the zonal mean zonal wind in intervals of $10\,\mathrm{m\,s^{-1}}$ starting at $0\,\mathrm{m\,s^{-1}}$ (bold contours) of the ICON simulation and the ERA5 reanalysis, respectively. Solid and dashed purple contours mark the $370\,\mathrm{K}$-isentrope, which is a proxy for the tropopause altitude, for the ICON simulation and the ERA5 reanalysis, respectively. **(b)** $10^\circ\,\mathrm{S}$–$10^\circ\,\mathrm{N}$ mean zonal wind in the ICON simulation and the ERA5 reanalysis as a function of altitude.

the shape of the distribution is approximately the same in both the ICON simulation and the ERA5 reanalysis. Only for small phase speeds there are some differences between ICON and ERA5, which can be attributed to the Doppler shift of the waves associated with the different background winds at $17\,\mathrm{km}$ (Fig. A.12a,b).

In contrast to the large-scale waves, the vertical EP flux associated with small-scale GWs, i.e. waves with $|k| > 70$, is much larger for ICON than for ERA5 (Fig. A.12c). However, the vertical EP flux for $|k| > 70$ is not associated with any organized wave modes in the ICON simulation, but rather appears as a noise-like continuous background, as indicated by the zonal wavenumber-frequency spectrum (Fig. A.12a). In addition, the vertical EP flux for $|k| > 70$ is eastward, i.e. negative, independent of the sign of the zonal wavenumber. We see this finding as a further imprint of the non-physical overestimation of the vertical wave forcing of the ICON-QBO for small-scale GWs, which ultimately causes the large TEM residual (cmp. Sec. A.4.2.1, Sec. A.4.3).

A.5.3 *Spectral variability of tropical precipitation and CCEWs*

Most of the upward propagating tropical waves that drive the QBO are generated by latent heat release in deep tropical convection (Holton, 1972; Salby and Garcia, 1987; Ricciardulli and Garcia, 2000; Fritts and Alexander, 2003; Horinouchi et al., 2003). Therefore, the underestimation of the vertical EP flux entering the lowermost tropical stratosphere, especially on planetary scales, indicates that wave generation in the tropical troposphere is likely underestimated in the ICON simulation. To investigate the wave sources in the ICON simulation in more detail, we will analyze the spectral variability of tropical precipitation, which is a widely used proxy

for latent heating by tropical deep convection. Therefore, we computed zonal wavenumber-frequency spectra of precipitation for the ICON simulation, the ERA5 reanalysis, and the observational precipitation dataset IMERG, for 29 tapered 92-day windows with a 34-day overlap spanning the entire simulation period from April 01, 2004–March 31, 2006. We then averaged these spectra over all 29 windows and between 15° S and 15° N, and the averaged spectra are shown in Figure A.14a-c.

Figure A.14a-c shows that the ICON simulation reproduces the basic qualitative aspects of the observed tropical precipitation spectrum reasonably well. The spectra of ICON, IMERG, and ERA5 are all red in zonal wavenumber and frequency, but the spectrum of the ICON simulation is slightly smoother than those of IMERG and ERA5. The ICON simulation also shows a clear preference for westward propagating tropical waves, in agreement with IMERG and ERA5. The spectra of the ICON simulation and IMERG both organize along the same lines of constant zonal phase speed, i.e. $|c| = 15\,\mathrm{m\,s^{-1}}$, while the spectrum of ERA5 organizes along lines of constant phase speed of slightly more than $|c| = 15\,\mathrm{m\,s^{-1}}$.

Quantitatively, however, the precipitation spectra differ substantially between the ICON simulation on the one hand and IMERG and ERA5 on the other. The ICON simulation substantially underestimates the tropical precipitation variance compared to IMERG, over a wide spectral range of about $|k| < 130$ and $\omega < 2\,\mathrm{cpd}$ (see white dashed lines in Fig. A.14a,b). Only for larger wavenumbers and frequencies, the ICON simulation has a slightly larger precipitation variance than IMERG, probably due to its higher native spatial and temporal resolution compared to the IMERG data. Compared to the ERA5 reanalysis, the ICON simulation has a larger tropical precipitation variance in most parts of the spectrum, except for the planetary-scale part, i.e. $|k| \leq 18$ and $\omega < 0.5\,\mathrm{cpd}$, where the tropical precipitation variance is still underestimated in ICON. The fact that the ICON simulation has a larger precipitation variance than the ERA5 reanalysis, except for the planetary-scale part of the spectrum, is due to the fact that ICON explicitly simulates deep convection, while ERA5 parameterizes it. The parameterization of deep convection has been shown to lead to an underestimation of high-frequency precipitation variance compared to observations (e.g., Kim and Alexander, 2013). The underestimation of planetary-scale precipitation variance in the ICON simulation compared to the ERA5 reanalysis is also not surprising, since planetary-scale precipitation features in ERA5 — although precipitation is a pure model product — are still well constrained by observations and thus, by definition, close to IMERG.

In general, planetary-scale precipitation variance in the tropics is dominated by CCEWs, which we will analyze in the following using the methodology of Wheeler and Kiladis (1999). Therefore, we computed the zonal wavenumber-frequency spectra of the symmetric and antisymmetric components of tropical precipitation (see Sec. A.2.3.1 for details) for the same 29 tapered 92-day windows with a 34-day overlap that we computed the raw spectra for. Afterwards, we normalized the symmetric and antisymmetric spectra by dividing them by a smoothed background spectrum to highlight spectral peaks representing CCEWs. We then averaged these spectra over all 29 windows and between 15° S and 15° N, and the averaged spectra are shown in Figure A.14d-j.

The normalized symmetric and antisymmetric spectra of the observational dataset IMERG and the ERA5 reanalysis are nearly identical. This can be explained by the good observational constraint on planetary-scale precipitation in ERA5. Both
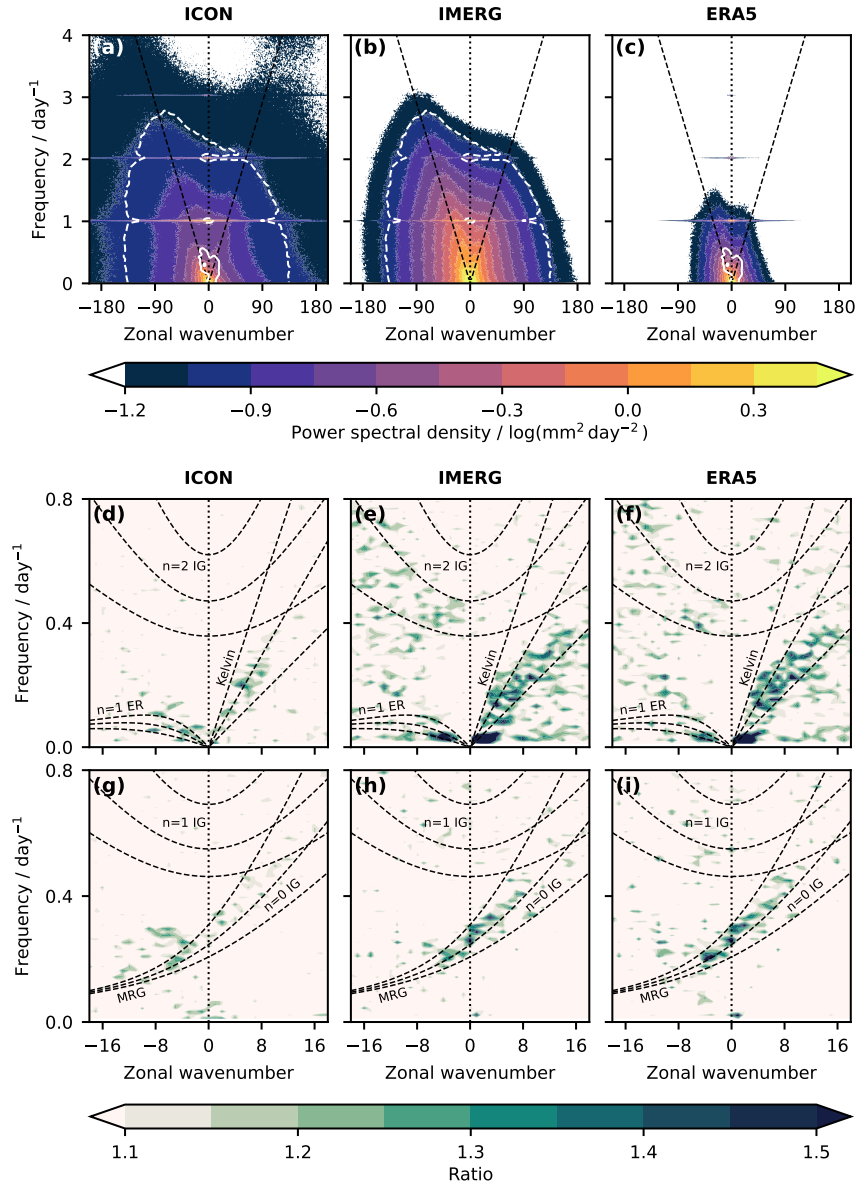
Figure A.14: 15° S–15° N mean zonal wavenumber-frequency spectra of precipitation variance for **(a)** the ICON simulation, **(b)** the observational dataset IMERG, and **(c)** the ERA5 reanalysis, averaged over 29 tapered 92-day windows with a 34-day overlap. White lines in panels **(a-c)** indicate isolines where the smoothed power spectral density of ICON agrees with (dashed) IMERG and (solid) ERA5. Black dashed lines in panels **(a-c)** mark a constant ground-based zonal phase speed of $c = 15\,\mathrm{m\,s^{-1}}$. Panels **(d-f)** and **(g-i)** show the 15° S–15° N mean zonal wavenumber-frequency spectra of normalized symmetric and antisymmetric precipitation variance, respectively, for **(d,g)** the ICON simulation, **(e,h)** IMERG, and **(f,i)** ERA5, averaged over 29 92-day windows with a 34-day overlap. The normalization has been performed according to Wheeler and Kiladis (1999). Black dashed lines in **(d-i)** mark ground-based theoretical dispersion curves of selected convectively coupled equatorial waves (CCEWs) with an equivalent depth h_e of 10 m, 30 m, and 90 m. Please note the following abbreviations: ER, Equatorial Rossby wave; IG, Inertia-gravity wave; and MRG, Mixed Rossby-gravity wave.

IMERG and ERA5 have a rich spectrum of symmetric and antisymmetric CCEWs, including equatorial Kelvin waves, long n = 0 equatorial Rossby waves, mixed Rossby-gravity waves, and n = 0 and n = 2 inertia-gravity waves. In contrast, the ICON simulation shows much less organization of precipitation into CCEWs than IMERG and ERA5. The ICON simulation has only weak signals of equatorial Kelvin waves, long n = 0 equatorial Rossby waves, and mixed Rossby-gravity waves. The signals of n = 0 and n = 2 inertia-gravity waves are practically absent, and the ICON simulation also shows no signal of the Madden-Julian oscillation (MJO). The latter is in stark contrast to IMERG and ERA5, where the MJO appears as a distinct spectral peak in the symmetric spectrum at $1 \leq k \leq 3$ and $\omega < 0.05$ cpd.

To conclude, the ICON simulation suffers from a substantial lack of CCEWs in combination with a general underestimation of spectral precipitation variance compared to the observational dataset IMERG. CCEWs are usually closely coupled to SEWs (Kawatani et al., 2009; Maury et al., 2013) that ultimately drive the QBO, and more generally, the spectral characteristics of the tropical precipitation variance have been shown to control the wave momentum fluxes in the lower tropical stratosphere (Ricciardulli and Garcia, 2000; Horinouchi et al., 2003). Therefore, we conclude that the substantial underestimation of CCEWs in the ICON simulation is likely the root cause of the lack of planetary-scale vertical wave momentum flux entering the lowermost stratosphere and, ultimately, the lack of downward propagation of the ICON-QBO.

A.6 DISCUSSION

A.6.1 *Answers to the research questions*

By performing a two-year-long simulation with the GSRM ICON with a horizontal resolution of ∼5 km and a vertical resolution between ∼350 m and ∼560 m in the stratosphere, we addressed the following research questions:

1. ***Is a state-of-the-art GSRM capable of directly simulating a full cycle of the QBO in a reasonable way? Which aspects of the QBO are well captured and which are not?***
   No, the current configuration of the state-of-the-art GSRM ICON is not yet capable of reasonably simulating a full QBO cycle, but it does maintain a QBO-like zonal wind structure in the tropical stratosphere throughout the whole simulation. Especially in the lowermost stratosphere (i.e., below 25 km), the ICON-QBO suffers from a pronounced lack of downward propagation right from the beginning of the simulation. During the second year of the simulation, the downward propagation of the ICON-QBO stops completely, and the ICON-QBO also suffers from too shallow and too weak jets. During the first year of the simulation, however, the representation of the ICON-QBO in the upper QBO domain (i.e., between 25 km and 35 km) is in good agreement with the ERA5-QBO. Here, both the magnitude of the jets of the ICON-QBO and the rate of downward propagation of the ICON-QBO are reasonably well represented in the ICON simulation.

2. ***Why does the model simulate the QBO the way it does?***
   If the QBO is reasonably simulated, how is it forced in the simulation? Is it
   reasonable for the right reasons, or is it the product of compensating errors?
   If the QBO is not reasonably simulated, what are the sources of QBO biases?
   Are QBO biases caused by biases in other aspects of the simulation?
   The reasonable downward propagation of the ICON-QBO in the upper QBO
   domain (i.e., between 25 km and 35 km) is the product of an overall reasonable
   QBO momentum budget. Both the total QBO wave forcing and the residual ad-
   vection of zonal momentum have a magnitude comparable to that of the ERA5
   reanalysis. This implies that the downward propagation of the ICON-QBO in
   the upper QBO domain in the first year of the ICON simulation occurs for the
   right reasons and is not the consequence of compensating errors. However,
   the contribution of the meridional wave forcing to the total wave forcing is
   about twice as large in the ICON simulation as in the ERA5 reanalysis. In the
   lowermost stratosphere (i.e., below 25 km), the lack of downward propagation
   of the westerly jet of the ICON-QBO is due to a substantial underestimation of
   the vertical wave momentum flux entering the lower stratosphere, especially
   at planetary scales. We attribute this underestimation of the wave momentum
   flux entering the stratosphere to an underestimation of tropical precipitation
   variability in general and a pronounced lack of CCEWs in particular. The
   lack of downward propagation of the upper easterly jet of the ICON-QBO
   in the second year of the simulation may also be due to the filtering of slow
   westward propagating waves by an upper-tropospheric easterly bias in the
   ICON simulation.

A.6.2 *Direct QBO simulations in a GSRM: What have we learned, where do we stand?*

The overall reasonable representation of QBO dynamics in the easterly shear zone
of the ICON-QBO between 25 km and 35 km during the first year of the simulation
is a promising result. Since the downward propagation of the QBO easterly shear
zone is mainly driven by GWs (see Anstey et al., 2022a, and references therein), we
take it as an indirect indication that a horizontal resolution of ∼5 km is sufficient
to resolve the GW spectrum relevant for driving the QBO. This is consistent with
the results of Polichtchouk et al. (2021), who showed that the total resolved tropical
GWMF in simulations with a horizontal grid spacing of $\mathcal{O}(10\,\text{km})$–$\mathcal{O}(1\,\text{km})$ is
nearly independent of horizontal resolution and thus may be already converged.
However, they also showed that the partitioning of the tropical GWMF to zonal
wavelengths still depends on the horizontal resolution, with the GWMF shifting
to shorter zonal wavelengths at higher resolutions. Therefore, our results do not
allow the conclusion that GWs that are no longer effectively resolved in our model
configuration, i.e. GWs with a horizontal wavelength less than 60 km (Stephan et al.,
2019a), are irrelevant for driving the QBO in reality.

   Furthermore, our results suggest that the wave forcing by meridionally propagat-
ing waves may be important for the QBO, at least in the upper QBO domain. Here,
the meridional wave forcing contributes about ∼25% to the total wave forcing of
the ICON-QBO (see Fig. A.6a). In contrast, the meridional wave forcing contributes
only 10%–15% to the total wave forcing in the same altitude range in the ERA5

reanalysis. The difference between ICON and ERA5 is mainly due to meridionally propagating GWs in the ICON simulation, since the GW parameterization employed by ERA5 does not allow meridional GW propagation at all (Orr et al., 2010). This finding supports recent results of Kim et al. (2023), which suggest that oblique GW propagation plays a crucial role in QBO dynamics based on results from a novel GW parameterization that allows oblique GW propagation (e.g., Bölöni et al., 2021; Kim et al., 2021). By implication, this also means that the QBO momentum budgets in conventional GCMs employing simple GW parameterizations may be biased towards too strong vertical wave forcing.

The main bias of the ICON-QBO is a substantial lack of downward propagation in the lowermost stratosphere, which is the result of an underestimation of the vertical wave forcing, primarily at the planetary scale. We have attributed this underestimation of planetary-scale wave forcing to a pronounced lack of CCEWs in the tropical troposphere. However, the root cause of the lack of CCEWs and, more generally, the misrepresentation of spatio-temporal variability of tropical deep convection across scales is unclear. Takasuka et al. (2024) showed that careful and targeted tuning of the remaining major parameterizations of a GSRM — that is, the parameterizations of cloud microphysics and turbulent mixing — can greatly improve the model's representation of tropical deep convection on a variety of spatio-temporal scales. Therefore, it seems plausible that an analog tuning approach in the present ICON configuration may help to achieve a more realistic representation of the spatio-temporal variability of tropical deep convection, including CCEWs. On the other hand, the lack of CCEWs and spatio-temporal variability of tropical convection may be related to the employed horizontal resolution of ∼5 km, which is in the convective gray zone and thus should be considered "convection-permitting" rather than "convection-resolving" (e.g., Prein et al., 2015). GSRMs operating in the gray zone have been shown to produce convective cells that are too small and too intense, preventing convective organization into larger and more long-lived organized convective systems (Crook et al., 2019; Becker et al., 2021). We speculate that this may also hinder the formation of CCEWs and the MJO, implying that a GSRM in the gray zone may still be too coarse to explicitly resolve the generation of the full wave spectrum necessary to drive the QBO in the lowermost stratosphere.

At this point, it should also be mentioned that the CCEWs in the ICON simulation are indeed weak, but not extraordinarily weak compared to conventional GCMs, such as those which participated in QBOi (see Fig. 2 of Holt et al., 2020). However, unlike the ICON simulation, the QBOi models simulated a reasonable QBO regardless of their weak CCEWs (Bushell et al., 2020). This is because conventional GCMs can compensate for potential biases in their resolved wave forcing via their GW parameterization, a tuning option GSRMs no longer have. This has further implications: first, it suggests that the simulated QBO in conventional GCMs is often the product of compensating errors, and their QBO momentum budget is rather arbitrary. Second, it implies that a realistic representation of the mean state and the variability of the tropical troposphere is crucial for a realistic representation of the QBO in GSRMs, probably even more so than in conventional GCMs.

Interestingly, a lack of downward propagation of the QBO to the tropopause and a too weak QBO amplitude in the lowermost stratosphere is also a common bias in conventional GCMs (Schenzinger et al., 2017; Bushell et al., 2020; Anstey et al., 2022a). In these models, the bias is typically attributed to an insufficient

vertical resolution, which does not adequately resolve the vertical propagation and wave-mean flow interactions of waves with small vertical wavelengths, especially planetary-scale Kelvin waves (Boville and Randel, 1992; Giorgetta et al., 2006; Anstey et al., 2016; Geller et al., 2016a; Garfinkel et al., 2022). The vertical resolution of the ICON configuration employed (i.e., 350 m to 560 m in the stratosphere) is usually considered sufficient in this regard, and indeed the vertical propagation and damping of Kelvin waves is represented reasonably in the ICON simulation (see Fig. A.11). However, as suggested by Bramberger et al. (2022), eastward-propagating inertia-gravity waves with large horizontal but very short vertical wavelengths (i.e., < 1 km) may also contribute substantially to driving the downward propagation of the QBO in the lowermost stratosphere. The vertical resolution of the ICON configuration employed is still too coarse to resolve these waves. In addition, Skamarock et al. (2019) showed that resolved flow features in the free atmosphere, especially mesoscale GWs, converge only at vertical grid spacings of $\leq$ 200 m. This suggests that the vertical resolution in the ICON configuration employed may still be too coarse to resolve the full QBO wave forcing.

A general limitation of our findings is that they are based on a relatively short simulation, which further is only representative of one specific QBO phase. Some of our results are based on an even shorter analysis period of less than five months. While we do not think that this limitations impact our key results, longer simulations are desirable to achieve statistically more robust results.

A.6.3   *On the TEM residual*

The TEM momentum budget of the ICON-QBO was found to be closed by a large residual, which counteracts a too large vertical EP flux divergence (see Sec. A.4.2.1). The overestimation of the vertical EP flux divergence is mostly associated with waves with $|k| > 70$, i.e. small-scale GWs. This prevented a reasonable quantification of the GW forcing of the ICON-QBO, which would have been highly desirable as a first direct estimate of the GW forcing of the QBO.

Our results suggest that the TEM residual cannot be interpreted as a direct damping and diffusion of the QBO (see Sec. A.4.2.1). Instead, we argue that the TEM residual is the imprint of unphysical noise, and in the following, we will discuss two possible root causes of this noise: first, spurious numerical noise as the result of suboptimal parameter setting of ICON, and second, aliasing introduced by suboptimal sampling of the model output.

Any numerical discretization applied in GCMs is inevitably associated with numerical noise, which is usually accounted for by various filtering, diffusion, and damping mechanisms (e.g., Jablonowski and Williamson, 2011). In the case of ICON, these are an explicit horizontal diffusion and a divergence damping scheme in the numerical core (Zängl et al., 2015). However, if these schemes are not set up properly, the numerical noise may appear as spurious features in the simulated atmospheric flow, including the horizontal and vertical wind components. In this case, the noise would be sampled by the instantaneous TEM diagnostics, which diagnose the flow disturbances associated with the noise as a physical feature. This may ultimately lead to an overestimation of the vertical component of the EP flux. However, if the noise is generated in-situ at individual model levels and does

not propagate upward, the divergence of the overestimated vertical EP flux would be purely diagnostic and would not correspond to wave-mean flow interactions of a vertically propagating wave, which accelerates the mean flow. In that case, the TEM momentum budget must be closed by a huge residual. A more detailed analysis provided some evidence that this might be the case in ICON, but further investigation is needed to verify this hypothesis.

As a second possible source of the noise causing the TEM residual, we suggest aliasing due to a poor temporal and spatial sampling of the simulated atmospheric flow. Fast GWs can have periods as short as 10 minutes, which is well below the output interval of 3 h, making our instantaneous output strategy prone to temporal aliasing. Remapping the output fields from the native grid to the n256 Gaussian grid can also result in significant aliasing. Our results suggest that the overestimation of the vertical EP flux divergence — and thus the TEM residual — could indeed be the imprint of pronounced aliasing. As demonstrated by Kirchner (2005), aliasing can cause pronounced white-noise tailing in power spectra, which can be distorted even far below the Nyquist frequency. This is the case in the ICON simulation: both the zonal wavenumber-frequency spectrum and the zonal wavenumber spectrum of the vertical EP flux indicate that the overestimation of the vertical EP flux at high zonal wavenumbers has characteristics of white noise (Fig. A.12a,c). The tail of the zonal wavenumber spectrum of the vertical EP flux in the ICON simulation is very similar to the theoretical examples of aliasing-induced white noise tailing in Figures 2 and 3 of Kirchner (2005). This suggests that the TEM residual may be a purely diagnostic problem, and therefore comparatively easy to fix.

A.7 SUMMARY AND PROSPECTS

In this study, we present the first attempt at a direct simulation of a full QBO cycle in a GSRM, employing neither a parameterization of deep convection nor GWs. This means that, for the first time, the generation, propagation, and dissipation of the entire wave spectrum driving a QBO in a model is resolved explicitly and thus in a physically meaningful way. For the simulation in this study, we used the state-of-the-art GSRM ICON. Although the details of the QBO-like winds simulated in ICON do not agree with the ERA5 reanalysis — as is to be expected for such a first-of-its-kind simulation — the overall results of the simulation are encouraging. The ICON simulation reproduced the basic zonal momentum budget in the QBO easterly shear zone between 25 km–35 km during the first boreal summer of the simulation with a high degree of fidelity. This indicates that a GSRM with a horizontal grid spacing of $\mathcal{O}(5\,\mathrm{km})$ basically resolves the relevant processes that drive the QBO in this altitude range, in particular its wave-driving by GWs. Furthermore, we were able to attribute the biases in the simulated QBO to biases in the tropical troposphere, namely an underestimation of the spatio-temporal variability of tropical convection and CCEWs, and excessive wave filtering by an upper-tropospheric easterly zonal wind bias. These results suggest that the realistic representation of the tropical troposphere, in particular the spatio-temporal variability of tropical convection across scales, is currently the biggest roadblock of a successful representation of the QBO in GSRMs — at least in the present one. In contrast, the propagation and

dissipation of the wave spectrum relevant for the QBO in the stratosphere do not seem to be a major problem.

Given the current advances in exascale computing, the ICON configuration employed may soon realistically reach a throughput of ~1 SYPD, putting multi-decadal global storm-resolving simulations of the QBO within reach (see Sec. 6.5 of Giorgetta et al., 2022). Direct simulations of a full QBO cycle at horizontal grid spacings close to 1 km or vertical grid spacings of ~100 m throughout the stratosphere also seem computationally plausible (cmp. Neumann et al., 2019). Such simulations have great potential to advance our understanding of the QBO and to resolve long-standing problems, such as the inability of conventional GCMs to reproduce the observed connection between the QBO and the MJO (Martin et al., 2021) or the large uncertainty in the possible response of the QBO to global warming (Richter et al., 2020b). Our goal of being able to exploit this exciting technological potential with ICON places clear demands on future work. First and foremost, we need to achieve a realistic representation of CCEWs in ICON — this is the necessary groundwork. Afterwards, more detailed sensitivity studies of the QBO with respect to the parameter setting of ICON would help to understand the stringent requirements for a reasonable representation of the QBO in a GSRM. Given this roadmap for future work, accompanied by the concurrently growing technological capabilities, we are optimistic that we will soon achieve the first realistic simulation of the QBO in a GSRM.

B

CHANGES OF TROPICAL GRAVITY WAVES AND THE QUASI-BIENNIAL OSCILLATION IN STORM-RESOLVING SIMULATIONS OF IDEALIZED GLOBAL WARMING

The work in this appendix has been published as:

AUTHOR CONTRIBUTIONS
Marco Giorgetta and me conceptualized the study and developed the methodology. I carried out the investigation, the formal analysis, the visualization of the results, and the writing of the manuscript. Peter Preusse contributed the small-volume few-wave decomposition technique for gravity waves analysis. Both, Marco Giorgetta and Peter Preusse contributed to the interpretation of the results and revised the initial manuscript. Marco Giorgetta supervised the study.

CHANGES OF TROPICAL GRAVITY WAVES AND THE QUASI-BIENNIAL OSCILLATION IN STORM-RESOLVING SIMULATIONS OF IDEALIZED GLOBAL WARMING

Henning Franke[1,2], Peter Preusse[3], Marco Giorgetta[1]

[1]*Max Planck Institute for Meteorology, Hamburg, Germany*
[2]*International Max Planck Research School on Earth System Modelling, Max Planck Institute for Meteorology, Hamburg, Germany*
[3]*Insitut für Energie- und Klimaforschung - Stratosphäre (IEK-7), Forschungszentrum Jülich GmbH, Jülich, Germany*

ABSTRACT

Gravity waves generated by tropical deep convection contribute significantly to driving the downward propagation of the quasi-biennial oscillation (QBO). However, it is currently uncertain how gravity waves, their interaction with the QBO, and thus the QBO itself will respond to a warming climate. Previous work showed that this uncertainty is a consequence of the parameterization of gravity waves employed in conventional general circulation models. In this study, we therefore perform short explicit simulations of the QBO for different idealized climate states with the model ICON-A in a deep convection-permitting setup, which means that neither a parameterization of convection nor a parameterization of gravity waves is employed and that the QBO is entirely driven by explicitly resolved waves. Thereby, our simulations allow us to provide a very first direct estimate of how tropical gravity waves and the QBO may change in a warming climate. We found that the lower-stratospheric gravity wave momentum flux that is relevant for the QBO increases substantially in the warmer climate states and shifts towards faster zonal phase speeds. As a consequence, the downward propagation of the QBO accelerates and the magnitude of the QBO jets in the upper QBO domain increases in the warmer climate states. Thus, our work builds an important first step toward a more comprehensive assessment of potential QBO changes using global storm-resolving models.

B.1   INTRODUCTION

The quasi-biennial oscillation (QBO) is the dominant mode of interannual variability in the equatorial stratosphere and is characterized by the descent of alternating easterly and westerly wind jets with a period of ~28 months (Baldwin et al., 2001). It has been shown that the QBO has a profound impact on stratospheric circulation and transport (Baldwin et al., 2001, and references therein) and that it influences tropical convection (Giorgetta et al., 1999; Collimore et al., 2003), the Madden-Julian oscillation (MJO) (Yoo and Son, 2016; Son et al., 2017), and extratropical surface

variability (Anstey and Shepherd, 2014). Thus, it is important to understand if and how the QBO may change in a warming climate and several studies have attempted to address this problem using conventional general circulation models (GCMs) (Giorgetta and Doege, 2005; Kawatani et al., 2011; Kawatani et al., 2012; Kawatani and Hamilton, 2013; Schirber et al., 2015; Butchart et al., 2020; Richter et al., 2020b). However, their results disagree with each other and results of single studies have been partly inconclusive. Schirber et al. (2015) and Richter et al. (2020b) showed that this is largely due to the inherent uncertainties in the gravity wave (GW) parameterizations that conventional GCMs have to employ in order to simulate a reasonable QBO. In this work we therefore use a high-resolution GCM that explicitly resolves rather than parameterizes GWs and deep convection to provide a more reliable estimate of how the gravity wave momentum flux (GWMF) and the QBO may change in a warming climate.

To understand how the QBO may change in a warming climate one first has to understand how the processes that control its downward propagation change in a warming climate. The first process is the interaction of the QBO jets with a broad spectrum of upward propagating equatorial waves, which drives the QBO's descent by depositing zonal momentum in the shear zones of the QBO jets. The wave spectrum driving the QBO ranges from planetary-scale waves, most prominently equatorial Kelvin, equatorial Rossby, and mixed Rossby-gravity waves, down to small-scale GWs with horizontal wavelengths of $\mathcal{O}(10\,\mathrm{km})$. All of these waves are predominantly generated by different modes of tropical deep convection. The second process controlling the QBO is the vertical advection of zonal momentum by the general tropical upwelling associated with the rising branch of the Brewer-Dobson circulation (BDC). The tropical upwelling usually opposes the wave-driven downward propagation of the QBO jets and thus slows it down (Baldwin et al., 2001; Anstey et al., 2022a).

Based on model projections it is now well established that the tropical upwelling will increase in a warmer climate (e.g., Butchart et al., 2006; Hardiman et al., 2014) and Shepherd and McLandress (2011) have presented a robust mechanism explaining this. They argue that the warming-induced strengthening of the subtropical jets pushes the critical levels of the waves driving the BDC upwards, allowing more wave activity to penetrate into the lower stratosphere, which accelerates the BDC. It has been shown that this increase in tropical upwelling acts to slow down the downward propagation of the QBO and to reduce its amplitude, especially in the lower stratosphere (Kawatani et al., 2011; Kawatani et al., 2012; Kawatani and Hamilton, 2013; Richter et al., 2020b). Kawatani and Hamilton (2013) further identified a decreasing lower-stratospheric QBO amplitude in the observational record, which they also attribute to an increase in tropical upwelling. The link between tropical upwelling and the downward propagation speed of the QBO can also operate in the opposite direction as Giorgetta and Doege (2005) and Watanabe and Kawatani (2012) showed that a decrease in tropical upwelling results in a faster QBO downward propagation. Thus, the impact of an increased tropical upwelling onto the QBO is relatively well understood and established and it can be found robustly across models.

In contrast, the response of the resolved and parameterized wave forcing of the QBO to a warming climate is much more uncertain and is strongly model-dependent (Richter et al., 2020b). Even though there seems to be a clear tendency towards an

increase in the total QBO wave forcing, the magnitude of this change differs strongly across studies and models (see Giorgetta and Doege, 2005; Kawatani et al., 2011; Richter et al., 2020b). Depending on whether the increase in the total QBO wave forcing will outweigh the increase in tropical upwelling or not, the QBO will either accelerate or decelerate in a warming climate, i.e. its period will shorten or lengthen, respectively. Consequently, some studies show a deceleration of the QBO (Kawatani et al., 2011; Kawatani and Hamilton, 2013) while others show an acceleration of the QBO (Giorgetta and Doege, 2005). More recently, Richter et al. (2020b) analyzed the response of the QBO to idealized warmer climates across eleven GCMs in the framework of the Stratosphere-troposphere Processes And their Role in Climate (SPARC) Quasi-Biennial Oscillation initiative (QBOi) project (Butchart et al., 2018). They also found that the QBO response to this warming is uncertain, with some models showing the QBO to speed up, some models showing it to slow down, and some models showing it to break down. The same lack of agreement in projections of the QBO period was found across Coupled Model Intercomparison Project phase 5 (CMIP5) (Kawatani and Hamilton, 2013) and Coupled Model Intercomparison Project phase 6 (CMIP6) (Butchart et al., 2020) models. Building up on the recent disruptions of the QBO in 2016 (Osprey et al., 2016; Coy et al., 2017) and 2019/2020 (Kang and Chun, 2021), Anstey et al. (2021) further suggest that the QBO may additionally become more susceptible to disruptions in a warming climate. Thus, the answer to the question of how the QBO may change in a warming climate ultimately remains uncertain.

Schirber et al. (2015) and Richter et al. (2020b) showed that a large part of this uncertainty in QBO projections by conventional GCMs stems from their GW parameterizations. The reasons for this are manifold. First of all, the tropical GWMF is still poorly constrained by observations even for current-day climate conditions. Therefore, GW parameterizations are often tuned towards a realistic current-day climate (Orr et al., 2010; Garcia et al., 2017), and this tuning setup may not be valid in different climate states. Additionally, a substantial number of current state-of-the-art GCMs still uses GW parameterizations which employ a fixed GW source spectrum. Thus, they are by design not able to respond to changes in GW sources due to a warming climate (Richter et al., 2020b). However, Richter et al. (2020b) showed that also those models which employ a GW parameterization coupled to the convective sources of GWs disagree with regard to changes in lower-stratospheric GWMF, even in the sign of change. Additional uncertainty stems from the fact that convection itself is also parameterized in conventional GCMs.

Obviously, it is necessary to reduce the uncertainty in the projections of tropical GWMF in the first place in order to ultimately reduce the uncertainty in QBO projections. One possibility to achieve a more realistic projection of the tropical GWMF is the explicit simulation of non-orographic GWs in global high-resolution models. However, because of the immense computational costs associated with this kind of simulation, they have so far been only feasible at resolutions which fail to resolve substantial parts of the GW spectrum and which still require the parameterization of deep convection (Watanabe et al., 2005; Kawatani et al., 2010a,b; Kawatani et al., 2011; Kawatani et al., 2012; Holt et al., 2016). Only one study explicitly investigated how the lower-stratospheric GWMF could change in a warming climate (Watanabe et al., 2005).

The continuous increase in computational power now finally allows for global simulations at horizontal resolutions at which deep convection and GWs with horizontal wavelengths of $\mathcal{O}(10)$ km become explicitly resolved and no longer need to be parameterized. The corresponding models are commonly referred to as global storm-resolving models (GSRMs). It has been shown that GSRMs are able to reproduce an overall realistic spectrum and global distribution of convectively generated GWs (Müller et al., 2018; Stephan et al., 2019a), even though substantial intermodel differences in the GWMF remain (Stephan et al., 2019b) and the resolution at which GSRMs resolve the GW spectrum truly sufficiently remains unclear (Lane and Knievel, 2005; Polichtchouk et al., 2021). Despite these limitations, GSRMs offer great potential to study how the tropical GWMF may change in a warming climate in general and how this may affect the QBO in particular.

In this study, we thus use the GSRM ICON-A (Zängl et al., 2015) to try to answer the two key research questions which emerge from the current uncertainty in QBO projections for a warming climate:

1. *How does the spectrum of convectively generated GWs in the tropics as well as their associated GWMF change in a warming climate?* This question is motivated by the substantial uncertainty of projections of tropical GWMF due to the inherent uncertainties of GW parameterizations and will be addressed in Section B.4.

2. *How does the QBO change in a warming climate if its GW forcing is simulated explicitly?* This question is motivated by the uncertainty in QBO projections due to the uncertainty in GWMF projections and will be answered in Section B.5.

B.2 METHODS

B.2.1 *ICON-A model configuration*

The numerical experiments of this study have been conducted with the global atmosphere-only GCM ICON-A (Giorgetta et al., 2018), which employs a non-hydrostatic dynamical core (Zängl et al., 2015). ICON-A is formulated on an unstructured triangular horizontal grid derived from a spherical icosahedron, which is obtained by projecting an icosahedron onto the sphere formed by its vertices (Wan et al., 2013). To allow for the intended direct simulation of deep convection, the simulations of this study make use of the R2B9 grid, which has an equivalent horizontal resolution of $\Delta x \approx 5$ km (see Table 1 in Giorgetta et al., 2018) and which has been shown to allow for a reasonable simulation of deep convection (Hohenegger et al., 2020) and GW spectra (Müller et al., 2018; Stephan et al., 2019a). The vertical grid of ICON-A used in this study is a terrain following hybrid sigma height grid (Leuenberger et al., 2010) consisting of 191 levels up to a height of 83 km. The resulting vertical grid spacing is $\Delta z \approx 350$ m in the tropopause region and $\Delta z \approx 560$ m in the stratopause region. Previous investigations indicate that this vertical resolution is sufficient to capture the main features of the wave-mean flow interactions that drive the QBO (Giorgetta et al., 2006; Geller et al., 2016a). In order to make simulations at this very high resolution feasible, the ICON-A model has

been adapted to run on graphics processing unit (GPU) architectures (Giorgetta et al., 2022), which is used in this study in version rc2.6.5.

As our model setup is intended to allow for the direct simulation of deep convection and convectively generated GWs, neither a parameterization of convection nor a parameterization of non-orographic GW drag is employed. Additionally, the parameterization of subgrid-scale orographic GW drag is switched off in order to ensure that the entire wave forcing in our simulations originates from explicitly resolved waves only. To avoid reflection of resolved waves at the model top as well as to reduce other numerical artifacts stemming from the upper model boundary, a Rayleigh damping on the vertical wind w is applied (Klemp et al., 2008), which starts at 50 km and therefore does not directly affect the QBO nor stratospheric dynamics in general. Vertical diffusion of heat, momentum, and tracers is parameterized using the total turbulent energy scheme of Mauritsen et al. (2007) in the setup described in Pithan et al. (2015). In contrast to the baseline version of ICON-A presented in Giorgetta et al. (2018), the GPU-enabled ICON-A version used in this study employs the RTE+RRTMGP radiation scheme (Pincus et al., 2019). To ensure numerical stability and to suppress numerical noise, ICON-A applies a combination of horizontal diffusion and divergence damping. The horizontal diffusion is set up as a second-order Smagorinsky diffusion on potential temperature and velocity combined with a fourth-order background diffusion on velocity. The approach for the divergence damping used in this study is a combined second-order and fourth-order damping acting on the three-dimensional velocity divergence. A more detailed description of the setup of the GPU-enabled ICON-A used in this study can be found in Giorgetta et al. (2022).

Giorgetta et al. (2022) have shown that the described setup of ICON-A is capable of simulating the downward progression of the QBO jets with time due to wave-mean flow interactions in the shear zones of the QBO. However, it must be noted that the downward progression of the QBO in their simulation was about three times faster compared to ECMWF Reanalysis v5 (ERA5).

B.2.2   *Experimental setup*

The experimental design of our study closely follows the protocol of the QBOi experiments 2, 3, and 4 (Butchart et al., 2018), which have been analyzed in Richter et al. (2020b). Accordingly, we have defined three idealized climate states, which are prescribed to ICON-A:

- *ref climate*: A reference climate with 1988–2007 monthly mean sea surface temperatures (SSTs) and sea ice concentrations (SICs) stemming from the CMIP6 input datasets (Durack and Taylor, 2019). The concentrations of CO_2 and other radiative trace gases have been specified to their 1988–2007 mean value; also based on their CMIP6 input dataset (Meinshausen et al., 2017), which gives a CO_2 concentration of 365.59 ppm.

- *+2K climate*: A double-CO_2 climate, in which the CO_2 concentration is doubled compared to the reference climate and a globally uniform SST increase of $+2$ K compared to the reference climate is employed. Despite the changes in SST and CO_2 concentration, SIC is kept at its reference climate values.

Concentrations of other radiative trace gases are also kept at their reference climate values.

- **+4K *climate***: A quadruple-CO_2 climate, in which the CO_2 concentration is quadrupled compared to the reference climate and a globally uniform SST increase of $+4\,K$ compared to the reference climate is employed. Despite the changes in SST and CO_2 concentration, SIC is kept at its reference climate values. Concentrations of other radiative trace gases are also kept at their reference climate values.

Based on the results of Deser et al. (2015), we don't expect the constant SIC to have a significant influence on the tropical atmosphere, including the QBO. In all three climate states, the solar forcing is fixed at its 2002 conditions. Furthermore, ozone is not simulated interactively within our model setup and instead three-dimensional ozone concentrations (Hegglin et al., 2016) are prescribed as their 2002 monthly mean values in all three climate states. Consequently, the QBO-ozone feedback as well as potential feedbacks stemming from projected ozone changes in the future are not recognized in our study. Thereby, our experimental setup guarantees that any change in the QBO and in stratospheric GWMF is solely attributable to the employed changes in CO_2 concentrations and SST. We chose the year 2002 as a reference year based on the QBOi experimental protocol (Butchart et al., 2018), which argues that the El Niño-Southern Oscillation and the Pacific decadal oscillation were in a neutral state in 2002 and further no explosive volcanic eruptions occurred. Nevertheless, it should be noted that the 2002 ozone amounts are impacted by a Southern Hemisphere sudden stratospheric warming (e.g., Shepherd et al., 2005).

For each idealized climate state we performed two experiments in order to account for the role of the QBO phase: the first set of experiments was initialized on 01 April 2004 0000 UTC when the QBO was in a phase of westerly shear (experiments ref-west, +2K-west, and +4K-west), while the second set of experiments was initialized on 01 April 2005 0000 UTC when the QBO was in a phase of easterly shear (experiments ref-east, +2K-east, and +4K-east). In both cases the model was initialized from the European Centre for Medium-Range Weather Forecasts' Integrated Forecasting System operational analysis for the corresponding date and time. The zonal wind profiles in the tropical stratosphere at the two initialization timesteps are shown in Figure B.1. Each experiment was integrated for 45 days and instantaneous output was written every 2 hours. The first 15 days out of the total simulated 45 days per experiment are considered as spin-up, which has been found to be reasonable based on the temporal evolution of thermodynamic properties of the tropical atmosphere (see Supporting Information B). Therefore, only the last 30 days of each experiment are used for analysis. An overview of all simulations performed for this study can be found in Table B.1.

B.2.3 *Postprocessing of model output*

The majority of the diagnostics used in our study require their input data to be provided on a regular latitude-longitude grid and on geometric height coordinates (see Sec. B.2.4). Additionally, disk space constraints made it impossible to store the raw output of all experiments, making it necessary to reduce the amount of data.
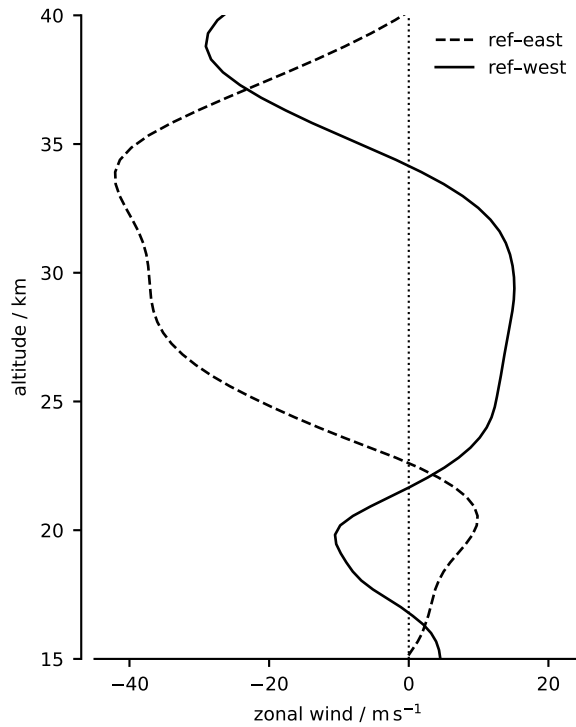
Figure B.1: 5°S–5°N zonal mean zonal wind profiles in the stratosphere at model initialization.

Table B.1: Setup of all performed simulations. Abbreviations: CO_2, carbon dioxide; SST, sea surface temperature.

Experiment	SST change	CO_2 change	Initialization
ref-west	—	—	April 01, 2004
+2K-west	+2 K	Doubling	April 01, 2004
+4K-west	+4 K	Quadrupling	April 01, 2004
ref-east	—	—	April 01, 2005
+2K-east	+2 K	Doubling	April 01, 2005
+4K-east	+4 K	Quadrupling	April 01, 2005

Therefore, we have performed a distance weighted average remapping of the raw model output coming on the triangular R2B9 grid to a regular n256 Gaussian grid (grid-spacing of $\sim$39 km near the equator) based on the 13 nearest neighbors. In the vertical, we have interpolated the raw model output coming on terrain following hybrid sigma height levels to the geometric height levels corresponding to the sigma height levels over ocean. Since the model levels transition from sigma height levels to constant height levels above 22.5 km on the whole globe, no vertical interpolation was performed above this height. This means that the largest part of the tropical stratosphere is not influenced by the vertical interpolation. All analysis in our study is based on the postprocessed data.

Diagnostics

Wave generation by deep convection

To investigate the generation of GWs by deep convection in the tropical troposphere, we make use of the analysis developed by Müller et al. (2018) and analyze the in-cloud vertical velocity w_{cld} and the in-cloud latent heating rate $Q_{\text{lat,cld}}$ within 15°S and 15°N. Additionally, we analyze the cloud fraction Γ_{cld}, which is defined as the amount of cloudy grid cells per altitude level divided by the total amount of grid cells within 15°S and 15°N. At any altitude, a grid cell is defined as cloudy if its total cloud condensate mass mixing ratio q_{T} exceeds $0.1\,\text{g}\,\text{kg}^{-1}$.

Furthermore, we calculate the zonal wave number power spectra of total precipitation (pr) in the tropics, which are a wide-used proxy of tropical tropospheric wave activity (see, e.g., Müller et al., 2018; Polichtchouk et al., 2021). The spectral power $P_{\text{pr}}(k)$ of precipitation estimates its variance as a function of zonal wave number k and is given by

$$P_{\text{pr}}(k) = F_{\text{pr}}(k)\tilde{F}_{\text{pr}}(k), \tag{B.1}$$

where $F_{\text{pr}}(k)$ denotes the complex Fourier transform of precipitation calculated by a fast Fourier transform in longitude and $\tilde{F}_{\text{pr}}(k)$ denotes its complex conjugate. We have calculated the spectra for each time step and along each latitude between 15°S and 15°N.

Spectral characteristics of the stratospheric wave field in the tropics are analogously analyzed by calculating the cospectral power $P_{\text{uw}}(k)$ of the zonal wind u and the vertical wind w as

$$P_{\text{uw}}(k) = \text{Re}\left(F_{\text{u}}(k)\tilde{F}_{\text{w}}(k)\right), \tag{B.2}$$

where $F_{\text{u}}(k)$ denotes the complex Fourier transform of u, $\tilde{F}_{\text{w}}(k)$ denotes the complex conjugate of the complex Fourier transform of w, and $\text{Re}()$ denotes the real part of a complex number. The product of $P_{\text{uw}}(k)$ and air density ρ may then be interpreted as the zonal momentum flux spectrum, i.e. the spectrum of the vertical flux of zonal momentum $\rho u'w'$, where the prime denotes departures from the zonal mean background wind.

Stratospheric gravity wave field

Our output interval of 2 h is clearly too coarse to temporally resolve the shortest GWs that are spatially resolved by the postprocessed data, which can have periods as short as ~17 min. Therefore, neither the GW pseudomomentum flux nor GW phase speed spectra can be diagnosed using the classical spectral approach via Fourier analysis in space and time. Instead, we decided to use the small-volume few-wave decomposition technique (S3D, Lehmann et al., 2012), which is suited to diagnose the characteristics of the stratospheric GWs as well as their associated momentum fluxes at individual timesteps. S3D has the additional advantage that it provides local information of GWs, since GW characteristics are given as function of physical space instead of spectral space. It has already been used by Stephan et al. (2019a) and Stephan et al. (2019b) to diagnose GW characteristics in global storm-resolving simulations.

Technically, S3D performs three-dimensional sinusoidal fits on subsets of perturbation temperature and vertical wind to calculate the local wave vector and amplitude in each subset. In the following, the individual steps of the S3D algorithm as employed in our study are explained in more detail:

1. *Vertical regridding.* The postprocessed output fields of temperature T, zonal wind u, meridional wind v, vertical wind w, and pressure p are linearly regridded to an evenly spaced height coordinate with a vertical spacing of 500 m starting at a height of 1.5 km.

2. *Split up into background and perturbation component.* Each vertically regridded variable ϑ is split into a background component ϑ_0 and a perturbation component ϑ' by performing a fast Fourier transform in the zonal direction, followed by a split at zonal wave number 18 (zonal wavelength $\lambda_x \approx 2220$ km near the equator). Thus, the background component contains most planetary waves as well as large-scale gradients, while the perturbation component retains mostly GW signals, at least in the stratosphere. In accordance with Strube et al. (2020) we have used a cutoff wave number of 18 which removes also synoptic Rossby waves present in the lower stratosphere. Furthermore, the background component is smoothed using a Savitzky-Golay filter (Savitzky and Golay, 1964) in latitude based on third-order polynomials over 5° latitude.

3. *Cuboid subsets.* The three-dimensional perturbation temperature within our analysis domain between ∼38°S and ∼38°N is divided into subsets of cuboids with a size of 330 km × 330 km in the horizontal and 10 km in the vertical. The chosen cuboid size agrees with Lehmann et al. (2012) and ensures that we can theoretically identify waves with horizontal wavelengths λ_h between ∼80 km and ∼3300 km and vertical wavelengths λ_z between ∼1 km and ∼35 km. However, wavelengths at the lower and upper edge of these ranges are not reliably identifiable (see S3D step 5). Within our analysis domain, the cuboid centers are placed every ∼3.51° in the zonal direction and every ∼3.16° in the meridional direction so that neighbouring cuboids within the deep tropics do not overlap. In the vertical direction, the cuboids are centered every 500 m between 20 km and 40 km so that only the very bottom of the lowest cuboid is located below the tropopause while the top of the highest cuboid is still located well below the sponge layer. We chose this very high vertical sampling interval to accurately resolve the vertical gradient of GWMF.

4. *Initial three-dimensional sinusoidal fit.* Within each cuboid separately, three subsequent three-dimensional sinusoidal fits are performed to the temperature perturbations to determine the wave component j which minimizes the remaining variance based on the least squares method. After the optimal solution for wave component j has been determined, it is subtracted from the perturbation temperature and the fit for wave component $j+1$ is performed. In this way, we derive the amplitude $\hat{T}_j$ and the three-dimensional wave vector $\boldsymbol{k}_j = (k_j, l_j, m_j)$ of all three wave components j.

5. *Rejecting unreliable fits.* As described in detail in Stephan et al. (2019b), fits resulting in a wave length λ_ζ much larger than the cuboid size Δ_ζ of a given

direction ζ must be considered as unreliable. Within our study, fits resulting in $\lambda_h > 3.5\Delta_h$ or $\lambda_z > 3\Delta_z$ are considered as unreliable and are therefore rejected from further analysis.

6. **Three-dimensional refit.** Using the previously determined wave vector k_j of each wave component j as an a priori information, a three-dimensional sinusoidal refit is performed to the same initial temperature perturbations as in S3D step 2 inside each cuboid for each wave component j. This refit helps to achieve a more reliable estimation of the wave amplitude $\hat{T}_j$ of each wave component j.

7. **Derive wave quantities.** Using the smoothed background fields determined in step 2, additional wave quantities such as GWMF are derived from the wave vector k_j and the amplitude $\hat{T}_j$. According to linear wave theory, the GWMF $F_{\mathrm{GW},j} = \left(F_{\mathrm{GW},j}^{(x)}, F_{\mathrm{GW},j}^{(y)} \right)$ of each wave component j can be estimated as (cf. Ern et al., 2004; Ern et al., 2017):

$$F_{\mathrm{GW},j} = \frac{\rho_0}{2} \frac{(k_j, l_j)}{m_j} \left(\frac{g}{N_0} \right)^2 \left(\frac{\hat{T}_j}{T_0} \right)^2 , \qquad (\text{B.3})$$

where ρ_0 denotes the background density, g denotes the gravitational acceleration, N_0 denotes the background buoyancy frequency, and T_0 denotes the background temperature. The assumption of upward propagating waves removes the ambiguity in the horizontal propagation direction of a wave. The total GWMF $F_{\mathrm{GW}} = \left(F_{\mathrm{GW}}^{(x)}, F_{\mathrm{GW}}^{(y)} \right)$ is calculated as

$$F_{\mathrm{GW}} = \sum_{j=0}^{2} F_{\mathrm{GW},j}. \qquad (\text{B.4})$$

Information on how the S3D algorithm calculates the ground-based zonal phase speed is given in Section A of the supplementary material.

B.3 CHANGES IN MEAN CLIMATE

B.3.1 *Temperatures and zonal winds*

Using experiment +4K-east as an example, Figure B.2a,c shows that ICON-A reliably simulates the basic atmospheric response to an increase in SST and CO_2 concentration. Compared to the reference climate, tropospheric temperatures increase substantially in +4K-east with the strongest increase in the upper tropical troposphere, while stratospheric temperatures decrease. Consistent with thermal wind balance, the subtropical jets in both hemispheres strengthen accordingly and shift upward and poleward. In contrast, zonal winds in the lower troposphere change little, especially in the tropics. These fundamental changes also occur in the other warming experiments, with the magnitude of change scaling with the magnitude of imposed idealized warming (not shown).

As shown by the 15°S–15°N mean temperature profile in Figure B.2b, the tropospheric warming leads to an upward shift of the tropical tropopause by about 1 km
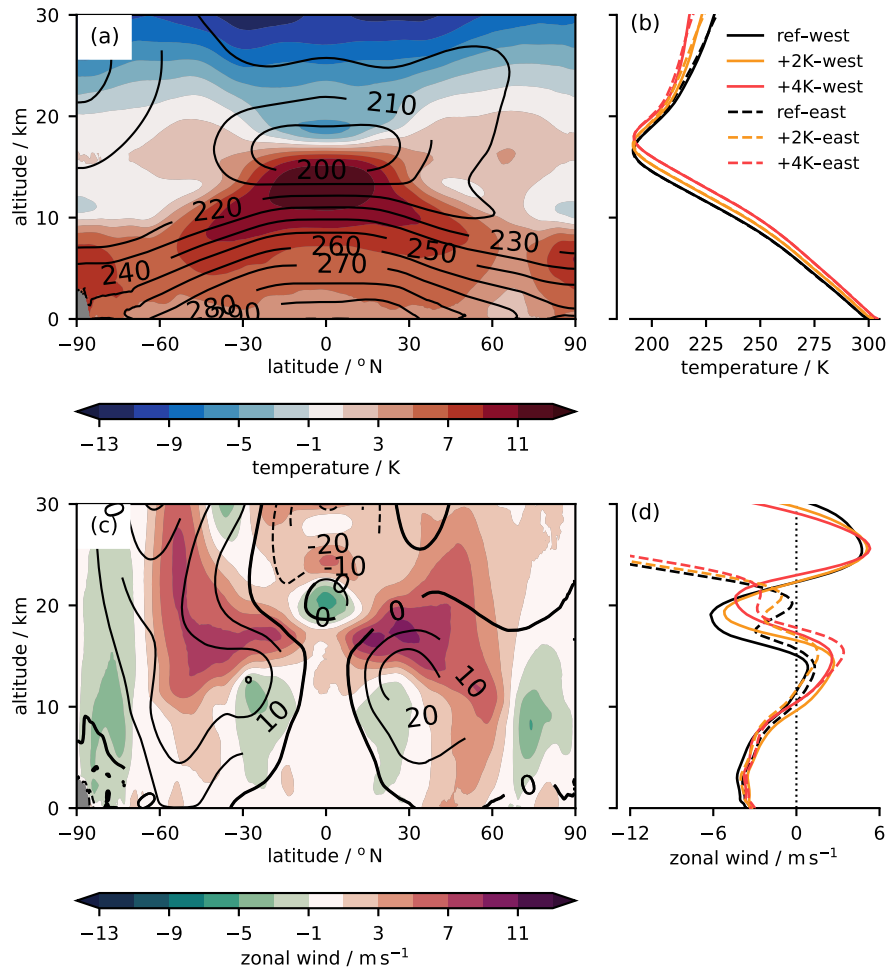
Figure B.2: Difference in **(a)** zonal mean temperature (colour shading) and **(c)** zonal mean zonal wind (colour shading) between experiment +4K-east and experiment ref-east averaged over the last 30 simulation days. Contour lines indicate **(a)** the zonal mean temperature and **(c)** the zonal mean zonal wind of experiment ref-east. Panels **(b)** and **(d)** show the 15°S–15°N zonal mean **(b)** temperature and **(d)** zonal wind profiles of all experiments averaged over the last 30 simulation days.

in the +2K climates and by about 2 km in the +4K climates. Since the QBO vanishes near the tropopause layer, the upward shift of the tropopause would have a direct impact on the vertical extent of the QBO domain. The 15°S–15°N mean zonal winds, shown in Figure B.2d, are generally weak in the troposphere in all experiments. In the upper troposphere, above an altitude of 10 km, the 15°S–15°N mean zonal winds have a clear westerly anomaly in the warmer climate states. Therefore, we do expect the idealized warming to have an impact on vertical wave propagation via critical level filtering within the upper troposphere.

Within the tropical troposphere, neither winds nor temperatures depend significantly on the QBO phase in all three climate states. This is different in the stratosphere, where the temperatures are directly influenced by adiabatic heating or cooling associated with the secondary meridional circulation of the QBO. Con-

sequently, lower-stratospheric temperatures in the westerly shear experiments are higher by about 2 K compared to their corresponding easterly shear experiments.

B.3.2 *Tropical precipitation*

Precipitation is a widely used proxy to assess the characteristics of tropical deep convection as the main trigger for tropical waves of all scales (e.g., Müller et al., 2018; Polichtchouk et al., 2021). This is based on the facts that in the tropics the majority of precipitation is produced by deep convection and that the total precipitation is proportional to the net latent heat release of a deep-convective cloud, which is the main mechanism by which deep convection generates GWs (see Fritts and Alexander, 2003, and reference therein). Consequently, it is important that our storm-resolving setup of ICON-A simulates a realistic spatio-temporal distribution of tropical precipitation in order to generate a realistic tropical wave spectrum. As shown by Figure B.3a, the zonal mean distribution of precipitation in our simulations agrees reasonably well with that of the satellite-based observational Integrated Multi-satellite Retrievals for the Global Precipitation Measurement (IMERG) dataset (Huffman et al., 2019) and the reanalysis product ERA5 (Hersbach et al., 2020), even though there are some obvious differences. Most notably, all of our simulations show a pronounced double Intertropical Convergence Zone (ITCZ) bias with a spurious southern hemispheric ITCZ resulting in too strong precipitation between $\sim$17°S and $\sim$5°S that is outside the range of internal variability for both ERA5 (years 1988–2007) and IMERG (years 2001–2007). As a further manifestation of the double ITCZ bias, equatorial precipitation is too weak in our simulations compared to IMERG and ERA5. However, it should be noted that the double ITCZ bias is not specific to ICON-A but instead is one of the most common biases in GCMs, regardless of whether they parameterize convection (Fiedler et al., 2020; Tian and Dong, 2020) or simulate it explicitly (Stevens et al., 2019, see their Fig. 5). Figure B.3b shows that the relative occurrence frequency of precipitation in our simulations matches the one in IMERG reasonably well, while ERA5 fails to produce a realistic amount of strong precipitation and overestimates weak precipitation. This finding highlights the added value of explicit convection in simulating tropical precipitation realistically as compared to parameterized convection, such as in ERA5. It further shows that ICON-A is capable of simulating intense smaller-scale deep convection, albeit too much compared to IMERG, which is an important source of small-scale GWs (Fritts and Alexander, 2003). These findings are also represented by the large values of zonal variance in our simulations compared to ERA5 and IMERG (see Table B.2).

In the warmer climate states, the characteristics of tropical precipitation change compared to their corresponding reference climate states. As shown in Table B.2, both the tropical mean (i.e., 15°S–15°N mean) precipitation and its zonal variance increase overall robustly in the warmer climate states. Apart from experiment +2K-west, the warming-induced anomalies in tropical mean precipitation are larger than its interannual variability during the analysis time span in IMERG (years 2001–2007) and ERA5 (years 1988–2007), as represented by their relative sample standard deviation of 2.9 % and 4.2 %, respectively. Therefore, we conclude that at least for an idealized exaggerated warming of +4 K the changes in precipitation amount can be
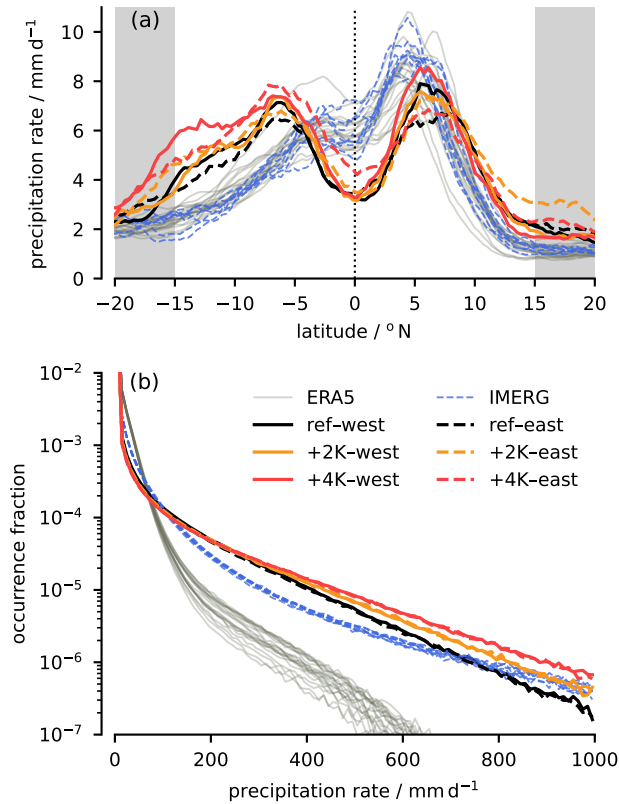
Figure B.3: Key tropical precipitation characteristics of our experiments, the satellite-based observational product IMERG, and the reanalysis product ERA5 during the analysis time span from 16 April to 15 May: **(a)** zonal mean precipitation as a function of latitude and **(b)** probability density function of precipitation between 15°S and 15°N; both based on two-hourly mean precipitation rates. To highlight the internal variability of tropical precipitation during our Atmospheric Modelling Intercomparison Project reference period (1988–2007), individual years in that period are plotted for ERA5 and IMERG (only 2001–2007 available). Grey bars in subfigure **(a)** denote areas outside of 15°S and 15°N, which are not used for calculating the probability density function in subfigure **(b)**.

attributed to the imposed warming with high confidence. Nevertheless, it must be noted that the quantitative estimates of changes in tropical mean precipitation in our short simulations are likely uncertain due to internal variability. This is highlighted by the fact that even between both reference experiments (ref-east and ref-west) the tropical mean precipitation differs by up to 6%. Additionally, Figure B.3a shows that warming-induced precipitation anomalies occur non-uniformly across latitudes. On a local scale, even for an idealized warming of +4 K the amount of precipitation change lies within the range of interannual variability in both ERA5 (years 1988–2007) and IMERG (years 2001–2007).

In contrast to the overall precipitation amount, warming-induced changes in precipitation intensity are much more robust across our simulations as shown in Figure B.3b. In the warmer climates we see a clear increase in the occurrence frequency of strong precipitation while the occurrence frequency of weak precipitation decreases. Thereby, the increase in strong precipitation scales approximately exponentially with the amount of idealized warming. These findings hold for both

the westerly and the easterly shear experiments and there are no significant quantitative differences between both sets of experiments. Recalling the fact that tropical precipitation is a reasonable proxy for the generation of tropical waves by deep convection, we expect the warming-induced changes in precipitation to have a notable impact on the tropical wave field.

Table B.2: 15°S–15°N mean precipitation statistics of our experiments, the satellite-based observational product Integrated Multi-satellite Retrievals for the Global Precipitation Measurement (IMERG), and the ECMWF Reanalysis v5 (ERA5) product averaged over the analysis time span from April 16 to May 15.

Experiment	$\overline{pr}$/mm day^{-1}	$\Delta\,\overline{pr}$/%	σ^2_{pr}/mm^2 day^{-2}	$\Delta\,\sigma^2_{pr}$/%
ref-west	5.07	—	1138.48	—
+2K-west	5.12	$+$0.92	1364.52	$+$19.85
+4K-west	5.53	$+$9.00	1668.00	$+$46.51
ref-east	4.77	—	1075.39	—
+2K-east	5.27	$+$10.50	1396.28	$+$29.84
+4K-east	5.49	$+$14.96	1651.71	$+$53.59
ERA5	4.78 $\pm$ 0.20	—	185.38 $\pm$ 26.79	—
IMERG	4.85 $\pm$ 0.14	—	975.79 $\pm$ 54.12	—

$\overline{pr}$: 15°S–15°N mean precipitation rate.

$\Delta\overline{pr}$: relative difference of 15°S–15°N mean precipitation rate between the warmer climate states and their corresponding reference climate state.

σ^2_{pr}: 15°S–15°N mean zonal variance of precipitation rate.

$\Delta\sigma^2_{pr}$: relative difference of 15°S–15°N mean zonal variance of precipitation rate between the warmer climate states and their corresponding reference climate.

To highlight the internal variability of tropical precipitation during our Atmospheric Modelling Intercomparison Project (AMIP) reference period (1988–2007 for ERA5, 2001–2007 for IMERG), the average value of these periods and the standard deviation ($\pm$) are given.

B.4 CHANGES IN TROPICAL GRAVITY WAVES

B.4.1 *Wave generation by deep convection*

The warming-induced changes in the characteristics of tropical precipitation clearly suggest a more vigorous generation of tropical waves, which means that the waves get stronger or their generation occurs more frequently or over a wider area. In order to investigate in more detail how the generation mechanisms of tropical waves in our simulations change, we analyse the in-cloud latent heating and the in-cloud vertical velocity as established by Müller et al. (2018) (see Sec. B.2.4.1). Here, the in-cloud latent heating serves as a direct proxy of the thermal forcing of GWs by latent heat release in deep convective storms (Fritts and Alexander, 2003). Similarly, the in-cloud vertical velocity serves as a proxy of the mechanical forcing of GWs by the oscillations of convective updrafts around their level of neutral buoyancy at the cloud top (Fritts and Alexander, 2003). However, Fritts and Alexander (2003) also point out that the thermal and mechanical forcing of GWs should not be

considered as two distinct processes but rather act in a coupled manner due to the inherent coupling between the latent heat release and the vertical velocity in a deep convective cloud.

As shown in Figure B.4a,b, for both the westerly and the easterly shear experiments the overall in-cloud latent heating increases in the warmer climate states, which is in agreement with the overall increase in tropical precipitation (see Sec. B.3.2). The increase in latent heating is most obvious for the strong and very strong convective events as represented by the 90th percentile and the 99th percentile of in-cloud latent heating, respectively. There, the absolute value of the peak latent heating between 6 km and 11 km increases by about 4.5–8.5 % for the +2K climates and by about 12–22 % for the +4K, which is a clear indication of more intense convection. Based on these results, we therefore expect the generation of stronger thermally forced GWs, i.e. GWs with a larger amplitude.

Figure B.4c,d shows the in-cloud vertical velocity w_{cld} as a proxy for the mechanical forcing of GWs. It is immediately evident that in the warmer climate states the mean w_{cld} and the 90th and 99th percentiles of w_{cld} increase compared to their corresponding reference climate states. This corresponds to stronger convective updrafts in a warmer climate, which is in agreement with the stronger latent heating seen in Figure B.4a,b. Above 15 km, the negative w_{cld} associated with the oscillation of a cloudy air mass around its level of neutral buoyancy due to strong overshooting convection also becomes stronger, i.e. more negative, as represented by the 1st and 10th percentile of w_{cld}. We interpret this finding as a clear indication of a more vigorous mechanical forcing of GWs in a warming climate.

Both the in-cloud latent heating and the in-cloud vertical velocity clearly indicate that a warming climate will result in stronger tropical deep convection associated with a more vigorous generation of GWs. However, the applied analyses do not allow for an evaluation of a change in the area occupied by deep convection and thus a change in the area in which waves are generated, i.e. the amount of deep convection and GWs. Therefore, we examine profiles of the 15°S–15°N mean cloud fraction Γ_{cld}, which is shown in Figure B.4e,f. Here, the lower peak in cloudiness at ∼5 km can be attributed to shallow cumuli and cumuli congesti, while the upper peak in cloudiness at ∼12.5 km can be mostly attributed to the cirrus anvils of deep convective storms. Deep convective storms itself normally reach from the level of condensation near the top of the boundary layer (∼2 km) to the upper troposphere (∼10 km–15 km). This means that all deep convective clouds must have cloudy grid cells also at the local minimum in Γ_{cld} located at an altitude of ∼10 km. Thus, changes in the area covered by deep convection can be evaluated based on the absolute value of Γ_{cld} at its local minimum at ∼10 km. As shown in Figure B.4e,f the absolute value of the local minimum of Γ_{cld} at ∼10 km stays approximately constant in the warmer climate states. This suggests that in contrast to its strength, the area covered by deep convection increases only little in a warmer climate, which implies that the more vigorous generation of waves should be interpreted as the generation of stronger waves, i.e. waves with a larger amplitude, instead of the more frequent generation of waves or their generation over a larger spatial area. Thus, we conclude that a warming climate will result in a strengthening of the existing tropical tropospheric wave field as a consequence of a more vigorous GW generation due to stronger deep convection.
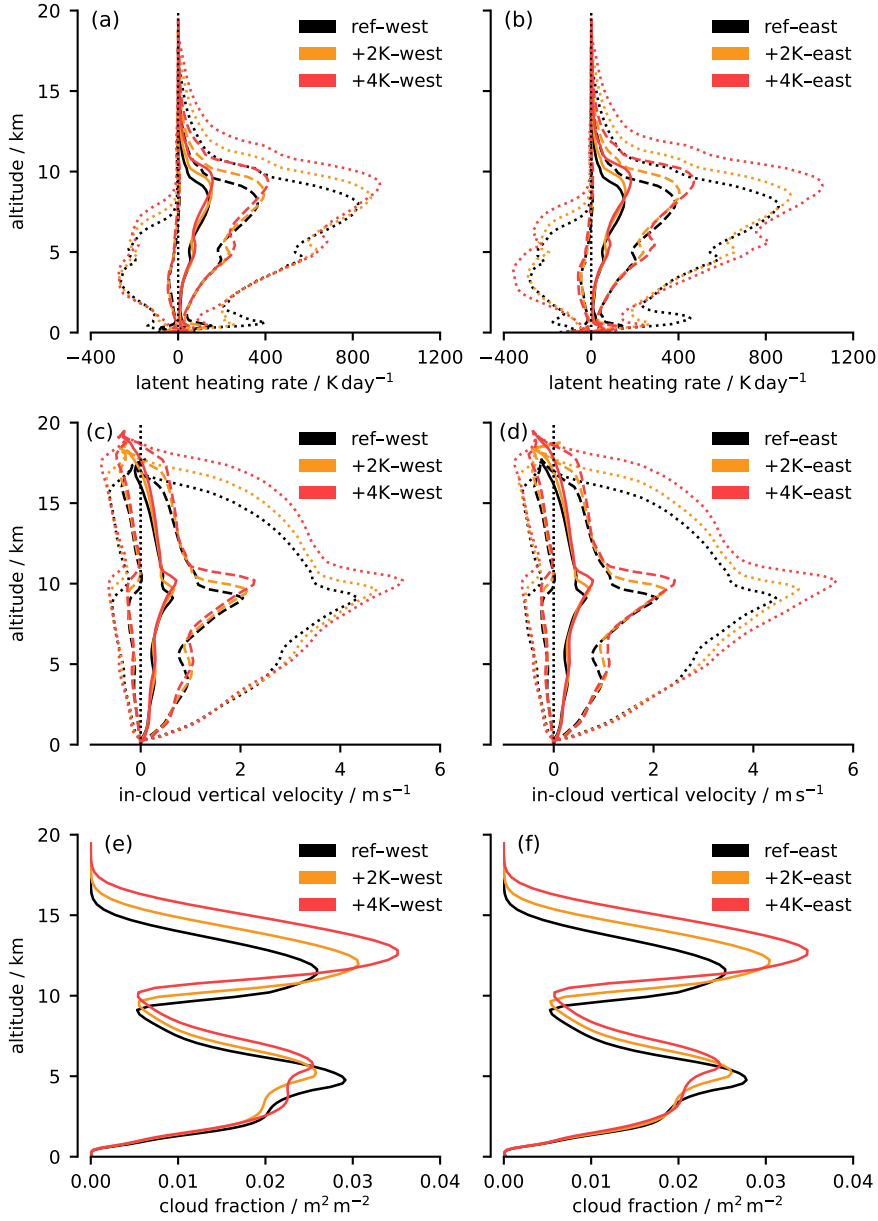
Figure B.4: Vertical profiles of different statistics of **(a,b)** in-cloud latent heating Q_{lat}, **(c,d)** in-cloud vertical velocity w_{cld}, and **(e,f)** cloud fraction Γ_{cld} averaged over the last 30 simulation days. Solid lines indicate the 15°S–15°N mean value, dashed lines indicate the 10th and the 90th percentile within 15°S–15°N, and dotted lines indicate the 1st and the 99th percentile within 15°S–15°N. The vertical dotted lines mark an **(a,b)** in-cloud latent heating of $Q_{lat} = 0\,\mathrm{K\,day^{-1}}$ and an **(c,d)** in-cloud vertical velocity of $w_{cld} = 0\,\mathrm{m\,s^{-1}}$. The left panels **(a,c,e)** show the westerly shear experiments, while the right panels **(b,d,f)** show the easterly shear experiments.

Besides becoming stronger, Figure B.4 also suggests that tropical deep convection becomes deeper in the warmer climate states by ∼0.75 km for the +2K climate states and by ∼1.5 km for the +4K climate states. A deepening of tropical convection has important implications for the dominant horizontal phase speed of the generated GW spectrum, which will be discussed in Section B.4.3.

B.4.2   *Zonal wave scales*

In order to investigate whether the strengthening of tropical deep convection has a scale preference or instead occurs uniformly across all scales, we calculate tropical mean zonal wave number power spectra of precipitation, i.e. the spectral power of precipitation as a function of zonal wave number k, as described in Section B.2.4.1. The spectra as well as their relative difference between the warmer climate states and the corresponding reference climate state are shown in Figure B.5a,c. In the warmer climate states the spectral power of precipitation is substantially larger than in the corresponding reference climate states across all zonal wave numbers. This confirms our previous finding of more vigorous convection in a warmer climate and in agreement with Parseval's theorem, it additionally agrees with the increase in tropical precipitation variance shown in Table B.2. Figure B.5c shows that the warming-induced strengthening of the precipitation spectra further occurs almost uniformly across all zonal wave numbers. Accordingly, the spectral shape of the precipitation spectrum does not change in the warmer climate states (Fig. B.5a). This suggests that the strengthening of convection is approximately uniform across its characteristic horizontal scales, ranging from individual cells to its planetary distribution associated with the land-sea distribution. In other words, convection becomes more intense in a warmer climate, but its large-scale pattern and its characteristic scales remain the same, which is in agreement with our findings in Section B.4.1. These results are qualitatively consistent for the westerly and the easterly shear experiments, but for the easterly shear experiments the individual spectra have lower absolute values than the corresponding westerly shear experiments, which is consistent with Figure B.3a. The root cause for this systematic difference between both sets of experiments is unclear.

Based on the changes in the tropical precipitation spectrum, we also expect the spectrum of tropical waves generated by deep convection to strengthen approximately uniformly across all zonal wave numbers. This hypothesis builds on the fact that the spectra of precipitation and tropical waves are coupled in a statistical sense, even though individual convective systems of a particular horizontal scale usually generate a broad spectrum of waves and, thus, features at a particular zonal wave number in the wave spectrum cannot be attributed to features at the same zonal wave number in the precipitation spectrum. Since we found the power spectrum of precipitation to increase uniformly across zonal wave number in the warmer climate states, also the power spectrum of the generated waves should increase uniformly across zonal wave number in a warmer climate, assuming that the relation between both spectra, i.e. the wave generation mechanisms, do not change in a warmer climate. To test this hypothesis, Figure B.5b shows the cospectra of zonal wind u and vertical wind w multiplied by density ρ at an altitude of $\sim 20\,\mathrm{km}$. These cospectra can be interpreted as the zonal momentum flux spectra, i.e. the spectra of the vertical flux of zonal momentum, in the equatorial lower stratosphere (see Sec. B.2.4.1). The wave field in the equatorial lower stratosphere is still largely determined by its tropospheric convective sources, even though filtering by upper-tropospheric zonal background winds may already cause some differences between the tropospheric and the lower-stratospheric wave spectra.

The slope of the zonal momentum flux spectra is approximately constant throughout the mesoscale ($k > 18$) and slightly shallower than -1, overall corresponding
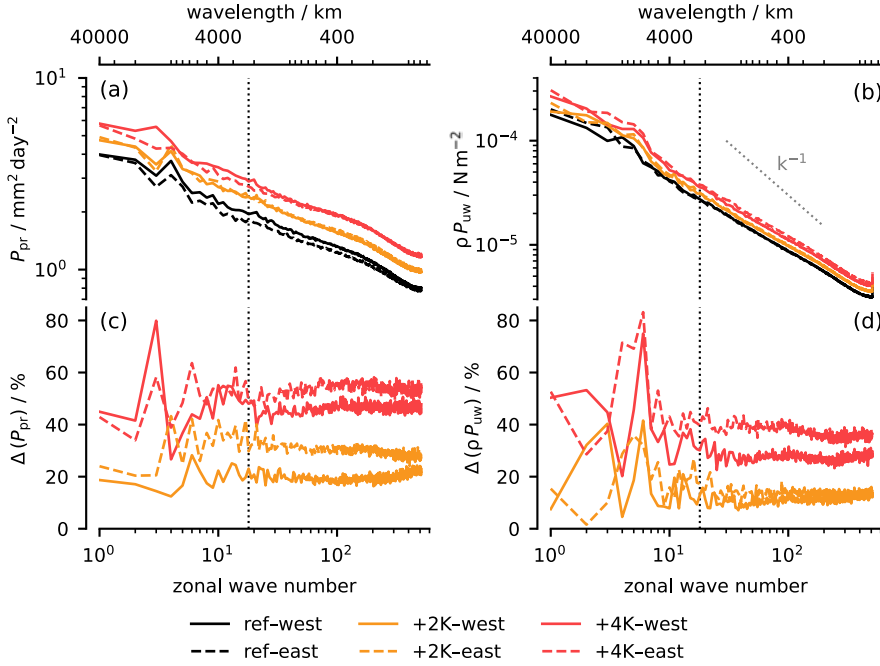
Figure B.5: 15°S–15°N mean **(a)** spectral power of precipitation P_{pr} and **(b)** density-weighted cospectral power of zonal and vertical wind ρP_{uw} at an altitude of ~ 20 km as a function of zonal wave number k, averaged over the last 30 simulation days. The relative difference of P_{pr} and ρP_{uw} between the warmer climate states and their corresponding reference climate is shown in **(c)** and **(d)**, respectively. The vertical dotted line marks $k = 18$, which is used to separate between planetary-scale waves ($k \leq 18$) and gravity waves ($k > 18$). The annotated grey dotted line in **(b)** highlights a spectral slope of -1. All spectra have been calculated by means of Fourier-spectral analysis (see Sec. B.2.4.1).

to what was found by Müller et al. (2018) in idealised model setups. The slopes of the individual power spectra of u and w are also close to their mesoscale canonical values of $-5/3$ (Nastrom and Gage, 1985; Gardner et al., 1993; Skamarock, 2004) and 0 (Terasaki et al., 2009; Skamarock et al., 2014; Morfa and Stephan, 2023), respectively (not shown), indicating that ICON-A generates an overall reasonable GW spectrum. At the short wavelength tail of the zonal momentum flux spectra (Fig. B.5b), we notice a pronounced flattening for zonal wavelengths $\lambda_x < 100$ km. This is an imprint of the aliasing which occurs due to the remapping from the fine ICON-A source grid ($\Delta_x \approx 5$ km) to the coarser n256 Gaussian grid ($\Delta_x \approx 40$ km), on which we calculate the spectra. Thus, the spectra should be considered reliable only for zonal wavelengths $\lambda_x > 100$ km, which is also well above the effective resolution of ICON-A of $\sim 12\Delta x$ (~ 60 km) (Stephan et al., 2019a).

Figure B.5d shows the relative difference between the zonal momentum flux spectra of the warmer climate states and the corresponding reference climate state. In the GW range of the spectra, i.e. $k > 18$ ($\lambda_x < 2200$ km), the relative increase in spectral power is approximately uniform across all zonal wave numbers. This implies that a warmer climate would result in an approximately uniform strengthening of the existing GW spectrum in the equatorial lower stratosphere which corresponds well with the uniform strengthening of the power spectrum of precipitation (see Fig. B.5c). Therefore, we conclude that the generation of stronger

GWs in the troposphere also results in stronger GWs in the lower stratosphere, accompanied by a net increase in GWMF entering the stratosphere. This finding may be further extendable to planetary scale waves, i.e. $k \leq 18$ ($\lambda_x \geq 2200 \, \mathrm{km}$), however, due to the short analysis time span the signal is too noisy for that claim to be certain.

The lower-stratospheric zonal momentum flux spectra also show a larger warming-induced increase in spectral power for the easterly than for the westerly shear experiments for a warming of +4K, which is in agreement with the precipitation spectra. While the root cause for this systematic difference between both sets of experiments is unclear in case of the precipitation spectra, in case of the lower-stratospheric zonal momentum flux spectra it could be at least partly attributable to warming-induced differences in upper tropospheric wave filtering. Warming-induced changes in upper-tropospheric wave-filtering will be investigated in more detail in Section B.4.3.

B.4.3   *Lower-stratospheric gravity wave momentum flux*

In this Section, we analyze changes in GWMF at an altitude of $\sim$20 km to investigate how the momentum carried by GWs, which is potentially available for driving the QBO, may change in a warmer climate. In order to quantify the GWMF we applied the S3D method because of the limitations of classical Fourier spectral methods (see Sec. B.2.4.2).

Figure B.6 shows that the warming-induced strengthening of the GW field in the equatorial lower stratosphere — indicated by the changes in the power spectra (Fig. B.5b) — results in a clear increase of the zonal GWMF at an altitude of $\sim$20 km. For both sets of experiments, both the eastward GWMF and the westward GWMF is stronger in the warmer climate states than in the reference climate and this strengthening is larger in the +4K-climate states than in the +2K-climate states. For the westerly shear experiments, the increase in eastward GWMF and westward GWMF seems to scale approximately linearly with the amount of warming, whereas this is clearly not the case for the easterly shear experiments. Here, the eastward GWMF increases much more strongly for the +4K-climate state compared to the +2K-climate state, whereas the increase of the westward GWMF is approximately the same for the +4K-climate state and the +2K-climate state.

In order to be available for the acceleration of the QBO jets, the warming-induced increase in GWMF must be carried by waves with zonal phase speeds relevant for the QBO. Thus, we have a look at the distribution of GWs as a function of their ground-based zonal phase speed c_x, which is determined by the S3D method (see Sec. B.2.4.2). Given there are in total N valid GW samples detected by the S3D method, each of them associated with a zonal GWMF B_x and a ground-based zonal phase speed c_x, we get the normalized zonal GWMF distribution as a function of zonal phase speed as $B_x(c_x)/N$ (Fig. B.7a,b). $B_x(c_x)/N$ is commonly referred to as the zonal GWMF spectrum and can be further separated into

$$\frac{B_x(c_x)}{N} = \frac{n(c_x)}{N} \cdot \frac{B_x(c_x)}{n(c_x)}, \tag{B.5}$$

where $n(c_x)$ is the absolute GW frequency distribution as a function of ground-based zonal phase speed. Accordingly, the first term on the right-hand side of
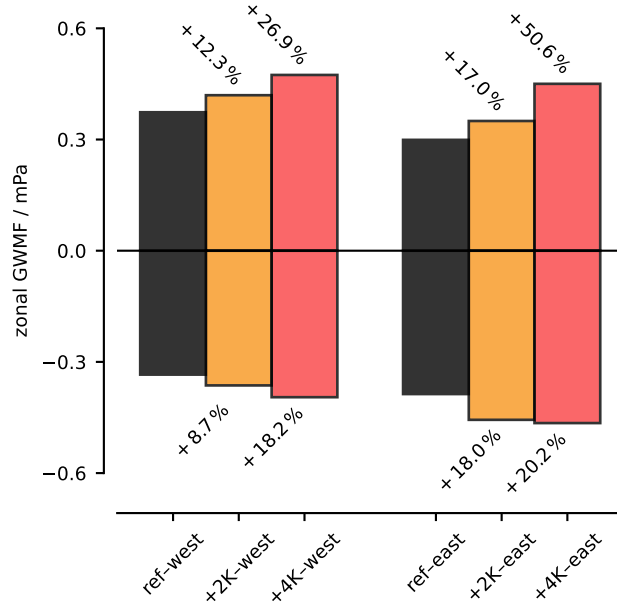
Figure B.6: Zonal mean zonal GWMF (i.e. vertical flux of zonal wave momentum), at an altitude of 20 km averaged over 15°S–15°N for the last 30 simulation days. Positive bars show eastward GWMF and negative bars show westward GWMF. Annotations show the increase in eastward and westward GWMF of the warmer climate states relative to their corresponding reference climate. The zonal GWMF has been calculated by means of the small-volume few-wave decomposition (S3D, see Sec. B.2.4.2).

Eq. B.5, $n(c_x)/N$, denotes the relative GW frequency distribution as a function of ground-based zonal phase speed (Fig. B.7c,d), while the second term on the right-hand side of Eq. B.5, $B_x(c_x)/n(c_x)$, denotes the mean zonal GWMF associated with a wave for a given ground-based zonal phase speed (Fig. B.7e,f).

As shown by Figure B.7a,b, both the eastward GWMF and the westward GWMF increase in a warmer climate nearly across the entire considered phase speed range of $-60\,\mathrm{m\,s^{-1}} \leq c_x \leq +60\,\mathrm{m\,s^{-1}}$. This holds true for both sets of experiments. The majority of the GWMF increase is associated with waves that have a zonal phase speed relevant for the QBO ($-40\,\mathrm{m\,s^{-1}} \lesssim c_x \lesssim +20\,\mathrm{m\,s^{-1}}$; see Fig. B.1; please note that the relevant phase speed range itself may also slightly differ between the different climate states). Only the small fraction of the GWMF increase which is associated with waves with $+20\,\mathrm{m\,s^{-1}} \leq c_x \leq +30\,\mathrm{m\,s^{-1}}$ is not relevant for the QBO. Thus, we expect the strengthening of the lower-stratospheric GW field to ultimately have a significant impact onto the QBO. This finding is in contrast to Kawatani et al. (2011), who found that the total zonal wave momentum flux predominantly increases at zonal phase speeds which are irrelevant for the QBO.

Figure B.7c-f shows that the root cause for the increase of zonal GWMF at most zonal phase speeds relevant for the QBO is twofold. First, the zonal GWMF that is on average carried by a GW increases in the warmer climate states for most of these phase speeds (Fig. B.7e,f). Following Eq. B.3, this means that the GWs have a larger amplitude on average or, to put it simply, are stronger. This confirms our findings from Section B.4.1, in which we found that a warmer climate will result in the generation of stronger convective GWs. Second, the relative frequency distribution

of the GWs tends to shift towards higher phase speeds (Fig. B.7c,d), which are stronger on average, independent of the climate state (Fig. B.7e,f). For both sets of experiment, the relative frequency of slow GWs with zonal phase speeds close to $0 \, \text{m} \, \text{s}^{-1}$ decreases while the relative frequency of faster waves increases in the warmer climate states, especially for eastward (westward) propagating GWs in the westerly (easterly) shear experiments. Furthermore, this shift towards faster zonal phase speeds is more pronounced in the +4K climate states than in the +2K climate states, suggesting a physical root cause for this behaviour.

We propose that the shift towards faster zonal phase speeds is a consequence of the warming-induced deepening of the convective latent heating. As shown in Figure B.4a,b, the imposed warming does not only cause an increase in the overall and peak latent heating, but also an increase in its vertical depth, which is in agreement with the deepening of the troposphere found in Section B.3.1. Salby and Garcia (1987) showed that a purely thermally forced wave has a preferred vertical wavelength of twice the vertical scale of the latent heating profile. Thus, we expect the increase of the latent heating depth d_{LH} in a warmer climate to result in an increase of the average vertical wavelength λ_z of the GWs. However, the vertical wavelength itself is coupled to its intrinsic horizontal phase speed $c_h - \overline{u}_h$ as shown by the simplified dispersion relation of medium-frequency GWs (compare Eq. 33 of Fritts and Alexander, 2003)

$$|c_h - \overline{u}_h| = \frac{N \cdot |\lambda_z|}{2\pi}, \tag{B.6}$$

where N is the buoyancy frequency, $\overline{u}_h$ is the local horizontal background wind, and c_h is the GW's horizontal ground-based phase speed. Thus, the warming-induced deepening of the latent heating would ultimately cause an increase in the ground-based horizontal phase speed of thermally forced GWs. Assuming that N and $\overline{u}_h$ in the tropical troposphere stay constant at their average values of $N = 0.0075 \, \text{s}^{-1}$ and $\overline{u}_h = 0 \, \text{m} \, \text{s}^{-1}$ independent of the climate state, which is reasonable to a first approximation, the observed deepening of the mean latent heating depth d_{LH} by $\sim 0.75 \, \text{km}$ ($\sim 1.5 \, \text{km}$) for the +2K (+4K) climate states (see Fig. B.4a,b) would result in an increase of the ground-based horizontal phase speed c_h by $\sim 1.8 \, \text{m} \, \text{s}^{-1}$ ($\sim 3.6 \, \text{m} \, \text{s}^{-1}$), assuming $2d_{\text{LH}} = \lambda_z$. Assuming that the GWs have no preferred horizontal propagation direction, the average horizontal and zonal phase speed relate as $|c_h| = |\sqrt{2} c_x|$. Thus, based on the observed increase of d_{LH} we would ultimately expect an increase of the tropospheric $|c_x|$ by $\sim 1.3 \, \text{m} \, \text{s}^{-1}$ and $\sim 2.5 \, \text{m} \, \text{s}^{-1}$ for the +2K climate states and the +4K climate states, respectively. Our S3D results show an increase of $|c_x|$ in the lower stratosphere by $\sim 0.38 \, \text{m} \, \text{s}^{-1}$ and $\sim 0.91 \, \text{m} \, \text{s}^{-1}$. Given the assumptions made in our idealized calculation, the warming-induced changes in latent heating depth d_{LH} and ground-based zonal phase speed c_x agree surprisingly well. Thus, we conclude that the observed shift towards faster zonal phase speeds can be reasonably attributed to the warming-induced deepening of the latent heating profile.

Coming back to the lower-stratospheric GWMF, we further investigated the role of potential warming-induced changes in upper-tropospheric wave filtering. Based on the warming-induced westerly anomaly of the zonal wind in the upper equatorial troposphere for both sets of experiments (see Fig. B.2d), one would expect that slow eastward propagating waves are increasingly filtered out in the warmer
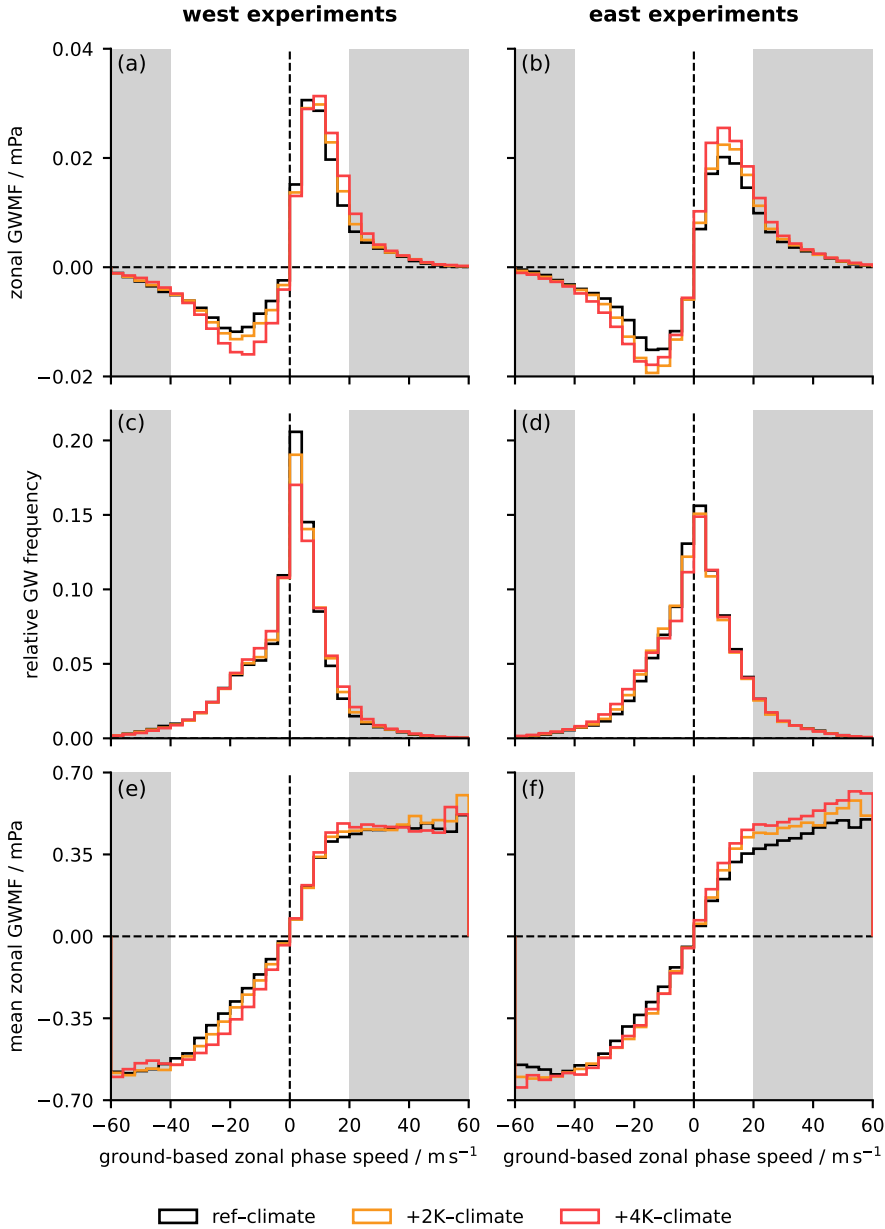
Figure B.7: Different GW distributions as a function of ground-based zonal phase speed within 15°S–15°N at an altitude of 20 km, averaged over the last 30 simulation days: **(a,b)** distribution of zonal GWMF, **(c,d)** relative frequency distribution of GWs, and **(e,f)** distribution of mean zonal GWMF per phase speed bin. The left panel **(a,c,e)** shows the westerly shear experiments and the right panel **(b,d,f)** shows the easterly shear experiments. Light grey shading highlights zonal phase speeds, which exceed the fastest 5°S–5°N mean zonal winds between an altitude of 15 km and 40 km and during the last 30 simulation days. Thus, GWs with these zonal phase speeds likely do not contribute in driving the QBO. The zonal GWMF and the ground-based zonal phase speed have been calculated by means of the small-volume few-wave decomposition (S3D, see Sec. B.2.4.2).

climate states, while slow westward propagating waves can propagate vertically increasingly well. However, only for the westerly shear experiments we notice that the zonal GWMF associated with slow eastward propagating GW with $c_x \leq 8\,\mathrm{m\,s^{-1}}$

decreases in the warmer climate states and the zonal GWMF associated with slow westward propagating GWs $c_x \geq -12\,\mathrm{m\,s}^{-1}$ strongly increases (Eq. B.5a). For the easterly shear experiments, we do not find similar warming-induced changes in upper-tropospheric filtering of slow eastward propagating waves at all. Therefore, we conclude that the impact of warming-induced changes in upper-tropospheric wave filtering is overall minor compared to the general warming-induced increase of lower-stratospheric GWMF due to stronger convection. At least partly, this may also be a consequence of the observed increase in the mean zonal phase speed of the GWs, which makes it potentially less likely for a wave to reach a critical level. Nevertheless, also methodological uncertainties of the S3D method and the local nature of small-scale GW filtering, which may not be captured by zonal mean views, may explain why we only see very small changes in upper-tropospheric wave filtering.

B.5   CHANGES IN THE QBO

B.5.1   *General aspects of the explicitly simulated QBO in ICON-A*

As shown by Giorgetta et al. (2022), the global storm-resolving setup of ICON-A used in our study simulates a downward propagation of the QBO jets as a product of resolved wave-mean flow interactions and advection by the tropical upwelling throughout a period of 45 days. However, the downward propagation of the QBO jets in ICON-A is much too fast compared to ERA5 above 27 km, which Giorgetta et al. (2022) attribute to a too strong total wave forcing. This finding corresponds to the fact that current GSRMs with high horizontal resolutions of $\Delta x < 10\,\mathrm{km}$ tend to have difficulties in simulating the total resolved wave momentum fluxes and the resulting wave forcing accurately (Polichtchouk et al., 2021; Stephan et al., 2019a,b). In our experiments, the too fast QBO is illustrated by the descent rates of the upper QBO shear zone between 30 km and 40 km, which in our reference experiments has an average value of $\sim$130 m day^{-1} and $\sim$100 m day^{-1} during the last 30 simulation days for the easterly and westerly shear experiments, respectively (see Fig. B.8a,d). Giorgetta et al. (2022) further showed that the magnitude of the QBO jets was sustained realistically throughout their simulation. This also applies to all simulations of this study as shown by Figure B.8.

In the lower stratosphere, ICON-A also reveals some of the common QBO biases of GCMs (see Anstey et al., 2022a, for an overview), namely a lack of downward propagation and a too weak amplitude. Giorgetta et al. (2022) showed that ICON-A does not simulate a reasonable downward propagation of the QBO jets below 25 km down to the tropopause, which is also clearly demonstrated by the stalling of the lowermost QBO shear zone below 25 km in our reference experiments (Fig. B.8a,d). Furthermore, for the easterly shear experiment the lowermost QBO jet is too weak compared to ERA5 (not shown). Insufficient vertical resolution is commonly believed to be one potential root cause for the weak amplitude bias in the lowermost stratosphere (Anstey et al., 2022a, and references therein) and using a high vertical resolution of $\Delta z \lesssim 500\,\mathrm{m}$ has been shown to reduce this bias significantly (Garcia and Richter, 2019). Given the high vertical resolution of $\Delta z \approx 375\,\mathrm{m}$ in the lower stratosphere in our ICON-A setup, the weak amplitude bias of the simulated QBO
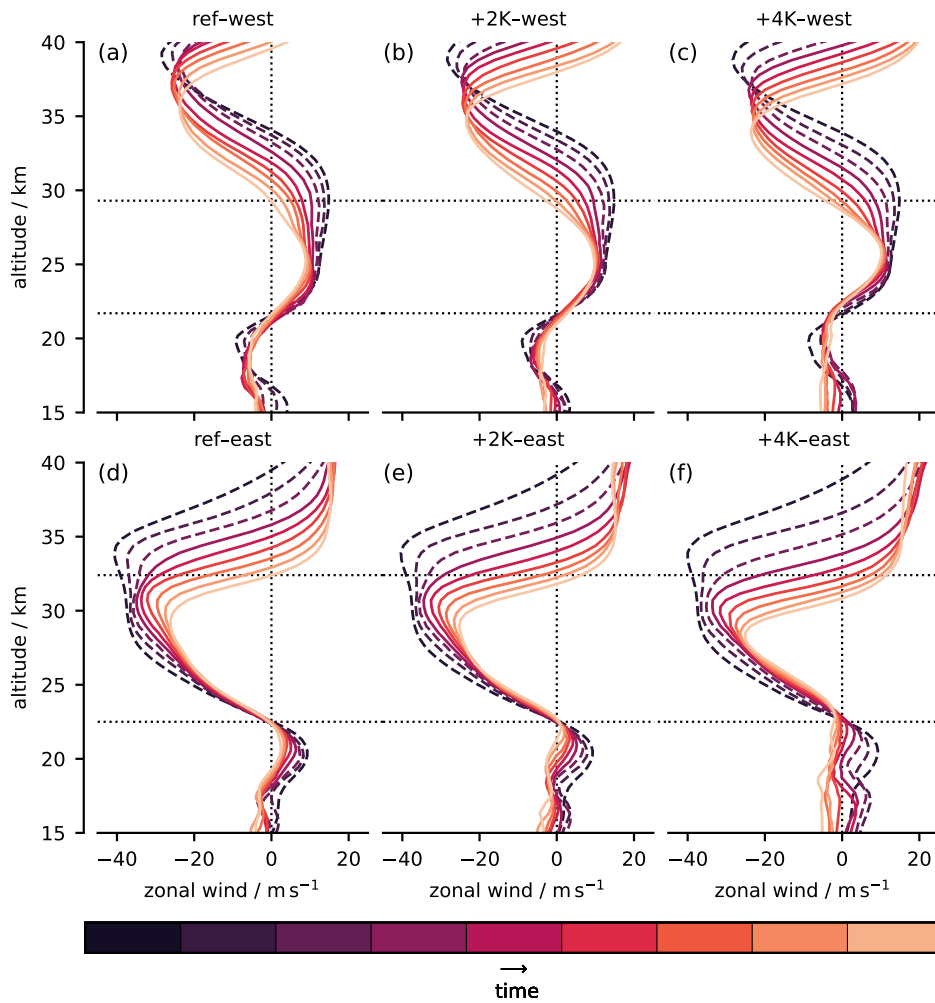
Figure B.8: Five-day mean 5°S–5°N zonal mean zonal wind profiles throughout **(a)** the experiments initialized with the QBO in its westerly phase and **(b)** the experiments initialized with the QBO in its easterly phase. The colours indicate the different five-day periods, thereby highlighting the downward propagation of the QBO throughout each experiment. The first three five-day periods, which are within the spin-up period, are marked by dashed lines. Horizontal dotted lines are plotted for highlighting differences between the experiments.

in the lowermost stratosphere is thus at least surprising and is planned to be addressed in a future study.

Since the general deficiencies of the simulated QBO in ICON-A are shared throughout all experiments, we do not expect them to have a significant influence on the comparison between the different climate states. Nevertheless, they should be borne in mind for further interpretation of our results.

B.5.2 *Downward propagation of QBO shear zones*

Figure B.8 shows the temporal evolution of the QBO jets throughout the experiments and allows for a direct evaluation of how the downward propagation of the QBO jets changes in the warmer climate states. The upper shear zone, initially located around or above ~35 km, propagates downward at an increasingly faster rate in the warmer

climate states. Consequently, with respect to the reference climate the zero-wind line of the upper shear zone at the end of the experiments is located ∼1 km lower in the +2K climates and ∼1 km (westerly shear experiment) or ∼2 km (easterly shear experiment) lower in the +4K climates, where we attribute the difference in case of the +4K climates to internal variability. Based on the faster downward propagation of the upper QBO shear zones we would ultimately expect the QBO to speed up in a warmer climate, i.e. to have a shorter period. However, it should be noted that a substantial part of the speed-up of the downward propagation of the upper shear zone occurs during the initial 15 days of the simulations, and is therefore likely influenced by the model spin-up. In contrast to the upper shear zone, the lower shear zone of the QBO (between 22 km and 25 km in the westerly shear experiments, between 22 km and 28 km in the easterly shear experiments) is increasingly shifted upward with time in the warmer climate states compared to the reference climate, especially for the +4K climates. Differences between the easterly and westerly shear experiments are negligible. Due to the short simulation period, we were not able to identify the root cause for this upward shift of the lower QBO shear zone.

In order to investigate the forcing of the faster downward propagation of the upper QBO shear zone, we created so-called QBO composite profiles. In our case, these QBO composite profiles refer to those 11-day mean zonal wind profiles for which the $-10\,\mathrm{m\,s^{-1}}$-wind line is closest to an altitude of 32 km. These profiles are shown in Figure B.9a. We chose an averaging period of 11 days as a pragmatic compromise between a robust, comparable mean and the unintended smoothing of potential warming signals. We chose the specific reference point based on the rather pragmatic consideration that it is one of the only possible reference points which lies within the upper QBO shear zone during the last 30 days of each set of experiments. This method allows a comparison of the QBO forcing between the different experiments at a fixed height instead of at a fixed time, which is necessary due the different downward propagation rates of the QBO shear zones in the different experiments. Figure B.9b shows the total zonal wind tendency during the 11-day period of each composite. The strongest total tendencies are located in the upper QBO shear zone, indicating its wave-driven downward propagation. Apart from experiment +2K-east, the total tendencies in the warmer climate states become larger, indicating a stronger downward forcing of the QBO jets, which agrees with the faster downward propagation of the shear zones seen in Figure B.8. For experiment +2K-east, we attribute the lack of increase in total tendency to internal variability, which may be still considerable during only 11 days of analysis.

B.5.3   *Magnitude of QBO jets*

In order to assess warming-induced anomalies in the magnitude of the QBO jets, we compare the composites of the QBO zonal wind profiles shown in Figure B.9a. These composite profiles show three distinct QBO jets in the stratosphere: a weak jet in the lowermost stratosphere centered around ∼20 km, the core QBO jet centered at ∼25 km and ∼30 km for the westerly and easterly shear experiments, respectively, and the uppermost QBO jet centered slightly above 35 km. The lowermost QBO jet centered around ∼20 km weakens in the warmer climate states for both sets of experiments, but the weakening appears to be slightly stronger for the easterly
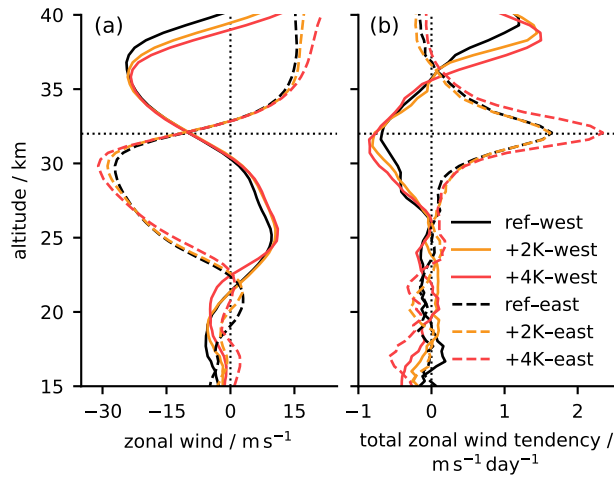
Figure B.9: 5° S–5° N mean QBO composites of the 11-day period during which the zonal mean zonal wind profiles cross the $-10\,\mathrm{m\,s^{-1}}$-wind line closest at a reference height of 32 km: **(a)** zonal wind and **(b)** total zonal wind tendency. The reference height is marked by the horizontal dotted black line.

shear experiments. It should be noted, however, that this result is probably strongly influenced by the rapid general erosion of the lower jet associated with the strong weak amplitude bias of the simulated QBO in ICON-A (see Sec. B.5.1), even though a decrease in the magnitude of the lowermost QBO jet is in agreement with previous studies which identified a decrease in QBO amplitude in the lowermost stratosphere due to a speed-up of the tropical upwelling associated with the BDC (Kawatani et al., 2011; Kawatani and Hamilton, 2013; Richter et al., 2020b). The peak magnitude of the core QBO jet, which is centered at 30 km for the easterly shear experiments and at 25 km for the westerly shear experiments, increases for both sets of experiments. The relative increase is very similar between both sets of experiments despite the different absolute strength of the jet. For the easterly shear experiments, the peak magnitude increases by 6.4 % for the +2K-climate and by 14.5 % for the +4K-climate. For the westerly shear experiments, the peak magnitude increases by 9.4 % for the +2K-climate and by 15.1 % for the +4K-climate. This strengthening of the core QBO jets in both sets of experiments would correspond to an increase in QBO amplitude in the central stratosphere between ∼24 km and ∼32 km. We suggest that the root cause for the strengthening of the core QBO jet is the warming-induced increase in the mean zonal phase speed of the GWs due to a deepening of the convective latent heating (see Sec. B.4.3). As shown by Saravanan (1990) and Geller et al. (2016b), the QBO amplitude mainly depends on the magnitude of the phase speeds of the waves that drive the QBO. Both studies found that the QBO jets are stronger if the mean absolute phase speed of the waves is larger, and vice versa. Thus, an increase of the upper QBO amplitude is reasonable based on the observed shift of the GW spectrum towards faster zonal phase speeds. However, this result strongly disagrees with previous model studies using coarse-resolution GCMs with GW parameterizations. These models typically project a decrease of the QBO amplitude in a warmer climate basically throughout the whole QBO vertical domain (Kawatani et al., 2011; Kawatani and Hamilton, 2013; Richter et al., 2020b) despite some of

them use interactive GW parameterizations that are coupled to convection and should therefore in principle be able to reproduce this mechanism discussed here.

For the uppermost QBO jet which is centered slightly above 35 km, the warming-induced zonal wind anomaly differs between both sets of experiments. The jet magnitude increases for the easterly shear experiments, while it decreases for the westerly shear experiments. We suggest that this difference is caused by the different sign of the vertical advection associated with the secondary meridional circulation of the QBO jets, which dominates the vertical movement in this altitude range (not shown). In addition, in case of the easterly experiments, which are initialized on 01 April 2005, the uppermost westerly jet is rather a jet of the semiannual oscillation than of the QBO (see Fig. 1 of Pahlavan et al., 2021a) and thus also changes in semiannual oscillation dynamics may be causal for the strengthening of the jet in the warmer climate states.

B.6 SUMMARY, DISCUSSION AND CONCLUSIONS

In this study, we performed global storm-resolving simulations of three idealized climate states to investigate how tropical GWs and the QBO may change in a warming climate. For the simulations, we used the GSRM ICON-A which explicitly resolves deep convection and GWs and thus does not employ corresponding parameterizations. In the warmer climate states, we found stronger convectively generated GWs across all scales due to a strengthening of tropical deep convection. As a consequence, the lower-stratospheric GWMF at zonal phase speeds relevant for the QBO increases substantially, especially for westward propagating GWs due to changes in upper-tropospheric wave filtering. The QBO itself speeds up in the warmer climate states but at the same time shows an increasingly strong weak amplitude bias in the lowermost stratosphere. Additionally, we found that in the warmer climate states the lower-stratospheric QBO jets weaken while the upper-stratospheric QBO jets strengthen. We attribute the strengthening of the upper-stratospheric QBO jets to a shift of the GW spectrum towards faster phase speeds, which itself is caused by a deepening of the convective latent heating profile.

The substantial increase of the total lower-stratospheric GWMF in the warmer climate states agrees well with the results of those QBOi models that use an interactive GW parameterization coupled to convective heating based on Beres et al. (2004) (see Richter et al., 2020b). Thus, the Beres et al. (2004) parameterization is apparently the only GW parameterization in the QBOi model ensemble that can adequately capture the substantial changes in convective GW generation which we found in the warmer climate states. The agreement between our results and the Beres et al. (2004) parameterization is not surprising given that it is the most physics-based parameterization in the QBOi model ensemble and the only one with a variable GW source level. In contrast, even slightly less sophisticated interactive GW parameterizations with a fixed GW source level are not capable of capturing the increase of the lower-stratospheric GWMF found in our explicit simulations. The same holds true for parameterizations using a fixed GW source spectrum and source level (see Richter et al., 2020b). Thus, our results clearly indicate that an advanced physics-based GW parameterization in conventional GCMs is necessary for being able to model a realistic response of the GWMF to a warming climate.

Our results further show that the impact of changes in upper-tropospheric wave-filtering on the total lower-stratospheric GWMF is clearly minor compared to the overall increase in tropospheric wave sources. This is in agreement with the results of Richter et al. (2020b), who also found no significant changes in upper-tropospheric wave filtering in the QBOi models. Therefore, we conclude that a decrease of the lower-stratospheric GWMF in the tropics in a warming climate can be virtually ruled out and a robust increase seems to be increasingly likely, with corresponding implications for the QBO.

However, it should be recognized that the horizontal resolution of ∼5 km in our simulations still is likely too coarse to resolve the short wavelength tail of the GW spectrum sufficiently as shown by Lane and Knievel (2005) and Polichtchouk et al. (2021). Following Lane and Knievel (2005) and Polichtchouk et al. (2021), we therefore think that the GWMF at long and mesoscale wavelengths with ∼2200 km $> \lambda_\mathrm{h} > 100$ km is artificially enhanced in our simulations due to an overestimation of the dominant horizontal wavelength. Whether this enhancement leads to an overestimation of the total GWMF in our simulations remains unclear. While Polichtchouk et al. (2021) found that the horizontal resolution only impacts the partitioning of GWMF across wavelengths but not the total GWMF, Lane and Knievel (2005) found that the overestimation of the dominant wavelength may reduce trapping and filtering of GWs and thus can also result in an overestimation of the total GWMF. However, given that all simulations were run with the same model setup and warming-induced anomalies in the zonal wave number spectra are approximately uniform across all scales (see Fig. B.5), we expect the impact of potential GWMF overestimations on the previously drawn conclusions to be minor.

As a consequence of the increased lower-stratospheric GWMF, we found the downward propagation of the QBO to accelerate in the warmer climate states. This would ultimately correspond to a shortening of the QBO period in a warming climate, but it must be mentioned that this conclusion should be considered tentative due to the very short simulation period of our experiments. A shortening of the QBO period, in turn, would agree with those QBOi models that employ the advanced Beres et al. (2004) GW parameterization. Based on these results and given that those QBOi models showing a lengthening of the QBO period employ rather primitive GW parameterizations (see Richter et al., 2020b), there appears to be some indication that a substantial lengthening of the QBO period in a warming climate may be rather unlikely.

However, the quantitative extent of any potential change in the QBO period will probably remain very model-dependent and thus highly uncertain even for those GCMs employing advanced physics-based GW parameterizations or simulating GWs explicitly. This is due to the large intermodel variability in the other QBO forcing terms, i.e. vertical advection by tropical upwelling and resolved planetary wave forcing. Richter et al. (2020b) showed that even though the qualitative response of these two QBO forcing terms to a warming climate is certain, large quantitative differences in the response remain. Additional uncertainty in changes of the QBO wave forcing stems from its strong dependency on the waves' phase speeds at which the changes occur. For example, the warming-induced increase of GWMF in our simulations occurs nearly entirely at phase speeds relevant for the QBO, while the increase of the resolved wave momentum flux in the simulations of Kawatani et al. (2011) occurs nearly entirely at phase speeds not relevant for the QBO. We

think that this spectral uncertainty in the QBO wave forcing could be in part related to the parameterization of deep convection in coarse-resolution GCMs. Therefore, additional simulations of the QBO with different GSRMs, which represent deep convection and GWs explicitly, are desirable to further constrain the response of the QBO to a warming climate quantitatively. However, even for GSRMs the parameterization of remaining unresolved dynamics, such as vertical diffusion, and the choice of the dynamical core itself will potentially cause intermodel spread (Yao and Jablonowski, 2015). Stephan et al. (2019b) further showed that also in GSRMs there is still a substantial intermodel spread in simulated GWMF.

Nevertheless, a first quantitatively more constrained estimate of changes in the QBO downward propagation rate for a single GSRM is urgently needed as a future baseline but cannot be provided by the short simulations of this study. The main reason for this is internal climate variability, which likely is considerable in our simulations at least for the large-scale, low frequency QBO forcing by planetary waves and residual advection associated with tropical upwelling. Additionally, any warming-induced change in the QBO momentum budget is likely specific to our selected simulation period of boreal spring, as both tropical wave activity associated with the latitudinal movement of the ITCZ (e.g., Vincent and Alexander, 2000) as well as tropical upwelling (e.g., Abalos et al., 2012) exhibit a substantial seasonal cycle. Therefore, our estimates of changes in the rate of QBO downward propagation may not be extendable to longer timescales. Consequently, simulations of at least one whole QBO cycle for a current reference climate state and a future warmer climate state are clearly necessary to determine a quantitatively more robust estimate of warming-induced changes in the QBO momentum balance in ICON-A and are planned for future research. To determine a robust change in the QBO period itself, even longer simulations of several QBO cycles would be necessary, which is currently not feasible due to computational constraints.

An interesting finding in our simulations is the warming-induced strengthening of the QBO jets in the middle stratosphere around an altitude of $\sim$30 km independent of QBO phase, which would correspond to an increase in QBO amplitude. The simulated warming-induced shift of the GW spectrum towards faster zonal phase speeds gives a plausible explanation for this finding based on the established link between the width of the zonal phase speed spectrum of the waves and the QBO amplitude (Saravanan, 1990; Geller et al., 2016b). Also observational data from the last $\sim$70 years, during which a warming of $\sim$1 K already took place (NOAA/NCEI, 2022), show an increase in QBO amplitude between 30 hPa and 10 hPa ($\sim$25 km–32 km) (Kawatani and Hamilton, 2013; Anstey et al., 2022a). However, in contrast to our results and the observational record, conventional GCMs usually simulate a warming-induced decrease in QBO amplitude throughout the whole vertical QBO domain (see, e.g., Anstey et al., 2022a, and references therein). While the reasons for the disagreement between the observations and the conventional GCMs have been unclear so far, our results appear to give some new indication that model deficiencies of the conventional GCMs might be a potential root cause. However, also here longer simulations are essential to support this suggestion and the uncertainties in simulated GW spectra in current GSRMs with high horizontal resolutions of $\Delta x < 10$ km (Polichtchouk et al., 2021; Stephan et al., 2019a,b) should be considered when interpreting changes in GW phase speeds.

In conclusion, we think that our study has shifted the uncertainty in QBO projections. Based on our results, it is now no longer unclear whether the GW forcing of the QBO will increase or decrease in a warming climate but instead whether the strengthening of the tropical upwelling or the strengthening in the total wave forcing will have a larger effect onto the QBO in a warming climate. Depending on which factor will outweigh the other, the QBO will either accelerate or decelerate. This shift in uncertainty achieved by our study is already a major step forward as it allows us to reject models employing unreliable GW parameterizations from the ensemble of potential QBO responses to a warming climate. However, we expect the net effect of the increase in the different QBO forcing terms to remain substantially model-dependent, at least quantitatively. For now, we thus expect QBO projections to remain overall uncertain.

CONFLICT OF INTEREST STATEMENT

The authors declare that they have no conflict of interest.

DATA AVAILABILITY STATEMENT

The ICON-A source code and scripts that are necessary to reproduce the model simulations of this study as well as all analysis code that is necessary to reproduce the results of this study, except for the S3D source code and S3D analysis scripts, is available under https://www.wdc-climate.de/ui/entry?acronym=DKRZ_ LTA_081_ds00002 (Franke et al., 2023b). The release versions of the ICON-A source code are available to individuals under license as described by MPI-M (2023). By downloading the ICON-A source code, the user accepts the license agreement. S3D source code can be obtained by contacting Peter Preusse, S3D analysis scripts can be obtained by contacting Henning Franke.

Abalos, M., W. J. Randel, and E. Serrano (2012). "Variability in upwelling across the tropical tropopause and correlations with tracers in the lower stratosphere." In: *Atmospheric Chemistry and Physics* 12.23, pp. 11505–11517. DOI: 10.5194/acp-12-11505-2012.

Achatz, U., M. J. Alexander, E. Becker, H.-Y. Chun, A. Dörnbrack, L. Holt, R. Plougonven, I. Polichtchouk, K. Sato, A. Sheshadri, C. C. Stephan, A. van Niekerk, and C. J. Wright (2024). "Atmospheric Gravity Waves: Processes and Parameterization." In: *Journal of the Atmospheric Sciences* 81.2, pp. 237 –262. DOI: 10.1175/JAS-D-23-0210.1.

Alexander, M. J. et al. (2010). "Recent developments in gravity-wave effects in climate models and the global distribution of gravity-wave momentum flux from observations and models." In: *Quarterly Journal of the Royal Meteorological Society* 136.650, pp. 1103–1124. DOI: 10.1002/qj.637.

Andrews, D. G. and M. E. McIntyre (1976). "Planetary Waves in Horizontal and Vertical Shear: The Generalized Eliassen-Palm Relation and the Mean Zonal Acceleration." In: *Journal of the Atmospheric Sciences* 33.11, pp. 2031–2048. DOI: 10.1175/1520-0469(1976)033<2031:PWIHAV>2.0.CO;2.

Angell, J. K. and J. Korshover (1964). "Quasi-Biennial Variations in Temperature, Total Ozone, and Tropopause Height." In: *Journal of Atmospheric Sciences* 21.5, pp. 479–492. DOI: 10.1175/1520-0469(1964)021<0479:QBVITT>2.0.CO;2.

Anstey, J. A., T. P. Banyard, N. Butchart, L. Coy, P. A. Newman, S. Osprey, and C. J. Wright (2021). "Prospect of Increased Disruption to the QBO in a Changing Climate." In: *Geophysical Research Letters* 48.15, e2021GL093058. DOI: 10.1029/2021GL093058.

Anstey, J. A., S. M. Osprey, J. Alexander, M. P. Baldwin, N. Butchart, L. Gray, Y. Kawatani, P. A. Newman, and J. H. Richter (2022a). "Impacts, processes and projections of the quasi-biennial oscillation." In: *Nature Reviews Earth & Environment* 3.9, pp. 588–603. DOI: 10.1038/s43017-022-00323-7.

Anstey, J. A. and T. G. Shepherd (2014). "High-latitude influence of the quasi-biennial oscillation." In: *Quarterly Journal of the Royal Meteorological Society* 140.678, pp. 1–21. DOI: 10.1002/qj.2132.

Anstey, J. A., J. F. Scinocca, and M. Keller (2016). "Simulating the QBO in an Atmospheric General Circulation Model: Sensitivity to Resolved and Parameterized Forcing." In: *Journal of the Atmospheric Sciences* 73.4, pp. 1649–1665. DOI: 10.1175/JAS-D-15-0099.1.

Anstey, J. A. et al. (2022b). "Teleconnections of the Quasi-Biennial Oscillation in a multi-model ensemble of QBO-resolving models." In: *Quarterly Journal of the Royal Meteorological Society* 148.744, pp. 1568–1592. DOI: 10.1002/qj.4048.

Baldauf, M., A. Seifert, J. Förstner, D. Majewski, M. Raschendorfer, and T. Reinhardt (2011). "Operational Convective-Scale Numerical Weather Prediction with the COSMO Model: Description and Sensitivities." In: *Monthly Weather Review* 139.12, pp. 3887–3905. DOI: 10.1175/MWR-D-10-05013.1.

Baldwin, M. P., B. Ayarzagüena, T. Birner, N. Butchart, A. H. Butler, A. J. Charlton-Perez, D. I. V. Domeisen, C. I. Garfinkel, H. Garny, E. P. Gerber, M. I. Hegglin, U. Langematz, and N. M. Pedatella (2021). "Sudden Stratospheric Warmings." In: *Reviews of Geophysics* 59.1, e2020RG000708. DOI: 10.1029/2020RG000708.

Baldwin, M. P., L. J. Gray, T. J. Dunkerton, K. Hamilton, P. H. Haynes, W. J. Randel, J. R. Holton, M. J. Alexander, I. Hirota, T. Horinouchi, D. B. A. Jones, J. S. Kinnersley, C. Marquardt, K. Sato, and M. Takahashi (2001). "The quasi-biennial oscillation." In: *Reviews of Geophysics* 39.2, pp. 179–229. DOI: 10.1029/1999RG000073.

Baldwin, M. P. and T. J. Dunkerton (1998). "Quasi-biennial modulation of the southern hemisphere stratospheric polar vortex." In: *Geophysical Research Letters* 25.17, pp. 3343–3346. DOI: 10.1029/98GL02445.

Becker, T., P. Bechtold, and I. Sandu (2021). "Characteristics of convective precipitation over tropical Africa in storm-resolving global simulations." In: *Quarterly Journal of the Royal Meteorological Society* 147.741, pp. 4388–4407. DOI: 10.1002/qj.4185.

Beres, J. H., M. J. Alexander, and J. R. Holton (2004). "A Method of Specifying the Gravity Wave Spectrum above Convection Based on Latent Heating Properties and Background Wind." In: *Journal of the Atmospheric Sciences* 61.3, pp. 324–337. DOI: 10.1175/1520-0469(2004)061<0324:AMOSTG>2.0.CO;2.

Boer, G. J. and K. Hamilton (2008). "QBO influence on extratropical predictive skill." In: *Climate Dynamics* 31.7-8, pp. 987–1000. DOI: 10.1007/s00382-008-0379-5.

Booker, J. R. and F. P. Bretherton (1967). "The critical layer for internal gravity waves in a shear flow." In: *Journal of Fluid Mechanics* 27.3, pp. 513–539. DOI: 10.1017/S0022112067000515.

Boville, B. A. and W. J. Randel (1992). "Equatorial Waves in a Stratospheric GCM: Effects of Vertical Resolution." In: *Journal of Atmospheric Sciences* 49.9, pp. 785–801. DOI: 10.1175/1520-0469(1992)049<0785:EWIASG>2.0.CO;2.

Bramberger, M., M. J. Alexander, S. Davis, A. Podglajen, A. Hertzog, L. Kalnajs, T. Deshler, J. D. Goetz, and S. Khaykin (2022). "First Super-Pressure Balloon-Borne Fine-Vertical-Scale Profiles in the Upper TTL: Impacts of Atmospheric Waves on Cirrus Clouds and the QBO." In: *Geophysical Research Letters* 49.5, e2021GL097596. DOI: 10.1029/2021GL097596.

Brewer, A. W. (1949). "Evidence for a world circulation provided by the measurements of helium and water vapour distribution in the stratosphere." In: *Quarterly Journal of the Royal Meteorological Society* 75.326, pp. 351–363. DOI: 10.1002/qj.49707532603.

Bushell, A. C. et al. (2020). "Evaluation of the Quasi-Biennial Oscillation in global climate models for the SPARC QBO-initiative." In: *Quarterly Journal of the Royal Meteorological Society* 148.744, pp. 1459–1489. DOI: 10.1002/qj.3765.

Bushell, A. C., N. Butchart, S. H. Derbyshire, D. R. Jackson, G. J. Shutts, S. B. Vosper, and S. Webster (2015). "Parameterized Gravity Wave Momentum Fluxes from Sources Related to Convection and Large-Scale Precipitation Processes in a Global Atmosphere Model." In: *Journal of the Atmospheric Sciences* 72.11, pp. 4349–4371. DOI: 10.1175/JAS-D-15-0022.1.

Butchart, N., A. A. Scaife, M. Bourqui, J. de Grandpré, S. H. E. Hare, J. Kettleborough, U. Langematz, E. Manzini, F. Sassi, K. Shibata, D. Shindell, and M. Sigmond (2006). "Simulations of anthropogenic change in the strength of the Brewer–Dobson circulation." In: *Climate Dynamics* 27.7-8, pp. 727–741. DOI: 10.1007/s00382-006-0162-4.

Butchart, N. et al. (2018). "Overview of experiment design and comparison of models participating in phase 1 of the SPARC Quasi-Biennial Oscillation initiative (QBOi)." In: *Geoscientific Model Development* 11.3, pp. 1009–1032. DOI: 10.5194/gmd-11-1009-2018.

Butchart, N., J. A. Anstey, Y. Kawatani, S. M. Osprey, J. H. Richter, and T. Wu (2020). "QBO Changes in CMIP6 Climate Projections." In: *Geophysical Research Letters* 47.7, e2019GL086903. DOI: 10.1029/2019GL086903.

Bölöni, G., Y.-H. Kim, S. Borchert, and U. Achatz (2021). "Toward Transient Subgrid-Scale Gravity Wave Representation in Atmospheric Models. Part I: Propagation Model Including Nondissipative Wave-Mean-Flow Interactions." In: *Journal of the Atmospheric Sciences* 78.4, pp. 1317–1338. DOI: 10.1175/JAS-D-20-0065.1.

Cariolle, D. and H. Teyssèdre (2007). "A revised linear ozone photochemistry parameterization for use in transport and general circulation models: multi-annual simulations." In: *Atmospheric Chemistry and Physics* 7.9, pp. 2183–2196. DOI: 10.5194/acp-7-2183-2007.

Choi, W., W. B. Grant, J. H. Park, K.-M. Lee, H. Lee, and J. M. Russell III (1998). "Role of the quasi-biennial oscillation in the transport of aerosols from the tropical stratospheric reservoir to midlatitudes." In: *Journal of Geophysical Research: Atmospheres* 103.D6, pp. 6033–6042. DOI: 10.1029/97JD03118.

Collimore, C. C., D. W. Martin, M. H. Hitchman, A. Huesmann, and D. E. Waliser (2003). "On The Relationship between the QBO and Tropical Deep Convection." In: *Journal of Climate* 16.15, pp. 2552–2568. DOI: 10.1175/1520-0442(2003)016<2552:OTRBTQ>2.0.CO;2.

Coy, L., P. A. Newman, S. Pawson, and L. R. Lait (2017). "Dynamics of the Disrupted 2015/16 Quasi-Biennial Oscillation." In: *Journal of Climate* 30.15, pp. 5661–5674. DOI: 10.1175/JCLI-D-16-0663.1.

Crook, J., C. Klein, S. Folwell, C. M. Taylor, D. J. Parker, R. Stratton, and T. Stein (2019). "Assessment of the Representation of West African Storm Lifecycles in Convection-Permitting Simulations." In: *Earth and Space Science* 6.5, pp. 818–835. DOI: 10.1029/2018EA000491.

DallaSanta, K., C. Orbe, D. Rind, L. Nazarenko, and J. Jonas (2021). "Dynamical and Trace Gas Responses of the Quasi-Biennial Oscillation to Increased CO_2." In: *Journal of Geophysical Research: Atmospheres* 126.6, e2020JD034151. DOI: 10.1029/2020JD034151.

Dee, D. P. et al. (2011). "The ERA-Interim reanalysis: configuration and performance of the data assimilation system." In: *Quarterly Journal of the Royal Meteorological Society* 137.656, pp. 553–597. DOI: 10.1002/qj.828.

Deser, C., R. A. Tomas, and L. Sun (2015). "The Role of Ocean–Atmosphere Coupling in the Zonal-Mean Atmospheric Response to Arctic Sea Ice Loss." In: *Journal of Climate* 28.6, pp. 2168–2186. DOI: 10.1175/JCLI-D-14-00325.1.

Doms, G., J. Förstner, E. Heise, H.-J. Herzog, D. Mironov, M. Raschendorfer, T. Reinhardt, B. Ritter, R. Schrodin, J.-P. Schulz, and G. Vogel (2021). *COSMO-Model Version 6.00: A Description of the Nonhydrostatic Regional COSMO-Model - Part II: Physical Parametrizations*. Tech. rep. last access: October 11, 2023. Deutscher Wetterdienst. DOI: 10.5676/DWD_PUB/NWV/COSMO-DOC_6.00_II.

Dunkerton, T. J. (1985). "A Two-Dimensional Model of the Quasi-Biennial Oscillation." In: *Journal of Atmospheric Sciences* 42.11, pp. 1151–1160. DOI: 10.1175/1520-0469(1985)042<1151:ATDMOT>2.0.CO;2.

Dunkerton, T. J. (1991). "Nonlinear Propagation of Zonal Winds in an Atmosphere with Newtonian Cooling and Equatorial Wavedriving." In: *Journal of the Atmospheric Sciences* 48.2, pp. 236–263. DOI: 10.1175/1520-0469(1991)048<0236:npozwi>2.0.co;2.

Dunkerton, T. J. (1997). "The role of gravity waves in the quasi-biennial oscillation." In: *Journal of Geophysical Research: Atmospheres* 102.D22, pp. 26053–26076. DOI: 10.1029/96JD02999.

Dunkerton, T. J. (2001). "Quasi-Biennial and Subbiennial Variations of Stratospheric Trace Constituents Derived from HALOE Observations." In: *Journal of the Atmospheric Sciences* 58.1, pp. 7–25. DOI: 10.1175/1520-0469(2001)058<0007:QBASVO>2.0.CO;2.

Dunkerton, T. J. and D. P. Delisi (1985). "Climatology of the Equatorial Lower Stratosphere." In: *Journal of Atmospheric Sciences* 42.4, pp. 376–396. DOI: 10.1175/1520-0469(1985)042<0376:COTELS>2.0.CO;2.

Durack, P. J. and K. E. Taylor (2019). *PCMDI AMIP SST and sea-ice boundary conditions version 1.1.6*. DOI: 10.22033/ESGF/input4MIPs.12381.

Ebdon, R. A. (1960). "Notes on the wind flow at 50 mb in tropical and sub-tropical regions in January 1957 and January 1958." In: *Quarterly Journal of the Royal Meteorological Society* 86.370, pp. 540–542. DOI: 10.1002/qj.49708637011.

Ern, M., L. Hoffmann, and P. Preusse (2017). "Supporting information for "Directional gravity wave momentum fluxes in the stratosphere derived from high-resolution AIRS temperature data"." In: *Geophysical Research Letters* 44.1, pp. 1–22. DOI: 10.1002/2016GL072007.

Ern, M., P. Preusse, M. J. Alexander, and C. D. Warner (2004). "Absolute values of gravity wave momentum flux derived from satellite data." In: *Journal of Geophysical Research: Atmospheres* 109.D20103. DOI: 10.1029/2004JD004752.

Fels, S. B. (1982). "A Parameterization of Scale-Dependent Radiative Damping Rates in the Middle Atmosphere." In: *Journal of Atmospheric Sciences* 39.5, pp. 1141–1152. DOI: 10.1175/1520-0469(1982)039<1141:APOSDR>2.0.CO;2.

Fiedler, S. et al. (2020). "Simulated Tropical Precipitation Assessed across Three Major Phases of the Coupled Model Intercomparison Project (CMIP)." In: *Monthly Weather Review* 148.9, pp. 3653–3680. DOI: 10.1175/MWR-D-19-0404.1.

Franke, H. and M. Giorgetta (2024). "Towards a direct simulation of a full cycle of the quasi-biennial oscillation in a global storm-resolving model." In: *preparation for submission to the Journal of Advances in Modeling Earth Systems*.

Franke, H., U. Niemeier, and D. Visioni (2021). "Differences in the quasi-biennial oscillation response to stratospheric aerosol modification depending on injection strategy and species." In: *Atmospheric Chemistry and Physics* 21.11, pp. 8615–8635. DOI: 10.5194/acp-21-8615-2021.

Franke, H., P. Preusse, and M. Giorgetta (2023a). "Changes of tropical gravity waves and the quasi-biennial oscillation in storm-resolving simulations of idealized global warming." In: *Quarterly Journal of the Royal Meteorological Society* 149.756, pp. 2838–2860. DOI: 10.1002/qj.4534.

Franke, H., P. Preusse, and M. Giorgetta (2023b). *PRIMARY DATA for "Changes in tropical gravity waves and the quasi-biennial oscillation in storm-resolving simulations of idealized global warming"*. URL: https://www.wdc-climate.de/ui/entry?acronym=DKRZ_LTA_081_ds00002.

Frierson, D. M. W., D. Kim, I.-S. Kang, M.-I. Lee, and J. Lin (2011). "Structure of AGCM-Simulated Convectively Coupled Kelvin Waves and Sensitivity to Convective Parameterization." In: *Journal of the Atmospheric Sciences* 68.1, pp. 26–45. DOI: 10.1175/2010JAS3356.1.

Fritts, D. C. and M. J. Alexander (2003). "Gravity wave dynamics and effects in the middle atmosphere." In: *Reviews of Geophysics* 41.1003. DOI: 10.1029/2001rg000106.

Fueglistaler, S. and P. H. Haynes (2005). "Control of interannual and longer-term variability of stratospheric water vapor." In: *Journal of Geophysical Research: Atmospheres* 110.D24. DOI: 10.1029/2005JD006019.

Garcia, R. R. and J. H. Richter (2019). "On the Momentum Budget of the Quasi-Biennial Oscillation in the Whole Atmosphere Community Climate Model." In: *Journal of the Atmospheric Sciences* 76.1, pp. 69–87. DOI: 10.1175/JAS-D-18-0088.1.

Garcia, R. R., A. K. Smith, D. E. Kinnison, A. de la Cámara, and D. J. Murphy (2017). "Modification of the Gravity Wave Parameterization in the Whole Atmosphere Community Climate Model: Motivation and Results." In: *Journal of the Atmospheric Sciences* 74.1, pp. 275–291. DOI: 10.1175/JAS-D-16-0104.1.

Gardner, C. S., C. A. Hostetler, and S. J. Franke (1993). "Gravity wave models for the horizontal wave number spectra of atmospheric velocity and density fluctuations." In: *Journal of Geophysical Research: Atmospheres* 98.D1, pp. 1035–1049. DOI: 10.1029/92JD02051.

Garfinkel, C. I., E. P. Gerber, O. Shamir, J. Rao, M. Jucker, I. White, and N. Paldor (2022). "A QBO cookbook: Sensitivity of the Quasi-Biennial Oscillation to resolution, resolved waves, and parameterized gravity waves." In: *Journal of Advances in Modeling Earth Systems* 14.3, e2021MS002568. DOI: 10.1029/2021MS002568.

Geller, M. A., W. Shen, M. Zhang, and W.-W. Tan (1997). "Calculations of the Stratospheric Quasi-Biennial Oscillation for Time-Varying Wave Forcing." In: *Journal of the Atmospheric Sciences* 54.7, pp. 883–894. DOI: 10.1175/1520-0469(1997)054<0883:COTSQB>2.0.CO;2.

Geller, M. A., T. Zhou, D. Shindell, R. Ruedy, I. Aleinov, L. Nazarenko, N. L. Tausnev, M. Kelley, S. Sun, Y. Cheng, R. D. Field, and G. Faluvegi (2016a). "Modeling the QBO—Improvements resulting from higher-model vertical resolution." In: *Journal of Advances in Modeling Earth Systems* 8.3, pp. 1092–1105. DOI: 10.1002/2016MS000699.

Geller, M. A., T. Zhou, and W. Yuan (2016b). "The QBO, gravity waves forced by tropical convection, and ENSO." In: *Journal of Geophysical Research: Atmospheres* 121.15, pp. 8886–8895. DOI: 10.1002/2015JD024125.

Geller, M. A., X. Zhou, and M. Zhang (2002). "Simulations of the Interannual Variability of Stratospheric Water Vapor." In: *Journal of the Atmospheric Sciences* 59.6, pp. 1076–1085. DOI: 10.1175/1520-0469(2002)059<1076:SOTIVO>2.0.CO;2.

Giorgetta, M. A., L. Bengtsson, and K. Arpe (1999). "An investigation of QBO signals in the east Asian and Indian monsoon in GCM experiments." In: *Climate Dynamics* 15.6, pp. 435–450. DOI: 10.1007/s003820050292.

Giorgetta, M. A., E. Manzini, E. Roeckner, M. Esch, and L. Bengtsson (2006). "Climatology and Forcing of the Quasi-Biennial Oscillation in the MAECHAM5 Model." In: *Journal of Climate* 19.16, pp. 3882–3901. DOI: 10.1175/JCLI3830.1.

Giorgetta, M. A. et al. (2018). "ICON-A, the Atmosphere Component of the ICON Earth System Model: I. Model Description." In: *Journal of Advances in Modeling Earth Systems* 10.7, pp. 1613–1637. DOI: `10.1029/2017ms001242`.

Giorgetta, M. A. et al. (2022). "The ICON-A model for direct QBO simulations on GPUs (version icon-cscs:baf28a514)." In: *Geoscientific Model Development* 15.18, pp. 6985–7016. DOI: `10.5194/gmd-15-6985-2022`.

Giorgetta, M. A. and M. C. Doege (2005). "Sensitivity of the quasi-biennial oscillation to CO_2 doubling." In: *Geophysical Research Letters* 32.L08701. DOI: `10.1029/2004GL021971`.

Giorgetta, M. A., E. Manzini, and E. Roeckner (2002). "Forcing of the quasi-biennial oscillation from a broad spectrum of atmospheric waves." In: *Geophysical Research Letters* 29.8. DOI: `10.1029/2002GL014756`.

Gray, L. J., J. A. Anstey, Y. Kawatani, H. Lu, S. Osprey, and V. Schenzinger (2018). "Surface impacts of the Quasi Biennial Oscillation." In: *Atmospheric Chemistry and Physics* 18.11, pp. 8227–8247. DOI: `10.5194/acp-18-8227-2018`.

Gray, L. J. and J. A. Pyle (1989). "A Two-Dimensional Model of the Quasi-biennial Oscillation of Ozone." In: *Journal of Atmospheric Sciences* 46.2, pp. 203–220. DOI: `10.1175/1520-0469(1989)046<0203:ATDMOT>2.0.CO;2`.

Hamilton, K., R. J. Wilson, and R. S. Hemler (1999). "Middle Atmosphere Simulated with High Vertical and Horizontal Resolution Versions of a GCM: Improvements in the Cold Pole Bias and Generation of a QBO-like Oscillation in the Tropics." In: *Journal of the Atmospheric Sciences* 56.22, pp. 3829–3846. DOI: `10.1175/1520-0469(1999)056<3829:MASWHV>2.0.CO;2`.

Hamilton, K., R. J. Wilson, and R. S. Hemler (2001). "Spontaneous Stratospheric QBO-like Oscillations Simulated by the GFDL SKYHI General Circulation Model." In: *Journal of the Atmospheric Sciences* 58.21, pp. 3271–3292. DOI: `10.1175/1520-0469(2001)058<3271:SSQLOS>2.0.CO;2`.

Hardiman, S. C., D. G. Andrews, A. A. White, N. Butchart, and I. Edmond (2010). "Using Different Formulations of the Transformed Eulerian Mean Equations and Eliassen–Palm Diagnostics in General Circulation Models." In: *Journal of the Atmospheric Sciences* 67.6, pp. 1983–1995. DOI: `10.1175/2010JAS3355.1`.

Hardiman, S. C., N. Butchart, and N. Calvo (2014). "The morphology of the Brewer–Dobson circulation and its response to climate change in CMIP5 simulations." In: *Quarterly Journal of the Royal Meteorological Society* 140.683, pp. 1958–1965. DOI: `10.1002/qj.2258`.

Hegglin, M., D. Kinnison, J.-F. Lamarque, and D. Plummer (2016). *CCMI ozone in support of CMIP6 - version 1.0*. DOI: `10.22033/ESGF/input4MIPs.1115`.

Hersbach, H., B. Bell, P. Berrisford, G. Biavati, A. Horányi, J. Muñoz Sabater, J. Nicolas, C. Peubey, R. Radu, I. Rozum, D. Schepers, A. Simmons, C. Soci, D. Dee, and J.-N. Thépaut (2018a). *ERA5 hourly data on pressure levels from 1979 to present*. Accesed at DKRZ on 10/13/2023. DOI: `10.24381/cds.bd0915c6`.

Hersbach, H., B. Bell, P. Berrisford, G. Biavati, A. Horányi, J. Muñoz Sabater, J. Nicolas, C. Peubey, R. Radu, I. Rozum, D. Schepers, A. Simmons, C. Soci, D. Dee, and J.-N. Thépaut (2018b). *ERA5 hourly data on single levels from 1979 to present*. Accesed at DKRZ on 10/13/2023. DOI: `10.24381/cds.adbb2d47`.

Hersbach, H. et al. (2020). "The ERA5 global reanalysis." In: *Quarterly Journal of the Royal Meteorological Society* 146.730, pp. 1999–2049. DOI: `10.1002/qj.3803`.

Hitchman, M. H., M. McKay, and C. R. Trepte (1994). "A climatology of stratospheric aerosol." In: *Journal of Geophysical Research: Atmospheres* 99.D10, pp. 20689–20700. DOI: 10.1029/94JD01525.

Hitchman, M. H., S. Yoden, P. H. Haynes, V. Kumar, and S. Tegtmeier (2021). "An Observational History of the Direct Influence of the Stratospheric Quasi-biennial Oscillation on the Tropical and Subtropical Upper Troposphere and Lower Stratosphere." In: *Journal of the Meteorological Society of Japan. Ser. II* 99.2, pp. 239–267. DOI: 10.2151/jmsj.2021-012.

Hohenegger, C., L. Kornblueh, D. Klocke, T. Becker, G. Cioni, J. F. Engels, U. Schulzweida, and B. Stevens (2020). "Climate Statistics in Global Simulations of the Atmosphere, from 80 to 2.5 km Grid Spacing." In: *Journal of the Meteorological Society of Japan. Ser. II* 98.1, pp. 73–91. DOI: 10.2151/jmsj.2020-005.

Holt, L. A., M. J. Alexander, L. Coy, A. Molod, W. Putman, and S. Pawson (2016). "Tropical Waves and the Quasi-Biennial Oscillation in a 7-km Global Climate Simulation." In: *Journal of the Atmospheric Sciences* 73.9, pp. 3771–3783. DOI: 10.1175/JAS-D-15-0350.1.

Holt, L. A. et al. (2020). "An evaluation of tropical waves and wave forcing of the QBO in the QBOi models." In: *Quarterly Journal of the Royal Meteorological Society* 148.744, pp. 1541–1567. DOI: 10.1002/qj.3827.

Holton, J. R. (1972). "Waves in the Equatorial Stratosphere Generated by Tropospheric Heat Sources." In: *Journal of Atmospheric Sciences* 29.2, pp. 368–375. DOI: 10.1175/1520-0469(1972)029<0368:WITESG>2.0.CO;2.

Holton, J. R. and R. S. Lindzen (1972). "An Updated Theory for the Quasi-Biennial Cycle of the Tropical Stratosphere." In: *Journal of the Atmospheric Sciences* 29.6, pp. 1076–1080. DOI: 10.1175/1520-0469(1972)029<1076:AUTFTQ>2.0.CO;2.

Holton, J. R. and H.-C. Tan (1980). "The Influence of the Equatorial Quasi-Biennial Oscillation on the Global Circulation at 50 mb." In: *Journal of the Atmospheric Sciences* 37.10, pp. 2200–2208. DOI: 10.1175/1520-0469(1980)037<2200:TIOTEQ>2.0.CO;2.

Horinouchi, T., S. Pawson, K. Shibata, U. Langematz, E. Manzini, M. A. Giorgetta, F. Sassi, R. J. Wilson, K. Hamilton, J. de Grandpré, and A. A. Scaife (2003). "Tropical Cumulus Convection and Upward-Propagating Waves in Middle-Atmospheric GCMs." In: *Journal of the Atmospheric Sciences* 60.22, pp. 2765–2782. DOI: 10.1175/1520-0469(2003)060<2765:TCCAUW>2.0.CO;2.

Hourdin, F., T. Mauritsen, A. Gettelman, J.-C. Golaz, V. Balaji, Q. Duan, D. Folini, D. Ji, D. Klocke, Y. Qian, F. Rauser, C. Rio, L. Tomassini, M. Watanabe, and D. Williamson (2017). "The Art and Science of Climate Model Tuning." In: *Bulletin of the American Meteorological Society* 98.3, pp. 589–602. DOI: 10.1175/BAMS-D-15-00135.1.

Huffman, G., E. Stocker, D. Bolvin, E. Nelkin, and J. Tan (2019). *GPM IMERG Final Precipitation L3 Half Hourly 0.1 degree x 0.1 degree V06*. Accessed: 03/03/2022, distributed in netCDF file format by ICDC, CEN, University of Hamburg. DOI: 10.5067/GPM/IMERG/3B-HH/06.

Huffman, G., E. Stocker, D. Bolvin, E. Nelkin, and J. Tan (2022). *GPM IMERG Final Precipitation L3 Half Hourly 0.1 degree x 0.1 degree V06*. Accessed on 10/06/2023, distributed in netCDF file format by ICDC, CEN, University of Hamburg. DOI: 10.5067/GPM/IMERG/3B-HH/06.

Jablonowski, C. and D. L. Williamson (2011). "The Pros and Cons of Diffusion, Filters and Fixers in Atmospheric General Circulation Models." In: *Numerical Techniques for Global Atmospheric Models*. Ed. by P. Lauritzen, C. Jablonowski, M. Taylor, and R. Nair. Springer, pp. 381–493. ISBN: 978-3-642-11640-7. DOI: 10.1007/978-3-642-11640-7_13.

Judt, F. and R. Rios-Berrios (2021). "Resolved Convection Improves the Representation of Equatorial Waves and Tropical Rainfall Variability in a Global Non-hydrostatic Model." In: *Geophysical Research Letters* 48.14, e2021GL093265. DOI: 10.1029/2021GL093265.

Kang, M.-J. and H.-Y. Chun (2021). "Contributions of equatorial waves and small-scale convective gravity waves to the 2019/20 quasi-biennial oscillation (QBO) disruption." In: *Atmospheric Chemistry and Physics* 21.12, pp. 9839–9857. DOI: 10.5194/acp-21-9839-2021.

Kawatani, Y., K. Hamilton, and S. Watanabe (2011). "The Quasi-Biennial Oscillation in a Double CO_2 Climate." In: *Journal of the Atmospheric Sciences* 68.2, pp. 265–283. DOI: 10.1175/2010JAS3623.1.

Kawatani, Y. and K. Hamilton (2013). "Weakened stratospheric quasibiennial oscillation driven by increased tropical mean upwelling." In: *Nature* 497.7450, pp. 478–481. DOI: 10.1038/nature12140.

Kawatani, Y., K. Hamilton, and A. Noda (2012). "The Effects of Changes in Sea Surface Temperature and CO_2 Concentration on the Quasi-Biennial Oscillation." In: *Journal of the Atmospheric Sciences* 69.5, pp. 1734–1749. DOI: 10.1175/JAS-D-11-0265.1.

Kawatani, Y., M. Takahashi, K. Sato, S. P. Alexander, and T. Tsuda (2009). "Global distribution of atmospheric waves in the equatorial upper troposphere and lower stratosphere: AGCM simulation of sources and propagation." In: *Journal of Geophysical Research: Atmospheres* 114.D01102. DOI: 10.1029/2008JD010374.

Kawatani, Y., S. Watanabe, K. Sato, T. J. Dunkerton, S. Miyahara, and M. Takahashi (2010a). "The Roles of Equatorial Trapped Waves and Internal Inertia–Gravity Waves in Driving the Quasi-Biennial Oscillation. Part I: Zonal Mean Wave Forcing." In: *Journal of the Atmospheric Sciences* 67.4, pp. 963–980. DOI: 10.1175/2009JAS3222.1.

Kawatani, Y., S. Watanabe, K. Sato, T. J. Dunkerton, S. Miyahara, and M. Takahashi (2010b). "The Roles of Equatorial Trapped Waves and Internal Inertia–Gravity Waves in Driving the Quasi-Biennial Oscillation. Part II: Three-Dimensional Distribution of Wave Forcing." In: *Journal of the Atmospheric Sciences* 67.4, pp. 981–997. DOI: 10.1175/2009JAS3223.1.

Kidston, J., A. A. Scaife, S. C. Hardiman, D. M. Mitchell, N. Butchart, M. P. Baldwin, and L. J. Gray (2015). "Stratospheric influence on tropospheric jet streams, storm tracks and surface weather." In: *Nature Geoscience* 8.6, pp. 433–440. DOI: 10.1038/ngeo2424.

Kim, H., J. M. Caron, J. H. Richter, and I. R. Simpson (2020). "The Lack of QBO-MJO Connection in CMIP6 Models." In: *Geophysical Research Letters* 47.11, e2020GL087295. DOI: 10.1029/2020GL087295.

Kim, J.-E. and M. J. Alexander (2013). "Tropical Precipitation Variability and Convectively Coupled Equatorial Waves on Submonthly Time Scales in Reanalyses and TRMM." In: *Journal of Climate* 26.10, pp. 3013 –3030. DOI: 10.1175/JCLI-D-12-00353.1.

Kim, Y.-H., G. S. Voelker, G. Bölöni, G. Zängl, and U. Achatz (2023). "Crucial role of obliquely propagating gravity waves in the quasi-biennial oscillation dynamics." In: *EGUsphere* 2023, pp. 1–18. DOI: 10.5194/egusphere-2023-2663.

Kim, Y.-H., G. Bölöni, S. Borchert, H.-Y. Chun, and U. Achatz (2021). "Toward Transient Subgrid-Scale Gravity Wave Representation in Atmospheric Models. Part II: Wave Intermittency Simulated with Convective Sources." In: *Journal of the Atmospheric Sciences* 78.4, pp. 1339–1357. DOI: 10.1175/JAS-D-20-0066.1.

Kinne, S., D. O'Donnel, P. Stier, S. Kloster, K. Zhang, H. Schmidt, S. Rast, M. Giorgetta, T. F. Eck, and B. Stevens (2013). "MAC-v1: A new global aerosol climatology for climate studies." In: *Journal of Advances in Modeling Earth Systems* 5.4, pp. 704–740. DOI: 10.1002/jame.20035.

Kirchner, J. W. (2005). "Aliasing in $1/f^\alpha$ noise spectra: Origins, consequences, and remedies." In: *Physical Review E* 71.6. DOI: 10.1103/physreve.71.066110.

Klemp, J. B., J. Dudhia, and A. D. Hassiotis (2008). "An Upper Gravity-Wave Absorbing Layer for NWP Applications." In: *Monthly Weather Review* 136.10, pp. 3987–4004. DOI: 10.1175/2008MWR2596.1.

Kobayashi, S., Y. Ota, Y. Harada, A. Ebita, M. Moriya, H. Onoda, K. Onogi, H. Kamahori, C. Kobayashi, H. Endo, K. Miyaoka, and K. Takahashi (2015). "The JRA-55 Reanalysis: General Specifications and Basic Characteristics." In: *Journal of the Meteorological Society of Japan. Ser. II* 93.1, pp. 5–48. DOI: 10.2151/jmsj.2015-001.

Krismer, T. R. and M. A. Giorgetta (2014). "Wave Forcing of the Quasi-Biennial Oscillation in the Max Planck Institute Earth System Model." In: *Journal of the Atmospheric Sciences* 71.6, pp. 1985–2006. DOI: 10.1175/JAS-D-13-0310.1.

Lane, T. P. and J. C. Knievel (2005). "Some Effects of Model Resolution on Simulated Gravity Waves Generated by Deep, Mesoscale Convection." In: *Journal of the Atmospheric Sciences* 62.9, pp. 3408–3419. DOI: 10.1175/jas3513.1.

Lehmann, C. I., Y.-H. Kim, P. Preusse, H.-Y. Chun, M. Ern, and S.-Y. Kim (2012). "Consistency between Fourier transform and small-volume few-wave decomposition for spectral and spatial variability of gravity waves above a typhoon." In: *Atmospheric Measurement Techniques* 5.7, pp. 1637–1651. DOI: 10.5194/amt-5-1637-2012.

Leuenberger, D., M. Koller, O. Fuhrer, and C. Schär (2010). "A Generalization of the SLEVE Vertical Coordinate." In: *Monthly Weather Review* 138.9, pp. 3683–3689. DOI: 10.1175/2010MWR3307.1.

Liess, S. and M. A. Geller (2012). "On the relationship between QBO and distribution of tropical deep convection." In: *Journal of Geophysical Research: Atmospheres* 117.D3. DOI: 10.1029/2011JD016317.

Lim, Y., S.-W. Son, A. G. Marshall, H. H. Hendon, and K.-H. Seo (2019). "Influence of the QBO on MJO prediction skill in the subseasonal-to-seasonal prediction models." In: *Climate Dynamics* 53.3–4, pp. 1681–1695. DOI: 10.1007/s00382-019-04719-y.

Lin, J.-L., M.-I. Lee, D. Kim, I.-S. Kang, and D. M. W. Frierson (2008). "The Impacts of Convective Parameterization and Moisture Triggering on AGCM-Simulated Convectively Coupled Equatorial Waves." In: *Journal of Climate* 21.5, pp. 883–909. DOI: 10.1175/2007JCLI1790.1.

Lindzen, R. S. and J. R. Holton (1968). "A Theory of the Quasi-Biennial Oscillation." In: *Journal of the Atmospheric Sciences* 25.6, pp. 1095–1107. DOI: 10.1175/1520-0469(1968)025<1095:ATOTQB>2.0.CO;2.

Logan, J. A., D. B. A. Jones, I. A. Megretskaia, S. J. Oltmans, B. J. Johnson, H. Vömel, W. J. Randel, W. Kimani, and F. J. Schmidlin (2003). "Quasibiennial oscillation in tropical ozone as revealed by ozonesonde and satellite data." In: *Journal of Geophysical Research: Atmospheres* 108.D8. DOI: 10.1029/2002JD002170.

Lott, F., S. Denvil, N. Butchart, C. Cagnazzo, M. A. Giorgetta, S. C. Hardiman, E. Manzini, T. Krismer, J.-P. Duvel, P. Maury, J. F. Scinocca, S. Watanabe, and S. Yukimoto (2014). "Kelvin and Rossby-gravity wave packets in the lower stratosphere of some high-top CMIP5 models." In: *Journal of Geophysical Research: Atmospheres* 119.5, pp. 2156–2173. DOI: 10.1002/2013JD020797.

MPI-M (2023). *Climate modelling at the Max Planck Institute for Meteorology: Code availability and licenses*. URL: https://mpimet.mpg.de/en/research/modeling (visited on 09/14/2023).

Marsham, J. H., N. S. Dixon, L. Garcia-Carreras, G. M. S. Lister, D. J. Parker, P. Knippertz, and C. E. Birch (2013). "The role of moist convection in the West African monsoon system: Insights from continental-scale convection-permitting simulations." In: *Geophysical Research Letters* 40.9, pp. 1843–1849. DOI: 10.1002/grl.50347.

Martin, Z., S.-W. Son, A. Butler, H. Hendon, H. Kim, A. Sobel, S. Yoden, and C. Zhang (2021). "The influence of the quasi-biennial oscillation on the Madden–Julian oscillation." In: *Nature Reviews Earth & Environment* 2.7, pp. 477–489. DOI: 10.1038/s43017-021-00173-9.

Match, A. and S. Fueglistaler (2021). "Large Internal Variability Dominates over Global Warming Signal in Observed Lower Stratospheric QBO Amplitude." In: *Journal of Climate* 34.24, pp. 9823–9836. DOI: 10.1175/JCLI-D-21-0270.1.

Matsuno, T. (1966). "Quasi-Geostrophic Motions in the Equatorial Area." In: *Journal of the Meteorological Society of Japan. Ser. II* 44.1, pp. 25–43. DOI: 10.2151/jmsj1965.44.1_25.

Mauritsen, T., G. Svensson, S. S. Zilitinkevich, I. Esau, L. Enger, and B. Grisogono (2007). "A Total Turbulent Energy Closure Model for Neutrally and Stably Stratified Atmospheric Boundary Layers." In: *Journal of the Atmospheric Sciences* 64.11, pp. 4113–4126. DOI: 10.1175/2007JAS2294.1.

Maury, P., F. Lott, L. Guez, and J.-P. Duvel (2013). "Tropical variability and stratospheric equatorial waves in the IPSLCM5 model." In: *Climate Dynamics* 40.9–10, pp. 2331–2344. DOI: 10.1007/s00382-011-1273-0.

Meinshausen, M. et al. (2017). "Historical greenhouse gas concentrations for climate modelling (CMIP6)." In: *Geoscientific Model Development* 10.5, pp. 2057–2116. DOI: 10.5194/gmd-10-2057-2017.

Morfa, Y. A. and C. C. Stephan (2023). "The Relationship Between Horizontal and Vertical Velocity Wavenumber Spectra in Global Storm-resolving Simulations." In: *Journal of the Atmospheric Sciences* 80, pp. 1087–1105. DOI: 10.1175/JAS-D-22-0105.1.

Mote, P. W., K. H. Rosenlof, M. E. McIntyre, E. S. Carr, J. C. Gille, J. R. Holton, J. S. Kinnersley, H. C. Pumphrey, J. M. Russell III, and J. W. Waters (1996). "An atmospheric tape recorder: The imprint of tropical tropopause temperatures on

stratospheric water vapor." In: *Journal of Geophysical Research: Atmospheres* 101.D2, pp. 3989–4006. DOI: doi.org/10.1029/95JD03422.

Müller, S. K., E. Manzini, M. Giorgetta, K. Sato, and T. Nasuno (2018). "Convectively Generated Gravity Waves in High Resolution Models of Tropical Dynamics." In: *Journal of Advances in Modeling Earth Systems* 10.10, pp. 2564–2588. DOI: 10.1029/2018MS001390.

NASA/GSFC (2024). *The quasi-biennial oscillation*. URL: https://acd-ext.gsfc.nasa.gov/Data_services/met/qbo/ (visited on 01/08/2024).

NOAA/NCEI (2022). *Monthly Global Climate Report for Annual 2021*. URL: https://www.ncei.noaa.gov/access/monitoring/monthly-report/global/202113 (visited on 01/11/2023).

Nastrom, G. D. and K. S. Gage (1985). "A climatology of atmospheric wavenumber spectra of wind and temperature observed by commercial aircraft." In: *J. Atmos. Sci* 42, pp. 950–960.

Naujokat, B. (1986). "An Update of the Observed Quasi-Biennial Oscillation of the Stratospheric Winds over the Tropics." In: *Journal of the Atmospheric Sciences* 43.17, pp. 1873–1877. DOI: 10.1175/1520-0469(1986)043<1873:AUOTOQ>2.0.CO;2.

Neumann, P., P. Düben, P. Adamidis, P. Bauer, M. Brück, L. Kornblueh, D. Klocke, B. Stevens, N. Wedi, and J. Biercamp (2019). "Assessing the scales in numerical weather and climate predictions: will exascale be the rescue?" In: *Philosophical Transactions of the Royal Society A: Mathematical, Physical and Engineering Sciences* 377.2142, p. 20180148. DOI: 10.1098/rsta.2018.0148.

O'Neill, B. C., C. Tebaldi, D. P. van Vuuren, V. Eyring, P. Friedlingstein, G. Hurtt, R. Knutti, E. Kriegler, J.-F. Lamarque, J. Lowe, G. A. Meehl, R. Moss, K. Riahi, and B. M. Sanderson (2016). "The Scenario Model Intercomparison Project (ScenarioMIP) for CMIP6." In: *Geoscientific Model Development* 9.9, pp. 3461–3482. DOI: 10.5194/gmd-9-3461-2016.

Orr, A., P. Bechtold, J. Scinocca, M. Ern, and M. Janiskova (2010). "Improved Middle Atmosphere Climate and Forecasts in the ECMWF Model through a Nonorographic Gravity Wave Drag Parameterization." In: *Journal of Climate* 23.22, pp. 5905–5926. DOI: 10.1175/2010JCLI3490.1.

Osprey, S. M., N. Butchart, J. R. Knight, A. A. Scaife, K. Hamilton, J. A. Anstey, V. Schenzinger, and C. Zhang (2016). "An unexpected disruption of the atmospheric quasi-biennial oscillation." In: *Science* 353.6306, pp. 1424–1427. DOI: 10.1126/science.aah4156.

Pahlavan, H. A., Q. Fu, J. M. Wallace, and G. N. Kiladis (2021a). "Revisiting the Quasi-Biennial Oscillation as Seen in ERA5. Part I: Description and Momentum Budget." In: *Journal of the Atmospheric Sciences* 78.3, pp. 673–691. DOI: 10.1175/JAS-D-20-0248.1.

Pahlavan, H. A., J. M. Wallace, Q. Fu, and G. N. Kiladis (2021b). "Revisiting the Quasi-Biennial Oscillation as Seen in ERA5. Part II: Evaluation of Waves and Wave Forcing." In: *Journal of the Atmospheric Sciences* 78.3, pp. 693–707. DOI: 10.1175/JAS-D-20-0249.1.

Pincus, R., E. J. Mlawer, and J. S. Delamere (2019). "Balancing Accuracy, Efficiency, and Flexibility in Radiation Calculations for Dynamical Models." In: *Journal of Advances in Modeling Earth Systems* 11, pp. 3074–3089. DOI: 10.1029/2019MS001621.

Pithan, F., W. Angevine, and T. Mauritsen (2015). "Improving a global model from the boundary layer: Total turbulent energy and the neutral limit Prandtl

number." In: *Journal of Advances in Modeling Earth Systems* 7.2, pp. 791–805. DOI: 10.1002/2014ms000382.

Plougonven, R., A. de la Cámara, A. Hertzog, and F. Lott (2020). "How does knowledge of atmospheric gravity waves guide their parameterizations?" In: *Quarterly Journal of the Royal Meteorological Society* 146.728, pp. 1529–1543. DOI: 10.1002/qj.3732.

Plumb, R. A. (1977). "The Interaction of Two Internal Waves with the Mean Flow: Implications for the Theory of the Quasi-Biennial Oscillation." In: *Journal of Atmospheric Sciences* 34.12. DOI: 10.1175/1520-0469(1977)034<1847:TIOTIW>2.0.CO;2.

Plumb, R. A. and R. C. Bell (1982). "A model of the quasi-biennial oscillation on an equatorial beta-plane." In: *Quarterly Journal of the Royal Meteorological Society* 108.456, pp. 335–352. DOI: 10.1002/qj.49710845604.

Polichtchouk, I., N. Wedi, and Y.-H. Kim (2021). "Resolved gravity waves in the tropical stratosphere: Impact of horizontal resolution and deep convection parametrization." In: *Quarterly Journal of the Royal Meteorological Society* 148.742, pp. 233–251. DOI: 10.1002/qj.4202.

Prein, A. F., A. Gobiet, M. Suklitsch, H. Truhetz, N. K. Awan, K. Keuler, and G. Georgievski (2013). "Added value of convection permitting seasonal simulations." In: *Climate Dynamics* 41.9–10, pp. 2655–2677. DOI: 10.1007/s00382-013-1744-6.

Prein, A. F., W. Langhans, G. Fosser, A. Ferrone, N. Ban, K. Goergen, M. Keller, M. Tölle, O. Gutjahr, F. Feser, E. Brisson, S. Kollet, J. Schmidli, N. P. M. van Lipzig, and R. Leung (2015). "A review on regional convection-permitting climate modeling: Demonstrations, prospects, and challenges." In: *Reviews of Geophysics* 53.2, pp. 323–361. DOI: 10.1002/2014RG000475.

Preusse, P., S. D. Eckermann, and M. Ern (2008). "Transparency of the atmosphere to short horizontal wavelength gravity waves." In: *Journal of Geophysical Research: Atmospheres* 113.D24. DOI: 10.1029/2007JD009682.

Quaglia, I., C. Timmreck, U. Niemeier, D. Visioni, G. Pitari, C. Brodowsky, C. Brühl, S. S. Dhomse, H. Franke, A. Laakso, G. W. Mann, E. Rozanov, and T. Sukhodolov (2023). "Interactive stratospheric aerosol models' response to different amounts and altitudes of SO_2 injection during the 1991 Pinatubo eruption." In: *Atmospheric Chemistry and Physics* 23.2, pp. 921–948. DOI: 10.5194/acp-23-921-2023.

Randel, W. J., F. Wu, J. M. Russell, A. Roche, and J. W. Waters (1998). "Seasonal Cycles and QBO Variations in Stratospheric CH_4 and H_2O Observed in UARS HALOE Data." In: *Journal of the Atmospheric Sciences* 55.2, pp. 163–185. DOI: 10.1175/1520-0469(1998)055<0163:SCAQVI>2.0.CO;2.

Reed, R. J. (1964). "A tentative model of the 26-month oscillation in tropical latitudes." In: *Quarterly Journal of the Royal Meteorological Society* 90.386, pp. 441–466. DOI: 10.1002/qj.49709038607.

Reed, R. J. (1967). "The structure and dynamics of the 26-month oscillation." In: *Proceedings of the International Symposium on the Dynamics of Large-Scale Processes in the Atmosphere*, pp. 376–387.

Reed, R. J., W. J. Campbell, L. A. Rasmussen, and D. G. Rogers (1961). "Evidence of a downward-propagating, annual wind reversal in the equatorial stratosphere." In: *Journal of Geophysical Research (1896-1977)* 66.3, pp. 813–818. DOI: 10.1029/JZ066i003p00813.

Ricciardulli, L. and R. R. Garcia (2000). "The Excitation of Equatorial Waves by Deep Convection in the NCAR Community Climate Model (CCM3)." In: *Journal of the Atmospheric Sciences* 57.21, pp. 3461–3487. DOI: `10.1175/1520-0469(2000)057<3461:TEOEWB>2.0.CO;2`.

Richter, J. H., J. A. Anstey, N. Butchart, Y. Kawatani, G. A. Meehl, S. Osprey, and I. R. Simpson (2020a). "Progress in Simulating the Quasi-Biennial Oscillation in CMIP Models." In: *Journal of Geophysical Research: Atmospheres* 125.8, e2019JD032362. DOI: `10.1029/2019JD032362`.

Richter, J. H., F. Sassi, and R. R. Garcia (2010). "Toward a Physically Based Gravity Wave Source Parameterization in a General Circulation Model." In: *Journal of the Atmospheric Sciences* 67.1, pp. 136–156. DOI: `10.1175/2009JAS3112.1`.

Richter, J. H. et al. (2020b). "Response of the Quasi-Biennial Oscillation to a warming climate in global climate models." In: *Quarterly Journal of the Royal Meteorological Society* 148.744, pp. 1490–1518. DOI: `10.1002/qj.3749`.

Rios-Berrios, R., F. Judt, G. Bryan, B. Medeiros, and W. Wang (2023). "Three-Dimensional Structure of Convectively Coupled Equatorial Waves in Aquaplanet Experiments with Resolved or Parameterized Convection." In: *Journal of Climate* 36.9, pp. 2895–2915. DOI: `10.1175/JCLI-D-22-0422.1`.

Russell, F. A. R. (1888). "Spread of the pheonmena round the world, with maps illustrative thereof." In: *The Eruption of Krakatoa and Subsequent Phenomena*, pp. 334–339.

SPARC (2022). *SPARC Reanalysis Intercomparison Project (S-RIP) Final Report*. DOI: `10.17874/800DEE57D13`.

Salby, M. L. and R. R. Garcia (1987). "Transient Response to Localized Episodic Heating in the Tropics. Part I: Excitation and Short-Time Near-Field Behavior." In: *Journal of Atmospheric Sciences* 44.2, pp. 458–498. DOI: `10.1175/1520-0469(1987)044<0458:TRTLEH>2.0.CO;2`.

Saravanan, R. (1990). "A Multiwave Model of the Quasi-biennial Oscillation." In: *Journal of Atmospheric Sciences* 47.21, pp. 2465–2474. DOI: `10.1175/1520-0469(1990)047<2465:AMMOTQ>2.0.CO;2`.

Satoh, M., T. Matsuno, H. Tomita, H. Miura, T. Nasuno, and S. Iga (2008). "Non-hydrostatic icosahedral atmospheric model (NICAM) for global cloud resolving simulations." In: *Journal of Computational Physics* 227.7, pp. 3486–3514. DOI: `10.1016/j.jcp.2007.02.006`.

Satoh, M., B. Stevens, F. Judt, M. Khairoutdinov, S.-J. Lin, W. M. Putman, and P. Düben (2019). "Global Cloud-Resolving Models." In: *Current Climate Change Reports* 5.3, pp. 172–184. DOI: `10.1007/s40641-019-00131-0`.

Satoh, M., H. Tomita, H. Yashiro, Y. Kajikawa, Y. Miyamoto, T. Yamaura, T. Miyakawa, M. Nakano, C. Kodama, A. T. Noda, T. Nasuno, Y. Yamada, and Y. Fukutomi (2017). "Outcomes and challenges of global high-resolution non-hydrostatic atmospheric simulations using the K computer." In: *Progress in Earth and Planetary Science* 4.1. DOI: `10.1186/s40645-017-0127-8`.

Savitzky, A. and M. J. Golay (1964). "Smoothing and differentiation of data by simplified least squares procedures." In: *Analytical chemistry* 36.8, pp. 1627–1639.

Scaife, A. A., N. Butchart, C. D. Warner, and R. Swinbank (2002). "Impact of a Spectral Gravity Wave Parameterization on the Stratosphere in the Met Office Unified Model." In: *Journal of the Atmospheric Sciences* 59.9, pp. 1473–1489. DOI: `10.1175/1520-0469(2002)059<1473:IOASGW>2.0.CO;2`.

Scaife, A. A., M. Athanassiadou, M. Andrews, A. Arribas, M. Baldwin, N. Dunstone, J. Knight, C. MacLachlan, E. Manzini, W. A. Müller, H. Pohlmann, D. Smith, T. Stockdale, and A. Williams (2014). "Predictability of the quasi-biennial oscillation and its northern winter teleconnection on seasonal to decadal timescales." In: *Geophysical Research Letters* 41.5, pp. 1752–1758. DOI: 10.1002/2013GL059160.

Scaife, A. A., N. Butchart, C. D. Warner, D. Stainforth, W. Norton, and J. Austin (2000). "Realistic quasi-biennial oscillations in a simulation of the global climate." In: *Geophysical Research Letters* 27.21, pp. 3481–3484. DOI: 10.1029/2000GL011625.

Schenzinger, V., S. Osprey, L. Gray, and N. Butchart (2017). "Defining metrics of the Quasi-Biennial Oscillation in global climate models." In: *Geoscientific Model Development* 10.6, pp. 2157–2168. DOI: 10.5194/gmd-10-2157-2017.

Schirber, S., E. Manzini, T. Krismer, and M. Giorgetta (2015). "The quasi-biennial oscillation in a warmer climate: sensitivity to different gravity wave parameterizations." In: *Climate Dynamics* 45.3-4, pp. 825–836. DOI: 10.1007/s00382-014-2314-2.

Schoeberl, M. R., A. R. Douglass, P. A. Newman, L. R. Lait, D. Lary, J. Waters, N. Livesey, L. Froidevaux, A. Lambert, W. Read, M. J. Filipiak, and H. C. Pumphrey (2008). "QBO and annual cycle variations in tropical lower stratosphere trace gases from HALOE and Aura MLS observations." In: *Journal of Geophysical Research: Atmospheres* 113.D5. DOI: 10.1029/2007JD008678.

Shepherd, T., R. A. Plumb, and S. C. Wofsy (2005). "Preface to J. Atmos. Sci. special issue on the Antarctic stratospheric sudden warming and split ozone hole of 2002." In: *Journal of the Atmospheric Sciences* 62.3, pp. 565–566. DOI: 10.1175/JAS-9999.1.

Shepherd, T. G. and C. McLandress (2011). "A Robust Mechanism for Strengthening of the Brewer–Dobson Circulation in Response to Climate Change: Critical-Layer Control of Subtropical Wave Breaking." In: *Journal of the Atmospheric Sciences* 68.4, pp. 784–797. DOI: 10.1175/2010JAS3608.1.

Shuckburgh, E., W. Norton, A. Iwi, and P. Haynes (2001). "Influence of the quasi-biennial oscillation on isentropic transport and mixing in the tropics and subtropics." In: *Journal of Geophysical Research: Atmospheres* 106.D13, pp. 14327–14337. DOI: 10.1029/2000JD900664.

Simmons, A., C. Soci, J. Nicolas, B. Bell, P. Berrisford, R. Dragani, J. Flemming, L. Haimberger, S. Healy, H. Hersbach, A. Horányi, A. Inness, J. Munoz-Sabater, R. Radu, and D. Schepers (2020). "Global stratospheric temperature bias and other stratospheric aspects of ERA5 and ERA5.1." In: *ECMWF Technical Memoranda* 859. DOI: 10.21957/rcxqfmg0.

Skamarock, W. C. (2004). "Evaluating Mesoscale NWP Models Using Kinetic Energy Spectra." In: *Monthly Weather Review* 132.12, pp. 3019–3032. DOI: 10.1175/MWR2830.1.

Skamarock, W. C., S. H. Park, J. B. Klemp, and C. Snyder (2014). "Atmospheric Kinetic Energy Spectra from Global High-Resolution Nonhydrostatic Simulations." In: *Journal of the Atmospheric Sciences* 71 (11), pp. 4369–4381. DOI: 10.1175/JAS-D-14-0114.1.

Skamarock, W. C., C. Snyder, J. B. Klemp, and S.-H. Park (2019). "Vertical Resolution Requirements in Atmospheric Simulation." In: *Monthly Weather Review* 147.7, pp. 2641–2656. DOI: 10.1175/MWR-D-19-0043.1.

Son, S.-W., Y. Lim, C. Yoo, H. H. Hendon, and J. Kim (2017). "Stratospheric Control of the Madden–Julian Oscillation." In: *Journal of Climate* 30.6, pp. 1909–1922. DOI: 10.1175/JCLI-D-16-0620.1.

Stephan, C. C., C. Strube, D. Klocke, M. Ern, L. Hoffmann, P. Preusse, and H. Schmidt (2019a). "Gravity Waves in Global High-Resolution Simulations With Explicit and Parameterized Convection." In: *Journal of Geophysical Research: Atmospheres* 124.8, pp. 4446–4459. DOI: 10.1029/2018jd030073.

Stephan, C. C., C. Strube, D. Klocke, M. Ern, L. Hoffmann, P. Preusse, and H. Schmidt (2019b). "Intercomparison of Gravity Waves in Global Convection-Permitting Models." In: *Journal of the Atmospheric Sciences* 76.9, pp. 2739–2759. DOI: 10.1175/JAS-D-19-0040.1.

Stevens, B. et al. (2019). "DYAMOND: the DYnamics of the Atmospheric general circulation Modeled On Non-hydrostatic Domains." In: *Progress in Earth and Planetary Science* 6.61. DOI: 10.1186/s40645-019-0304-z.

Stevens, B. et al. (2020). "The Added Value of Large-eddy and Storm-resolving Models for Simulating Clouds and Precipitation." In: *Journal of the Meteorological Society of Japan. Ser. II* 98.2, pp. 395–435. DOI: 10.2151/jmsj.2020-021.

Stockdale, T. N. et al. (2020). "Prediction of the quasi-biennial oscillation with a multi-model ensemble of QBO-resolving models." In: *Quarterly Journal of the Royal Meteorological Society*. DOI: 10.1002/qj.3919.

Straub, K. H., P. T. Haertel, and G. N. Kiladis (2010). "An Analysis of Convectively Coupled Kelvin Waves in 20 WCRP CMIP3 Global Coupled Climate Models." In: *Journal of Climate* 23.11, pp. 3031–3056. DOI: 10.1175/2009JCLI3422.1.

Strube, C., M. Ern, P. Preusse, and M. Riese (2020). "Removing spurious inertial instability signals from gravity wave temperature perturbations using spectral filtering methods." In: *Atmospheric Measurement Techniques* 13.9, pp. 4927–4945. DOI: 10.5194/amt-13-4927-2020.

Takahashi, M. (1996). "Simulation of the stratospheric Quasi-Biennial Oscillation using a general circulation model." In: *Geophysical Research Letters* 23.6, pp. 661–664. DOI: 10.1029/95GL03413.

Takahashi, M. (1999). "Simulation of the Quasi-Biennial Oscillation in a general circulation model." In: *Geophysical Research Letters* 26.9, pp. 1307–1310. DOI: 10.1029/1999GL900188.

Takasuka, D., C. Kodama, T. Suematsu, T. Ohno, Y. Yamada, T. Seiki, H. Yashiro, M. Nakano, H. Miura, A. T. Noda, T. Nasuno, T. Miyakawa, and R. Masunaga (2024). "How Can We Improve the Seamless Representation of Climatological Statistics and Weather Toward Reliable Global K-Scale Climate Simulations?" In: *Journal of Advances in Modeling Earth Systems* 16.2, e2023MS003701. DOI: 10.1029/2023MS003701.

Terasaki, K., H. L. Tanaka, and M. Satoh (2009). "Characteristics of the Kinetic Energy Spectrum of NICAM Model Atmosphere." In: *SOLA* 5 (1), pp. 180–183. DOI: 10.2151/SOLA.2009-046.

Tian, B. and X. Dong (2020). "The Double-ITCZ Bias in CMIP3, CMIP5, and CMIP6 Models Based on Annual Mean Precipitation." In: *Geophysical Research Letters* 47.8. e2020GL087232. DOI: 10.1029/2020GL087232.

Tomassini, L., M. Willett, A. Sellar, A. Lock, D. Walters, M. Whitall, C. Sanchez, J. Heming, P. Earnshaw, J. M. Rodriguez, D. Ackerley, P. Xavier, C. Franklin, and C. A. Senior (2023). "Confronting the Convective Gray Zone in the Global

Configuration of the Met Office Unified Model." In: *Journal of Advances in Modeling Earth Systems* 15.5, e2022MS003418. DOI: 10.1029/2022MS003418.

Tomita, H. and M. Satoh (2004). "A new dynamical framework of nonhydrostatic global model using the icosahedral grid." In: *Fluid Dynamics Research* 34.6, pp. 357–400. DOI: 10.1016/j.fluiddyn.2004.03.003.

Trepte, C. R. and M. H. Hitchman (1992). "Tropical stratospheric circulation deduced from satellite aerosol data." In: *Nature* 355.6361, pp. 626–628. DOI: 10.1038/355626a0.

Vergara-Temprado, J., N. Ban, D. Panosetti, L. Schlemmer, and C. Schär (2020). "Climate Models Permit Convection at Much Coarser Resolutions Than Previously Considered." In: *Journal of Climate* 33.5, pp. 1915–1933. DOI: 10.1175/JCLI-D-19-0286.1.

Veryard, R. G. and R. A. Ebdon (1961). "Fluctuations in tropical stratospheric winds." In: *Meteorol. Mag.* 90, pp. 125–143.

Vincent, R. A. and M. J. Alexander (2000). "Gravity waves in the tropical lower stratosphere: An observational study of seasonal and interannual variability." In: *Journal of Geophysical Research: Atmospheres* 105.D14, pp. 17971–17982. DOI: 10.1029/2000JD900196.

Wallace, J. M. (1973). "General circulation of the tropical lower stratosphere." In: *Reviews of Geophysics* 11.2, pp. 191–222. DOI: doi.org/10.1029/RG011i002p00191.

Wan, H., M. A. Giorgetta, G. Zängl, M. Restelli, D. Majewski, L. Bonaventura, K. Fröhlich, D. Reinert, P. Rípodas, L. Kornblueh, and J. Förstner (2013). "The ICON-1.2 hydrostatic atmospheric dynamical core on triangular grids – Part 1: Formulation and performance of the baseline version." In: *Geoscientific Model Development* 6.3, pp. 735–763. DOI: 10.5194/gmd-6-735-2013.

Watanabe, S. and Y. Kawatani (2012). "Sensitivity of the QBO to Mean Tropical Upwelling under a Changing Climate Simulated with an Earth System Model." In: *J. Meteor. Soc. Japan* 90A, pp. 351–360. DOI: 10.2151/jmsj.2012-A20.

Watanabe, S., T. Nagashima, and S. Emori (2005). "Impact of Global Warming on Gravity Wave Momentum Flux in the Lower Stratosphere." In: *SOLA* 1, pp. 189–192. DOI: 10.2151/sola.2005-049.

Weisenstein, D. K., D. Visioni, H. Franke, U. Niemeier, S. Vattioni, G. Chiodo, T. Peter, and D. W. Keith (2022). "An interactive stratospheric aerosol model intercomparison of solar geoengineering by stratospheric injection of SO_2 or accumulation-mode sulfuric acid aerosols." In: *Atmospheric Chemistry and Physics* 22.5, pp. 2955–2973. DOI: 10.5194/acp-22-2955-2022.

Wheeler, M. and G. N. Kiladis (1999). "Convectively Coupled Equatorial Waves: Analysis of Clouds and Temperature in the Wavenumber–Frequency Domain." In: *Journal of the Atmospheric Sciences* 56.3, pp. 374–399. DOI: 10.1175/1520-0469(1999)056<0374:CCEWAO>2.0.CO;2.

Yao, W. and C. Jablonowski (2013). "Spontaneous QBO-like oscillations in an atmospheric model dynamical core." In: *Geophysical Research Letters* 40.14, pp. 3772–3776. DOI: 10.1002/grl.50723.

Yao, W. and C. Jablonowski (2015). "Idealized Quasi-Biennial Oscillations in an Ensemble of Dry GCM Dynamical Cores." In: *Journal of the Atmospheric Sciences* 72.6, pp. 2201–2226. DOI: 10.1175/JAS-D-14-0236.1.

Yoo, C. and S.-W. Son (2016). "Modulation of the boreal wintertime Madden-Julian oscillation by the stratospheric quasi-biennial oscillation." In: *Geophysical Research Letters* 43.3, pp. 1392–1398. DOI: 10.1002/2016GL067762.

Zawodny, J. M. and M. P. McCormick (1991). "Stratospheric Aerosol and Gas Experiment II measurements of the quasi-biennial oscillations in ozone and nitrogen dioxide." In: *Journal of Geophysical Research: Atmospheres* 96.D5, pp. 9371–9377. DOI: 10.1029/91JD00517.

Zhou, T., K. DallaSanta, L. Nazarenko, G. A. Schmidt, and Z. Jin (2021). "The impact of increasing stratospheric radiative damping on the quasi-biennial oscillation period." In: *Atmospheric Chemistry and Physics* 21.9, pp. 7395–7407. DOI: 10.5194/acp-21-7395-2021.

Zängl, G., D. Reinert, P. Rípodas, and M. Baldauf (2015). "The ICON (ICOsahedral Non-hydrostatic) modelling framework of DWD and MPI-M: Description of the non-hydrostatic dynamical core." In: *Quarterly Journal of the Royal Meteorological Society* 141.687, pp. 563–579. DOI: 10.1002/qj.2378.

EIDESSTATTLICHE VERSICHERUNG

Eidesstattliche Versicherung
Declaration on Oath

Hiermit erkläre ich an Eides statt, dass ich die vorliegende Dissertationsschrift selbst verfasst und keine anderen als die angegebenen Quellen und Hilfsmittel benutzt habe.

I hereby declare upon oath that I have written the present dissertation independently and have not used further resources and aids than those stated.

Hamburg, den 26. Januar 2024
Hamburg, January 26, 2024

Henning Franke

ERKLÄRUNG

Ich versichere, dass dieses gebundene Exemplar der Dissertation und das in elektronischer Form eingereichte Dissertationsexemplar (über den Docata-Upload) und das bei der Fakultät (zuständiges Studienbüro) zur Archivierung eingereichte gedruckte gebundene Exemplar der Dissertationsschrift identisch sind.

I, the undersigned, declare that this bound copy of the dissertation and the dissertation submitted in electronic form (via the Docata upload) and the printed bound copy of the dissertation submitted to the faculty (responsible Academic Office) for archiving are identical.

Hamburg, den 26. Januar 2024
Hamburg, January 26, 2024

_____
Henning Franke

Hinweis / Reference

Die gesamten Veröffentlichungen in der Publikationsreihe des MPI-M
„Berichte zur Erdsystemforschung / Reports on Earth System Science",
ISSN 1614-1199

sind über die Internetseiten des Max-Planck-Instituts für Meteorologie erhältlich:
https://mpimet.mpg.de/forschung/publikationen

All the publications in the series of the MPI -M
„Berichte zur Erdsystemforschung / Reports on Earth System Science",
ISSN 1614-1199

are available on the website of the Max Planck Institute for Meteorology:
https://mpimet.mpg.de/en/research/publications